



micromachines

Micro/Nano Devices for Blood Analysis

Edited by

Rui A. Lima, Graça Minas and Susana Catarino

Printed Edition of the Special Issue Published in *Micromachines*

Micro/Nano Devices for Blood Analysis

Micro/Nano Devices for Blood Analysis

Special Issue Editors

Rui A. Lima

Graça Minas

Susana Catarino

MDPI • Basel • Beijing • Wuhan • Barcelona • Belgrade



Special Issue Editors

Rui A. Lima
Minho University
Portugal

Graça Minas
Minho University
Portugal

Susana Catarino
Universidade do Minho
Portugal

Editorial Office

MDPI
St. Alban-Anlage 66
4052 Basel, Switzerland

This is a reprint of articles from the Special Issue published online in the open access journal *Micromachines* (ISSN 2072-666X) from 2018 to 2019 (available at: https://www.mdpi.com/journal/micromachines/special_issues/micro_nano_devices_for_blood_analysis).

For citation purposes, cite each article independently as indicated on the article page online and as indicated below:

LastName, A.A.; LastName, B.B.; LastName, C.C. Article Title. <i>Journal Name</i> Year , Article Number, Page Range.

ISBN 978-3-03921-824-0 (Pbk)

ISBN 978-3-03921-825-7 (PDF)

Cover image courtesy of Rui A. Lima, Graça Minas and Susana Catarino.

© 2019 by the authors. Articles in this book are Open Access and distributed under the Creative Commons Attribution (CC BY) license, which allows users to download, copy and build upon published articles, as long as the author and publisher are properly credited, which ensures maximum dissemination and a wider impact of our publications.

The book as a whole is distributed by MDPI under the terms and conditions of the Creative Commons license CC BY-NC-ND.

Contents

About the Special Issue Editors vii

Susana O. Catarino, Graça Minas and Rui Lima

Editorial for the Special Issue on Micro/Nano Devices for Blood Analysis
Reprinted from: *Micromachines* **2019**, *10*, 708, doi:10.3390/mi10100708 1

Susana O. Catarino, Raquel O. Rodrigues, Diana Pinho, João M. Miranda, Graça Minas and Rui Lima

Blood Cells Separation and Sorting Techniques of Passive Microfluidic Devices: From Fabrication to Applications
Reprinted from: *Micromachines* **2019**, *10*, 593, doi:10.3390/mi10090593 5

Misa Kawaguchi, Tomohiro Fukui, Kenichi Funamoto, Miho Tanaka, Mitsuru Tanaka, Shigeru Murata, Suguru Miyauchi and Toshiyuki Hayase

Viscosity Estimation of a Suspension with Rigid Spheres in Circular Microchannels Using Particle Tracking Velocimetry
Reprinted from: *Micromachines* **2019**, *10*, 675, doi:10.3390/mi10100675 25

Naoki Takeishi, Hiroaki Ito, Makoto Kaneko and Shigeo Wada

Deformation of a Red Blood Cell in a Narrow Rectangular Microchannel
Reprinted from: *Micromachines* **2019**, *10*, 199, doi:10.3390/mi10030199 38

Vera Faustino, Raquel O. Rodrigues, Diana Pinho, Elísio Costa, Alice Santos-Silva, Vasco Miranda, Joana S. Amaral and Rui Lima

A Microfluidic Deformability Assessment of Pathological Red Blood Cells Flowing in a Hyperbolic Converging Microchannel
Reprinted from: *Micromachines* **2019**, *10*, 645, doi:10.3390/mi10100645 53

Liliana Vilas Boas, Vera Faustino, Rui Lima, João Mário Miranda, Graça Minas, Carla Sofia Veiga Fernandes and Susana Oliveira Catarino

Assessment of the Deformability and Velocity of Healthy and Artificially Impaired Red Blood Cells in Narrow Polydimethylsiloxane (PDMS) Microchannels
Reprinted from: *Micromachines* **2018**, *9*, 384, doi:10.3390/mi9080384 68

Yang Jun Kang and Byung Jun Kim

Multiple and Periodic Measurement of RBC Aggregation and ESR in Parallel Microfluidic Channels under On-Off Blood Flow Control
Reprinted from: *Micromachines* **2018**, *9*, 318, doi:10.3390/mi9070318 84

J. Ponmozhi, J. M. R. Moreira, F. J. Mergulhão, J. B. L. M. Campos and J. M. Miranda

Fabrication and Hydrodynamic Characterization of a Microfluidic Device for Cell Adhesion Tests in Polymeric Surfaces
Reprinted from: *Micromachines* **2019**, *10*, 303, doi:10.3390/mi10050303 101

Shukei Sugita, Risa Munechika and Masanori Nakamura

Multinucleation of Incubated Cells and Their Morphological Differences Compared to Mononuclear Cells
Reprinted from: *Micromachines* **2019**, *10*, 156, doi:10.3390/mi10020156 117

Masanori Nakamura, Daichi Ono and Shukei Sugita

Mechanophenotyping of B16 Melanoma Cell Variants for the Assessment of the Efficacy of (-)-Epigallocatechin Gallate Treatment Using a Tapered Microfluidic Device

Reprinted from: *Micromachines* **2019**, *10*, 207, doi:10.3390/mi10030207 **127**

Zhigang Gao, Zongzheng Chen, Jiu Deng, Xiaorui Li, Yueyang Qu, Lingling Xu, Yong Luo, Yao Lu, Tingjiao Liu, Weijie Zhao and Bingcheng Lin

Measurement of Carcinoembryonic Antigen in Clinical Serum Samples Using a Centrifugal Microfluidic Device

Reprinted from: *Micromachines* **2018**, *9*, 470, doi:10.3390/mi9090470 **141**

Yuan Fang, Ningmei Yu, Yuquan Jiang and Chaoliang Dang

High-Precision Lens-Less Flow Cytometer on a Chip

Reprinted from: *Micromachines* **2018**, *9*, 227, doi:10.3390/mi9050227 **151**

About the Special Issue Editors

Rui A. Lima is Associate Professor at the Department of Mechanical Engineering, University of Minho (UMinho), and Researcher at the Mechanical Engineering and Resource Sustainability Center (MEtRICs, UMinho) and Transport Phenomena Research Center (CEFT), FEUP, University of Porto. His research is mostly centered on the area of microfluidics, nanofluidics, and blood flow in biomedical microdevices. Currently, he lectures as part of several Master courses in Mechanical and Industrial Engineering. In the past, he has delivered lectures as part of several Master courses in Biomedical Technology, including Cardiovascular Biomechanics and Micro/Nanotechnologies and Biomedical Applications at the Bragança Polytechnic Institute (IPB). Currently, he also supervises several PhD and Master students in the field of Mechanical and Biomedical Engineering.

Graça Minas is Associate Professor and Deputy Director at the Department of Industrial Electronics, as well as Researcher at the CMEMS-UMinho (Center for Microelectromechanical Systems), University of Minho, Portugal. Her research is mostly centered on the area of biomedical microdevices, specifically, in lab-on-a-chip integration of electronic circuits, optical filters, solid-state integrated sensors, biosensors, and actuators in those LOC devices. She is also developing organ-on-a-chip systems that aim to mimic human responses to various chemicals in vitro. She has published more than 130 articles and 7 patents. She supervised 2 postdoctoral fellows, 11 PhD theses (7 finished), 40 Master theses, and numerous research fellows (in the scope of project grants). Furthermore, she has participated in 18 national and European projects and has been Principal Investigator in 8 of them (6 completed).

Susana Catarino received her PhD degree in Biomedical Engineering in 2014 from the University of Minho, Portugal. She is currently Researcher at the Center for Microelectromechanical Systems (CMEMS-UMinho) at the same University. From October 2016, she was also Visiting Assistant Professor at the same institution, lecturing at the Dept. of Industrial Electronics in the areas of Modeling and Simulation for Microtechnologies, Electronics, Microsensors, and Microactuators. She has published more than 40 articles in international journals, conferences, and book chapters, and 1 patent. She currently supervises 2 PhD thesis, 10 Master theses (7 completed), and 1 research fellow. She has also participated in 6 funded projects, in which she was Principal Investigator in 2 of these. Her research interests include diagnosis and lab-on-a-chip devices, optical and acoustic sensors and actuators, and numerical studies of acoustic streaming and microfluidic devices.

*Editorial*

Editorial for the Special Issue on Micro/Nano Devices for Blood Analysis

Susana O. Catarino^{1,*}, **Graça Minas**^{1,*} and **Rui Lima**^{2,3,*}

¹ Center for MicroElectromechanical Systems (CMEMS-UMinho), University of Minho, Campus de Azurém, 4800-058 Guimarães, Portugal

² CEFT, Faculdade de Engenharia da Universidade do Porto (FEUP), Rua Roberto Frias, 4200-465 Porto, Portugal

³ METRICs, Mechanical Engineering Department, University of Minho, Campus de Azurém, 4800-058 Guimarães, Portugal

* Correspondence: scatarino@dei.uminho.pt (S.O.C.); gminas@dei.uminho.pt (G.M.); rl@dem.uminho.pt (R.L.)

Received: 14 October 2019; Accepted: 15 October 2019; Published: 18 October 2019

The development of microdevices for blood analysis is an interdisciplinary subject that demands an integration of several research fields such as biotechnology, medicine, chemistry, informatics, optics, electronics, mechanics, and micro/nanotechnologies.

Over the last few decades, there has been a notably fast development in the miniaturization of mechanical microdevices, later known as microelectromechanical systems (MEMS), which combine electrical and mechanical components at a microscale level. The integration of microflow and optical components in MEMS microdevices, as well as the development of micropumps and microvalves, have promoted the interest of several research fields dealing with fluid flow and transport phenomena happening at microscale devices.

Microfluidic systems have many advantages over macroscale by offering the ability to work with small sample volumes, providing good manipulation and control of samples, decreasing reaction times and allowing parallel operations in one single step. Despite the enormous scientific achievements that microfluidics have had in the last decades in the field of biomedical applications, this technology is still considered in an early stage, with some pullbacks, such as the difficulty to achieve a cost-effective large-scale production, and a lack of complete understanding of the physics of fluids at the microscale level over the biological species. Consequently, enormous efforts have been performed in microfabrication and microfluidics research to enhance the potential of microdevices to develop portable and point-of-care diagnostic devices, particularly for blood analysis.

In this special issue, Catarino et al. [1] present one review paper on an overview of the techniques used for sorting and separation of red blood cells (RBCs) and the respective micro- and nanofabrication techniques, as well as examples of lab-on-a-chip devices with high potential for the integration of separation and detection tools in a single microfluidic platform [1].

Additionally, the special issue also contains 10 research papers covering different subjects related to microfluidic structures and cells characterization. Particularly, Kawaguchi et al. [2] have proposed a method to assess the changes in the rheological properties of a suspension containing fluorescent particles. On one side, the authors used a microchannel with a circular cross section and measured the distribution of suspended microparticles in the radial direction from the recorded images. On the other side, the authors evaluated the non-Newtonian rheological properties of the suspension using the velocity distribution obtained by the particle tracking velocimetry (PTV) and a power-law fluid model [2].

Three of the research papers focus are focused on assessing the deformability of RBCs in microchannels [3–5]. Takeishi et al. [3] numerically investigated the dynamics of RBCs flowing at different velocities in a narrow rectangular microchannel, for different capillary (Ca) numbers.

The authors found that RBCs confined in the microchannel assumed a nearly unchanged biconcave shape at low Ca numbers, which became an asymmetrical slipper shape at moderate Ca numbers, and a symmetrical parachute shape at high Ca values, showing that the measurement of the configurations of the flowing cells can be a valuable tool to quantify the cell state [3].

Faustino et al. [4] have presented a passive microfluidic tool that provides the assessment of motions and deformations of RBCs of end-stage kidney disease (ESKD) patients (comparing patients with and without diabetes type II). The experimental flow studies were performed within a hyperbolic converging microchannel where single-cell deformability was assessed under a controlled homogeneous extensional flow field, using a high-speed video microscopy system. The velocities and deformability ratios were calculated for 27 individuals, 20 of them having ESKD, and the results showed that the proposed device was able to detect changes in the deformability ratio of the RBCs, allowing for distinguishing the samples from the healthy controls and the patients. The RBCs deformability of ESKD patients with and without diabetes was lower than of the healthy controls, with this difference being more evident for the group of ESKD patients with diabetes [4].

Vilas Boas et al. [5] reported an experimental study of the deformability and velocity assessment of healthy and artificially impaired red blood cells (RBCs), in narrow (8 μm width) polydimethylsiloxane (PDMS) microchannels, with the purpose of potentially mimicking malaria effects. The authors modified the RBCs by adding different concentrations of glucose, glutaraldehyde, or diamide in order to increase the cells' rigidity, and obtained a velocity/deformability relation in the microchannel contraction, which shows great potential to relate the RBCs' behavior with the various stages of malaria, helping to establish the development of new diagnostic systems towards point-of-care devices [5].

Kang and Kim [6] studied the RBCs aggregation and sedimentation rate in a microfluidic device, fabricated by xurography. In this study, multiple and periodic measurements were obtained by pulling blood from a pipette tip into parallel microfluidic channels, and quantifying the image intensity. The authors have considered two indices (aggregation index and erythrocyte-sedimentation-rate aggregation index) and have evaluated the effect of hematocrit and dextran solution on these values, showing that the erythrocyte-sedimentation-rate aggregation index varies linearly within a specific concentration of dextran solution [6].

Ponmozhi et al. [7] developed and characterized a low-cost microfluidic device for adhesion tests in polymeric surfaces, which can be fabricated in a laboratory with low resources. The fabrication method consisted of a modification of the existing PDMS soft lithography method and, therefore, is compatible with sealing methods and equipment of most microfluidic laboratories. The molds were produced by xurography, and the fabrication method was tested by evaluating the bacterial adhesion in five different materials, with different surface hydrophobicity and charges. The authors also performed a computation fluid dynamics analysis of the flow in the microfluidic device [7].

Four research papers studied clinical applications of microfluidic devices, in particular for quantification of tumor markers, as well as the characterization of the morphological properties of other cell cultures and counting cells. In particular, Sugita et al. [8] developed a method to efficiently obtain in vitro multinucleated cells and characterized their morphological properties. The authors seeded a *Xenopus* tadpole epithelium tissue-derived cell line (XTC-YF) in different hydrophobicity dishes and with or without supplements, and verified that 88% of the cells cultured on a less hydrophilic dish in medium supplemented with Y-27632 became multinucleate 48 h after seeding [8].

Since metastatic cancer cells are known to have a smaller cell stiffness than healthy cells, Nakamura et al. [9] developed a simple microfluidic system to assess metastatic capacity of the cancer cells from a mechanical point of view, by evaluating the viscoelastic properties of cancer cells on a tapered microchannel. Two metastasis B16 melanoma variants (B16-F1 and B16-F10) were examined and the shape recovery process of the cell from a compressed state was evaluated with the Kelvin-Voigt model. The shape recovery time constant became larger as cancer cells had higher metastatic potential [9].

Gao et al. [10] developed a high-throughput centrifugal microfluidic device for detecting carcinoembryonic antigen (CEA) in serum, which is a broad-spectrum tumor marker used in clinical applications, without the need for cumbersome washing steps normally used in immunoreactions. This centrifugal microdevice contains 14 identical pencil-like units, and the CEA molecules were separated from the bulk serum for subsequent immunofluorescence detection using density gradient centrifugation in each unit simultaneously. The proposed device can achieve a high-throughput detection [10].

Finally, Fang et al. [11] presented a low cost and small size flow cytometer on a microfluidic chip, integrating an inline lens-free holographic microscope. The authors proposed an S-type microchannel with a pulse injection flow, and obtained a less than 2% cell counting error. This on-chip flow cytometer can continuously count cells and continuously collect a large number of cell images for subsequent cell analysis, and is in full compliance with the current development trend of point-of-care testing [11].

We hope this issue can provide an opportunity to the engineering and biomedical community, and those who are interested in the general field of MEMS and micro/nanofluidics, to access novel knowledge and information, especially in its applications to biomedical areas. Particularly, we hope this issue can contribute as a display of the latest achievements, breakthroughs, challenges and future trends in microdevices for diagnostics and blood analysis, micro- and nanofluidics, technologies for flows visualization, MEMS, biochips and lab-on-a-chip devices and their application to research and industry.

Finally, we would like to congratulate, acknowledge and thank all the authors for submitting their original manuscripts to this special issue, as well as all the reviewers for the time and help to improve the quality of the submitted papers.

Conflicts of Interest: The authors declare no conflicts of interest.

References

1. Catarino, S.O.; Rodrigues, R.O.; Pinho, D.; Miranda, J.M.; Minas, G.; Lima, R. Blood Cells Separation and Sorting Techniques of Passive Microfluidic Devices: From Fabrication to Applications. *Micromachines* **2019**, *10*, 593. [[CrossRef](#)] [[PubMed](#)]
2. Kawaguchi, M.; Fukui, T.; Funamoto, K.; Tanaka, M.; Murata, S.; Hayase, T. Viscosity Estimation of a Suspension with Rigid Spheres in Circular Microchannels Using Particle Tracking Velocimetry. *Micromachines* **2019**, *10*, 675. [[CrossRef](#)]
3. Takeishi, N.; Ito, H.; Kaneko, M.; Wada, S. Deformation of a Red Blood Cell in a Narrow Rectangular Microchannel. *Micromachines* **2019**, *10*, 199. [[CrossRef](#)]
4. Faustino, V.; Rodrigues, R.O.; Pinho, D.; Costa, E.; Santos-Silva, A.; Miranda, V.; Lima, R. A Microfluidic Deformability Assessment of Pathological Red Blood Cells Flowing in a Hyperbolic Converging Microchannel. *Micromachines* **2019**, *10*, 645. [[CrossRef](#)] [[PubMed](#)]
5. Boas, L.; Faustino, V.; Lima, R.; Miranda, J.; Minas, G.; Fernandes, C.; Catarino, S. Assessment of the Deformability and Velocity of Healthy and Artificially Impaired Red Blood Cells in Narrow Polydimethylsiloxane (PDMS) Microchannels. *Micromachines* **2018**, *9*, 384. [[CrossRef](#)] [[PubMed](#)]
6. Kang, Y.; Kim, B. Multiple and Periodic Measurement of RBC Aggregation and ESR in Parallel Microfluidic Channels under On-Off Blood Flow Control. *Micromachines* **2018**, *9*, 318. [[CrossRef](#)] [[PubMed](#)]
7. Ponomozhi, J.; Moreira, J.M.R.; Mergulhão, F.J.; Campos, J.B.L.M.; Miranda, J.M. Fabrication and Hydrodynamic Characterization of a Microfluidic Device for Cell Adhesion Tests in Polymeric Surfaces. *Micromachines* **2019**, *10*, 303. [[CrossRef](#)] [[PubMed](#)]
8. Sugita, S.; Munechika, R.; Nakamura, M. Multinucleation of Incubated Cells and Their Morphological Differences Compared to Mononuclear Cells. *Micromachines* **2019**, *10*, 156. [[CrossRef](#)] [[PubMed](#)]
9. Nakamura, M.; Ono, D.; Sugita, S. Mechanophenotyping of B16 Melanoma Cell Variants for the Assessment of the Efficacy of (-)-Epigallocatechin Gallate Treatment Using a Tapered Microfluidic Device. *Micromachines* **2019**, *10*, 207. [[CrossRef](#)] [[PubMed](#)]

10. Gao, Z.; Chen, Z.; Deng, J.; Li, X.; Qu, Y.; Xu, L.; Lin, B. Measurement of Carcinoembryonic Antigen in Clinical Serum Samples Using a Centrifugal Microfluidic Device. *Micromachines* **2018**, *9*, 470. [[CrossRef](#)] [[PubMed](#)]
11. Fang, Y.; Yu, N.; Jiang, Y.; Dang, C. High-Precision Lens-Less Flow Cytometer on a Chip. *Micromachines* **2018**, *9*, 227. [[CrossRef](#)] [[PubMed](#)]



© 2019 by the authors. Licensee MDPI, Basel, Switzerland. This article is an open access article distributed under the terms and conditions of the Creative Commons Attribution (CC BY) license (<http://creativecommons.org/licenses/by/4.0/>).



Review

Blood Cells Separation and Sorting Techniques of Passive Microfluidic Devices: From Fabrication to Applications

Susana O. Catarino ^{1,†}, Raquel O. Rodrigues ^{1,†}, Diana Pinho ^{2,3,†,‡}, João M. Miranda ³, Graça Minas ¹ and Rui Lima ^{3,4,*}

¹ Center for MicroElectromechanical Systems (CMEMS-UMinho), University of Minho, Campus de Azurém, 4800-058 Guimarães, Portugal

² Research Centre in Digitalization and Intelligent Robotics (CeDRI), Instituto Politécnico de Bragança, Campus de Santa Apolónia, 5300-253 Bragança, Portugal

³ CEFT, Faculdade de Engenharia da Universidade do Porto (FEUP), Rua Roberto Frias, 4200-465 Porto, Portugal

⁴ MEtRICs, Mechanical Engineering Department, University of Minho, Campus de Azurém, 4800-058 Guimarães, Portugal

* Correspondence: rl@dem.uminho.pt; Tel.: +351-253-510190

† These authors contributed equally to this work.

‡ Current affiliation: INL – International Iberian Nanotechnology Laboratory, Av. Mestre José Veiga, 4715-330 Braga, Portugal.

Received: 2 August 2019; Accepted: 6 September 2019; Published: 10 September 2019

Abstract: Since the first microfluidic device was developed more than three decades ago, microfluidics is seen as a technology that exhibits unique features to provide a significant change in the way that modern biology is performed. Blood and blood cells are recognized as important biomarkers of many diseases. Taken advantage of microfluidics assets, changes on blood cell physicochemical properties can be used for fast and accurate clinical diagnosis. In this review, an overview of the microfabrication techniques is given, especially for biomedical applications, as well as a synopsis of some design considerations regarding microfluidic devices. The blood cells separation and sorting techniques were also reviewed, highlighting the main achievements and breakthroughs in the last decades.

Keywords: microfluidics; red blood cells (RBCs); microfabrication; polymers; separation and sorting techniques

1. Introduction

Since the development of the first microfluidic device, microfluidics heralded the promise to change life science and industry [1]. Despite the enormous scientific achievements that microfluidics have had in the last decades in the field of biomedical applications, this technology is still considered in its “adolescence” [2]. Among the pullbacks, are the difficulty to achieve a cost-effective large-scale production that allows its commercialization for clinical application, the so-called lab-on-a-chip, and the complete understanding of the physics of fluids at the microscale level over the biological species, such as blood and blood cells.

Blood and blood cells are important for scientific and clinical purposes because they can be used as indicators of many pathological conditions, including arterial hypertension, ischemia, inflammation, and diabetes [3,4]. Based on the fact that abnormal blood cells typically have distinctive biological and physicochemical properties (e.g., size, deformability and chemical composition), with different hydrodynamic properties when compared to healthy ones, these features can be used for rapid, low-cost cell separation and diagnosis.

In parallel, recent developments in microfabrication with polymers and elastomers made possible to fabricate low-cost transparent micrometre-sized channels and, as a result, several studies have been proposed using microfluidics to measure the motion and dynamic behaviour of cells flowing through microfluidic devices [5–12]. Taken into consideration that since its origins, microfluidics has flourished and paved its path in parallel with the development of new fabrication technologies, the present review aims to give an overview perspective of this technology for blood cells separation and sorting from the fabrication to application, and thus, revising the main achievements and breakthroughs in the last decades.

This review is organized as follows: Section 2 presents a description of different techniques for the fabrication of microfluidic devices, as well as a comparison between them; Section 3 approaches design considerations regarding microfluidic devices for biomedical applications; Section 4 describes and compares the main passive methods for cells sorting and separation; and Section 5 briefly discusses future challenges and perspectives regarding microfluidic devices and their applications.

2. Fabrication of Polymeric Microfluidic Devices

The beginning of microfluidics and its early systems, in the late 1970s (Figure 1), were derived from microelectronics and microelectromechanical systems (MEMS) technology and techniques, such as photolithography and etching, which were highly developed at the time [2,13].

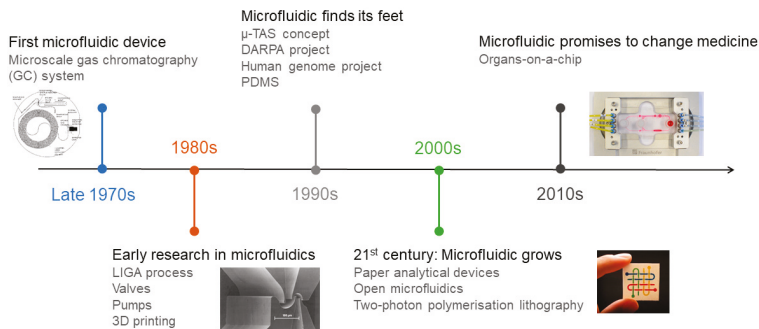


Figure 1. Timeline of the main microfluidics achievements from the first microfluidic device until the present.

Initially, silicon and glass were the select material to produce those microfluidic devices. Although, silicon had a big impact in microelectronics, initiating the Silicon Valley revolution, the material has some disadvantages for microfluidics, such as its opacity in the Ultra-Violet/Visible (UV/Vis) region of the electromagnetic spectrum and relative high cost [13,14]. Glass, on the other hand, is transparent, but due to its amorphous structure is difficult to etch compared with pure SiO₂. For the pattern of small size structures, sandblast and wet etching are the most used techniques. Nevertheless, sandblast is typically limited for patterns below 100 nm and leads to rough surfaces, while wet etching allows smooth sidewalls but has low aspect ratio [15]. Therefore, among the glass micromachining limitations are the low etching aspect ratio and rate, limited mask selectivity and surface roughness [15]. Other disadvantages are that both materials required that each device is made in cleanroom facilities and its sealing made with high voltages and temperatures, which makes the microfabrication laborious and expensive [13]. In contrast to glass and silicon, polymers and elastomers, are less expensive and the channels can be obtained by molding or embossing that makes the fabrication faster and less expensive [14]. Among the most popular polymers used to fabricate microfluidic devices are poly(methyl methacrylate) (PMMA), cyclic olefin copolymer (COC), poly(styrene) (PS), poly(carbonate) (PC), poly(ethyleneterephthalate glycol) (PETG) and poly(dimethylsiloxane) (PDMS) [14]. Derived from this effort to find alternative materials, PDMS,

a transparent elastomeric polymer pioneered by George Whitesides and his group at Harvard in the 1990s, quickly become the most popular material used in microfluidic devices [2]. The use of this new material made possible the massification of soft-lithography technique, with rapid prototyping and replica molding (Figure 2).

Figure 2 shows the main steps involved in the design and fabrication of microfluidic devices using the soft-lithography technique. The detailed description of these steps is well described elsewhere [13].

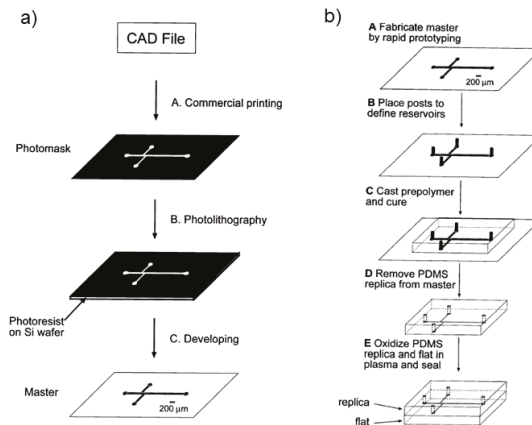


Figure 2. Soft lithography technique introduced by Whitesides and co-workers in 1998. (a) Rapid prototyping using photolithography and (b) replica molding with poly(dimethylsiloxane) (PDMS). Reproduced with permission from [13].

This innovation allowed the growth of microfluidics field due to the many advantages of this material: (i) high fidelity to replicate by molding features at the micro-scale level; (ii) its optically transparent down to 280 nm; (iii) low temperature and time to cure; (iv) biocompatibility and nontoxicity to cells; (v) possibility to change surface chemistry accordingly to the application needs; (vi) gas permeability, allowing culture of cells; (vii) reversal and self-bonding, among others [13,16,17].

In general, soft-lithography follows four major steps: (i) pattern design, drawn in computer-aided design (CAD) software programs for the fabrication of photomasks on transparency films (Figure 2a); (ii) fabrication of the mask and master, photomasks on transparency films are designed in high-resolution printers followed by photolithography technique (Figure 2a); (iii) fabrication of the PDMS stamp, fabricated by casting PDMS (pre-polymer mixed with cure agent) against a master whose surface has been patterned (Figure 2b) and (iv) fabrication of micro- and nanostructures with the stamp by printing, molding and embossing [18].

Although the several advantages of the soft-lithography method with PDMS, the standard prototyping method (i.e., photolithography) requires the access to cleanroom facilities and high-trained people. Additionally, the replica molding with PDMS is achieved by casting the masters one by one, which make the large-scale production slow. Nevertheless, this process is an ideal and fast solution to test prototypes. Another important aspect is that despite the common statement that BioMEMS is straightforward and inexpensive, the fabrication of microfluidic devices is, in general, complex and costly. For instance, it is estimated that the user fee in the United States for a fully staffed cleanroom, in a major research university, is in the order of \$100/h per student [19]. This must include the typical time for training that can take several weeks for the basic operation of equipment and familiarization of techniques, such as spin coater, masker aligner and developing station [19]. An alternative is the contract of manufacturers that can provide custom master molds for a relatively low fee. However, this process can take several weeks from manufacturing to shipping [20]. To suppress the high cost and constrains of photolithography, alternatives have been developed in the last decade

for the low-cost of microstructures without the need of cleanroom facilities. An example of this effort was published by Pinto et al., 2014 [21], describing the fabrication and optimization of microstructures in SU-8 (commonly used as epoxy-based negative photoresist), without the need of cleanroom facilities. The proposed fabrication technique uses an alternative photomask printed in transparent photographic sheet using standard tools and equipment employed in the printed circuit board (PCB) industry. Even though the outstanding achievement of the proposed technique, the SU-8 shows a resolution limitation of 10 μm and the need to control the room temperature and humidity to optimize the fabrication procedure.

In parallel, alternative non-lithographic techniques have also emerged from these requirements of specific facilities and equipment that has inhibited many scientific groups to pursue new microfluidic innovations, namely print and peel techniques, e.g., xurography, micromilling or direct laser plotting (Figure 3), which are well reviewed elsewhere [22].

Briefly, xurography allows the generation of master molds (or masks) using a cutting plotter machine and adhesive vinyl film. Recently, Pinto et al. (2014) [23] have shown that xurography can be used as a rapid technique with good resolution to produce microfluidic structures down to 500 μm . By using this technique Bento et al. [24] were able to successfully produce microchannels contractions with dimensions down to 350 μm and as a result they have investigated how Taylor bubbles disturb the blood flow at the scale of blood cells.

Micromilling, is another low-cost fabrication technique that creates microscale structures by removing bulk material with cutting tools [25]. This technique was shown by Lopes and co-workers to have the ability to produce reusable microfluidic devices with widths down to 30 μm [26].

Direct laser plotting is a microfabrication technique similar to micromilling that uses laser beams to create microchannels. This technique can typically generate microchannels widths up to 100 μm . Although it has been shown the possibility to down to 20 μm by using short laser pulses [22].

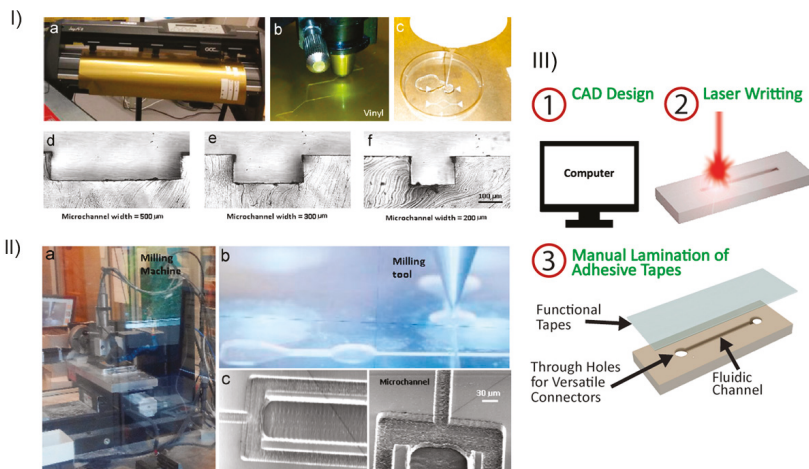


Figure 3. Low-cost print-and-peel microfabrication techniques. (I) Xurography: (a) cutting plotter machine; (b) features being cut by the cutting plotter; (c) PDMS being added to a petri dish containing the vinyl mask; (d), (e) and (f) Cross sections of microchannels with 500, 300 and 200 μm of width, respectively. (II) Micromilling; (a) milling machine; (b) operating milling tool and (c) microchannels. Reproduced with permission from [22]. (III) Direct laser plotting main steps. Reproduced with permission from [27].

3D-printing fabrication techniques have also gained a growing interest to fabricate microfluidic devices, offering the possibility to generate devices with complex architectures from a broader range of materials and avoiding multi-step processing [28]. The main 3D-printing techniques are

stereolithography (SLA), fused deposition modelling (FDM), selective laser sintering (SLS) and direct ink writing (inkjet) [28–30], allowing a broad range of applications. Among the advantages, the simplicity, fast and efficient prototyping with no need of photomask and cleanroom facilities, are some of the most important.

FDM, is the most simple and low-cost 3D-printing method, working by extruding a thermoplastic polymer through a hot nozzle to print layers of the object. The technique can be used to produce directly the microfluidic devices or the 3D mask that combined with PDMS replication molding allows the fabrication of 3D-biomodels, such as macro and micro-scale vascular system models [30,31].

An overview of the main advantages and disadvantages of the most representative fabrication techniques used to develop microfluidic devices in polymer substrates is given in Table 1.

Table 1. Main advantages, disadvantages, resolution range and aspect ratio of microfabrication techniques used to develop microfluidic devices using polymer substrates. Adapted from [14].

Fabrication Technique	Advantages	Disadvantages	Resolution Range and Aspect Ratio
Hot embossing	Precise and rapid in the replication of microstructures. Mass production.	Restricted to thermoplastics. Time-consuming. Complex 3D structures are difficult to be fabricated.	Resolution between sub-100 nm and millimetre. Moderate aspect ratio (5:1) [32,33]
Injection molding	Mass production. Fine features. Low cycle time. Highly automated.	Restricted to thermoplastics. High cost mold. Nano-size precision is limited.	Resolution between sub-100 nm and millimetre. High aspect ratio (20:1) [34]
Laser photoablation	Rapid. Large format production.	Limited materials. Multiple treatment session. Difficulties for mass production. Micro-size precision is limited.	Resolution between micrometre and millimetre. High aspect ratio (30:1) [35,36]
X-ray lithography	High-resolution. Straight and smooth walls.	Complex and difficult master fabrication. Time consuming and high cost process.	Resolution between few nanometres and micrometres. Ultra-high aspect ratio (350:1) [37]
Soft-lithography	High-resolution and 3D geometries. Cost-effective. Excellent micro-size precision.	Pattern deformation and vulnerability to defects. Difficult to fabricate circular 3D geometries.	Resolution between 30 nm and 500 m. High aspect ratio (20:1) [18]
Xurography	Low-cost and rapid technique.	Complex 3D structures are difficult to be fabricated. Micro-size precision is limited.	Resolution between 150 m and millimetre. Moderate aspect ratio (8:1) [21,23,38,39]
Direct laser plotting	Low-cost and rapid technique. Free-mask technique. Good micro-size precision.	Complex 3D structures are difficult to be fabricated. Micro-size precision is limited. Reproducibility of the microdevices.	Resolution between 10–500 m. Moderate aspect ratio (7:1) [40,41]

Table 1. Cont.

Fabrication Technique	Advantages	Disadvantages	Resolution Range and Aspect Ratio
Micromilling	Low-cost and rapid technique. Free-mask technique.	Complex 3D structures are difficult to be fabricated. Micro-size precision is limited. Reproducibility of the microdevices. Roughness.	Resolution between 30 m and millimetre. Moderate aspect ratio (8:1) [26,42]
Desktop fused deposition modeling (FDM), 3D-printing	Low-cost and rapid technique to fabricate prototypes.	Micro-size precision is limited. High roughness and complex to perform flow visualizations. Not suitable for mass production.	Resolution between 100 m and millimetre. Moderate aspect ratio (10:1) [43–45]
Nanofabrication	High-resolution of 2D and 3D geometries. Excellent nano-size precision. Highly repeatable, periodical structures.	High cost. Multiple process steps. Limited for microfluidic applications.	Resolution between 1–800 nm. Ultra-high aspect ratio (100:1) [17,46]

With the recent development of nanotechnology for several applications and fields, nanofabrication techniques for microfluidic devices have also been developed. In general, these new techniques are based in advanced nanoscale photolithographic methods, such as extreme ultraviolet, electron beam and nanoimprint lithography, or non-lithographic methods, such as anodic aluminium oxidation. All these new nanofabrication approaches are well described elsewhere [17]. With the ability to generate features with just a few nanometres, the main application of these nanofabrication techniques are lab-on-a-chip microdevices, with high potentiality to medicine, biology and chemical applications [47–49].

3. Design of Microfluidic Devices for Biomedical Applications

Biomedical science found a fruitful field in microfluidics to replace routine analysis and diagnosis tests, as well as to conduct fundamental biological studies in cells and diseases. Among the biomedical applications, microfluidics research has allowed the emerging of a wide range of promising applications from microscale genomic and proteomic analysis kits, biosensors, point-of-care diagnostic devices, drug screening and delivery platforms, implantable devices, novel biomaterials to tissue engineering and single cell studies [50].

Depending on the final application of the microfluidic device, different micro- or nanofabrication techniques are available and can be used. In general, most of the research groups try to pursue a time-cost effectiveness to fabricate their own microdevices. Based on this standpoint, Figure 4 gives an overview of the fabrication techniques listed in Table 1, from a time and cost perspective.

The material selection also has an important role in the application. For biomedical applications the selection of the material must consider important parameters, namely biocompatibility, bio-culture, permeability and porosity, protein crystallization, reusability and disposable device use. Some of these characteristics are listed in Table 2, for the most common materials used for biomedical applications.

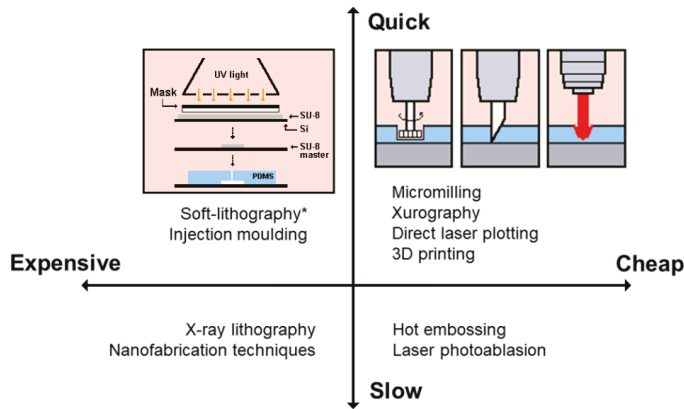


Figure 4. Fabrication techniques from a time and cost perspective. Adapted from [14]. * Despite standard soft-lithography technique is considered expensive, new alternatives without the need of cleanroom facilities significantly drop the cost, being considered as low-cost, as the work published by Pinto et al., 2014 [21].

Table 2. Significant characteristics of the most common materials used for biomedical applications. Adapted from [51].

Characteristics	Silicon	Glass	Thermoplastics	Elastomers (PDMS)
Protein crystallization	Poor	Poor	Good	Moderate
Droplet formation	Excellent	Excellent	Good	Moderate
Porosity	Poor	Poor	Moderate	Moderate
Permeability	Poor	Poor	Moderate	Good
Bio-culture	Moderate	Moderate	Moderate	Good
Reusability	Yes	Yes	Yes	No
Disposable device use	Expensive	Expensive	Good	Good

Another important aspect for the fabrication of microfluidic devices is the interfacing and/or integration of modules for the applications that the device is being designed. Among them, integration of microheaters, valves, sensors, electroosmotic fluid pumps, readout electronics, among others, can be accomplished to complete microfluidic devices with remarkable capabilities [52].

4. Microfluidic Cell Separation and Sorting Techniques

Despite all the research and development of microfluidic systems, several challenges remain related to the miniaturization of the lab-on-a-chip devices. At the microscale level, the mixture, pumping, separation and control of fluids are limited, on the one hand, by the minimum sample volumes and flow rates required by the biological analysis and, on the other hand, by the microscale dimensions of the systems. The dominant physical and chemical effects at the microscale level are different from the ones at the macroscale, leading to an increased complexity of the flow and mass transport phenomena. In order to overcome those limitations, significant research efforts have been performed for improving the design of micropumps, valves, mixers and separation devices that can be incorporated on lab-on-a-chip devices [53–55], while addressing the non-Newtonian behaviour of the majority of physiological fluids [56,57].

Microfluidic systems can integrate different kinds of sorting methods based on the physical parameters of cells, providing a perfect interface for the manipulation of single cells and access forces in a variety of ways and allowing a fully autonomous measurement of physical parameters [58].

Particularly, cell separation techniques have been developed for cell concentration purposes (removal of plasma and increase of the cell concentration, mainly haematocrit increase); plasma enrichment (removal of cells from plasma and cells dilution); blood fractioning (separation of blood into different components); cell sorting (separation of cells by type); and cell removal (specific cell sorting that removes only some specific cells), that can work as cell isolation or removal of pathogens [59].

The manipulating of forces for the separation techniques can be active, passive or both (label-free cell sorting mechanism), as shown in Figure 5. Apart from these, there are other methods such as paper-based [60,61] and CD based [62,63] methods to separate mainly the plasma from blood [64]. Active technologies, based on microelectromechanical systems, improve the control of fluids using mobile parts or external mechanical forces, and can be based on dielectrophoresis, magnetophoresis, acoustophoresis and optical tweezers mechanisms [58,64]. Passive technologies for controlling fluids do not include external forces or mobile parts, and their control is promoted by diffusion as a function of the channel geometry [64–70], or intrinsic hydrodynamic forces, such as punch flow fraction, deterministic lateral displacement, inertial forces and intrinsic physical property of the cells [69–74], including sieving, which uses the size of micropores, microweirs, membranes and the gap between micropillars arrays for the separation of cells [26,69–78]. The passive microfluidic technologies bring more interest in the lab-on-a-chip and microfluidics research field due to its precise manipulation, low cost fabrication, simple structure, simple integration and lower maintenance in lab-on-a-chip devices and high throughput [79–82].

Therefore, this paper presents, in addition to an overview over the microfabrication techniques using polymers as substrates, a review and discussion of different passive techniques and microfluidic devices for separation of cells, categorized according to the separation phenomena: hydrodynamic phenomena (as punch flow, inertial forces or deterministic lateral displacement); hemodynamic phenomena (based on the intrinsic physical properties of the cells); and filters and physical filtration (based on micropores, microweirs, membranes and the gap between micropillars), as shown in Figure 5.

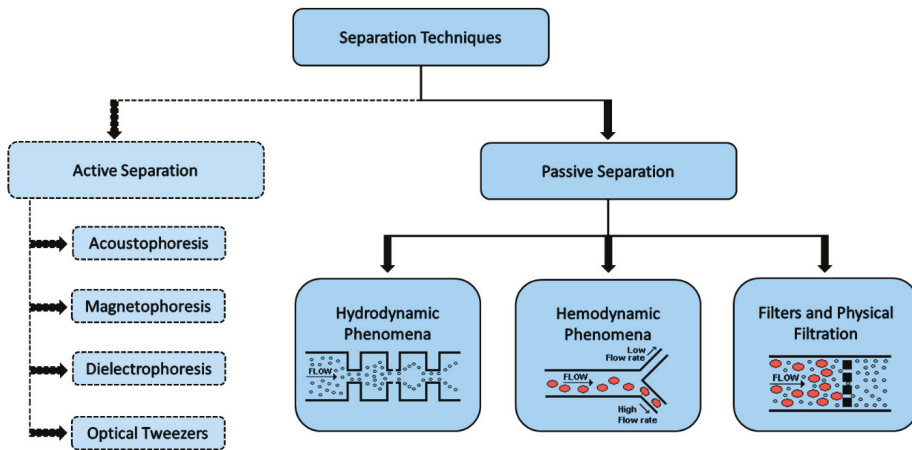


Figure 5. Classification of the main active and passive separation techniques used in microfluidic systems.

4.1. Hydrodynamic Separation and Sorting Techniques

The hydrodynamic separation techniques are adequate for low Reynolds number flows ($Re < 1$) in the microfluidic devices. In a purely hydrodynamic flow separation technique, the laminar flow conditions exist, i.e., viscous forces are strong enough to have any disturbances in the pumped flow through the microchannel. In this process, the aligned cells are separated through multiple side branching outlets (Figure 6b), so that particles of different sizes will follow different paths, achieving

size-based separation [83]. The hydrodynamic focusing is able to achieve narrow streams through sheath flows unlike the inertial focusing that occurs in a single flow stream.

Particles or cells exposed to a shear flow experience a lift force perpendicular to the flow direction and a force from the wall. The equilibrium of these two forces is responsible for the cells or particles migration and depends on several factors, such as channel geometry, flow rate, rheological properties of the carrier fluid and mechanical properties of the elements, as in Figure 6a. By manipulating the flow, for example, controlling the flow rate through one or more inlets, it is possible to achieve size-based cell separation and sorting [84].

The inertial separation methods generate the deflection of larger particles away from the flow, while smaller ones are carried on or near the original flow streamline. These mechanisms occur in curved and focused flow segments, and result from the combination of asymmetrical sheath flows and specific channel geometries, which are able to create a soft inertial force on the fluid. By using channels with curvature (as in Figure 6e), an additional drag force arising from secondary flows (called Dean vortices) enhances the speed of particle migration to more stable equilibrium positions, achieving a faster focusing of cells and particles than in straight channels, with high-throughput and continuous blood separation [64,70]. The inertial migration phenomenon has been widely recognised by the counteraction of two inertial effects, i.e., the shear gradient lift and the wall lift forces [85]. Many of the microfluidic devices have combined this separation inertial focusing strategy with other microfluidic methodologies to enhance blood cells separation, as different examples are presented in Figure 6.

Hydrodynamic Phenomena

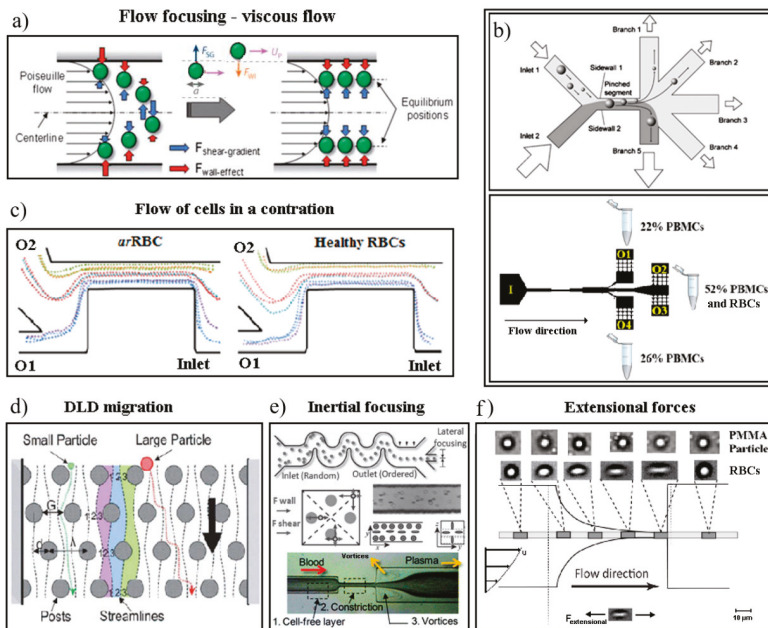


Figure 6. Hydrodynamic methods of separation: (a) the implied forces in a Poiseuille flow for cell separation. Reproduced with permission from [86] (b) the principle of hydrodynamic filtration in a microchannel with many outlets. Reproduced with permission from [81,84]. (c) trajectories analysis of rigid and deformable cells through a contraction for cell separation in two outlets. Reproduced with permission from [87]. (d) principle of deterministic lateral displacement. Reproduced with permission from [86]. (e) separation using inertial flow forces and at high flow rates creating vortices downstream a contraction. Reproduced with permission from [64,88]. (f) extensional forces for cell separation and mechanical analysis. Reproduced with permission from [89].

Wang et al. [90], reported an inertial microfluidic device for continuous extraction of large particles or cells with high size-selectivity (under 2 μm) and high efficiency (above 90%). The authors developed a simple geometry with four key parts: a main microchannel, with a high-aspect-ratio geometry, to assure the inertial particle flow; two chambers for the formation of microvortices, symmetrically positioned; two side outlets, positioned at the chambers' corners, for the creation of sheath flow and removal of large particles; and, finally, an outlet for the small particles.

One of the hydrodynamic separation methods is based on the principle known as deterministic lateral displacement (DLD). This method employs arrays of pillars placed within a microchannel (array of obstacles). The laminar flow together with interactions in the array, forces the particles or cells to flow with specific trajectories through the device. The distance among the pillars is tailored according to the size of the cells or the particles to be sorted. The array pattern determines the displacement of cells or particles [84], i.e., the gap between posts and their offset determines the critical particle size for the fractionation. If the particles and/or cells are smaller than the critical size, they tend to flow through the array gaps without net displacement from the original central streamline. If the particles are bigger than the critical size, they will displace laterally, traveling at an angle predetermined by the posts offset distance (as shown in Figure 6d) [84]. Liu et al. [91] developed a rapid and label-free microfluidic structure for isolation of cancer cells from peripheral whole blood, using deterministic lateral displacement arrays (based on the size-dependent hydrodynamic forces), and achieved cells separation efficiency between 80% and 99% with a 2 mL/min throughput [91]. A high-throughput cytometry microsystem was reported by Rosenbluth et al. [92], to distinguish and quantify blood cell properties and help to prevent different hematologic problems (as sepsis, occlusion or leukostasis). The proposed microsystem presents a trifurcation into two bypass channels, and a network of bifurcations that split into 64 parallel capillary-like microchannels.

4.2. Hemodynamic Phenomena on Cell Separation Techniques

Microfluidic biomimetic cell separation techniques are based on mimicking the hemodynamic phenomena and the intrinsic properties of plasma and blood cells when flowing in microvessels. Different hemodynamic phenomena have been observed in vivo and replicated in microfluidic systems, including: plasma layer; Fåhræus–Lindqvist effect (decrease of the apparent viscosity of blood in small vessels), which causes the tendency of the RBCs to migrate toward the centre of the microchannel, creating the cell-free layer (CFL) [11,93] (Figure 7b); leukocyte margination (migration of leukocytes, that are less deformable than RBCs, to the wall of the microchannel due to collisions between leucocytes and erythrocytes) [86]; plasma skimming (uneven distribution of red blood cells and plasma between the small side branch and the main channel); and the Zweifach–Fung bifurcation effect (in asymmetric bifurcations in which the vessel with the smaller flow rate gets a higher concentration of plasma), as represented in Figure 7c [64,93]. A number of microdevices have been developed to take advantage of these effects. For instance, in blood vessels with luminal diameter less than 300 μm , RBCs tend to migrate radially to the axial centre line of the vessel (Fåhræus–Lindqvist effect), as shown in Figure 7a. Figure 7 summarizes the main hemodynamic phenomena of cell separation in microdevices. In microcirculation, the Zweifach–Fung bifurcation law is a relevant effect describing the cells tendency to travel to the daughter channel with a higher flow rate [86,88,94].

Hemodynamic Phenomena

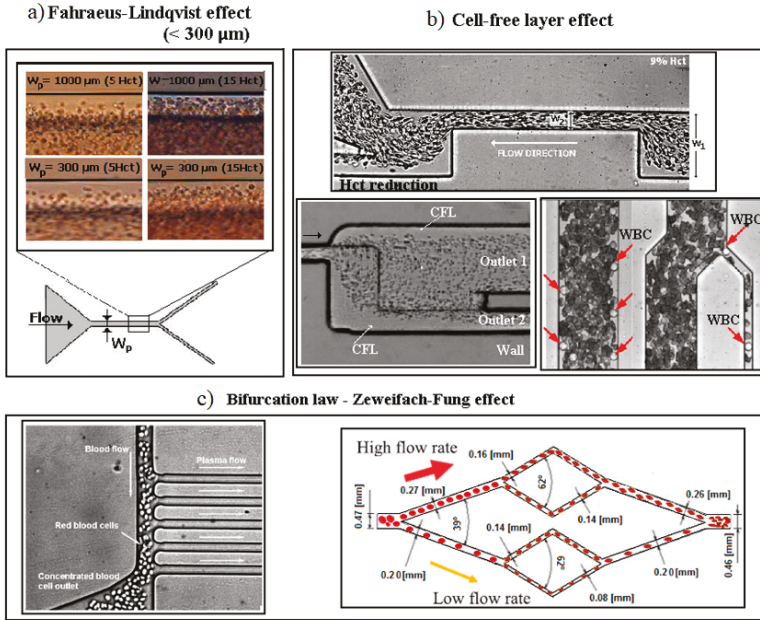


Figure 7. Blood separation microdevices based on hemodynamic flow separation techniques: (a) the Fahraeus–Lindqvist effect in a microchannels with dimensions < 300 μm. Reproduced with permission from [23]. (b) cell-free layer as an advantage for cell and plasma separation and plasma skimming effect, WBCs margination. Adapted from [86,95,96]. (c) the Bifurcation law manipulated to remove cell-free plasma from blood and to mimic the microvasculature networks. Reproduced with permission from [86,97].

Jaggi et al. [94] developed a poly(methyl methacrylate) (PMMA) microdevice for blood plasma separation at high flow rates, based on the bifurcation law. The authors obtained, for Hct 4.5% and whole blood Hct of 45%, at a $5 \text{ mL}\cdot\text{min}^{-1}$ flow rate, separation efficiencies of 92% and 30%, respectively. The plasma yield obtained was 4% for the 45% Hct. The authors reported shear stress values much lower than the shear stress at which hemolysis occurs [94]. Lopes et al. [26] developed a microfluidic device able to perform separation of RBCs from plasma due to the cell-free layer (CFL) created upstream a contraction in a microchannel. The authors produced the device using a micromilling technique, and concluded that the geometric contraction produced by that technique was able to enhance the CFL, resulting in a low cost and efficient way to separate blood cells from plasma [26]. Faivre et al. [98] developed a microchannel with a constriction-expansion region for studying the Fahraeus effect, showing the increase of the cell-free region downstream of the constriction region. The authors collected almost pure plasma with Hct 16% at a flow rate of $200 \mu\text{L}\cdot\text{h}^{-1}$, with a 24% yield (the separation efficiency was not mentioned explicitly). Lima et al. [99] successfully studied the behavior of RBCs in a $75 \mu\text{m}$ circular polydimethylsiloxane (PDMS) microchannel. The authors tracked individual RBCs (for 3% and 23% hematocrit) and observed that the trajectories of the solutions with higher RBC concentrations exhibit higher fluctuations in the direction normal to the flow. Additionally, the authors concluded that the RBCs flowing in a higher concentration environment tend to undergo multi-body collisions, increasing the amplitude of the RBCs' lateral motion. Yang et al. [13] described a PDMS microfluidic device based on the Zweifach–Fung bifurcation law. The separation efficiency was defined in terms of hematocrit and quantified using an image processing program. The authors obtained, with the microdevice continuously running during 30 min without clogging, a separation efficiency of

100% for an inlet Hct of 45%, using defibrinated sheep blood, at a $10 \mu\text{L}\cdot\text{h}^{-1}$ flow rate, with a yield or plasma volume percentage obtained of 15–25% [65]. During the last decade, Ishikawa et al., [67], Leble et al., [9] and Pinto et al., [23] have performed in vitro blood flow studies in simple microchannels with symmetric bifurcations and confluences and more recently Bento et al. [100,101] have performed similar studies in more complex geometries such as in microchannel networks. In those works, it was observed a clear cell-depleted layer at the region of the confluence apex that can be used to perform blood plasma separation.

4.3. Microfluidic Filters-Physical Filtration Techniques

Combined with the mentioned separation techniques, microfluidic filters are usually introduced to increment the efficiency of the microfluidic devices [82,102]. Microscale filters, such as micropillar arrays, microweir structures or microporous membranes, are able to separate cells and particles based on their size and/or deformability. Although these filters allow the precise adjustment of the filter pore size to the required needs, they need to overcome different challenges, such as clogging of the microchannels, fouling and heterogeneity of the cell sizes [84]. Additionally, the design of the filters and barriers needs to take into consideration the different physical properties of the cells, including density, shape and deformability. Physical filtration microstructures, besides being a simple and non-destructive separation method, also allow the integration with other separation strategies. A major problem of the latter separation methodology is the high tendency to have clogging, jamming and possible blockage of the microdevice [103]. One way to minimize such a problem is by using cross-flow filters [83,104–106], since in cross-flow filtration, the fluid flows tangentially rather than through the filter as it does in membrane filtration (see Figure 8). This technique allows the particles to stay in a suspended state, avoiding their deposition, and can be used for separation of particles and cells. Crowley et al., [107] fabricated a passive crossflow filtration microdevice, operating entirely on capillary action, for the isolation of plasma from whole blood. Another method is by using micro-pillars that are suitably placed within the microchannel in a way that cells larger than the critical diameter follow a deterministic path while smaller cells maintain an average downward flow direction around the pillars, leading to the formation of multiple streams based size [86]. Chen et al., [105] developed a set of microfluidic chips based on the crossflow filtration principle, in which parallel micropillar-array and parallel microweirs were used to separate cells via their different sizes. Under the optimal conditions, more than 95% of the RBCs in a sample can be removed from the initial whole blood, while 27.4% of the white blood cells (WBCs) can be obtained. Plasma, WBCs and RBCs can be simultaneously separated and collected at different outlet ports with multilevel filtration barriers [105]. This principle is presented in Figure 8.

Zhang et al., [108] combined the use of hydrodynamic forces with passive filters comprised of artificial microbarriers of varying dimensions (that range in size from 15 to $7 \mu\text{m}$, following the direction of fluid flow) in a chip to promote the flow and the separation of cells. By combining hydrodynamic forces with passive filters, the authors reported the separation of cancer cells based on their deformability. Additionally, by arranging the microbarriers in a rectangular, matrix-like structure, and by placing wide channels between post arrays, the authors ensured that the most flexible cells were able to seek alternate routes in the event of a blockage, as well as to regulate and equalize hydrodynamic pressure throughout the chip. The microscale geometry of the flow channels and post arrays ensured that the fluid flow is laminar, resulting in continuous cell movement and deformation in the device [108].

Filters and Physical Filtration

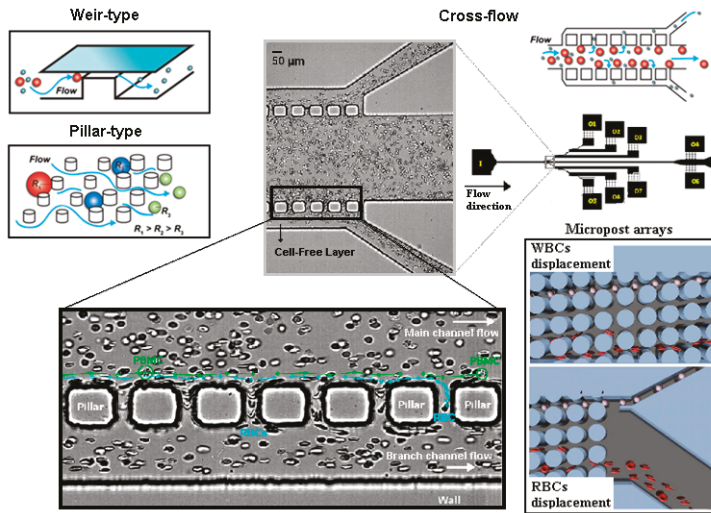


Figure 8. Schematic illustration for weir, pillar and cross-flow microfluidic filters. Images adapted from [81,84,109].

4.4. Comparison between the Separation Methods

Table 3 presents a comparison between the different categories of microfluidic cell separation, in terms of separation criteria, efficiency and throughput.

Table 3. Comparison between the passive separation phenomena.

Method	Hydrodynamic Separation	Hemodynamic Separation	Physical Filtration
Separation criteria	Size	Size, deformability, cells concentration (hematocrit), cell aggregation [102]	Size, shape, deformability
Target sample	Cells, microparticles	RBCs, WBCs, plasma	Cells, particles
Separation Efficiency	Above 90% [90,110]; 80–99% [91]; 62.2% [111]	100% separation efficiency with 15–25% plasma separation volume [65]; 92% separation efficiency with diluted blood (Hct 4.5%) and 37% with whole blood (Hct 45%) [94]	More than 95% of the RBCs and 27% of the WBCs removed from whole blood [105]; 65–100% [102]; 98%, 8% (plasma from whole blood) [112,113]
Throughput	2 mL/min [91]; 10 ⁶ cells/min [110]; 1.2 mL/h (10 ¹⁰ cells/min) [111]	3–4 μL/min [112]; 5 mL/min [94]	2 × 10 ³ cells/s [112,113]
Potential effects on cells	Shear stress	Shear stress	Clogging, fouling, shear stress
Required instrumentation	Fluidic pumps	Fluidic pumps	Fluidic pumps
Processing layout	Continuous flow	Continuous flow	Batch; Continuous flow

The referred passive separation methods are able to separate cells in a simple and non-destructive way and, furthermore, they allow easy integration of other processes in a single microdevice [114]. Ideally, a lab-on-a-chip platform should be small, simple and portable, by combining simple fluid

driving mechanisms, reaction chambers and integrated detection systems for easy readout, making it able to be used by an end user or as a research tool, as a support for other laboratory technology [115].

Several authors have been approaching attempts for integration of passive separation of target cells and analysis, particularly of RBCs deformability assessment in a single microfluidic chip, which is still a challenge. Shevkopylas et al. [116] developed a passive microfluidic device with a microvascular network perfusion system for cells separation and for measuring of the RBCs deformability. Faustino et al. [117] developed a microfluidic device in PDMS, with pillars and geometric variations, for the passive separation of RBCs, as well as to deform the cells and assess their deformability, by analyzing the acquired images. However, the proposed device is not fully integrated yet, since it still requires an external microscope for images evaluation and an external pumping system [117]. The described examples open new opportunities for research and show that lab-on-a-chip devices have high potential for integration of separation and detection tools in a single microfluidic platform.

There are still a lot of challenges to overcome regarding the integration of passive separation techniques in autonomous, functional and portable microdevices. Particularly, clogging, hematocrit, the amount of the sample and preparation time, mechanical stress (under relatively high pressure in microfluidic structures, several biological entities are at risk of rupturing, such as RBCs, or starting an adverse activation, such as platelets), contamination and biocompatibility are still challenging for the design and implementation of blood separation devices [64]. However, they also open new avenues for the miniaturization of analysis systems, requiring multidisciplinary synergies to assure the integration of microfluidics, actuation, detection, and readout systems in a single chip.

5. Perspectives

The research in the lab-on-a-chip area opens new possibilities for the miniaturization of analysis systems, requiring multidisciplinary synergies to assure the integration of microfluidics, actuation, detection, and readout systems in a single chip. All the developed efforts in this field are focused on the development of low-cost, portable, autonomous, multifunctional and commercial devices, with high sensitivity.

This paper presented an overview of the techniques used for separation of RBCs and the respective micro- and nanofabrication techniques, as well as examples of lab-on-a-chip devices with high potential for the integration of separation and detection tools in a single microfluidic platform. However, the use of these methods for separation of RBCs and detection of their properties has still a lot of challenges to overcome. Particularly, most separation methods, despite being able to separate particles, still need further development to be able to separate large cells, as RBCs, in microdevices, and require additional external equipment, which limits the methods' portability.

As the lab-on-a-chip devices become multifunctional tools for separation and analysis of cells, without altering their state, efforts are converging into new analytical chemistry, diagnostic and treatment applications [118,119]. Further advances include lab-on-a-cell platforms [120,121] for isolation and individual characterization of cells and organ-on-a-chip devices for, among other applications, oxygenation studies [122,123], improvement of the clinical translation of nanomaterials for cancer theranostics, drug screening and personalized medicine [124,125].

Author Contributions: Conceptualization, S.O.C., R.O.R., D.P. and R.L.; Writing-Original Draft Preparation, S.O.C., R.O.R. and D.P.; Writing-Review & Editing, J.M.M., G.M. and R.L.; Supervision, G.M. and R.L.; Funding Acquisition, S.O.C, G.M. and R.L.

Funding: This work was supported by projects UID/EEA/04436/2019, UID/EMS/04077/2019, UID/EMS/00532/2019 from FCT; and by projects NORTE-01-0145-FEDER-028178, NORTE-01-0145-FEDER-029394, and NORTE-01-0145-FEDER-030171 funded by NORTE 2020 Portugal Regional Operational Programme, under PORTUGAL 2020 Partnership Agreement, through the European Regional Development Fund and by Fundação para a Ciência e Tecnologia (FCT), IP.

Conflicts of Interest: The authors declare no conflicts of interest.

References

1. Whitesides, G.M. The origins and the future of microfluidics. *Nature* **2006**, *442*, 368–373. [[CrossRef](#)] [[PubMed](#)]
2. Convery, N.; Gadegaard, N. 30 years of microfluidics. *Micro Nano Eng.* **2019**, *2*, 76–91. [[CrossRef](#)]
3. Mchedlishvili, G.; Maeda, N. Blood flow structure related to red cell flow: A determinant of blood fluidity in narrow microvessels. *Jpn. J. Physiol.* **2001**, *51*, 19–30. [[CrossRef](#)] [[PubMed](#)]
4. Bukowska, D.M.; Derzsi, L.; Tamborski, S.; Szkulmowski, M.; Garstecki, P.; Wojtkowski, M. Assessment of the flow velocity of blood cells in a microfluidic device using joint spectral and time domain optical coherence tomography. *Opt. Express* **2013**, *21*, 24025–24038. [[CrossRef](#)] [[PubMed](#)]
5. Abkarian, M.; Faivre, M.; Stone, H.A. High-speed microfluidic differential manometer for cellular-scale hydrodynamics. *Proc. Natl. Acad. Sci. USA* **2006**, *103*, 538–542. [[CrossRef](#)] [[PubMed](#)]
6. Bhattacharya, S.; DasGupta, S.; Chakraborty, S. Collective dynamics of red blood cells on an in vitro microfluid platform. *Lab Chip* **2018**, *18*, 3939–3948.
7. Zhao, R.; Antaki, J.F.; Naik, T.; Bachman, T.N.; Kameneva, M.V.; Wu, Z.J. Microscopic investigation of erythrocyte deformation dynamics. *Biorheology* **2006**, *43*, 747–765. [[PubMed](#)]
8. Fujiwara, H.; Ishikawa, T.; Lima, R.; Matsuki, N.; Imai, Y.; Kaji, H.; Nishizawa, M.; Yamaguchi, T. Red blood cell motions in high-hematocrit blood flowing through a stenosed microchannel. *J. Biomech.* **2009**, *42*, 838–843. [[CrossRef](#)]
9. Leble, V.; Lima, R.; Dias, R.; Fernandes, C.; Ishikawa, T.; Imai, Y.; Yamaguchi, T. Asymmetry of red blood cell motions in a microchannel with a diverging and converging bifurcation. *Biomicrofluidics* **2011**, *5*, 044120. [[CrossRef](#)]
10. Manouk, A.; Magalie, F.; Renita, H.; Kristian, S.; Catherine, A.B.-P.; Howard, A.S. Cellular-scale hydrodynamics. *Biomed. Mater.* **2008**, *3*, 034011.
11. Lima, R.; Ishikawa, T.; Imai, Y.; Yamaguchi, T. Blood Flow Behavior in Microchannels: Past, Current and Future Trends. In *Single and Two-Phase Flows on Chemical and Biomedical Engineering*; Dias, R., Martins, A.A., Lima, R., Mata, T.M., Eds.; Bentham Science: Sharjah, UAE, 2012; pp. 513–547.
12. Tomaiuolo, G.; Barra, M.; Preziosi, V.; Cassinese, A.; Rotoli, B.; Guido, S. Microfluidics analysis of red blood cell membrane viscoelasticity. *Lab Chip* **2011**, *11*, 449–454. [[CrossRef](#)] [[PubMed](#)]
13. McDonald, J.C.; Duffy, D.C.; Anderson, J.R.; Chiu, D.T.; Wu, H.; Schueller, O.J.; Whitesides, G.M. Fabrication of microfluidic systems in poly(dimethylsiloxane). *Electrophoresis* **2000**, *21*, 27–40. [[CrossRef](#)]
14. Rodrigues, R.O.; Lima, R.; Gomes, H.T.; Silva, A.M.T. Polymer microfluidic devices: An overview of fabrication methods. *U. Porto J. Eng.* **2015**, *1*, 67–79. [[CrossRef](#)]
15. Van Toan, N.; Toda, M.; Ono, T. An Investigation of Processes for Glass Micromachining. *Micromachines* **2016**, *7*, 51. [[CrossRef](#)] [[PubMed](#)]
16. Halldorsson, S.; Lucumi, E.; Gómez-Sjöberg, R.; Fleming, R.M.T. Advantages and challenges of microfluidic cell culture in polydimethylsiloxane devices. *Biosens. Bioelectron.* **2015**, *63*, 218–231. [[CrossRef](#)] [[PubMed](#)]
17. Gale, B.; Jafek, A.; Lambert, C.; Goenner, B.; Moghimifam, H.; Nze, U.; Kamarapu, S. A Review of current methods in microfluidic device fabrication and future commercialization prospects. *Inventions* **2018**, *3*, 60. [[CrossRef](#)]
18. Qin, D.; Xia, Y.; Whitesides, G.M. Soft lithography for micro- and nanoscale patterning. *Nat. Protoc.* **2010**, *5*, 491. [[CrossRef](#)] [[PubMed](#)]
19. Folch, A. *Introduction to BioMEMS*; CRC Press: Boca Raton, FL, USA, 2013; p. 528.
20. Walsh, D.I.; Kong, D.S.; Murthy, S.K.; Carr, P.A. Enabling microfluidics: From clean rooms to makerspaces. *Trends Biotechnol.* **2017**, *35*, 383–392. [[CrossRef](#)]
21. Pinto, V.C.; Sousa, P.J.; Cardoso, V.F.; Minas, G. Optimized SU-8 processing for low-cost microstructures fabrication without cleanroom facilities. *Micromachines* **2014**, *5*, 738–755. [[CrossRef](#)]
22. Faustino, V.; Catarino, S.O.; Lima, R.; Minas, G. Biomedical microfluidic devices by using low-cost fabrication techniques: A review. *J. Biomech.* **2016**, *49*, 2280–2292. [[CrossRef](#)] [[PubMed](#)]
23. Pinto, E.; Faustino, V.; Rodrigues, R.; Pinho, D.; Garcia, V.; Miranda, J.; Lima, R. A rapid and low-cost nonlithographic method to fabricate biomedical microdevices for blood flow analysis. *Micromachines* **2015**, *6*, 121–135. [[CrossRef](#)]

24. Bento, D.; Sousa, L.; Yaginuma, T.; Garcia, V.; Lima, R.; Miranda, J.M. Microbubble moving in blood flow in microchannels: Effect on the cell-free layer and cell local concentration. *Biomed. Microdevices* **2017**, *19*, 6. [[CrossRef](#)] [[PubMed](#)]
25. Guckenberger, D.J.; de Groot, T.E.; Wan, A.M.D.; Beebe, D.J.; Young, E.W.K. Micromilling: A method for ultra-rapid prototyping of plastic microfluidic devices. *Lab Chip* **2015**, *15*, 2364–2378. [[CrossRef](#)] [[PubMed](#)]
26. Lopes, R.; Rodrigues, R.O.; Pinho, D.; Garcia, V.; Schütte, H.; Lima, R.; Gassmann, S. Low cost microfluidic device for partial cell separation: Micromilling approach. In Proceedings of the 2015 IEEE International Conference on Industrial Technology (ICIT), Seville, Spain, 17–19 March 2015; pp. 3347–3350.
27. Ren, Y.; Ray, S.; Liu, Y. Reconfigurable Acrylic-tape Hybrid Microfluidics. *Sci. Rep.* **2019**, *9*, 4824. [[CrossRef](#)] [[PubMed](#)]
28. Gaal, G.; Mendes, M.; de Almeida, T.P.; Piazzetta, M.H.; Gobbi, Â.L.; Riul, A., Jr.; Rodrigues, V. Simplified fabrication of integrated microfluidic devices using fused deposition modeling 3D printing. *Sens. Actuators B Chem.* **2017**, *242*, 35–40. [[CrossRef](#)]
29. Li, Z.A.; Yang, J.; Li, K.; Zhu, L.; Tang, W. Fabrication of PDMS microfluidic devices with 3D wax jetting. *RSC Adv.* **2017**, *7*, 3313–3320. [[CrossRef](#)]
30. Faria, C.L.; Pinho, D.; Santos, J.; Gonçalves, L.M.; Lima, R. Low cost 3D printed biomodels for biofluid mechanics applications. *J. Mech. Eng. Biomech.* **2018**, *3*, 1–7. [[CrossRef](#)]
31. Rodrigues, R.O.; Pinho, D.; Bento, D.; Lima, R.; Ribeiro, J. Wall expansion assessment of an intracranial aneurysm model by a 3D Digital Image Correlation System. *Measurement* **2016**, *88*, 262–270. [[CrossRef](#)]
32. Miller, R.; Glinsner, T.; Kreindl, G.; Lindner, P.; Wimplinger, M. *Industrial Applications Demanding Low and High Resolution Features Realized by Soft UV-NIL and Hot Embossing*; SPIE: Bellingham, WA, USA, 2009; 72712].
33. He, Y.; Fu, J.-Z.; Chen, Z.-C. Research on optimization of the hot embossing process. *J. Micromech. Microeng.* **2007**, *17*, 2420–2425. [[CrossRef](#)]
34. Stormonth-Darling, J.M.; Pedersen, R.H.; How, C.; Gadegaard, N. Injection molding of ultra high aspect ratio nanostructures using coated polymer tooling. *J. Micromech. Microeng.* **2014**, *24*, 075019. [[CrossRef](#)]
35. Sarig-Nadir, O.; Livnat, N.; Zajdman, R.; Shoham, S.; Seliktar, D. laser photoablation of guidance microchannels into hydrogels directs cell growth in three dimensions. *Biophys. J.* **2009**, *96*, 4743–4752. [[CrossRef](#)] [[PubMed](#)]
36. Yang, C.-R.; Hsieh, Y.-S.; Hwang, G.-Y.; Lee, Y.-D. Photoablation characteristics of novel polyimides synthesized for high-aspect-ratio excimer laser LIGA process. *J. Micromech. Microeng.* **2004**, *14*, 480–489. [[CrossRef](#)]
37. Hartley, F.T.; Malek, C.G.K. Nanometer X-ray Lithography. In Proceedings of the Asia Pacific Symposium on Microelectronics and MEMS, Gold Coast, Australia, 8 October 1999.
38. Hizawa, T.; Takano, A.; Parthiban, P.; Doyle, P.S.; Iwase, E.; Hashimoto, M. Rapid prototyping of fluoropolymer microchannels by xurography for improved solvent resistance. *Biomicrofluidics* **2018**, *12*, 064105. [[CrossRef](#)] [[PubMed](#)]
39. Bartholomeusz, D.A.; Boutte, R.W.; Andrade, J.D. Xurography: Rapid prototyping of microstructures using a cutting plotter. *J. Microelectromech. Syst.* **2005**, *14*, 1364–1374. [[CrossRef](#)]
40. Lamont, A.C.; Alsharhan, A.T.; Sochol, R.D. Geometric Determinants of In-Situ Direct Laser Writing. *Sci. Rep.* **2019**, *9*, 394. [[CrossRef](#)] [[PubMed](#)]
41. Do, M.T.; Li, Q.; Nguyen, T.T.N.; Benisty, H.; Ledoux-Rak, I.; Lai, N.D. High aspect ratio submicrometer two-dimensional structures fabricated by one-photon absorption direct laser writing. *Microsyst. Technol.* **2014**, *20*, 2097–2102. [[CrossRef](#)]
42. Friedrich, C.R.; Vasile, M.J. The micromilling process for high aspect ratio microstructures. *Microsyst. Technol.* **1996**, *2*, 144–148. [[CrossRef](#)]
43. Kitson, P.J.; Rosnes, M.H.; Sans, V.; Dragone, V.; Cronin, L. Configurable 3D-Printed millifluidic and microfluidic ‘lab on a chip’ reactionware devices. *Lab Chip* **2012**, *12*, 3267–3271. [[CrossRef](#)]
44. Au, A.K.; Huynh, W.; Horowitz, L.F.; Folch, A.V. 3D-Printed microfluidics. *Angew. Chem. Int. Ed.* **2016**, *55*, 3862–3881. [[CrossRef](#)]
45. Waheed, S.; Cabot, J.M.; Macdonald, N.P.; Lewis, T.; Guijt, R.M.; Paull, B.; Breadmore, M.C. 3D printed microfluidic devices: Enablers and barriers. *Lab Chip* **2016**, *16*, 1993–2013. [[CrossRef](#)]
46. Chang, C.; Sakdinawat, A. Ultra-high aspect ratio high-resolution nanofabrication for hard X-ray diffractive optics. *Nat. Commun.* **2014**, *5*, 4243. [[CrossRef](#)] [[PubMed](#)]

47. Isobe, G.; Kanno, I.; Kotera, H.; Yokokawa, R. Perfusible multi-scale channels fabricated by integration of nanoimprint lithography (NIL) and UV lithography (UVL). *Microelectron. Eng.* **2012**, *98*, 58–63. [[CrossRef](#)]
48. Kim, J.; Gale, B.K. Quantitative and qualitative analysis of a microfluidic DNA extraction system using a nanoporous AlOx membrane. *Lab Chip* **2008**, *8*, 1516–1523. [[CrossRef](#)] [[PubMed](#)]
49. Zhang, R.; Larsen, N.B. Stereolithographic hydrogel printing of 3D culture chips with biofunctionalized complex 3D perfusion networks. *Lab Chip* **2017**, *17*, 4273–4282. [[CrossRef](#)] [[PubMed](#)]
50. Yeo, L.Y.; Chang, H.C.; Chan, P.P.; Friend, J.R. Microfluidic devices for bioapplications. *Small* **2011**, *7*, 12–48. [[CrossRef](#)] [[PubMed](#)]
51. Ren, K.; Zhou, J.; Wu, H. Materials for Microfluidic Chip Fabrication. *Acc. Chem. Res.* **2013**, *46*, 2396–2406. [[CrossRef](#)] [[PubMed](#)]
52. Friend, J.; Yeo, L. Fabrication of microfluidic devices using polydimethylsiloxane. *Biomicrofluidics* **2010**, *4*, 026502. [[CrossRef](#)] [[PubMed](#)]
53. Cardoso, V.F.; Minas, G. Micro Total Analysis Systems. In *Microfluidics and Nanofluid. Handbook: Fabrication, Implementation and Applications*; CPTF Group, Ed.; LLC Publishers: Boca Raton, FL, USA, 2011; Volume 5, pp. 319–366.
54. Haerberle, S.; Zengerle, R. Microfluidic platforms for lab-on-a-chip applications. *Lab Chip* **2007**, *7*, 1094–1110. [[CrossRef](#)]
55. Rife, J.C.; Bell, M.I.; Horwitz, J.S.; Kabler, M.N.; Auyeung, R.C.Y.; Kim, W.J. Miniature valveless ultrasonic pumps and mixers. *Sens. Actuators A Phys.* **2000**, *86*, 135–140. [[CrossRef](#)]
56. Fung, Y.C. *Biomechanics-Circulation*; Springer: New York, NY, USA, 1997.
57. Roselli, R.J.; Diller, K.R. *Biotransport: Principles and Applications*; Springer: New York, NY, USA, 2011.
58. Mohamed, M. Use of Microfluidic Technology for Cell Separation. In *Blood Cell-An Overview of Studies in Hematology*; InTech: London, UK, 2012.
59. Shields, C.W., 4th; Reyes, C.D.; Lopez, G.P. Microfluidic cell sorting: A review of the advances in the separation of cells from debulking to rare cell isolation. *Lab Chip* **2015**, *15*, 1230–1249. [[CrossRef](#)]
60. Songjaroen, T.; Dungchai, W.; Chailapakul, O.; Henry, C.S.; Laiwattanapaisal, W. Blood separation on microfluidic paper-based analytical devices. *Lab Chip* **2012**, *12*, 3392–3398. [[CrossRef](#)] [[PubMed](#)]
61. Kim, J.-H.; Woenker, T.; Adamec, J.; Regnier, F.E. Simple, Miniaturized blood plasma extraction method. *Anal. Chem.* **2013**, *85*, 11501–11508. [[CrossRef](#)] [[PubMed](#)]
62. Haerberle, S.; Brenner, T.; Zengerle, R.; Ducrée, J. Centrifugal extraction of plasma from whole blood on a rotating disk. *Lab Chip* **2006**, *6*, 776–781. [[CrossRef](#)] [[PubMed](#)]
63. Amasia, M.; Madou, M. Large-volume centrifugal microfluidic device for blood plasma separation. *Bioanalysis* **2010**, *2*, 1701–1710. [[CrossRef](#)] [[PubMed](#)]
64. Kersaudy-Kerhoas, M.; Sollier, E. Micro-scale blood plasma separation: From acoustophoresis to egg-beaters. *Lab Chip* **2013**, *13*, 3323–3346. [[CrossRef](#)] [[PubMed](#)]
65. Yang, S.; Undar, A.; Zahn, J.D. A microfluidic device for continuous, real time blood plasma separation. *Lab Chip* **2006**, *6*, 871–880. [[CrossRef](#)]
66. Shevkopyas, S.S.; Yoshida, T.; Munn, L.L.; Bitensky, M.W. Biomimetic autoseparation of leukocytes from whole blood in a microfluidic device. *Anal. Chem.* **2005**, *77*, 933–937. [[CrossRef](#)]
67. Ishikawa, T.; Fujiwara, H.; Matsuki, N.; Yoshimoto, T.; Imai, Y.; Ueno, H.; Yamaguchi, T. Asymmetry of blood flow and cancer cell adhesion in a microchannel with symmetric bifurcation and confluence. *Biomed. Microdevices* **2011**, *13*, 159–167. [[CrossRef](#)]
68. Karimi, A.; Yazdi, S.; Ardekani, A.M. Hydrodynamic mechanisms of cell and particle trapping in microfluidics. *Biomicrofluidics* **2013**, *7*, 21501. [[CrossRef](#)]
69. Martel, J.M.; Toner, M. Inertial focusing in microfluidics. *Annu. Rev. Biomed. Eng.* **2014**, *16*, 371–396. [[CrossRef](#)]
70. Zhang, J.; Yan, S.; Yuan, D.; Alici, G.; Nguyen, N.T.; Warkiani, M.E.; Li, W. Fundamentals and applications of inertial microfluidics: A review. *Lab Chip* **2016**, *16*, 10–34. [[CrossRef](#)] [[PubMed](#)]
71. Lee, C.-Y.; Chang, C.-L.; Wang, Y.-N.; Fu, L.-M. Microfluidic mixing: A review. *Int. J. Mol. Sci.* **2011**, *12*, 3263–3287. [[CrossRef](#)] [[PubMed](#)]
72. Suh, Y.K.; Kang, S. A Review on mixing in microfluidics. *Micromachines* **2010**, *1*, 82–111. [[CrossRef](#)]
73. Pamme, N.; Manz, A. On-chip free-flow magnetophoresis: Continuous flow separation of magnetic particles and agglomerates. *Anal. Chem.* **2004**, *76*, 7250–7256. [[CrossRef](#)] [[PubMed](#)]

74. Pamme, N. Continuous flow separations in microfluidic devices. *Lab Chip* **2007**, *7*, 1644–1659. [[CrossRef](#)] [[PubMed](#)]
75. Lee, G.-H.; Kim, S.-H.; Ahn, K.; Lee, S.-H.; Park, J.Y. Separation and sorting of cells in microsystems using physical principles. *J. Micromech. Microeng.* **2015**, *26*, 013003. [[CrossRef](#)]
76. Kang, T.G.; Yoon, Y.-J.; Ji, H.; Lim, P.Y.; Chen, Y. A continuous flow micro filtration device for plasma/blood separation using submicron vertical pillar gap structures. *J. Micromech. Microeng.* **2014**, *24*, 087001. [[CrossRef](#)]
77. Pinho, D.; Rodrigues, R.O.; Faustino, V.; Yaginuma, T.; Exposto, J.; Lima, R. Red blood cells radial dispersion in blood flowing through microchannels: The role of temperature. *J. Biomech.* **2016**, *49*, 2293–2298. [[CrossRef](#)]
78. Hou, H.W.; Bhagat, A.A.; Chong, A.G.; Mao, P.; Tan, K.S.; Han, J.; Lim, C.T. Deformability based cell margination—a simple microfluidic design for malaria-infected erythrocyte separation. *Lab Chip* **2010**, *10*, 2605–2613. [[CrossRef](#)]
79. Chung, Y.C.; Hsu, Y.L.; Jen, C.P.; Lu, M.C.; Lin, Y.C. Design of passive mixers utilizing microfluidic self-circulation in the mixing chamber. *Lab Chip* **2004**, *4*, 70–77. [[CrossRef](#)]
80. Khosravi Parsa, M.; Hormozi, F.; Jafari, D. Mixing enhancement in a passive micromixer with convergent–divergent sinusoidal microchannels and different ratio of amplitude to wave length. *Comput. Fluids* **2014**, *105*, 82–90. [[CrossRef](#)]
81. Rodrigues, R.O.; Pinho, D.; Faustino, V.; Lima, R. A simple microfluidic device for the deformability assessment of blood cells in a continuous flow. *Biomed. Microdevices* **2015**, *17*, 108. [[CrossRef](#)] [[PubMed](#)]
82. Squires, T.M.; Quake, S.R. Microfluidics: Fluid physics at the nanoliter scale. *Rev. Mod. Phys.* **2005**, *77*, 977–1026. [[CrossRef](#)]
83. Tsutsui, H.; Ho, C.-M. Cell separation by non-inertial force fields in microfluidic systems. *Mech. Res. Commun.* **2009**, *36*, 92–103. [[CrossRef](#)] [[PubMed](#)]
84. Gossett, D.R.; Weaver, W.M.; Mach, A.J.; Hur, S.C.; Tse, H.T.; Lee, W.; Amini, H.; Di Carlo, D. Label-free cell separation and sorting in microfluidic systems. *Anal. Bioanal. Chem.* **2010**, *397*, 3249–3267. [[CrossRef](#)] [[PubMed](#)]
85. Di Carlo, D. Inertial microfluidics. *Lab Chip* **2009**, *9*, 3038–3046. [[CrossRef](#)] [[PubMed](#)]
86. Bhagat, A.A.; Bow, H.; Hou, H.W.; Tan, S.J.; Han, J.; Lim, C.T. Microfluidics for cell separation. *Med. Biol. Eng. Comput.* **2010**, *48*, 999–1014. [[CrossRef](#)] [[PubMed](#)]
87. Pinho, D.; Rodrigues, R.O.; Yaginuma, T.; Faustino, V.; Bento, D.; Fernandes, C.S.; Garcia, V.; Pereira, A.I.; Lima, R. Motion of rigid particles flowing in a microfluidic device with a pronounced stenosis: Trajectories and deformation index. In Proceedings of the 11th World Congress on Computational Mechanics, Barcelona, Spain, 20–25 July 2014.
88. Yu, Z.T.F.; Aw Yong, K.M.; Fu, J. Microfluidic blood cell sorting: Now and beyond. *Small* **2014**, *10*, 1687–1703. [[CrossRef](#)] [[PubMed](#)]
89. Calejo, J.; Pinho, D.; Galindo-Rosales, F.J.; Lima, R.; Campo-Deaño, L. Particulate blood analogues reproducing the erythrocytes cell-free layer in a microfluidic device containing a hyperbolic contraction. *Micromachines* **2015**, *7*, 4. [[CrossRef](#)] [[PubMed](#)]
90. Wang, X.; Zhou, J.; Papautsky, I. Vortex-aided inertial microfluidic device for continuous particle separation with high size-selectivity, efficiency, and purity. *Biomicrofluidics* **2013**, *7*, 44119. [[CrossRef](#)] [[PubMed](#)]
91. Liu, Z.; Huang, F.; Du, J.; Shu, W.; Feng, H.; Xu, X.; Chen, Y. Rapid isolation of cancer cells using microfluidic deterministic lateral displacement structure. *Biomicrofluidics* **2013**, *7*, 11801. [[CrossRef](#)] [[PubMed](#)]
92. Rosenbluth, M.J.; Lam, W.A.; Fletcher, D.A. Analyzing cell mechanics in hematologic diseases with microfluidic biophysical flow cytometry. *Lab Chip* **2008**, *8*, 1062–1070. [[CrossRef](#)]
93. Pinho, D.; Campo-Deaño, L.; Lima, R.; Pinho, F.T. In vitro particulate analogue fluids for experimental studies of rheological and hemorheological behavior of glucose-rich RBC suspensions. *Biomicrofluidics* **2017**, *11*, 054105. [[CrossRef](#)]
94. Jäggi, R.D.; Sandoz, R.; Effenhauser, C.S. Microfluidic depletion of red blood cells from whole blood in high-aspect-ratio microchannels. *Microfluid. Nanofluid.* **2007**, *3*, 47–53. [[CrossRef](#)]
95. Singhal, J.; Pinho, D.; Lopes, R.; C Sousa, P.; Garcia, V.; Schütte, H.; Lima, R.; Gassmann, S. Blood Flow Visualization and Measurements in Microfluidic Devices Fabricated by a Micromilling Technique. *Micro Nanosyst.* **2015**, *7*, 148–153. [[CrossRef](#)]
96. Pinho, D.; Yaginuma, T.; Lima, R. A microfluidic device for partial cell separation and deformability assessment. *Biochip J.* **2013**, *7*, 367–374. [[CrossRef](#)]

97. Cidre, D.; Rodrigues, R.O.; Faustino, V.; Pinto, E.; Pinho, D.; Bento, D.; Correia, T.; Fernandes, C.S.; Dias, R.P.; Lima, R. Flow of red blood cells in microchannel networks: In vitro studies. In *Perspectives in Fundamental and Applied Rheology*; Rubio-Hernández, F.J., Gómez-Merino, A.I., Pino, C., Parras, L., Campo-Deaño, L., Galindo-Rosales, F.J., Velázquez-Navarro, J.F., Eds.; In Iberian Meeting on Rheology: Málaga, Spain, 2013; pp. 271–275.
98. Faivre, M.; Abkarian, M.; Bickraj, K.; Stone, H.A. Geometrical focusing of cells in a microfluidic device: An approach to separate blood plasma. *Biorheology* **2006**, *43*, 147–159. [[PubMed](#)]
99. Lima, R.; Oliveira, M.S.; Ishikawa, T.; Kaji, H.; Tanaka, S.; Nishizawa, M.; Yamaguchi, T. Axisymmetric polydimethylsiloxane microchannels for in vitro hemodynamic studies. *Biofabrication* **2009**, *1*, 035005. [[CrossRef](#)]
100. Bento, D.; Pereira, A.I.; Lima, J.; Miranda, J.M.; Lima, R. Cell-free layer measurements of in vitro blood flow in a microfluidic network: An automatic and manual approach. *Comput. Methods Biomech. Biomed. Eng. Imaging Vis.* **2018**, *6*, 629–637. [[CrossRef](#)]
101. Bento, D.; Fernandes, C.S.; Miranda, J.M.; Lima, R. In vitro blood flow visualizations and cell-free layer (CFL) measurements in a microchannel network. *Exp. Therm. Fluid Sci.* **2019**, *109*, 109847. [[CrossRef](#)]
102. Tripathi, S.; Varun Kumar, Y.V.B.; Prabhakar, A.; Joshi, S.S.; Agrawal, A. Passive blood plasma separation at the microscale: A review of design principles and microdevices. *J. Micromech. Microeng.* **2015**, *25*, 083001. [[CrossRef](#)]
103. Bacchin, P.; Meireles, M.; Aimar, P. Modelling of filtration: From the polarised layer to deposit formation and compaction. *Desalination* **2002**, *145*, 139–146. [[CrossRef](#)]
104. Keskinler, B.; Yildiz, E.; Erhan, E.; Dogru, M.; Bayhan, Y.K.; Akay, G. Crossflow microfiltration of low concentration-nonliving yeast suspensions. *J. Membr. Sci.* **2004**, *233*, 59–69. [[CrossRef](#)]
105. Chen, X.; Cui, D.F.; Liu, C.C.; Li, H. Microfluidic chip for blood cell separation and collection based on crossflow filtration. *Sens. Actuators B Chem.* **2008**, *130*, 216–221. [[CrossRef](#)]
106. Lee, Y.; Clark, M.M. Modeling of flux decline during crossflow ultrafiltration of colloidal suspensions. *J. Membr. Sci.* **1998**, *149*, 181–202. [[CrossRef](#)]
107. Crowley, T.A.; Pizziconi, V. Isolation of plasma from whole blood using planar microfilters for lab-on-a-chip applications. *Lab Chip* **2005**, *5*, 922–929. [[CrossRef](#)] [[PubMed](#)]
108. Zhang, W.; Kai, K.; Choi, D.S.; Iwamoto, T.; Nguyen, Y.H.; Wong, H.; Landis, M.D.; Ueno, N.T.; Chang, J.; Qin, L. Microfluidics separation reveals the stem-cell-like deformability of tumor-initiating cells. *Proc. Natl. Acad. Sci. USA* **2012**, *109*, 18707–18712. [[CrossRef](#)] [[PubMed](#)]
109. Choi, J.; Hyun, J.-C.; Yang, S. On-chip Extraction of Intracellular Molecules in White Blood Cells from Whole Blood. *Sci. Rep.* **2015**, *5*, 15167. [[CrossRef](#)] [[PubMed](#)]
110. Kuntaegowdanahalli, S.S.; Bhagat, A.A.; Kumar, G.; Papautsky, I. Inertial microfluidics for continuous particle separation in spiral microchannels. *Lab Chip* **2009**, *9*, 2973–2980. [[CrossRef](#)] [[PubMed](#)]
111. Lee, M.G.; Choi, S.; Kim, H.J.; Lim, H.K.; Kim, J.H.; Huh, N.; Park, J.K. Inertial blood plasma separation in a contraction–expansion array microchannel. *Appl. Phys. Lett.* **2011**, *98*, 253702. [[CrossRef](#)]
112. Van Delinder, V.; Groisman, A. Perfusion in microfluidic cross-flow: Separation of white blood cells from whole blood and exchange of medium in a continuous flow. *Anal. Chem.* **2007**, *79*, 2023–2030. [[CrossRef](#)] [[PubMed](#)]
113. Van Delinder, V.; Groisman, A. Separation of plasma from whole human blood in a continuous cross-flow in a molded microfluidic device. *Anal. Chem.* **2006**, *78*, 3765–3771. [[CrossRef](#)] [[PubMed](#)]
114. Yang, X.; Yang, J.M.; Tai, Y.-C.; Ho, C.-M. Micromachined membrane particle filters. *Sens. Actuators A Phys.* **1999**, *73*, 184–191. [[CrossRef](#)]
115. Streets, A.M.; Huang, Y. Chip in a lab: Microfluidics for next generation life science research. *Biomicrofluidics* **2013**, *7*, 11302. [[CrossRef](#)] [[PubMed](#)]
116. Shevkoplyas, S.S.; Yoshida, T.; Gifford, S.C.; Bitensky, M.W. Direct measurement of the impact of impaired erythrocyte deformability on microvascular network perfusion in a microfluidic device. *Lab Chip* **2006**, *6*, 914–920. [[CrossRef](#)] [[PubMed](#)]
117. Faustino, V.; Catarino, S.O.; Pinho, D.; Lima, R.A.; Minas, G. A passive microfluidic device based on crossflow filtration for cell separation measurements: A spectrophotometric characterization. *Biosensors* **2018**, *8*, 125. [[CrossRef](#)] [[PubMed](#)]

118. Catarino, S.O.; Lima, R.; Minas, G. Smart devices: Lab-on-a-chip. In *Bioinspired Materials for Drug Delivery and Analysis*; Rodrigues, L., Mota, M., Eds.; Woodhead Publishing: Cambridge, UK, 2017; pp. 331–369.
119. Minas, G.; Catarino, S.O. Lab-on-a-chip devices for chemical analysis. In *Encyclopedia of Microfluidics and Nanofluidics*; Li, D., Ed.; Springer: New York NY, USA, 2015; pp. 1511–1531.
120. Clausell-Tormos, J.; Lieber, D.; Baret, J.C.; El-Harrak, A.; Miller, O.J.; Frenz, L.; Blouwolf, J.; Humphry, K.J.; Köster, S.; Duan, H.; et al. Droplet-based microfluidic platforms for the encapsulation and screening of mammalian cells and multicellular organisms. *Chem. Biol.* **2008**, *15*, 427–437. [[CrossRef](#)] [[PubMed](#)]
121. Wang, M.; Orwar, O.; Olofsson, J.; Weber, S.G. Single-cell electroporation. *Anal. Bioanal. Chem.* **2010**, *397*, 3235–3248. [[CrossRef](#)] [[PubMed](#)]
122. Wood, D.K.; Soriano, A.; Mahadevan, L.; Higgins, J.M.; Bhatia, S.N. A biophysical indicator of vaso-occlusive risk in sickle cell disease. *Sci. Transl. Med.* **2012**, *4*, 123ra26. [[CrossRef](#)]
123. Di Caprio, G.; Stokes, C.; Higgins, J.M.; Schonbrun, E. Single-cell measurement of red blood cell oxygen affinity. *Proc. Natl. Acad. Sci. USA* **2015**, *112*, 9984–9989. [[CrossRef](#)]
124. Bhise, N.S.; Ribas, J.; Manoharan, V.; Zhang, Y.S.; Polini, A.; Massa, S.; Dokmeci, M.E.R.; Khademhosseini, A. Organ-on-a-chip platforms for studying drug delivery systems. *J. Control. Release* **2014**, *190*, 82–93. [[CrossRef](#)] [[PubMed](#)]
125. Zhang, B.; Radisic, M. Organ-on-a-chip devices advance to market. *Lab Chip* **2017**, *17*, 2395. [[CrossRef](#)] [[PubMed](#)]



© 2019 by the authors. Licensee MDPI, Basel, Switzerland. This article is an open access article distributed under the terms and conditions of the Creative Commons Attribution (CC BY) license (<http://creativecommons.org/licenses/by/4.0/>).



Article

Viscosity Estimation of a Suspension with Rigid Spheres in Circular Microchannels Using Particle Tracking Velocimetry

Misa Kawaguchi ¹, Tomohiro Fukui ^{1,*}, Kenichi Funamoto ², Miho Tanaka ¹, Mitsuru Tanaka ¹, Shigeru Murata ¹, Suguru Miyauchi ² and Toshiyuki Hayase ²

¹ Department of Mechanical Engineering, Kyoto Institute of Technology, Kyoto 606-8585, Japan; d9821001@edu.kit.ac.jp (M.K.); m9623015@edu.kit.ac.jp (M.T.); mtanaka@kit.ac.jp (M.T.); murata@kit.ac.jp (S.M.)

² Institute of Fluid Science, Tohoku University, Sendai 980-8577, Japan; funamoto@tohoku.ac.jp (K.F.); miyauchi@reynolds.ifs.tohoku.ac.jp (S.M.); hayase@ifs.tohoku.ac.jp (T.H.)

* Correspondence: fukui@kit.ac.jp; Tel.: +81-75-724-7314

Received: 17 September 2019; Accepted: 2 October 2019; Published: 4 October 2019

Abstract: Suspension flows are ubiquitous in industry and nature. Therefore, it is important to understand the rheological properties of a suspension. The key to understanding the mechanism of suspension rheology is considering changes in its microstructure. It is difficult to evaluate the influence of change in the microstructure on the rheological properties affected by the macroscopic flow field for non-colloidal particles. In this study, we propose a new method to evaluate the changes in both the microstructure and rheological properties of a suspension using particle tracking velocimetry (PTV) and a power-law fluid model. Dilute suspension (0.38%) flows with fluorescent particles in a microchannel with a circular cross section were measured under low Reynolds number conditions ($Re \approx 10^{-4}$). Furthermore, the distribution of suspended particles in the radial direction was obtained from the measured images. Based on the power-law index and dependence of relative viscosity on the shear rate, we observed that the non-Newtonian properties of the suspension showed shear-thinning. This method will be useful in revealing the relationship between microstructural changes in a suspension and its rheology.

Keywords: suspension; rheology; power-law fluid; circular microchannel; pressure-driven flow; particle tracking velocimetry; microstructure

1. Introduction

The rheological properties of a suspension (solid particles dispersed in a fluid) vary depending on the particle volume fraction, particle shape, interactions between particles, spatial arrangement of particles, and nature of the solvent [1]. Non-Newtonian phenomenon is commonly accompanied by shear-thinning [2] or shear-thickening [3] behavior, or yield stress [4] resulting from the complex influence of many factors. Suspension flows are ubiquitous in industry and nature. In the industrial field, the rheology of suspension directly influences product quality such as food and paint [5]. Furthermore, suspensions are also important for industrial processes such as filtration [6] and ceramic processing [7,8], since they are the precursors to the manufacturing of numerous products. In nature, examples of suspensions include mud, which is essentially a dispersion of rigid particles, and blood, which is a suspension of red blood cells dispersed in plasma [9,10]. Therefore, understanding rheological properties of suspensions is expected to lead to control of suspension rheology and elucidation of hemorheology.

When the size of particles increases with respect to the channel size, wall effects and interactions between particles are observed. Sangani et al. [11] reported that the presence of walls increases the

particle stresslet. Fukui et al. [12] found that particles rotate to achieve a kinetic balance with the surrounding hydrodynamic forces, which results in a decrease in fluid resistance. Moreover, some researchers reported that viscosity significantly decreased for strongly confined conditions [13–16]. The above phenomena are reflected in the strong correlation between suspension viscosity and microstructure defined by spatial particle arrangements.

Many researchers have addressed the connection between the microstructure and rheology of a suspension [1,17,18]. A numerical approach is useful in assessing the relationship between microstructure and rheology. It is easy to obtain information on the microstructure of a suspension because particle distribution can be captured accurately at all times. Fukui et al. [19] conducted a two-way coupling simulation and reported that non-Newtonian properties change because of particle migration. However, the experimental evaluation of the microstructure is difficult. Light scattering techniques are often used to obtain the structure factor of suspensions, and, although these techniques are useful for colloidal suspensions, their application to non-colloidal suspensions becomes difficult because the size of the particles is large compared with the wavelength of light [20]. Talini et al. [21] proposed a nuclear magnetic resonance (NMR) technique for non-colloidal suspensions, which is capable of measuring structures up to 1 mm. However, this technique could only be applied to static conditions because particles must stay in their positions during the scanning. Thus, for non-colloidal suspensions, it is difficult to evaluate the influence of the change of the microstructure on the rheological properties affected by the macroscopic flow field.

Various methods for measuring viscosity in complex fluids using microfluidic devices have been proposed [22], and several studies have evaluated the velocity field of complex fluids using particle imaging velocimetry (PIV) [23–25]. Degré et al. [24] evaluated the viscosity of polymer solutions by PIV. Jesinghausen et al. [26] report that the viscosity evaluated using PIV was 10%–20% lower than the value measured by a viscometer. These studies were conducted using rectangular channels. However, from an engineering and hemorheological point of view, it is important to consider the relationship between particle distribution and rheology in circular channels of pipe flow.

The purpose of this study is to propose a new method for evaluating both the microscopic structure and viscosity of non-colloidal hard sphere suspension flows. In this paper, a microchannel with a circular cross section was fabricated, and the suspension flow with fluorescent particles was measured using a microscope. The velocity distribution was obtained using a particle tracking velocimetry (PTV), and the particle radial distributions were also determined. The non-Newtonian properties of a suspension were examined using the power-law fluid model.

2. Materials and Methods

2.1. Suspension

Dilute suspensions of rigid spherical particles in a Newtonian fluid were used. Fluorescent polymer microspheres with a diameter $d_p = 25 \mu\text{m}$ (35-5, Thermo Fisher Scientific, Waltham, MA, USA) were suspended in a mixture of water and glycerol (075-00616, Wako, Osaka, Japan) to attain neutral buoyancy. The density of the mixture was equivalent to that of the particle density (1.05 g/cm^3). A small amount (<0.5%) of surfactant Tween 20 (17-1316-01, GE Healthcare, Chicago, IL, USA) was added to fully disperse the dry powder of fluorescent particles. The volume fraction (ϕ) of the suspended particles measured by using a chip (C-Chip, NanoEntech, Seoul, Korea) was 0.38%. The suspension viscosity was $1.73 \text{ mPa}\cdot\text{s}$, which was measured using an oscillation-type viscometer (VM-10A, CBC Co., Ltd., Tokyo, Japan) at room temperature ($27 \text{ }^\circ\text{C}$).

2.2. Microchannel

Circular cross section polydimethylsiloxane (PDMS) microchannels (Figure 1) were fabricated using a fishing gut [27]. Most PDMS microfluidic channels are fabricated using photolithographic techniques and their cross section is typically rectangular [28]. Recently, some methods [29,30] have

been developed to form more complex microchannels. Because pipe flow is important for many applications, such as industrial or blood flow, circular cross section PDMS microchannels are often used [31–33]. The fabrication of a circular PDMS microchannel using a fishing gut is explained below.

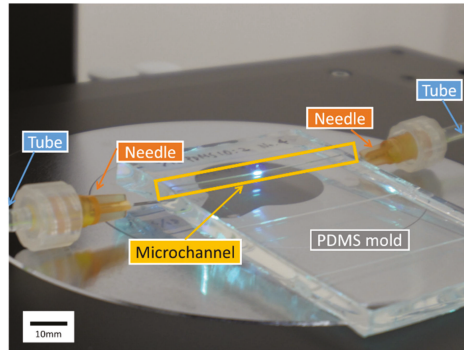


Figure 1. Circular polydimethylsiloxane (PDMS) microchannel in the PDMS mold. Needles were inserted on both sides of the microchannel and connected by tubes.

- (1) Holes were drilled in a case (Styrol square case type 3, As One, Osaka, Japan) and a fishing gut with a diameter $D = 520 \mu\text{m}$ (Type 10, Matsuura Industry, Osaka, Japan) was passed through the holes.
- (2) PDMS (Silgard 184 Silicone Elastomer Kit, Dow Corning, Midland, MI, USA) was synthesized by mixing the elastomer base with its curing agent in a weight ratio of 10:2. The ratio of the curing agent was increased to twice the recommended value to suppress the effects of PDMS elasticity. Next, PDMS was poured into the case and cured in an oven (75°C) overnight.
- (3) Lastly, the gut was pulled out gently and the PDMS mold with the microchannel was taken out from the case. For the measurement, needles (NN-2516R, TERUMO, Tokyo, Japan) were inserted on both sides of the microchannel and connected by tubes.

2.3. Experimental Setup

Figure 2 shows a schematic of the experimental apparatus. A suspension was injected into the microchannel by a syringe pump (KDS210, KD Scientific, Holliston, MA, USA) in a steady state. Fluorescent images of the flow field and phase contrast images were obtained for calibration. The Reynolds number was altered by presetting the flow rate to approximately $5\text{--}20 \mu\text{L}/\text{min}$, which corresponds to the Re range from 0.125 to 0.5. In this study, confinement C [11] is defined as $C = d_p/D = 0.05$, which is the ratio of the particle size to tube size. The particle Reynolds number (Re_p) [34] is defined as $Re_p = Re \times C^2$ and it corresponds to Re_p in the range of $2.9 \times 10^{-4}\text{--}1.2 \times 10^{-3}$.

The measurement area was set parallel to the flow direction passing through the tube axis. The particle distribution in the radial direction and flow velocity were measured. To eliminate the influence of the attachment of the connector on the tube, the flow field was measured at a location $20D$ away from the inlet. Measurement conditions were fixed as recorded in Table 1. Different frame rates were set for each condition so that the particles travel similar distances (about $0.3D$ on the centerline) at each shutter interval. Furthermore, the flow fields were measured three times for each condition using a disk scanning microscope system (IX83-DSU, Olympus, Tokyo, Japan) at $10\times$ magnification.

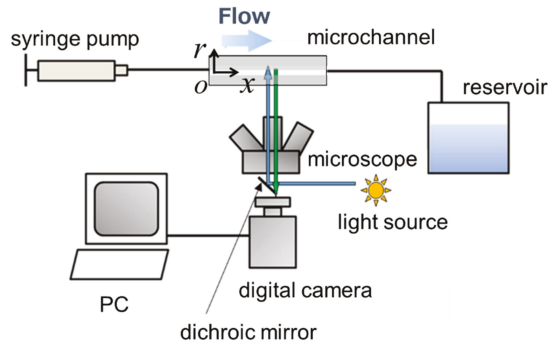


Figure 2. Schematic view of experimental apparatus. The measurement area was set parallel to the flow direction passing through the tube axis to measure both particle distribution in the radial direction and flow velocity.

Table 1. Measurement conditions.

Re (-)	Re_p (-)	Time (s)	Frame Rate (fps)
0.125	2.9×10^{-4}	200	5
0.25	5.8×10^{-4}	100	10
0.5	1.2×10^{-3}	50	20

2.4. Image Processing

Figure 3 shows the sample of images used for analysis. The procedure for obtaining particle concentration profiles and axial velocity profiles using image processing software (ImageJ/Fiji, National Institutes of Health (NIH), Bethesda, MD, USA) [35,36] is as follows.

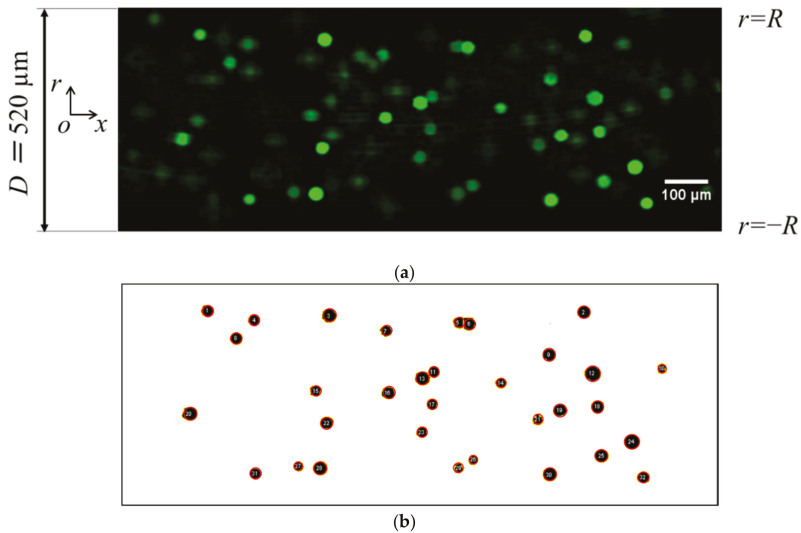


Figure 3. Representative images of particles in a microchannel. (a) Fluorescent image after background subtraction and (b) a sample of extracted particles in a binary image. Particles are encircled in red in Figure 3b for clarity.

1. Fluorescent particle images were converted to binary images using the “subtract background” command given as a preparation, and the binarization was conducted based on the threshold determined using the Otsu method [37].
2. Particle size for analysis was set to 200 pixel², which corresponds to the particle diameter of ~ 22 μm, and the coordinates of the particle center point were extracted using macros. Figure 3b shows a sample of extracted particles obtained from a binary image. The particles are encircled in red in Figure 3b for clarity. In this step, “watershed segmentation” was used for identifying each particle, and the function of automatically separated or cut apart particles were recognized as a single cluster due to overlapping.
3. The measurement region was equally divided in the radial direction, and the number of particles in each section was counted from their radial positions. The existence probability of particles in the radial direction σ was then obtained with respect to the number of particles in the entire image.
4. Steps 1–3 were repeated for all images, and these data were analyzed for a time-averaged particle concentration profile.
5. PTV was also employed, and time-averaged velocity profiles were obtained. The non-Newtonian properties of the suspension were evaluated by comparing the time-averaged measured velocity profiles with those from a power-law fluid. Details have been provided in Section 2.5.

Sizes of the particles in the images were certainly different from each other, as shown in Figure 3. This could be attributed to the particle distance with respect to the focus plane of the microscope. Since the apparently large particles might be out of the focal area, the translational velocity of the particles could be decreased when compared to the theoretical value. On the other hand, the apparent particle size variation was also caused by the difference in the refractive index between the fluid and the microchannel. The refractive index of PDMS is 1.41 while that of water is 1.33, or 1.47 for glycerol. The refractive index of a water/glycerol mixture of 61% glycerol matches that of PDMS [30,38]. However, in order to satisfy the neutrally buoyant condition according to priority, a water/glycerol mixture with approximately 20% glycerol was used in this study. Therefore, the refractive index of the fluid may not be well-matched with that of the microchannel. Nevertheless, the error of the flow rate was, at most, 5%, as described later, and these effects might be negligible in this study.

2.5. Non-Newtonian Properties

A power-law model is a simple model used to represent viscosity as a function of the shear rate. The non-Newtonian properties of the suspension were assessed by comparing the measured velocity profiles acquired by PTV with those from a power-law fluid. The velocity profiles of power-law fluids [39] are as follows.

$$u(r) = \frac{3n+1}{n+1} u_0 \left[1 - \left| \frac{r}{R} \right|^{\frac{n+1}{n}} \right], \quad (1)$$

where $u(r)$ is the axial velocity, n is the power-law fluid index, u_0 is the characteristic velocity, R is the radius of the microchannel, and r is the radial position in a range satisfying the condition $-R < r < R$. If $n = 1$, the fluid is Newtonian. Otherwise, it is classified as a non-Newtonian fluid, which exhibits shear-thinning (thixotropy) for $n < 1$ and shear-thickening (dilatancy) for $n > 1$.

Power-law fitting was applied using the least-absolute-value method [12] to minimize the following cost function.

$$\text{cost function} = \sum_{\text{all particles}} |u_m(r) - u(r)| \rightarrow \min., \quad (2)$$

where $u_m(r)$ is the measured axial velocity and $u(r)$ is the axial velocity estimated using the power-law fluid equation (Equation (1)) at the corresponding radial position. The cost function was defined as a sum of the absolute differences for all particles.

2.6. Relative Viscosity

The relative viscosity was assessed using the viscosity equation for power-law fluids. The effective viscosity η_{eff} is defined in the following equation.

$$\eta_{\text{eff}} = \eta_0 |\dot{\gamma}|^{n-1}, \tag{3}$$

where η_0 is the viscosity of a suspension, and $\dot{\gamma}$ is the shear rate. Note that when $\dot{\gamma} = 1$, the relative viscosity equals 1, regardless of the power-law fluid index n .

The viscous resistance is equivalent to the pressure drop in a fully developed laminar tube flow. For dilute suspensions, the drag force acting on the particles can be neglected when the suspension flows steadily [12], and the flow energy dissipates on the walls. Thus, the pressure drop is equal to the spatially integrated wall shear stress value. The wall shear stress can be calculated from the shear rate on the walls using Newton’s law, and, therefore, the relative viscosity η_{eff}/η_0 can be approximated using the shear rate on the wall. The shear rate on the wall is analytically expressed in Equation (4), and the relative viscosity η_{eff}/η_0 was evaluated from the equation using the power-law index n by the velocity profile fitting.

$$\frac{\eta_{\text{eff}}}{\eta_0} = \left| \frac{\partial u}{\partial r} \right|^{n-1} \Bigg|_{r=R} = \left(\frac{3n+1}{n} \frac{u_0}{R} \right)^{n-1}. \tag{4}$$

3. Results and Discussion

Figure 4 shows the particle concentration profiles in the radial direction for different particle Reynolds number conditions. In this study, the number of divisions in the radial direction was set to 20, which is approximately equivalent to the ratio of the channel diameter to the particle size ($=1/C$). Therefore, the value of the probability density function becomes $\sigma = 1/20 = 0.05$ (shown with a solid black line) when the spatial arrangement of suspended particles is uniform. Figure 4 shows that the particles were distributed around $\sigma = 0.05$ with minor deviation, regardless of the particle Reynolds number.

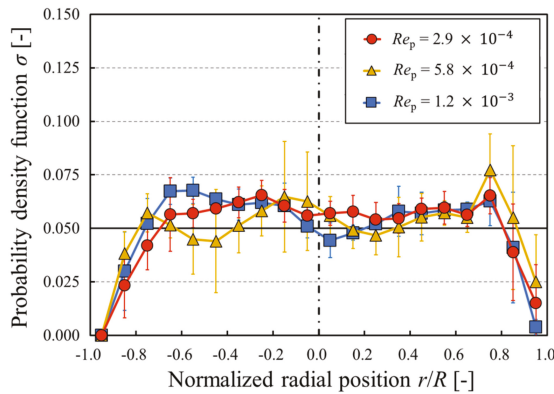


Figure 4. Concentration profiles. The data plotted are the mean \pm 1 SD. The solid black line represents uniform distribution, and the black dash-dot line at $r/R = 0.0$ indicates the center of the microchannel.

Choi et al. [40] investigated the distributions of neutrally buoyant spherical particles suspended in a micro-scale pipe flow using a digital holography technique, which showed a qualitatively similar distribution when compared to our experimental results.

The following reduced tube length L_3 is defined by Segré and Silberberg [41].

$$L_3 = Re \left(\frac{L}{D} \right) \left(\frac{d_p}{D} \right)^3, \quad (5)$$

where L is the distance from the inlet of a microchannel. Choi et al. [40] observed that the particle distribution changes due to an inertial effect under the following condition.

$$L_3 \geq 3. \quad (6)$$

In this study, the reduced tube length L_3 was in the order of 10^{-4} – 10^{-3} , and hence, slight changes in radial particle distribution can be observed due to weak inertial effects. Fukui et al. [42] in their numerical study demonstrated that the dispersion of the particles was relatively uniform under low particle Reynolds number conditions. In this study, a mixture of water and glycerol was selected as a solvent for neutrally buoyant conditions. A similar distribution has been confirmed for low concentration suspensions under neutrally buoyant conditions by Yan and Koplik [43].

Figure 5 shows the axial velocity profiles for each particle Reynolds number condition. The measured flow rate decreased by, at most, 5% when compared with the presetting flow rate value. When the measured velocity profiles were compared with those from the power-law fluid model, the velocity profile (Equation (1)) with an equivalent measured flow rate was applied. Moreover, the fully developed boundary layer can be observed because the length of the measurement area from the inlet of the tube was sufficiently long when compared with the inlet length.

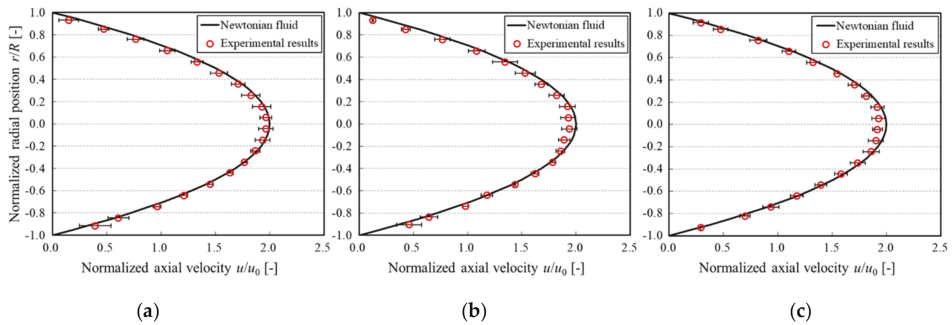


Figure 5. Normalized axial velocity profiles. The red plots and error bars are the mean ± 1 SD, and the black solid line is the velocity profile of Newtonian fluid ($n = 1$) for comparison. (a) $Re_p = 2.9 \times 10^{-4}$, (b) $Re_p = 5.8 \times 10^{-4}$, and (c) $Re_p = 1.2 \times 10^{-3}$.

From Figure 5, it can be seen that the velocity profiles were slightly blunted with an increasing particle Reynolds number. Hampton et al. [44] experimentally observed blunted velocity profiles. Jabeen et al. [45] reported a similar trend by numerical approach. Moreover, it has also been observed that velocity profiles become more blunted at high concentration conditions [43,46]. In this study, the suspension was dilute. Therefore, the velocity profiles were observed to be slightly blunted.

Figure 6 shows the relationship between the power-law index n and particle Reynolds number. The power-law fluid index decreases with an increasing particle Reynolds number. Although the experimental conditions were limited, this tendency was consistent with that of the previous study [42] by numerical simulation. Non-Newtonian properties of the suspension showed shear-thinning because the power-law index n is smaller than 1. Moreover, it is considered that the shear-thinning is more enhanced with an increasing particle Reynolds number.

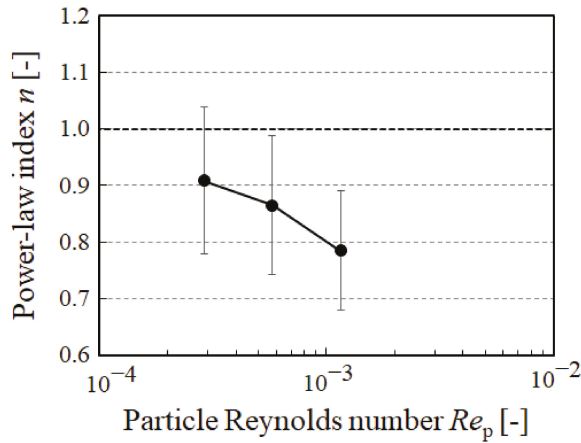


Figure 6. Relationship between power-law index n and particle Reynolds number Re_p . The plots are the mean \pm 1 SD.

Figure 7 shows the relationship between relative viscosity η_{eff}/η_0 and shear rate $\dot{\gamma}$. In this study, because non-Newtonian properties were evaluated by the power-law fluid, the relative viscosity equals 1 when $\dot{\gamma} = 1$ analytically (Equation (3)). This is also plotted in Figure 7 as an analytical value. From Figure 7, it was found that the relative viscosity η_{eff}/η_0 decreased with an increasing shear rate $\dot{\gamma}$.

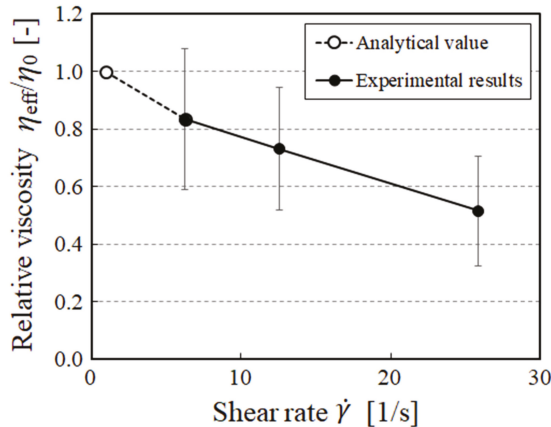


Figure 7. Relationship between relative viscosity η_{eff}/η_0 and the shear rate $\dot{\gamma}$. The plots are the mean \pm 1 SD. The relative viscosity was estimated using Equation (4).

The viscosity of the suspension was determined from the velocity distribution using the power-law fluid model. Degré et al. [24] measured the viscosity of polymer solutions using PIV. Jesinghaus et al. [26] applied a similar method for suspension flow in a rectangular channel. In this study, the viscosity of the suspension flow in a circular channel was evaluated by PTV. The benefit of using PTV lies in its application to the dilute suspensions or to a suspension with larger particles. In this study, we focus on the relationship between the microstructure and the consequential rheological properties of a suspension. Especially, we also focus on change in microstructure due to inertia. In order to investigate the inertial effects of suspended particles, experimental works should be conducted for a wide range of particle Reynolds number conditions. Particle Reynolds number can be changed by

two parameters, i.e., flow velocity or particle size. If larger particles are used, the number of particles are decreased for the same particle concentration condition. When the number of particles contained in an interrogation window is not enough, accuracy of the PIV analysis becomes poor. Therefore, in this sense, PTV may be preferable to PIV. Moreover, one of the advantages of our method is that it is capable of evaluating rheological properties while considering the microstructure changes of the suspension, which is difficult with a classical rheometer. It has been reported in previous research that wall shear stress decreases locally in micro-vessels due to the motion of blood cell and hydrodynamic interactions [47,48]. Furthermore, in numerical simulations, the relative viscosity could be below 1 locally for dense (highly concentrated) suspensions with rigid particles [16]. These findings are important for considering blood flow in bioengineering. Endothelial cells covering the inner surface of blood vessels sense the wall shear stress (WSS) and respond to it mechanically. For example, when the WSS increases, endothelial cells produce vasodilators, such as nitric oxide (NO) [49]. It is also suggested that endothelial cells can sense changes in WSS not only temporally but also spatially [50]. Therefore, it is important to understand the local WSS distribution and the local viscosity changes. On the other hand, this proposed method is limited in the case of non-transparent fluid or highly concentrated suspension.

Figure 8 shows the spatially averaged axial distances between particles referring to the radial direction. Note that the particle–particle distance was normalized by the channel diameter. The difference in the distance referring to the radial direction was not significant. In addition, these distributions are independent of the particle Reynolds number. Doyeux et al. [13] mentioned that the intrinsic viscosity can be expressed as a function of the particle–wall distance. In order to consider suspension rheology in terms of the microstructure, the radial particle distributions have been investigated in many studies. On the other hand, according to Fukui et al. [12], when the rotational velocity decreases due to the particle–particle interactions, the macroscopic viscosity of the suspension increases. Therefore, it is important to consider particle–particle distance not only in the radial direction but also in the axial direction in order to evaluate the microstructure and consequential rheological properties.

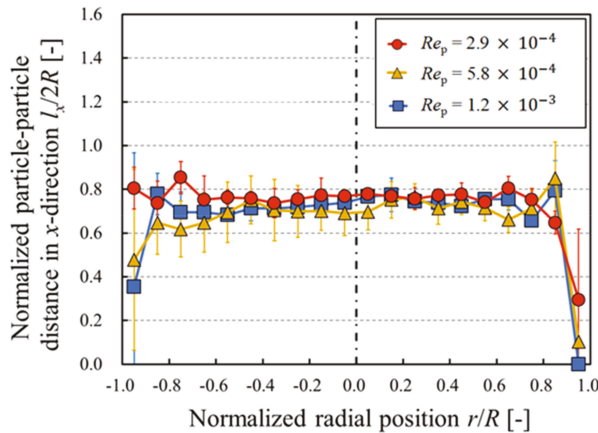


Figure 8. Spatially averaged axial distances between particles referring to the radial direction. The data plotted are the mean \pm 1 SD. The value of distance was normalized by the diameter of the microchannel.

Microstructure is key to understanding the mechanism of suspension rheology [1,17,18]. Red blood cells move to the axis of the blood vessel due to their deformability, which is known as axial accumulation [51]. On the other hand, for rigid particles, when the bulk or particle Reynolds number increase, particles begin migrating due to inertia toward the radial equilibrium positions at $0.6R$. When particle migration occurs, the distribution of particles in the cross section becomes annulus,

which is known as the “tubular pinch effect” or the “Segré–Silberberg effect” [41,52]. Analysis by numerical approaches suggest that the non-Newtonian properties are altered due to these microstructure changes [42,45]. According to previous research, the equilibrium position is around $0.6R$, and the equilibrium position shifts toward the wall with an increasing Reynolds number [53,54], while it shifts toward the tube axis with increasing confinement [54]. In the future works, we will elucidate the influence of these equilibrium positions, i.e., the difference in microstructure, on the suspension rheology in detail.

In previous studies, velocimetry-based viscometers rely on measuring the velocity profile at a given pressure drop. The shear rate can be calculated from the gradient of the velocity profiles (Equation (4)), and shear stress was calculated from the pressure drop. A curve of shear stress versus the shear rate can be obtained directly. Thus, the previous method allows for direct quantification of the rheology of complex fluids [22]. On the contrary, in the proposed method, the relative viscosity is examined using the power-law fluid model in consideration of the microstructure. However, only a qualitative evaluation of non-Newtonian properties of a suspension is implemented in this paper. Therefore, quantitative validation of our method is required. This includes measuring the relative viscosity using a Couette rheometer or introducing a pressure sensor to the experimental system as seen in previous research [24,26]. Such quantitative examinations will be necessary in future works.

4. Conclusions

Suspension flows containing fluorescent particles in a microchannel with a circular cross section were measured. We proposed a new method for evaluating the changes of the microstructure and rheological properties of a suspension using PTV and a power-law fluid model. The distribution of suspended particles in the radial direction was obtained from measured images. In addition, non-Newtonian properties of the suspension were evaluated using the velocity distribution obtained by PTV and the power-law fluid model. This method is useful for revealing the relationship between microstructural changes of a suspension and rheology.

Author Contributions: Conceptualization, M.K., T.F., and K.F. Methodology, M.K., T.F., and K.F. Software, S.M. Validation, M.T. (Mitsuru Tanaka), S.M. (Shigeru Murata), S.M. (Suguru Miyauchi), and T.H. Formal analysis, M.K. and M.T. (Miho Tanaka). Writing—original draft preparation, M.K. Writing—review and editing, T.F. Supervision, T.H. Project administration, T.F. and T.H.

Funding: This research was funded by the Collaborative Research Project of the Institute of Fluid Science, Tohoku University grant number J18L025 and J19I028.

Acknowledgments: The authors would like to thank Daisuke Yoshino for technical assistance with the experiments. Part of the work was carried out under the Collaborative Research Project of the Institute of Fluid Science, Tohoku University.

Conflicts of Interest: The authors declare no conflict of interest.

References

1. Mueller, S.; Llewellyn, E.W.; Mader, H.M. The rheology of suspensions of solid particles. *Proc. Math. Phys. Eng. Sci.* **2010**, *466*, 1201–1228. [[CrossRef](#)]
2. Chatté, G.; Comtet, J.; Niguès, A.; Bocquet, L.; Siria, A.; Ducouret, G.; Lequeux, F.; Lenoir, N.; Ovarlez, G.; Colin, A. Shear thinning in non-Brownian suspensions. *Soft Matter* **2018**, *14*, 879–893. [[CrossRef](#)] [[PubMed](#)]
3. Cwalina, C.D.; Wagner, N.J. Material properties of the shear-thickened state in concentrated near hard-sphere colloidal dispersions. *J. Rheol.* **2014**, *58*, 949–967. [[CrossRef](#)]
4. Nelson, A.Z.; Ewoldt, R.H. Design of yield-stress fluids: A rheology-to-structure inverse problem. *Soft Matter* **2017**, *13*, 7578–7594. [[CrossRef](#)] [[PubMed](#)]
5. Yziquel, F.; Carreau, P.J.; Moan, M.; Tanguy, P.A. Rheological modeling of concentrated colloidal suspensions. *J. Non-newton. Fluid Mech.* **1999**, *86*, 133–155. [[CrossRef](#)]
6. Dong, K.J.; Zou, R.P.; Yang, R.Y.; Yu, A.B.; Roach, G. DEM simulation of cake formation in sedimentation and filtration. *Miner. Eng.* **2009**, *22*, 921–930. [[CrossRef](#)]

7. Shao, X.; Dong, D.; Parkinson, G.; Li, C.-Z. Microstructure control of oxygen permeation membranes with templated microchannels. *J. Mater. Chem. A Mater.* **2014**, *2*, 410–417. [[CrossRef](#)]
8. Ness, C.; Ooi, J.Y.; Sun, J.; Marigo, M.; McGuire, P.; Xu, H.; Stitt, H. Linking particle properties to dense suspension extrusion flow characteristics using discrete element simulations. *AIChE J.* **2017**, *63*, 3069–3082. [[CrossRef](#)]
9. Omori, T.; Ishikawa, T.; Imai, Y.; Yamaguchi, T. Shear-induced diffusion of red blood cells in a semi-dilute suspension. *J. Fluid Mech.* **2013**, *724*, 154–174. [[CrossRef](#)]
10. Macmeccan, R.M.; Clausen, J.R.; Neitzel, G.P.; Aidun, C.K. Simulating deformable particle suspensions using a coupled lattice-Boltzmann and finite-element method. *J. Fluid Mech.* **2009**, *618*, 13–39. [[CrossRef](#)]
11. Sangani, A.S.; Acrivos, A.; Peyla, P. Roles of particle-wall and particle-particle interactions in highly confined suspensions of spherical particles being sheared at low Reynolds numbers. *Phys. Fluids* **2011**, *23*, 083302. [[CrossRef](#)]
12. Fukui, T.; Kawaguchi, M.; Morinishi, K. A two-way coupling scheme to model the effects of particle rotation on the rheological properties of a semidilute suspension. *Comput. Fluids* **2018**, *173*, 6–16. [[CrossRef](#)]
13. Doyeux, V.; Priem, S.; Jibuti, L.; Farutin, A.; Ismail, M.; Peyla, P. Effective viscosity of two-dimensional suspensions: Confinement effects. *Phys. Rev. Fluids* **2016**, *1*, 043301. [[CrossRef](#)]
14. Fornari, W.; Brandt, L.; Chaudhuri, P.; Lopez, C.U.; Mitra, D.; Picano, F. Rheology of confined non-Brownian suspensions. *Phys. Rev. Lett.* **2016**, *116*, 018301. [[CrossRef](#)] [[PubMed](#)]
15. Davit, Y.; Peyla, P. Intriguing viscosity effects in confined suspensions: A numerical study. *EPL* **2008**, *83*, 64001. [[CrossRef](#)]
16. Ramaswamy, M.; Lin, N.Y.C.; Leahy, B.D.; Ness, C.; Fiore, A.M.; Swan, J.W.; Cohen, I. How confinement-induced structures alter the contribution of hydrodynamic and short-ranged repulsion forces to the viscosity of colloidal suspensions. *Phys. Rev. X* **2017**, *7*, 041005. [[CrossRef](#)]
17. Morris, J.F. A review of microstructure in concentrated suspensions and its implications for rheology and bulk flow. *Rheol. Acta* **2009**, *48*, 909–923. [[CrossRef](#)]
18. Stickel, J.J.; Powell, R.L. Fluid mechanics and rheology of dense suspensions. *Annu. Rev. Fluid Mech.* **2005**, *37*, 129–149. [[CrossRef](#)]
19. Fukui, T.; Kawaguchi, M.; Morinishi, K. Numerical study on the inertial effects of particles on the rheology of a suspension. *Adv. Mech. Eng.* **2019**, *11*, 1–10. [[CrossRef](#)]
20. Yin, X.; Koch, D.L. Hindered settling velocity and microstructure in suspensions of solid spheres with moderate Reynolds numbers. *Phys. Fluids* **2007**, *19*, 093302. [[CrossRef](#)]
21. Talini, L.; Leblond, J.; Feuillebois, F. A pulsed field gradient NMR technique for the determination of the structure of suspensions of non-Brownian particles with application to packings of spheres. *J. Magn. Reson.* **1998**, *132*, 287–297. [[CrossRef](#)] [[PubMed](#)]
22. Gupta, S.; Wang, W.S.; Vanapalli, S.A. Microfluidic viscometers for shear rheology of complex fluids and biofluids. *Biomicrofluidics* **2016**, *10*, 043402. [[CrossRef](#)] [[PubMed](#)]
23. Goyon, J.; Colin, A.; Ovarlez, G.; Ajdari, A.; Bocquet, L. Spatial cooperativity in soft glassy flows. *Nature* **2008**, *454*, 84–87. [[CrossRef](#)]
24. Degré, G.; Joseph, P.; Tabeling, P.; Lerouge, S.; Cloitre, M.; Ajdari, A. Rheology of complex fluids by particle image velocimetry in microchannels. *Appl. Phys. Lett.* **2006**, *89*, 024104. [[CrossRef](#)]
25. Nordstrom, K.N.; Verneuil, E.; Arratia, P.E.; Basu, A.; Zhang, Z.; Yodh, A.G.; Gollub, J.P.; Durian, D.J. Microfluidic rheology of soft colloids above and below jamming. *Phys. Rev. Lett.* **2010**, *105*, 175701. [[CrossRef](#)]
26. Jesinghausen, S.; Weiffen, R.; Schmid, H.-J. Direct measurement of wall slip and slip layer thickness of non-Brownian hard-sphere suspensions in rectangular channel flows. *Exp. Fluids* **2016**, *57*, 153. [[CrossRef](#)]
27. Kawaguchi, M.; Fukui, T.; Funamoto, K.; Miyauchi, S.; Hayase, T. Experimental study on the effects of radial dispersion of spherical particles on the suspension rheology. In Proceedings of the AJK Fluids 2019, San Francisco, CA, USA, 28 July–1 August 2019; Volume 5322, pp. 1–6.
28. Borenstein, J.T.; Tupper, M.M.; MacK, P.J.; Weinberg, E.J.; Khalil, A.S.; Hsiao, J.; García-Cardena, G. Functional endothelialized microvascular networks with circular cross-sections in a tissue culture substrate. *Biomed. Microdevices* **2010**, *12*, 71–79. [[CrossRef](#)]
29. Jia, Y.; Jiang, J.; Ma, X.; Li, Y.; Huang, H.; Cai, K.; Cai, S.; Wu, Y. PDMS microchannel fabrication technique based on microwire-molding. *Chin. Sci. Bull.* **2008**, *53*, 3928–3936. [[CrossRef](#)]

30. Verma, M.K.S.; Majumder, A.; Ghatak, A. Embedded template-assisted fabrication of complex microchannels in PDMS and design of a microfluidic adhesive. *Langmuir* **2006**, *22*, 10291–10295. [[CrossRef](#)]
31. Lima, R.; Oliveira, M.S.N.; Ishikawa, T.; Kaji, H.; Tanaka, S.; Nishizawa, M.; Yamaguchi, T. Axisymmetric polydimethylsiloxane microchannels for in vitro hemodynamic studies. *Biofabrication* **2009**, *1*, 035005. [[CrossRef](#)]
32. Choi, J.S.; Piao, Y.; Seo, T.S. Fabrication of a circular PDMS microchannel for constructing a three-dimensional endothelial cell layer. *Bioprocess Biosyst. Eng.* **2013**, *36*, 1871–1878. [[CrossRef](#)] [[PubMed](#)]
33. Dolega, M.E.; Wagh, J.; Gerbaud, S.; Kermarrec, F.; Alcaraz, J.-P.; Martin, D.K.; Gidrol, X.; Picollet-D'Hahan, N. Facile bench-top fabrication of enclosed circular microchannels provides 3D confined structure for growth of prostate epithelial cells. *PLoS ONE* **2014**, *9*, e99416. [[CrossRef](#)] [[PubMed](#)]
34. Miura, K.; Itano, T.; Sugihara-Seki, M. Inertial migration of neutrally buoyant spheres in a pressure-driven flow through square channels. *J. Fluid Mech.* **2014**, *749*, 320–330. [[CrossRef](#)]
35. Schneider, C.A.; Rasband, W.S.; Eliceiri, K.W. NIH Image to ImageJ: 25 years of image analysis. *Nat. Methods* **2012**, *9*, 671–675. [[CrossRef](#)] [[PubMed](#)]
36. Schindelin, J.; Arganda-Carreras, I.; Frise, E.; Kaynig, V.; Longair, M.; Pietzsch, T.; Preibisch, S.; Rueden, C.; Saalfeld, S.; Schmid, B.; et al. Fiji: An open-source platform for biological-image analysis. *Nat. Methods* **2012**, *9*, 676–682. [[CrossRef](#)] [[PubMed](#)]
37. Otsu, N. Threshold selection method from gray level histograms. *IEEE Trans. Syst. Man Cybern.* **1979**, *9*, 62–66. [[CrossRef](#)]
38. Doutel, E.; Carneiro, J.; Oliveira, M.S.N.; Campos, J.B.L.M.; Miranda, J.M. Fabrication of 3d mili-scale channels for hemodynamic studies. *J. Mech. Med. Biol.* **2015**, *15*, 1550004. [[CrossRef](#)]
39. Bird, R.B.; Stewart, W.E.; Lightfoot, E.N. *Transport Phenomena*, 2nd ed.; Wiley Text Books: New York, NY, USA, 2002; pp. 232–233.
40. Choi, Y.-S.; Lee, S.-J. Holographic analysis of three-dimensional inertial migration of spherical particles in micro-scale pipe flow. *Microfluid. Nanofluidics* **2010**, *9*, 819–829. [[CrossRef](#)]
41. Segré, G.; Silberberg, A. Behaviour of macroscopic rigid spheres in Poiseuille flow: Part 2. Experimental results and interpretation. *J. Fluid Mech.* **1962**, *14*, 136–157. [[CrossRef](#)]
42. Fukui, T.; Kawaguchi, M.; Morinishi, K. Relationship between macroscopic rheological properties and microstructure of a dilute suspension by a two-way coupling numerical scheme. In Proceedings of the AJK Fluids 2019, San Francisco, CA, USA, 28 July–1 August 2019; Volume 5449, pp. 1–6.
43. Yan, Y.; Koplik, J. Transport and sedimentation of suspended particles in inertial pressure-driven flow. *Phys. Fluids* **2009**, *21*, 013301. [[CrossRef](#)]
44. Hampton, R.E.; Mammoli, A.A.; Graham, A.L.; Tetlow, N.; Altobelli, S.A. Migration of particles undergoing pressure-driven flow in a circular conduit. *J. Rheol.* **1997**, *41*, 621–640. [[CrossRef](#)]
45. Jabeen, Z.; Yu, H.-Y.; Eckmann, D.M.; Ayyaswamy, P.S.; Radhakrishnan, R. Rheology of colloidal suspensions in confined flow: Treatment of hydrodynamic interactions in particle-based simulations inspired by dynamical density functional theory. *Phys. Rev. E* **2018**, *98*, 042602. [[CrossRef](#)] [[PubMed](#)]
46. Lecampion, B.; Garagash, D.I. Confined flow of suspensions modelled by a frictional rheology. *J. Fluid Mech.* **2014**, *759*, 197–235. [[CrossRef](#)]
47. Xiong, W.; Zhang, J. Shear stress variation induced by red blood cell motion in microvessel. *Ann. Biomed. Eng.* **2010**, *38*, 2649–2659. [[CrossRef](#)] [[PubMed](#)]
48. Freund, J.B.; Vermot, J. The wall-stress footprint of blood cells flowing in microvessels. *Biophys. J.* **2014**, *106*, 752–762. [[CrossRef](#)] [[PubMed](#)]
49. Tare, M.; Parkington, H.C.; Coleman, H.A.; Neild, T.O.; Dusting, G.J. Hyperpolarization and relaxation of arterial smooth muscle caused by nitric oxide derived from the endothelium. *Nature* **1990**, *346*, 69–71. [[CrossRef](#)] [[PubMed](#)]
50. Dolan, J.M.; Kolega, J.; Meng, H. High wall shear stress and spatial gradients in vascular pathology: A review. *Ann. Biomed. Eng.* **2013**, *41*, 1411–1427. [[CrossRef](#)]
51. Goldsmith, H.L. Red cell motions and wall interactions in tube flow. *Fed. Proc.* **1971**, *30*, 1578–1590.
52. Segré, G.; Silberberg, A. Radial particle displacements in poiseuille flow of suspensions. *Nature* **1961**, *189*, 209–210. [[CrossRef](#)]

53. Matas, J.-P.; Morris, J.F.; Guazzelli, É. Inertial migration of rigid spherical particles in Poiseuille flow. *J. Fluid Mech.* **2004**, *515*, 171–195. [[CrossRef](#)]
54. Inamuro, T.; Maeba, K.; Ogino, F. Flow between parallel walls containing the lines of neutrally buoyant circular cylinders. *Int. J. Multiph. Flow* **2000**, *26*, 1981–2004. [[CrossRef](#)]



© 2019 by the authors. Licensee MDPI, Basel, Switzerland. This article is an open access article distributed under the terms and conditions of the Creative Commons Attribution (CC BY) license (<http://creativecommons.org/licenses/by/4.0/>).



Article

Deformation of a Red Blood Cell in a Narrow Rectangular Microchannel

Naoki Takeishi ^{1,*}, Hiroaki Ito ^{2,3}, Makoto Kaneko ² and Shigeo Wada ¹

¹ Graduate School of Engineering Science, Osaka University, 1-3 Machikaneyama, Toyonaka, Osaka 560-8531, Japan; shigeo@me.es.osaka-u.ac.jp

² Department of Mechanical Engineering, Osaka University, Suita, Osaka 565-0871, Japan; ito@hh.mech.eng.osaka-u.ac.jp (H.I.); mk@mech.eng.osaka-u.ac.jp (M.K.)

³ Department of Physics, Graduate School of Science, Chiba University, Chiba 263-8522, Japan

* Correspondence: ntakeishi@me.es.osaka-u.ac.jp; Tel./Fax: +81-6-6850-6173

Received: 14 February 2019; Accepted: 16 March 2019; Published: 21 March 2019

Abstract: The deformability of a red blood cell (RBC) is one of the most important biological parameters affecting blood flow, both in large arteries and in the microcirculation, and hence it can be used to quantify the cell state. Despite numerous studies on the mechanical properties of RBCs, including cell rigidity, much is still unknown about the relationship between deformability and the configuration of flowing cells, especially in a confined rectangular channel. Recent computer simulation techniques have successfully been used to investigate the detailed behavior of RBCs in a channel, but the dynamics of a translating RBC in a narrow rectangular microchannel have not yet been fully understood. In this study, we numerically investigated the behavior of RBCs flowing at different velocities in a narrow rectangular microchannel that mimicked a microfluidic device. The problem is characterized by the capillary number Ca , which is the ratio between the fluid viscous force and the membrane elastic force. We found that confined RBCs in a narrow rectangular microchannel maintained a nearly unchanged biconcave shape at low Ca , then assumed an asymmetrical slipper shape at moderate Ca , and finally attained a symmetrical parachute shape at high Ca . Once a RBC deformed into one of these shapes, it was maintained as the final stable configurations. Since the slipper shape was only found at moderate Ca , measuring configurations of flowing cells will be helpful to quantify the cell state.

Keywords: red blood cells; Lattice–Boltzmann method; finite element method; immersed boundary method; narrow rectangular microchannel; computational biomechanics

1. Introduction

It is well known that many blood-related diseases are associated with alterations in the geometry and membrane properties of red blood cells (RBCs) that result in reduced functionality [1]. For instance, RBCs in patients with diabetes mellitus exhibit impaired cell deformability [2], as do those in patients with sepsis [3]. As another example, malaria-infected RBCs demonstrate membrane stiffening as well as shape distortion [4–6]. Hence, cell deformability may be an important indicator of cell state, and might be used to diagnose relevant blood diseases. To date, various experimental techniques have been proposed to evaluate RBC deformability, e.g., optical tweezers and atomic force microscopy, but they usually suffer from low throughput. Recently, several microfluidic techniques that are capable of high-throughput measurement have been developed [7–11]. For instance, Ito et al. (2017) successfully developed a novel high-throughput assay to quantify the mechanical response of RBCs after spatial constriction, and found a characteristic mechanical response to long-term deformation that may have been related to chemical energy content [9].

Along with these experimental studies, recent computer simulation techniques have successfully been used to investigate aspects of cell dynamics such as stresses, velocities, and deformations, and have been shown to reproduce single-cell dynamics [12–14]. Mokbel et al. (2017) quantitatively related cell deformation to mechanical parameters in an experiment involving microfluidic flow through a square channel [13]. To elucidate patient-specific blood rheology, RBCs in diabetes mellitus and sickle-cell anemia were modeled in terms of cell rigidity and membrane viscosity, and their hydrodynamic interactions were quantified [15,16]. Since such numerical models allow us to investigate cell behavior in large parameter spaces, the coupling of experimental and numerical approaches may constitute a useful bioengineering strategy to quantify the cell state.

Despite the studies referred to above, much is still unknown about the behavior of flowing RBCs, especially in a confined microchannel or between two closely spaced parallel plates (i.e., Hele-Shaw cell). Since the deformation of a RBC in a narrow rectangular microchannel is limited to an almost two-dimensional space, it is relatively easy to quantify the deformed configuration [17,18]. Although a number of studies using microfluidic devices have reported cellular-scale dynamics [19–24] as well as numerical studies [20,25–28], the dynamics of a translating RBC in a narrow rectangular microchannel have not yet been fully investigated. Recently our developed on-chip feedback manipulation system allowed us to investigate the two-dimensionally projected shape profile of RBCs, and showed RBC heterogeneity in a narrow rectangular microchannel [17,18]. However, a precise deformation especially in thickness direction of RBCs cannot be captured by means of the experimental observation.

One of the pioneering theoretical works about the behavior of the cell membrane in a confined channel was reported by Secomb & Skalak (1982) [29]. More recently, Tahiri et al. (2013) systematically investigated the shape transition of confined RBCs modeled as vesicles, and showed a phase diagram of the mode of RBCs [28]. Since these works were limited to the two-dimensional behavior of RBCs, it is unknown whether their insights are applicable to estimating the three-dimensional deformation of a RBC in a narrow rectangular microchannel. Fedosov et al. (2014) systematically investigated the behavior of a single RBC in cylindrical microchannels for a wide range of channel confinements ($2a/D$, being the radius of the RBC a and the channel diameter D) using a three-dimensional dissipative particle dynamics model [30]. However, their microchannels ($2a/D < 0.8$) had relatively large cross-sectional area comparing to a narrow rectangular microchannel represented in [17,18,31]. Zhu et al. (2016) numerically investigated the behavior of a droplet in a Hele-Shaw cell, and identified characteristic flow structures that were induced by the translating droplet [31]. Since forces acting on an interface depend on the constitutive law, it is expected that the hydrodynamic interaction between the fluid and cell membrane will differ from that observed in the droplet model.

The objective in this study, therefore, is to clarify the detailed behavior of translating RBCs in a narrow rectangular microchannel. The RBCs were modeled as biconcave capsules, whose membranes followed the Skalak constitutive law [32]. We quantified the stable configuration of deformed RBCs in a narrow rectangular microchannel, mimicking a microfluidic device [17], for different values of the capillary number Ca , which is the ratio between the fluid viscous force and the membrane elastic force. We also investigated the effect on this configuration of altering parameters such as bending rigidity and viscosity ratio. To accelerate numerical simulations, we resorted to computing with a graphics processing unit (GPU), using the Lattice–Boltzmann method (LBM) for the inner and outer fluids and the finite element method to follow the deformation of the RBC membrane. These models were previously successfully applied to the analysis of cellular hydrodynamic interactions in channel flows [12,33–35].

2. Materials and Methods

2.1. Flow and RBC Model

We considered a cellular flow consisting of an external/internal fluid and a RBC membrane with radius a in a rectangular box representing a microfluidic device with $10 \mu\text{m} \times 3.5 \mu\text{m}$ along

the wall-normal and span-wise directions (Figure A1a). Representative images of a flowing RBC in a microfluidic device (Figure A1b,c) are shown in Figure A1d. The stream-wise distance for the computational domain was set to be 50 μm (Figure 1). Each RBC was modeled as a biconcave capsule, or a Newtonian fluid enclosed by a thin elastic membrane, with a major diameter 8 μm ($=2a$) and maximum thickness 2 μm ($=a/2 = t^R$). The flow was driven by a pressure gradient. Periodic boundary conditions were imposed on the inlet and outlet. To reproduce in vivo human RBC condition experimentally, the cytoplasmic viscosity was taken to be $\mu_1 = 6.0 \times 10^{-3}$ Pa·s, which is five times higher than the external fluid viscosity, $\mu_0 = 1.2 \times 10^{-3}$ Pa·s. Hence, the viscosity ratio $\lambda (= \mu_1 / \mu_0)$ was set to be 5. The computational domain and the initial state or steady deformed state of the RBC are shown in Figure 1. The problem was characterized by the capillary number (Ca),

$$Ca = \frac{\mu_0 \dot{\gamma} a}{G_s}, \quad (1)$$

where G_s is the surface shear elastic modulus, and $\dot{\gamma} (= U_m^\infty / H)$ is the shear rate defined by the mean velocity of the external fluid without cell U_m^∞ and channel height $H (= 10 \mu\text{m})$. Since the inertial effect can be negligible in the microfluidic device, we set Re as small enough to assume the Stokes flow. To reduce the computational costs, we set $Re = \rho U^\infty H / \mu_0 = 0.2$, where ρ is the external fluid density and U^∞ is the maximum velocity of the external fluid with no cell. This value accurately represents the capsule dynamics solved by the boundary integral method in Stokes flow [12,33].

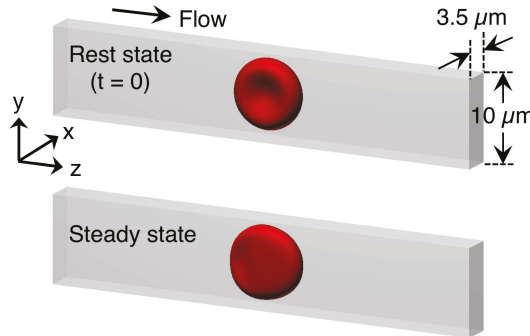


Figure 1. Computational domain to reproduce a translating red blood cell (RBC) in the narrow rectangular microchannel. The domain mimicked a microfluidic device as shown in Figure A1. The domain cross-section was 10 $\mu\text{m} \times 3.5 \mu\text{m}$ along the wall-normal and span-wise directions, respectively, and the stream-wise distance was set to be 50 μm . Flow direction is from left to right.

The membrane was modeled as an isotropic and hyperelastic material that followed the Skalak constitutive (SK) law [32]. The strain energy w and principal tensions in the membrane T_1 and T_2 ($T_1 \geq T_2$) of the SK law are given by

$$w = \frac{G_s}{4} \left(I_1^2 + 2I_1 - 2I_2 + CI_2^2 \right), \quad (2)$$

and

$$T_1 = \frac{G_s \lambda_1}{\lambda_2} \left[\lambda_1^2 - 1 + C \lambda_2^2 \left(\lambda_1^2 \lambda_2^2 - 1 \right) \right], \quad (\text{likewise for } T_2), \quad (3)$$

where C is a coefficient representing the area incompressibility, $I_1 (= \lambda_1^2 + \lambda_2^2 - 2)$ and $I_2 (= \lambda_1^2 \lambda_2^2 - 1 = J_s^2 - 1)$ are the first and second invariants of the strain tensor, λ_1, λ_2 are the two principal in-plane stretch ratios, and $J_s = \lambda_1 \lambda_2$ is the Jacobian, which expresses the ratio of the deformed to reference surface areas. If I_2 equals zero (i.e., $J_s = 1$), the membrane satisfies perfect incompressibility. In this

study, the surface shear elastic modulus and area incompressibility coefficient of RBCs were determined to be $G_s = 4.0 \mu\text{N/m}$ and $C = 10^2$, respectively [6,33]. The bending resistance k_b was also considered [36], with a bending modulus $k_b = 1.2 \times 10^{-19} \text{ J}$, according to the order of the value of k_b [37].

2.2. Numerical Simulation

We used the LBM [38] coupled with the finite element method (FEM) [39]. The membrane mechanics were solved by the FEM, and are given by

$$\int_S \hat{\mathbf{u}} \cdot \mathbf{q} dS = \int_S \hat{\boldsymbol{\varepsilon}} : \mathbf{T} dS, \tag{4}$$

where \mathbf{T} is the Cauchy stress tensor, \mathbf{q} is the load on the membrane, $\hat{\mathbf{u}}$ is the virtual displacement, and $\hat{\boldsymbol{\varepsilon}} = (\nabla_s \hat{\mathbf{u}} + \nabla_s \hat{\mathbf{u}}^T)/2$ is the virtual strain tensor. The fluid mechanics were solved by the LBM [38] as,

$$f_i(\mathbf{x} + \mathbf{c}_i \Delta t, t + \Delta t) - f_i(\mathbf{x}, t) = -\frac{1}{\tau} [f_i(\mathbf{x}, t) - f_i^{eq}(\mathbf{x}, t)] + F_i \Delta t, \tag{5}$$

where f_i is the particle distribution function for ideal particles with velocity \mathbf{c}_i at position \mathbf{x} , Δt is the time step size, f_i^{eq} is the equilibrium distribution, τ is the nondimensional relaxation time, and F_i is the external force term. Subscript i represents the distribution direction of an ideal particle ($i = 0-18$). The D3Q19 LBM was used. FEM and LBM were coupled by the immersed boundary method [40]. All procedures were fully implemented on a GPU to accelerate the numerical simulation [41]. Our coupling method has been successfully applied to numerical analyses of cellular flow [33–35] and cell adhesion [12]. The solid and fluid mesh sizes were set to be 125 nm (an unstructured mesh with 20,480 elements was used for the RBC membrane). This resolution has been shown to successfully represent single-cell dynamics in a channel [12]. The results of cell deformation did not change with twice the fluid-mesh resolution (Figure 2b).

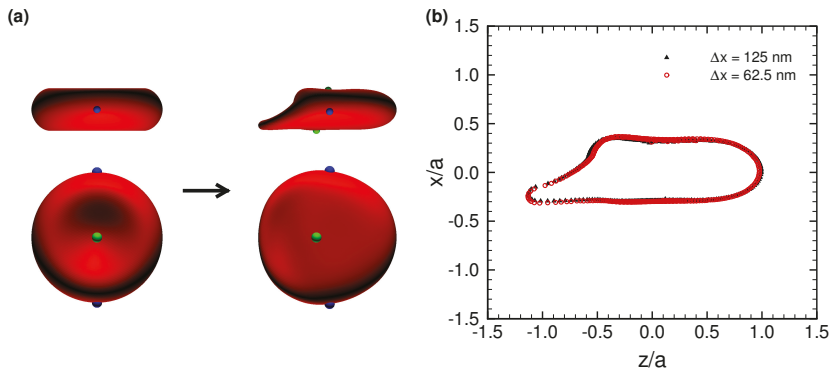


Figure 2. (a) Typical snapshots of a deformed RBC subjected to $Ca = 0.15$ at the initial state (left) and steady state (right). Two views, from the span-wise and stream-wise directions, are shown above and below, respectively. The markers represent node points. (b) Superposition of the fully deformed RBC projected on the x - z plane at $Ca = 0.15$. The two lines obtained with $\Delta x = 125 \text{ nm}$ (black) and 62.5 nm (red), respectively. The membrane position is normalized by the reference radius a .

3. Results

3.1. Deformation of a Translating RBC in a Narrow Rectangular Microchannel

We performed numerical simulations to reproduce a translating RBC in a narrow rectangular microchannel, as shown in Figure A1d, and found that the RBC demonstrated an asymmetrical shape, the so-called slipper shape [42], which was also observed in the experiment as shown in Figure A2

(see also Videos S1 and S2). A typical asymmetrical shape of a deformed RBC subjected to $Ca = 0.15$ is shown in Figure 2a, where the markers represent membrane node points. The result clearly shows that the membrane does not rotate; in other words, the RBC stably translates without a tank-treading motion. The outlines of the deformed RBC at different fluid mesh resolutions are shown in Figure 2b, projected on the z - x plane. The result remains the same with twice the fluid mesh resolution ($\Delta x = 62.5$ nm). Therefore, the present resolution ($\Delta x = 125$ nm) successfully reproduces the fluid dynamics between the membrane and wall, and will be used in this study.

Figure 3a shows snapshots of a stable RBC configuration for different Ca at fully developed flow. The RBC demonstrated an almost unchanged (symmetrical) biconcave shape at small $Ca = 10^{-3}$, then shifted to an asymmetrical slipper shape as Ca increased (see also Video S3 for $Ca = 0.1$), and finally attained a symmetrical parachute shape at $Ca \geq 0.35$ (see also Video S4 for $Ca = 0.5$). To quantify the symmetry of the stable configuration of the deformed RBC, we propose a symmetry index ID_{sym} , which is defined by the volume ratio of two volumes that are divided by a plane parallel to the flow direction at the midline of the channel, as shown in Figure 3b. Using volume 1 (Vol_1) and volume 2 (Vol_2), ID_{sym} is given as

$$ID_{sym} = \frac{\text{MIN}(Vol_1, Vol_2)}{\text{MAX}(Vol_1, Vol_2)}. \tag{6}$$

A complete symmetrical shape is expressed as $ID_{sym} = 1$. We show the results of ID_{sym} as a function of Ca in Figure 3c. An asymmetrical parachute shape abruptly appeared for $Ca \geq 0.01$, but it gradually recovered and finally reached $ID_{sym} = 1$ for $Ca \geq 0.35$. These results suggest that there exists the following specific range of Ca that allows a RBC to deform into an asymmetrical slipper shape: $5 \times 10^{-3} < Ca < 0.35$.

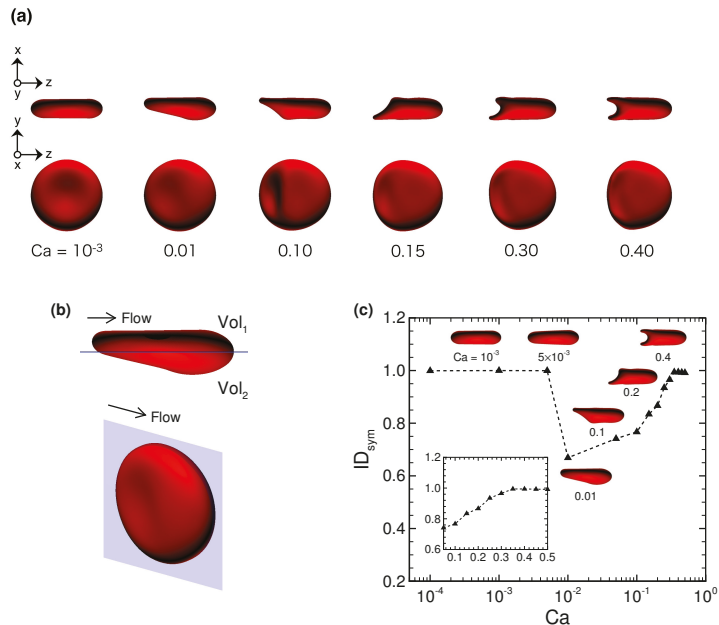


Figure 3. (a) Snapshots of a fully deformed RBC for different Ca . (b) Typical snapshots of a RBC at $Ca = 0.01$, where the blue plane denotes the center of the x - z -plane parallel to the flow direction, dividing the cell into the volume 1 (Vol_1) and volume 2 (Vol_2). (c) The symmetry index ID_{sym} as a function of Ca . The insets represent snapshots of deformed RBCs at specific Ca .

Figure 4a shows one example of the temporal history of the RBC centroid velocity V_c at $Ca = 0.01$, where V_c is normalized by the characteristic (maximum) fluid velocity without cell U^∞ . The centroid velocity of RBC is calculated as a volume-averaged velocity, and is given by,

$$V_c = \frac{1}{V} \int_{\mathcal{V}} \mathbf{v}(x_m) d\mathcal{V} = \frac{1}{V} \int_{\mathcal{V}} \nabla \cdot (\mathbf{v} \otimes \mathbf{r}) d\mathcal{V} = \frac{1}{V} \int_S \mathbf{n} \cdot (\mathbf{v} \otimes \mathbf{r}) dS, \quad (7)$$

and

$$V = \int_{\mathcal{V}} dV = \frac{1}{3} \int_{\mathcal{V}} \nabla \cdot \mathbf{r} d\mathcal{V} = \frac{1}{3} \int_S \mathbf{n} \cdot \mathbf{r} dS, \quad (8)$$

where $\mathbf{v}(x_m)$ is the interfacial velocity of the membrane at the membrane node point x_m , \mathbf{r} is the membrane position relative to the center of the RBC, \mathbf{n} is the surface normal vector, \mathcal{V} the volume of the RBC, and S is the surface area of the membrane. The velocity slightly ($\sim 3\%$) decreased when the RBC shape changed from a symmetrical to asymmetrical shapes at $Ca = 0.01$ (Figure 4a). Because the membrane of a slipper-shaped RBC is dragged by the fluid near the wall, V_c is slower than that of a symmetrically shaped RBC. Once the membrane deformed into an asymmetrical shape, that shape persisted. In this study, we defined the “steady state” as the condition wherein the centroid velocity reached a plateau (this time is hereafter referred to as $\dot{\gamma}t = 0$), and used data after $\dot{\gamma}t = 0$ to reduce the influence of the initial conditions. A time average was performed for the period $\dot{\gamma}t \geq 100$ after $\dot{\gamma}t = 0$. Figure 4b shows the time average of centroid velocity V_c and total fluid velocity V_{total} for different Ca , where those values are normalized by characteristic velocity U^∞ . The tendency that V_c/U^∞ slightly decreases as Ca increases (Figure 4b) agrees with previous numerical results of a spherical capsule in a square channel [43] and constricted channel [44]. Note that the dimensional cell velocity basically increases as Ca increases, for instance, $V_c \sim 0.12 \mu\text{m/s}$ for the lowest $Ca (=10^{-4})$ and $V_c \sim 1200 \mu\text{m/s}$ for the highest $Ca (=0.5)$.

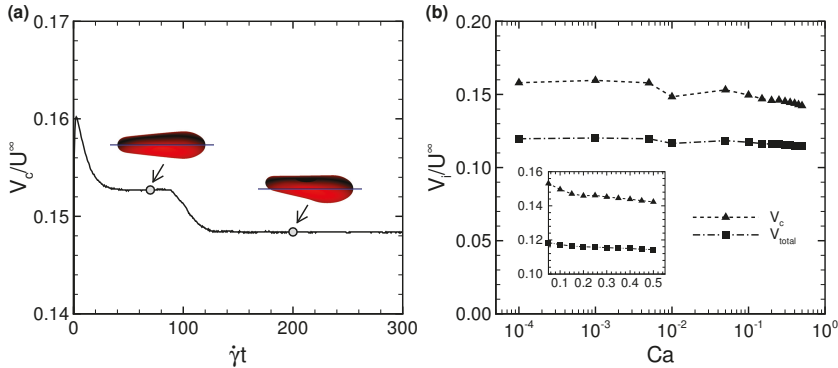


Figure 4. (a) Time history of the RBC centroid velocity (V_c) at $Ca = 0.01$, where $V_c = 24.7 \mu\text{m/s}$ at $\dot{\gamma}t = 200$ corresponding to $t = 12 \text{ s}$. The images represent snapshots of the deformed RBC at $\dot{\gamma}t = 70$ ($t = 4.2 \text{ s}$) and 200 ($t = 12 \text{ s}$), respectively. The blue line denotes the center axis of the channel. (b) Time average of the RBC centroid velocity V_c and total fluid velocity V_{total} as a function of Ca . The velocity V_i is normalized by the characteristic fluid velocity without cell U^∞ , where V_i represents V_c and V_{total} by the index $i = \text{“c”}$ or “total” .

The deformation of each axis in a steady-state membrane is quantified by the deformation index L_i/L_i^{ref} , which is the ratio between each axis length of a deformed RBC L_i and each reference axis length L_i^{ref} (i.e., without flow), where subscript i represents the maximum, middle and minimum axes (i.e., $i = \text{“max”}$, “mid” , and “min”). The results of L_i/L_i^{ref} are shown in Figure 5a. We found that only the minimum axis (i.e., thickness) increases as Ca increases, while the maximum and middle axes decrease.

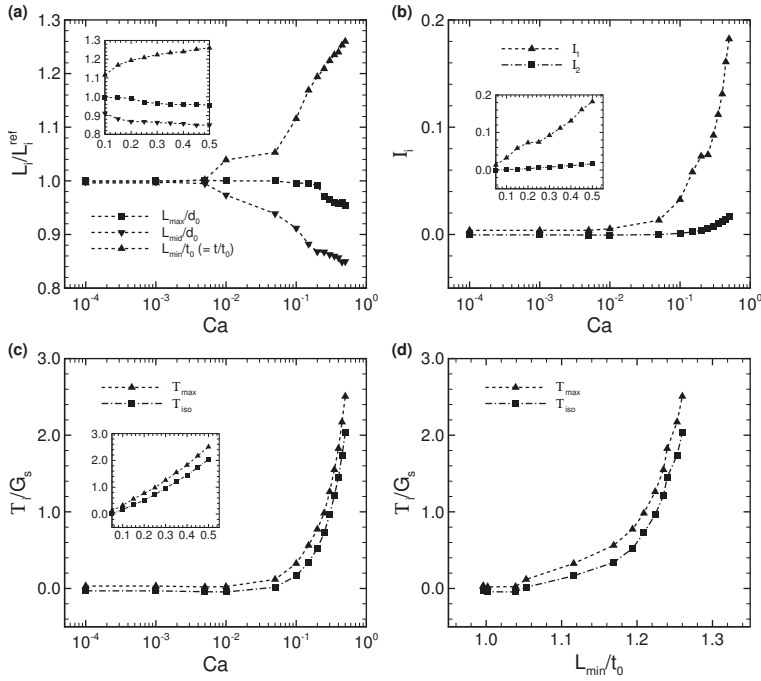


Figure 5. (a) Time average of the deformation index L_i/L_i^{ref} as a function of Ca , where the maximum, middle, and minimum axis lengths (L_{max} , L_{min} , and L_{mid} , respectively) are normalized by each reference length L_i^{ref} (i.e., no flow condition), where the reference major and minor axis lengths are d_0 and t_0 (thickness), respectively. (b) Averaged first and second invariants I_i ($i = 1$ and 2) as a function of Ca . (c) Averaged maximum and isotropic tensions; T_{max} and T_{iso} , respectively. These values are normalized by the shear elastic modulus G_s . (d) The average of these tensions, T_i , as a function of the deformation index L_{min}/t_0 , which is the ratio between the minimum axis length of the deformed RBC (thickness) and the reference thickness.

To quantify the strain of an isotropic elastic membrane, the first and second invariants of the strain tensor I_i ($i = 1$ and 2) are calculated, and are given in Figure 5b. These are averaged by the total number of membrane meshes and the analysis duration, i.e.,

$$\mathcal{I}_i = \frac{1}{\mathcal{T}S} \int_t \int_S I_i(x_g, t) dS dt \quad (i = 1 \text{ and } 2), \quad (9)$$

where \mathcal{T} is the period of analysis duration, and x_g is the centroid of the triangle element of the membrane. According to Figure 5b, the second invariant \mathcal{I}_2 is almost zero for $Ca \leq 0.1$, and only slightly increases for $Ca > 0.1$. Therefore, the membrane incompressibility is well maintained even after the membrane demonstrates the slipper/parachute shape. The first invariant \mathcal{I}_1 , on the other hand, starts to increase from $Ca \geq 0.01$ and grows rapidly compared to \mathcal{I}_2 . Therefore, the symmetrical parachute-like deformation results from greater membrane extension than the asymmetrical slipper-like deformation.

We also investigated the maximum in-plane principal tension T_{max} ($T_1 \geq T_2$) and the isotropic tension $T_{iso} (= T_1 + T_2)/2$ in the deformed RBC, and show the results in Figure 5c. We calculated the average value of those tensions as \mathcal{T}_{max} and \mathcal{T}_{iso} by using Equation (9). As expected, both tensions start to increase simultaneously when \mathcal{I}_1 increases (i.e., $Ca = 0.01$). The isotropic tension \mathcal{T}_{iso} is always lower than the maximum principal tension \mathcal{T}_{max} . To demonstrate the relationship between tension and

deformation, \bar{T}_i is described as a function of the deformation index L_{min}/t_0 in Figure 5d. The result clearly shows the strain-hardening behavior of the RBC due to the nonlinearity of the SK law.

3.2. Effects of Perturbations on Stable Membrane Configuration

To clarify the reproducibility of the stable configuration of a deformed RBC in the narrow rectangular microchannel, we investigated the effects of potential perturbations, e.g., the initial centroid position x_0 , bending rigidity k_b , and viscosity ratio λ . Figure 6 shows the centroid velocity V_c of a RBC subjected to low $Ca (= 5 \times 10^{-3})$ and maximum $Ca (= 0.5)$ for different initial centroid positions along the span-wise direction of the channel. When the centroid of the RBC was initially placed two fluid meshes away from the midline of the channel (i.e., $x_0 = -2\Delta x$), the RBC started to flow with an asymmetrical slipper shape, but gradually migrated to the channel axis due to the lift forces induced by the wall and shear gradient, and finally attained a symmetrical shape for both Ca values with the same velocity as that obtained with $x_0 = 0$ (Figure 4; see also Videos S5 and S6). Therefore, the stable configuration of the deformed RBC is insensitive to the initial position. Note that although the RBC subjected to low $Ca (= 5.0 \times 10^{-3})$ did not perfectly orient parallel to the flow direction (Figure 6a) and suffered from decreasing the cell velocity, the symmetry index ID_{sym} remained the same (Figure 7a).

We also tested different values for bending rigidity k_b , where the value of k_b was set to a quarter of the original bending resistance ($k_b = 3.0 \times 10^{-20}$), and twice the original bending resistance ($k_b = 2.4 \times 10^{-19}$). As shown in Figure 7a, the symmetry index ID_{sym} remained same regardless of the value of k_b . Therefore, bending rigidity does not affect the stable configuration of the translating RBC in the narrow rectangular microchannel, at least within the parameter space that we investigated, namely $3.0 \times 10^{-20} \leq k_b \leq 2.4 \times 10^{-19}$.

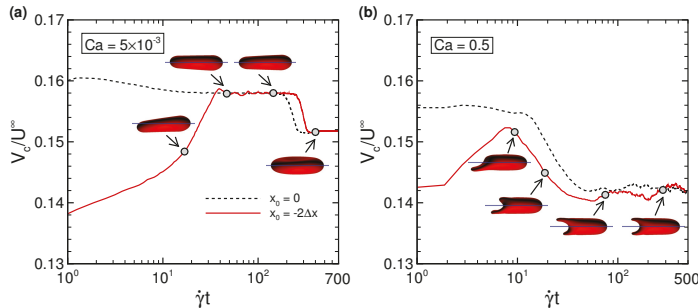


Figure 6. Time history of the RBC centroid velocity (V_c) at (a) low $Ca = 5 \times 10^{-3}$, and (b) high $Ca = 0.5$ for different initial positions along the span-wise direction x_0 , where one RBC is initially placed at the midline of the channel ($x_0 = 0$, dashed line) and the other RBC is placed two fluid meshes away from the midline ($x_0 = -2\Delta x$, red line). The images represent snapshots of the RBC with $x_0 = -2\Delta x$ at the indicated times (see also Videos S5 and S6). Note that $V_c = 12.7 \mu\text{m/s}$ for $Ca = 5 \times 10^{-3}$ at $\dot{\gamma}t = 500$ ($t = 60$ s), and $V_c = 1180 \mu\text{m/s}$ for $Ca = 0.5$ at $\dot{\gamma}t = 500$ ($t = 0.6$ s).

However, DI_{sym} was affected by the viscosity ratio λ . When λ decreased to unity (i.e., $\lambda = 1$), the membrane tended to assume a symmetrical shape even at relatively low $Ca = 0.01$. The most asymmetrical shape was found at $\lambda = 5$, and the minimum $DI_{sym}|_{\lambda=1}$ shifted to larger $Ca \approx 0.1$ (Figure 7a). The value of DI_{sym} at $\lambda = 1$ started to recover beginning at $Ca = 0.1$, and finally almost reached 1 at $Ca = 0.3$. To see the effect of λ , we compared the centroid velocity V_c and membrane tension \bar{T}_i between different λ ($= 1$ and 5). V_c at $\lambda = 1$ tended to be larger, and was approximately 4% greater than that obtained with $\lambda = 5$ (Figure 7b). The results of \bar{T}_i , on the other hand, tended to decrease as λ decreased (Figure 7c).

Figure 7d shows the membrane tensions as a function of the deformation index L_{min}/t_0 . When L_{min}/t_0 was invariant, the tensions acting on the membrane \bar{T}_i tended to be lower as λ decreased.

This tendency was inconsistent with the previous numerical results of the RBC in simple shear flow [45]. Compared with the previous results in [45], the similarities or discrepancies in the values of \mathcal{T}_i (Figure 7c,d) for different λ would arise from different flow modes and confined geometries. Even though tensions acting on the membrane and deformation depend on λ , the RBC in the narrow rectangular microchannel underwent the same history of deformation as a function of Ca ; the almost original biconcave shape at low Ca , and an asymmetrical slipper shape at low/moderate Ca , and finally a symmetrical parachute shape at high Ca . These results suggest that the stable configuration of the translating RBC in the narrow rectangular microchannel was reproducible independently of any perturbations that we investigated.

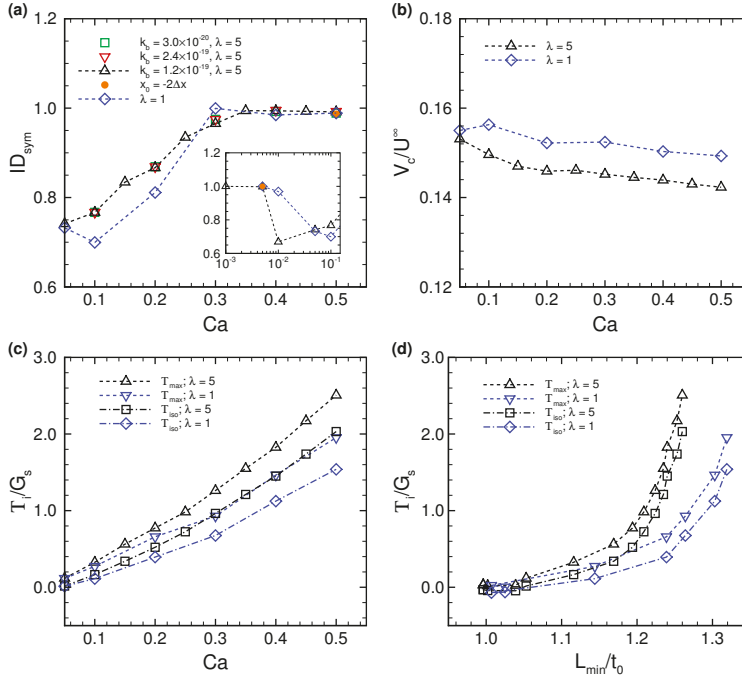


Figure 7. (a) The symmetry index ID_{sym} as a function of Ca for different values of bending modulus $k_b = 3.0 \times 10^{-20}$ J (square), 1.2×10^{-19} J (triangle), and 2.4×10^{-19} J (inverted triangle). The results obtained with a viscosity ratio of unity (i.e., $\lambda = 1$) are also displayed (diamond). The circular dot represents the result of $x_0 = -2\Delta x$ at low Ca ($= 5 \times 10^{-3}$) and high Ca ($= 0.5$) and $\lambda = 5$. These results were obtained with $k_b = 1.2 \times 10^{-19}$ J. (b) Time average of the RBC centroid velocity (V_c) as a function of Ca for different viscosity ratios ($\lambda = 1$ and 5). (c) Averaged maximum and isotropic tensions, \mathcal{T}_{max} and \mathcal{T}_{iso} , respectively. (d) Averaged tension \mathcal{T}_i as a function of the deformation index L_{min}/t_0 .

4. Discussion

The asymmetric slipper shape of RBCs has been found in capillaries [42], and the motion has been systematically investigated both in experiments [19–23] and in numerical simulations [20,26,28,30]. An experiment using microfluidic devices showed that RBCs undergo a transition from a symmetrical parachute shape to an asymmetrical slipper shape as cell velocity increased [23]. Other experimental results showed that viscous shear stresses controlled this transition, and confinement was not necessary for the slipper shape [19]. The results reported in [19] are consistent with the numerical results obtained using a two-dimensional (2D) droplet model [26]. The numerical studies reported in [26] clearly showed that the shape transition in an unbounded Piseuille flow occurred when a dimensionless

vesicle deflation number, representing shape stability, fell below a certain value. Other numerical results reported in [28] demonstrated that 2D droplets also assumed the slipper shape, not only in an unbounded Piseuille flow but also in a confined channel. These numerical studies also clarified the effect of the viscosity ratio λ on stable configuration, showing specifically that a droplet with $\lambda = 1$ transitioned from a parachute shape to a slipper shape as the flow strength decreased [26], while a droplet with $\lambda \approx 5$ made this same transition as the flow strength increased [28]; these findings were consistent with the experimental results reported in [23]. Since the above numerical analyses were performed using a 2D droplet model, it is uncertain whether their results are applicable to the dynamics of a translating three-dimensional (3D) RBC in a confined rectangular channel when taking membrane elasticity into account. Fedosov et al. (2014) systematically investigated the behavior of single RBC in cylindrical microchannels for a wide range of channel confinements ($2a/D$, being a channel diameter D) using a 3D dissipative particle dynamics model [30], but the cross-sectional area of the microchannels were relatively large ($2a/D < 0.8$) comparing to a narrow rectangular microchannel represented in [17], where the channel confinement is characterized as $2a/H = 0.8$ and $2a/W \sim 2.29$ using the wall-normal length H and span-wise length W (Figure A1a–c). We thus numerically investigated the behavior of translating RBCs in a narrow rectangular microchannel that mimicked a microfluidic device (Figure A1) [17] with different Ca . Our numerical results demonstrated that the confined RBCs maintained a nearly unchanged, biconcave shape at low Ca , then shifted to an asymmetrical slipper shape at low/moderate Ca , and finally attained a symmetrical parachute shape at high Ca . Such asymmetrical slipper shape was also observed in the experiment (Figure A2). The finding that RBCs tended to show a symmetrical shape with increasing Ca contradicted previous experimental results [23] as well as numerical results obtained using a 2D-droplet model with $\lambda \approx 5$ [28]. This discrepancy may have been caused by the effects of three-dimensional flow structures in a confined channel and by the membrane constitutive law. Our numerical results of the transition from slipper to parachute shapes qualitatively agree with those obtained in cylindrical microchannels for $2a/D < 0.8$ [30]. To the best of our knowledge, such shape transition in a narrow rectangular microchannel that was presented here is the first of its kind. We also showed that the stable configuration of the translating RBC in the narrow rectangular microchannel was reproducible independently of any perturbations that we investigated such as the initial centroid position, bending rigidity, and viscosity ratio. If the fully deformed configuration or the transition mode is related to membrane shear elasticity, which is characterized by Ca , these insights will help us identify the cell state. Since different motions of individual RBCs may affect the bulk suspension rheology [46], identifying a stable mode of RBCs in a channel will be also helpful to evaluate the blood rheology.

In our experiment using microfluidic devices, we observed a slipper-shaped RBC whose velocity was almost 1.2 mm/s (Figure A2), while the numerical results showed that a velocity this high resulted in a RBC with a symmetrical parachute shape (Figure 3c). This discrepancy may have been due to the duration of the observation. Since experimental observation periods are limited to 0.1 s or less, the slipper-shaped RBC in the microfluidic device may have been in the transition. According to our numerical results shown in Figure 6, the transition from slipper shape to parachute shape takes at least $\dot{\gamma}t \sim 300$, corresponding to ~ 0.3 s for $Ca = 0.5$ ($V_c \sim 1.2$ mm/s). Another possible reason may have been due to RBC heterogeneity as reported in our previous experiments [17,18]. The experimental observations of an asymmetrical slipper shape in a microfluidic device are required for precise statistical analysis, which will be addressed in future study.

We are not sure what perturbations are needed to destroy the stable symmetrical shape. Thermal energy is unlikely to be affecting the state: indeed, although the RBC membrane usually demonstrates Brownian motion in the free state, the Peclet number ($Pe = \dot{\gamma}a/D_p$, being a radius of the RBC a and a diffusion coefficient D_p) is estimated as approximately $O(Pe) = 10^1$, even at $Ca = 10^{-4}$, by using the Stokes–Einstein equation, and thus the Brownian diffusion (thermal fluctuations) should have little effect. Although the membrane bending rigidity did not affect the stable membrane configuration at least for 3×10^{-20} J $\leq Ca \leq 2.4 \times 10^{-19}$ J, further investigation will be required for larger parameter

spaces. In this study, we defined the initial shape of RBCs as a biconcave disc. Since some recent numerical studies have debated the stress-free shape of RBCs [47–49], it will be interesting to study how the reference shape (biconcave, oblate spheroid, and sphere) affects the stable configuration of translating RBCs in a narrow rectangular microchannel.

5. Conclusions

We numerically investigated the dynamics of translating RBCs in a narrow rectangular microchannel for different capillary numbers (Ca). Our numerical results demonstrated that a confined RBC in a narrow rectangular microchannel maintained a nearly unchanged, biconcave shape at low Ca , then assumed an asymmetrical slipper shape at moderate Ca , and finally attained a symmetrical parachute shape at high Ca . Once the RBC deformed into either of the latter two shapes, they sustained that shape as their final stable configurations. The membrane deformation as a function of Ca remained the same even when the viscosity ratio λ decreased from physiological relevant value ($\lambda = 5$) to unity. The final stable configuration was insensitive to bending resistance and initial position. If these shapes are found in diseased RBCs translating at specific velocities, the shapes will be an important indicator of cell state.

Supplementary Materials: Following materials are available at <http://www.mdpi.com/2072-666X/10/3/199/s1>, Video S1: experimental result at the speed of the cell being 1200 $\mu\text{m/s}$, corresponding to $Ca \approx 0.5$; Video S2: numerical result at $Ca = 0.01$; Video S3: numerical result at $Ca = 0.1$; Video S4: numerical result at $Ca = 0.5$; Videos S5 and Video S6: numerical results of initial RBC centroid position two meshes away from the midline for $Ca = 5 \times 10^{-3}$ and $Ca = 0.5$, respectively. These numerical results were obtained with $\lambda = 5$ and $k_b = 1.2 \times 10^{-19}$ J.

Author Contributions: N.T., analyzed data; H.I. performed experiments; N.T., and H.I. interpreted results of simulations and experiments; N.T. and H.I. prepared figures; N.T. and H.I. drafted manuscript; N.T. and H.I. edited and revised manuscript; N.T., H.I., M.K., and S.W. approved final version of manuscript; N.T. contributed to research conception and design.

Funding: This research was supported by JSPS KAKENHI Grant Number JP17K13015 (N.T.), JP18J00259 (H.I.), JP17K18759 (H.I.); the Sumitomo foundation (181161) (H.I.), JP15H05761 (M.K.); and by the Keihanshin Consortium for Fostering the Next Generation of Global Leaders in Research (K-CONNEX), established by the Human Resource Development Program for Science and Technology and by MEXT as “Priority Issue on Post-K computer” (Integrated Computational Life Science to Support Personalized and Preventive Medicine) (Project ID:hp180202). Part of this work was supported by the Nanotechnology Platform Project (Nanotechnology Open Facilities in Osaka University) of the Ministry of Education, Culture, Sports, Science and Technology, Japan.

Acknowledgments: We thank M. Chimura, T. Ohtani, and Y. Sakata for providing blood samples. Last but not least, Naoki Takeishi thanks Yohsuke Imai and also Toshihiro Omori for helpful discussions.

Conflicts of Interest: No conflicts of interest, financial or otherwise, are declared by the author(s).

Abbreviations

The following abbreviations are used in this manuscript:

RBC	Red blood cell
LBM	Lattice–Boltzmann method
FEM	Finite element method
IBM	Immersed boundary method
GPU	Graphics processing unit

Appendix A. Sample Preparation and Observation

Adult blood was drawn from healthy donors based on the informed consent. All the experiments and experimental protocols in microchannels were approved by the Ethical Committee of Osaka University and performed according to the appropriate guidelines and regulations. Immediately after the blood was drawn, it was maintained in an intact condition by dispersal at a concentration of 1% (v/v) in standard saline.

A microfluidic channel was constructed between a glass slide and poly (dimethylsiloxane) (PDMS) that was designed and printed from a master mold made of SU-8 photoresist using

standard photolithography. The cross-section of the rectangular microchannel was $10\ \mu\text{m} \times 3.5\ \mu\text{m}$ (Figure A1a,b). The experimental system was composed of a high-speed camera (IDP-Express R2000, Photron) and microscope (IX71, Olympus) equipped with an $\times 40$ (N.A. = 0.6) or $\times 50$ (N.A. = 0.42) objective lenses. Images were captured at 1000 frames/s with exposure time of 1 ms. The spatial resolutions of captured images were $0.24\ \mu\text{m}/\text{pixel}$ (Figure A1d) and $0.26\ \mu\text{m}/\text{pixel}$ (Figure A2) for $\times 40$ and $\times 50$ objective lenses, respectively. Flow of the solution inside the microchannel was basically driven by a constant pressure difference between the inlet and outlet of the channel, maintained by atmospheric pressure and gravitational force.

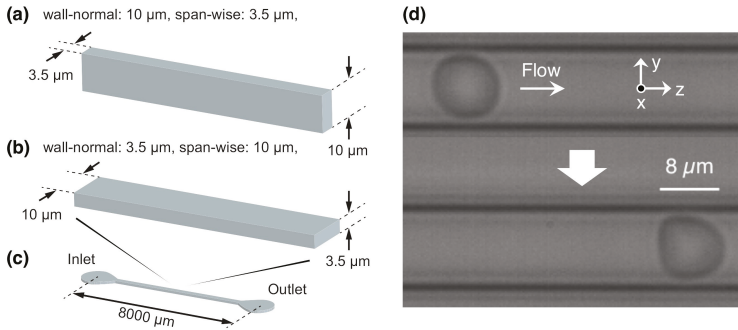


Figure A1. Detailed channel geometry. Magnified view of the channels with the cross-sections of (a) $10\ \mu\text{m} \times 3.5\ \mu\text{m}$ and (b) $3.5\ \mu\text{m} \times 10\ \mu\text{m}$, which were used in Figure A2 and Figure A1, respectively. (c) Schematic view of the whole channel, whose stream-wise length was $8000\ \mu\text{m}$. (d) Representative images of a flowing RBC in a microfluidic device. Flow direction is from left to right.

Figure A2 shows representative snapshot images of a RBC flowing at a velocity of $1200\ \mu\text{m}/\text{s}$; imaging was performed at 1000 frames/s, perpendicular to the span-wise direction of the microchannel. The RBC deformed into an asymmetrical shape, the so-called slipper shape [42]. Interestingly, this configuration was also found in a numerical simulation with $Ca = 0.01$, where the RBC centroid velocity was $V_c \sim 25\ \mu\text{m}/\text{s}$ (Figure A2). Although we reported RBC heterogeneity in [17], the asymmetrical shape of RBCs by means of the experimental observations is required for a precise statistical analysis, which is however future study.

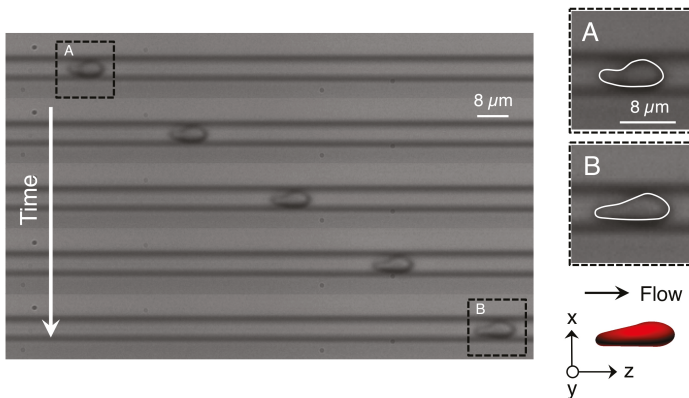


Figure A2. Representative images of the flowing RBC at frame numbers 0 (top), 20, 40, 60, and 80 (bottom), respectively, where the speed of the cell is $1200\ \mu\text{m}/\text{s}$ (see also Video S1). A representative numerical result of a stable slipper-shaped RBC subjected to $Ca = 0.01$ (calculated centroid velocity $V_c \sim 25\ \mu\text{m}/\text{s}$) is also displayed (see also Video S2).

References

- Chen, S. Red cell deformability and its relevance to blood flow. *Annu. Rev. Physiol.* **1987**, *49*, 177–192. [[CrossRef](#)]
- Caimi, G.; Presti, R.L. Techniques to evaluate erythrocyte deformability in diabetes mellitus. *Acta Diabetol.* **2004**, *41*, 99–103. [[CrossRef](#)] [[PubMed](#)]
- Johannes, M.B.P.; Leray, C.; Ruef, P.; Cazenave, J.P.; Linderkamp, O. Endotoxin binding to erythrocyte membrane and erythrocyte deformability in human sepsis and in vitro. *Crit. Care Med.* **2003**, *31*, 924–928.
- Glenister, F.K.; Coppel, R.L.; Cowman, A.F.; Mohandas, N.; Cooke, B.M. Contribution of parasite proteins to altered mechanical properties of malaria-infected red blood cells. *Blood* **2002**, *99*, 1060–1063. [[CrossRef](#)]
- Park, Y.; Diez-Silva, M.; Popescu, G.; Lykotrafitis, G.; Choi, W.; Feld, M.S.; Suresh, S. Refractive index maps and membrane dynamics of human red blood cells parasitized by *Plasmodium falciparum*. *Proc. Natl. Acad. Sci. USA* **2008**, *112*, 6068–6073. [[CrossRef](#)] [[PubMed](#)]
- Suresh, S.; Spatz, J.; Mills, J.P.; Micoulet, A.; Dao, M.; Lim, C.T.; Beil, M.; Seufferlein, T. Connections between single-cell biomechanics and human disease states: Gastrointestinal cancer and malaria. *Acta Biomater.* **2005**, *1*, 15–30. [[CrossRef](#)]
- Fregin, B.; Czerwinski, F.; Biedeweg, D.; Girardo, S.; Gross, S.; Aurich, K.; Otto, O. High-throughput single-cell rheology in complex samples by dynamic real-time deformability cytometry. *Nat. Commun.* **2019**, *10*, 415. [[CrossRef](#)] [[PubMed](#)]
- Gossett, D.R.; Tse, H.T.K.; Lee, S.A.; Ying, Y.; Lindgren, A.G.; Yang, O.O.; Rao, J.; Clark, A.T.; Carloa, D.D. Hydrodynamic stretching of single cells for large population mechanical phenotyping. *Proc. Natl. Acad. Sci. USA* **2012**, *109*, 7630–7635. [[CrossRef](#)]
- Ito, H.; Murakami, R.; Sakuma, S.; Tsai, C.-H.D.; Gutschmann, T.; Brandenburg, K.; Poöschl, J.M.B.; Arai, F.; Kaneko, M.; Tanaka, M. Mechanical diagnosis of human erythrocytes by ultra-high speed manipulation unraveled critical time window for global cytoskeletal remodeling. *Sci. Rep.* **2017**, *7*, 43134. [[CrossRef](#)]
- Otto, O.; Rosendahl, P.; Mietke, A.; Golfier, S.; Herold, C.; Klaue, D.; Girardo, S.; Pagliara, S.; Ekpenyong, A.; Jacobi, A.; et al. Real-time deformability cytometry: On-the-fly cell mechanical phenotyping. *Nat. Methods* **2015**, *12*, 199–202. [[CrossRef](#)]
- Tsai, C.-H.D.; Tanaka, J.; Kaneko, M.; Horade, M.; Ito, H.; Taniguchi, T.; Ohtani, T.; Sakata, Y. An on-chip RBC deformability checker significantly improves velocity-deformation correlation. *Micromachines* **2016**, *7*, 176. [[CrossRef](#)]
- Takeishi, N.; Imai, Y.; Ishida, S.; Omori, T.; Kamm, R.D.; Ishikawa, T. Cell adhesion during bullet motion in capillaries. *Am. J. Physiol. Heart Circ. Physiol.* **2016**, *311*, H395–H403. [[CrossRef](#)] [[PubMed](#)]
- Mokbel, M.; Mokbel, D.; Mietke, A.; Traßer, N.; Girardo, S.; Otto, O.; Guck, J.; Aland, S. Numerical simulation of real-time deformability cytometry to extract cell mechanical properties. *ACS Biomater. Sci. Eng.* **2017**, *3*, 2962–2973. [[CrossRef](#)]
- Mauer, J.; Mendez, S.; Lanotte, L.; Nicoud, F.; Abkarian, M.; Gompper, G.; Fedosov, D.A. Flow-induced transitions of red blood cell shapes under shear. *Phys. Rev. Lett.* **2018**, *121*, 118103. [[CrossRef](#)] [[PubMed](#)]
- Chang, H.-Y.; Yazdani, A.; Li, X.; Douglas, K.A.A.; Mantzoros, C.S.; Karniadakis, G.E. Quantifying platelet margination in diabetic blood flow. *Biophys. J.* **2018**, *115*, 1–12. [[CrossRef](#)]
- Li, X.; Du, E.; Lei, H.; Tang, Y.-H.; Dao, M.; Suresh, S.; Karniadakis, G.E. Patient-specific blood rheology in sickle-cell anaemia. *Interf. Focus* **2016**, *6*, 20150065. [[CrossRef](#)] [[PubMed](#)]
- Ito, H.; Takeishi, N.; Kirimoto, A.; Chimura, M.; Ohtani, T.; Sakata, Y.; Horade, M.; Takayama, T.; Wada, S.; Kaneko, M. How to measure cellular shear modulus inside a chip: Detailed correspondence to the fluid-structure coupling analysis. In Proceedings of the MEMS2019, Seoul, Korea, 27–31 January 2019; pp. 336–433.
- Kirimoto, A.; Ito, H.; Tsai, C.D.; Kaneko, M. Measurement of both viscous and elastic constants of a red blood cell in a microchannel. In Proceedings of the MEMS2018, Belfast, UK, 21–25 January 2018; doi:10.1109/MEMSYS.2018.8346569.
- Abkarian, M.; Faivre, M.; Horton, R.; Smistrup, K.; Best-Popescu, C.A.; Stone, H.A. Cellular-scale hydrodynamics. *Biomed. Mater.* **2008**, *3*, 034011. [[CrossRef](#)] [[PubMed](#)]
- Guckenberger, A.; Kihm, A.; John, T.; Wagner, C.; Gekle, S. Numerical-experimental observation of shape bistability of red blood cells flowing in a microchannel. *Soft Matter* **2018**, *14*, 2032–2043. [[CrossRef](#)]

21. Prado, G.; Farutin, A.; Misbah, C.; Bureau, L. Viscoelastic transient of confined red blood cells. *Biophys. J.* **2015**, *108*, 2126–2136. [[CrossRef](#)]
22. Suzuki, Y.; Tateishi, N.; Soutani, M.; Maeda, N. Deformation of erythrocytes in microvessels and glass capillaries: Effects of erythrocyte deformability. *Microcirculation* **1996**, *3*, 49–57. [[CrossRef](#)]
23. Tomaiuolo, G.; Simeone, M.; Martinelli, V.; Rotolib, B.; Guido, S. Red blood cell deformation in microconfined flow. *Soft Matter* **2009**, *5*, 3736–3740. [[CrossRef](#)]
24. Tomaiuolo, G.; Lanotte, L.; D'Apollito, R.; Cassinese, A.; Guido, S. Microconfined flow behavior of red blood cells. *Med. Eng. Phys.* **2016**, *38*, 11–16. [[CrossRef](#)] [[PubMed](#)]
25. Brust, M.; Aouane, O.; Thiébaud, M.; Flormann, D.; Verdier, C.; Kaestner, L.; Laschke, M.W.; Selmi, H.; Benyoussef, A.; Podgorski, T.; et al. The plasma protein fibrinogen stabilizes clusters of red blood cells in microcapillary flows. *Sci. Rep.* **2014**, *4*, 4348. [[CrossRef](#)] [[PubMed](#)]
26. Kaoui, B.; Biros, G.; Misbah, C. Why do red blood cells have asymmetric shapes even in a symmetric flow? *Phys. Rev. Lett.* **2009**, *103*, 188101. [[CrossRef](#)] [[PubMed](#)]
27. Lázaro, G.R.; Hernández-Machado, A.; Pagonbarraga, I. Rheology of red blood cells under flow in highly confined microchannels. II. Effect of focusing and confinement. *Soft Matter* **2014**, *10*, 7207–7217. [[CrossRef](#)] [[PubMed](#)]
28. Tahiri, N.; Biben, T.; Ez-Zahraouy, H.; Benyoussef, A.; Misbah, C. On the problem of slipper shapes of red blood cells in the microvasculature. *Microvasc. Res.* **2013**, *85*, 40–45. [[CrossRef](#)] [[PubMed](#)]
29. Secomb, T.W.; Skalak, R. A two-dimensional model for capillary flow of an asymmetric cell. *Microvasc. Res.* **1982**, *24*, 194–203. [[CrossRef](#)]
30. Fedosov, D.A.; Peltomäki, M.; Gompper, G. Deformation and dynamics of red blood cells in flow through cylindrical microchannels. *Soft Matter* **2014**, *10*, 4258–4267. [[CrossRef](#)]
31. Zhu, L.; Gallaire, F. A pancake droplet translating in a Hele-Shaw cell: Lubrication film and flow field. *J. Fluid Mech.* **2016**, *798*, 955–969. [[CrossRef](#)]
32. Skalak, R.; Tozeren, A.; Zarda, R.P.; Chien, S. Strain energy function of red blood cell membranes. *Biophys. J.* **1973**, *13*, 245–264. [[CrossRef](#)]
33. Takeishi, N.; Imai, Y.; Nakaaki, K.; Yamaguchi, T.; Ishikawa, T. Leukocyte margination at arteriole shear rate. *Physiol. Rep.* **2014**, *2*, e12037. [[CrossRef](#)] [[PubMed](#)]
34. Takeishi, N.; Imai, Y.; Yamaguchi, T.; Ishikawa, T. Flow of a circulating tumor cell and red blood cells in microvessels. *Phys. Rev. E* **2015**, *92*, 063011. [[CrossRef](#)]
35. Takeishi, N.; Imai, Y. Capture of microparticles by bolus of red blood cells in capillaries. *Sci. Rep.* **2017**, *7*, 5381. [[CrossRef](#)] [[PubMed](#)]
36. Li, J.; Dao, M.; Lim, C.T.; Suresh, S. Spectrin-level modeling of the cytoskeleton and optical tweezers stretching of the erythrocyte. *Phys. Fluid* **2005**, *88*, 3707–6719. [[CrossRef](#)] [[PubMed](#)]
37. Puig-de-Morales-Marinkovic, M.; Turner, K.T.; Butler, J.P.; Fredberg, J.J.; Suresh, S. Viscoelasticity of the human red blood cell. *Am. J. Physiol. Cell Physiol.* **2007**, *293*, C597–C605. [[CrossRef](#)] [[PubMed](#)]
38. Chen, S.; Doolen, G.D. Lattice boltzmann method for fluid flow. *Annu. Rev. Fluid. Mech.* **1998**, *30*, 329–364. [[CrossRef](#)]
39. Walter, J.; Salsac, A.V.; Barthès-Biesel, D.; Le Tallec, P. Coupling of finite element and boundary integral methods for a capsule in a stokes flow. *Int. J. Numer. Meth. Eng.* **2010**, *83*, 829–850. [[CrossRef](#)]
40. Peskin, C.S. The immersed boundary method. *Acta Numer.* **2002**, *11*, 479–517. [[CrossRef](#)]
41. Miki, T.; Wang, X.; Aoki, T.; Imai, Y.; Ishikawa, T.; Takase, K.; Yamaguchi, T. Patient-specific modeling of pulmonary air flow using GPU cluster for the application in medical particle. *Comput. Meth. Biomech. Biomed. Eng.* **2012**, *15*, 771–778. [[CrossRef](#)] [[PubMed](#)]
42. Skalak, R.; Branemark, P.I. Deformation of red blood cells in capillaries. *Science* **1969**, *164*, 717–719. [[CrossRef](#)] [[PubMed](#)]
43. Kuriakose, S.; Dimitrakopoulos, P. Motion of an elastic capsule in a square microfluidic channel. *Phys. Rev. E* **2011**, *84*, 011906. [[CrossRef](#)]
44. Rorai, C.; Touchard, A.; Zhu, L.; Brandt, L. Motion of an elastic capsule in a constricted microchannel. *Eur. Phys. J. E* **2015**, *38*, 49. [[CrossRef](#)]
45. Omori, T.; Ishikawa, T.; Barthès-Biesel, D.; Salsac, A.-V.; Imai, Y.; Yamaguchi, T. Tension of red blood cell membrane in simple shear flow. *Phys. Rev. E* **2012**, *86*, 056321. [[CrossRef](#)]

46. Lanotte, L.; Mauer, J.; Mendez, S.; Fedosov, D.A.; Fromental, J.-M.; Claveria, V.; Nicoul, F.; Gompper, G.; Abkarian, M. Red cells' dynamic morphologies govern blood shear thinning under microcirculatory flow conditions. *Proc. Natl. Acad. Sci. USA* **2016**, *113*, 13289–13294. [[CrossRef](#)]
47. Peng, Z.; Mashayekh, A.; Zhu, Q. Erythrocyte responses in low-shear-rate flows: Effects of non-biconcave stress-free state in the cytoskeleton. *J. Fluid. Mech.* **2014** *742*, 96–118. [[CrossRef](#)]
48. Sinha, K.; Graham, M.D. Dynamics of a single red blood cell in simple shear flow. *Phys. Rev. E* **2015**, *92*, 042710. [[CrossRef](#)]
49. Tsubota, K.; Wada, S.; Liu, H. Elastic behavior of a red blood cell with the membrane's nonuniform natural state: Equilibrium shape, motion transition under shear flow, and elongation during tank-treading motion. *Biomech. Model. Mechanobiol.* **2014**, *13*, 735–746. [[CrossRef](#)]



© 2019 by the authors. Licensee MDPI, Basel, Switzerland. This article is an open access article distributed under the terms and conditions of the Creative Commons Attribution (CC BY) license (<http://creativecommons.org/licenses/by/4.0/>).

Article

A Microfluidic Deformability Assessment of Pathological Red Blood Cells Flowing in a Hyperbolic Converging Microchannel

Vera Faustino ^{1,2}, Raquel O. Rodrigues ¹, Diana Pinho ^{1,2,3,*†}, Elísio Costa ⁴, Alice Santos-Silva ⁴, Vasco Miranda ⁵, Joana S. Amaral ^{6,7} and Rui Lima ^{2,8}

¹ Center for MicroElectromechanical Systems (CMEMS-Uminho), University of Minho, Campus de Azurém, 4800-058 Guimarães, Portugal; id5778@alunos.uminho.pt (V.F.); d8605@dei.uminho.pt (R.O.R.)

² MEtRICs, Mechanical Engineering Department, University of Minho, Campus de Azurém, 4800-058 Guimarães, Portugal; rl@dem.uminho.pt

³ Research Centre in Digitalization and Intelligent Robotics (CeDRI), Instituto Politécnico de Bragança, Campus de Santa Apolónia, 5300-253, Portugal

⁴ UCIBIO-REQUINTE, Faculty of Pharmacy of University of Porto, Rua de Jorge Viterbo Ferreira, 4150-755 Porto, Portugal; emcosta@ff.up.pt (E.C.); assilva@ff.up.pt (A.S.-S.)

⁵ Dialysis Clinic of Gondomar, Rua 5 de Outubro, 4420-086 Gondomar, Portugal; mail@vascomiranda.com

⁶ CIMO, Centro de Investigação de Montanha, Instituto Politécnico de Bragança, Campus de Sta. Apolónia, 5300-253 Bragança, Portugal; jamaral@ipb.pt

⁷ REQUIMTE-LAQV, Pharmacy Faculty, University of Porto, 4099-002 Porto, Portugal

⁸ CEFT, Faculdade de Engenharia da Universidade do Porto (FEUP), R. Dr. Roberto Frias, 4200-465 Porto, Portugal

* Correspondence: diana@ipb.pt; Tel./Fax: +253-510-233

† Current affiliation: INL—International Iberian Nanotechnology Laboratory, Av. Mestre José Veiga, 4715-330 Braga, Portugal.

Received: 9 June 2019; Accepted: 24 September 2019; Published: 25 September 2019

Abstract: The loss of the red blood cells (RBCs) deformability is related with many human diseases, such as malaria, hereditary spherocytosis, sickle cell disease, or renal diseases. Hence, during the last years, a variety of technologies have been proposed to gain insights into the factors affecting the RBCs deformability and their possible direct association with several blood pathologies. In this work, we present a simple microfluidic tool that provides the assessment of motions and deformations of RBCs of end-stage kidney disease (ESKD) patients, under a well-controlled microenvironment. All of the flow studies were performed within a hyperbolic converging microchannels where single-cell deformability was assessed under a controlled homogeneous extensional flow field. By using a passive microfluidic device, RBCs passing through a hyperbolic-shaped contraction were measured by a high-speed video microscopy system, and the velocities and deformability ratios (DR) calculated. Blood samples from 27 individuals, including seven healthy controls and 20 having ESKD with or without diabetes, were analysed. The obtained data indicates that the proposed device is able to detect changes in DR of the RBCs, allowing for distinguishing the samples from the healthy controls and the patients. Overall, the deformability of ESKD patients with and without diabetes type II is lower in comparison with the RBCs from the healthy controls, with this difference being more evident for the group of ESKD patients with diabetes. RBCs from ESKD patients without diabetes elongate on average 8% less, within the hyperbolic contraction, as compared to healthy controls; whereas, RBCs from ESKD patients with diabetes elongate on average 14% less than the healthy controls. The proposed strategy can be easily transformed into a simple and inexpensive diagnostic microfluidic system to assess blood cells deformability due to the huge progress in image processing and high-speed microvisualization technology.

Keywords: microfluidic devices; cell deformability; chronic renal disease; diabetes; red blood cells (RBCs); hyperbolic microchannel; blood on chips

1. Introduction

Blood is a complex and an extremely information-rich fluid that can be used to diagnose different kinds of blood diseases with multiple biophysical techniques and tools [1,2]. Under normal healthy conditions, the red blood cells (RBCs) comprise about 42% in adult females and 47% in adult males of the total blood volume [3]. As RBCs are the most abundant cells in blood, their deformable properties strongly influence the blood rheological properties, particularly in microvessels with complex geometries and diameters of less than 300 μm [4]. Several research works have found that complex microgeometries, such as contractions [5,6] and bifurcations [2,7–9], promote the presence of strong shear and extensional flows that elongate the RBCs without reaching the rupture.

Ever since the RBCs deformability became a potential biomarker for blood diseases, such as malaria [10,11], sickle cell disease [1,12], and diabetes [13–15], several techniques have been developed to measure the biomechanical properties of the RBCs. Additionally, there have been several reviews that discuss different kind of experimental methods to measure the RBC deformability [1,2,16–18]. The available methods can be divided in two main kinds, i.e., the high-throughput methods that measure high concentrations or diluted suspensions of RBCs, and the single-cell techniques. The most popular high-throughput methods, which include the conventional rotational viscometer [19–21], ektacytometer [9,14] and micro-pore filtration assay [9], have been used to measure the blood viscosity and other rheological properties, but they are generally expensive, labor intensive, and do not provide a direct and detailed source of information on the mechanical properties of the RBCs. A recent study that was performed by Sosa et al. [9] has shown that the results from the micro-pore filtration and ektacytometry were often in disagreement, and that neither of them represent the actual blood flow conditions occurring in microvascular networks. Other methods, known as single-cell techniques, which include the micropipette aspiration and optical tweezers, are also extremely popular for measuring the mechanical properties of the RBC membrane [1,13]. However, these techniques also have several drawbacks, such as a low-throughput, labor intensive, and static process. Additionally, it is argued that these methods do not represent the actual RBC deformability that happens during microcirculation [2].

The progress in microfabrication made fabricating microfluidic devices with the ability to directly visualize, measure, and control the motion and deformation of RBCs flowing through constricted [19,22–24] and bifurcated microchannels [7,9,24] possible. The distinctive advantage of the microfluidic devices, such as the need of small sample's volumes and their ability to reproduce more realistic conditions of the microcirculation, have promoted a vast amount of studies on the cell motion and deformability, mainly under the shear flow effect [3,6,16,20,25–27]. Some examples are the deformability measurements that were performed under transient high shear stress in sudden constriction channels, [16,28] and in microchannels with dimensions that were comparable to cell size [2,16]. Besides the shear flow effect, the extensional flow and the combination of both can be often found in the microcirculation system, such as in microstenosis and microvascular networks. Hence, during the last decade, several extensional blood flow studies have been performed in cross slot devices [29,30] and in microfluidic devices with hyperbolic channels [31–36]. Recent studies that were performed in cross slot devices [37] and sudden constriction channels [26] have shown that cells entrance location and angular orientation strongly affect the cells deformability. On the other hand, extensional flows, where cells are deformed at almost constant strain rates, has been demonstrated to be a microfluidic methodology that is capable of efficiently and accurately probing single-cell deformability with high throughputs [16,29].

Additionally, the ability of hyperbolic-shaped contraction channels to generate constant strain-rates makes them a promising strategy for measuring RBCs deformability under a well-controlled microenvironment. Taking these advantage into account, the present study investigates the ability

of hyperbolic microfluidic channels to measure the deformation and cell motion of RBCs that were obtained from healthy and diseased individuals (having end-stage kidney disease (ESKD), with or without diabetes type II) and exploits the relevance of this flow technique to be used as a viable tool suitable for detecting and diagnosing RBC related diseases.

Chronic kidney disease (CKD) is a pathological condition that results from a gradual, permanent loss of kidney function over time, usually, months to years, which can lead to an end-stage kidney disease (ESKD) [38]. This condition is associated with a decreased quality of life [39], increased hospitalization [39,40], cardiovascular complications, such as angina, left ventricular hypertrophy (LVH), and chronic heart failure, and increased mortality [41,42].

The remainder of this paper is organized, as follows: Section 2 comprises several subsections to explain the experimental framework around blood samples, setups used to acquire the data, and methods used to analyze it. Sections 3 and 4 presents and results and discussion, respectively.

2. Materials and Methods

2.1. Patients

In this study, a total of 20 ESKD patients under online hemodiafiltration (OL-HDF) that voluntary accepted to participate in the study, have been tested. From those, eight additionally showed diabetic nephropathy. Patients were excluded if they: (1) did not accept to participate in the study; (2) were under 18 years old; (3) were cognitively impaired; (4) had a severe speech or hearing impairment; (5) were in the dialysis program for less than three months; and, (6) presented malignancy, autoimmune, inflammatory, or infectious diseases.

The control group included seven healthy volunteers presenting normal haematological and biochemical values, with no history of renal or inflammatory diseases, and, as far as possible, age- and gender-matched with ESKD patients. The controls did not receive any medication known to interfere with the studied variables. Blood samples (using EDTA as anticoagulant) were drawn from the fasting controls or before the second dialysis session of the week in ESKD patients.

All of the blood samples were obtained from dialysis patients at the hemodialysis clinic of Gondomar, in Porto, Portugal. Informed consent was obtained from all the participants and this study was approved by the clinic's ethics review board.

2.2. Microfluidic Device, Experimental Setup and Parameters

The polydimethylsiloxane (PDMS) microfluidic devices that were evaluated in this work were fabricated by using a conventional soft-lithographic technique [22]. To perform the deformability assessment, hyperbolic converging microchannels were fabricated with 382 μm of length (L_c), as well as maximum width of 400 μm (W_1) and minimum width of 20 μm (W_2) at the wide and narrow sizes, respectively (cf. Figure 1). This particular geometry corresponds to a hyperbolic contraction with a Hencky strain (ε_H) of ~ 3 . Note that the ε_H can be defined as $\ln(W_1/W_2)$ [32]. The advantages of the use of this hyperbolic geometry for RBCs screening have already been ascribed in previous studies [43,44]. The hyperbolic contraction geometry was chosen, mainly due to the strong extensional flow that was generated in the middle of the microchannel, which is dominant over the shear flow. The cells by passing through the hyperbolic contraction are submitted to a strong extensional flow, where the velocity almost linearly increases, but the strain rate stays approximately constant. Note that the depth was about 50 μm along the full length of the device.

Figure 1b also shows the main advantage of using hyperbolic converging microchannels. At the entrance of these kinds of geometries, the RBCs tend to exhibit a linear increase of their velocities and consequently the strain rates within the hyperbolic contractions are close to a constant. This flow phenomenon imposes a homogenous mechanical fluid behaviour to the RBCs and avoids some possible motions (tumbling, twisting, and rolling rotations), often observed in abrupt contractions [26]. Hence, by using hyperbolic converging microchannels, most of the RBCs tend to elongate when they

flow through the contraction. It is worth mentioning that RBCs motions, such as tumbling, twisting, and rolling rotations, were never observed during our experiments.

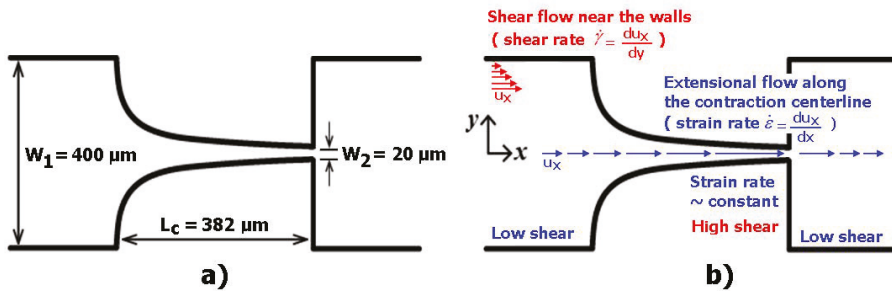


Figure 1. Microfluidic device fabricated in polydimethylsiloxane (PDMS) with a hyperbolic-shaped contraction to assess the of the red blood cells (RBCs) deformability: (a) main dimensions; (b) flow phenomena happening in this kind of geometry. Adapted with permission from [45].

The visualization and measurements of the motion of the RBCs were performed by means of a high-speed video microscopy system that includes an inverted microscope (IX71, Olympus, Tokyo, Japan) combined with a high-speed camera (Fastcam SA3, Photron, San Diego, CA, USA). The microfluidic device was placed on the microscope stage and the flow rate of the working fluids was kept constant at 3 μL/min. by using a syringe pump (PHD Ultra, Harvard Apparatus, Holliston, MA, USA) with a 1 mL disposable syringe (Terumo) (Figure 2). For all of the flow measurements, the average shear rate at the hyperbolic contraction region was about 1750 s⁻¹. The average or pseudo shear rate was calculated by $\bar{\gamma} = \frac{U}{D_h}$, where U is the mean velocity of the blood cells that were obtained at the contraction region, and D_h is the hydraulic diameter at the end of the contraction region.

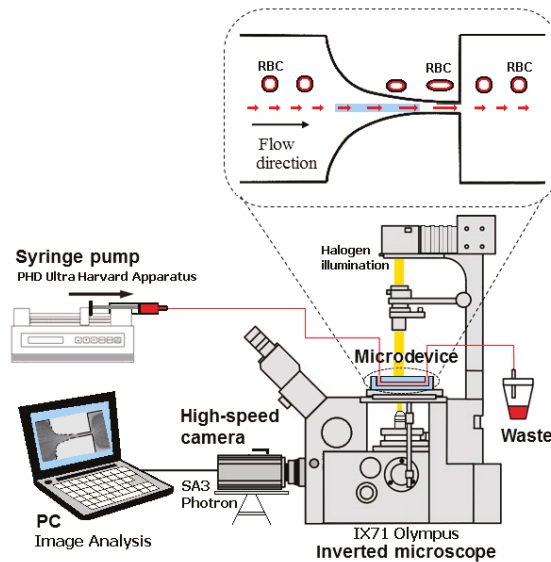


Figure 2. Experimental set-up used to perform the motion and measurements of the RBCs deformability.

The images of the RBCs flowing through the hyperbolic contraction were captured by the high-speed camera with a frame rate of 3000 frames/s and a shutter speed ratio of 1/75,000 s. These

parameters were selected in order to obtain well defined RBCs and avoid possible image distortions that are caused by the high flow velocities at the contraction region. Table 1 shows the most of the relevant experimental parameters that were used to perform the RBCs deformability measurements.

Table 1. Main experimental parameters used to perform the RBCs deformability measurements.

Main Experimental Parameters	
Maximum width of the microchannel	400 μm
Minimum width of the microchannel	20 μm
Total length of the contraction region	382 μm
Depth of the microchannel	50 μm
Flow rate (syringe of 1 mL)	3 $\mu\text{L}/\text{min}$
Average shear rate	1750 s^{-1}
Shear viscosity of the Dextran 40	4.5×10^{-3} Pa·s
Density of the Dextran 40	1046 kg/m^3
Haematocrit of the working fluid	1%
Temperature of the working fluid	22 $^{\circ}\text{C}$
Magnification (M)	40 \times
Numerical Aperture (NA)	0.75
Frame rate	3000 frames/s
Exposure time	1/75,000 s

2.3. Working Fluids

To perform the RBCs deformability studies, Dextran 40 (Sigma-Aldrich, Saint Louis, MO, USA) at 10% (*w/v*) solution containing 1% of haematocrit (Hct 1%, *v/v*) of RBCs was used as the working fluid. Briefly, venous blood samples from both patients and healthy donors were collected into 10 mL BD-Vacutainers (BD, Franklin Lakes, NJ, USA) tubes containing ethylenediaminetetraacetic acid (EDTA) to prevent coagulation. The RBCs and buffy coat were separated from the plasma after centrifugation (2500 rpm for 10 min., at 4 $^{\circ}\text{C}$). The RBCs were then washed with physiological salt solution (PSS) and then centrifuged, with this procedure repeated twice. The RBCs were suspended in Dextran 40 to make several samples with low hematocrit levels of \sim 1% by volume (cf. Figure 3) to obtain the measurements of individual RBC flowing through hyperbolic contraction. Dextran 40 was used as substitute of the blood plasma, since it prevents not only the sedimentation of the RBCs during the experimental assays, but also the cell clogging phenomenon. All of the analyses were performed within a maximum period of 12 h, with blood samples being hermetically stored at 4 $^{\circ}\text{C}$ until being used in the flow experiments.

Image analysis was essential to obtain sharper, brighter, and clearer images of the RBCs flowing through the contraction, and to consequently obtain reliable velocity and deformability measurements, at the regions of interest (ROI) in both contraction and expansion regions, where the RBCs deform and recover to their normal circular shape, respectively (see Figure 3a and supplementary video). The first step of this process involves the capture of videos with a resolution of 1024×576 pixels at frame intervals of 330 μs at the end of the contraction region. Figure 4a shows a typical obtained image. In order to reduce static artifacts in the images, a background image (Figure 4b) was created from the original stack images, by averaging each pixel over the sequence of static images while using an ImageJ function, called *Z project*, and then subtracted from the stack images. This process eliminates all the static objects including the microchannel walls and some possible attached cells, which resulted in having at the end, only the RBCs of interest (Figure 4c). *Brightness/Contrast* adjustment was also applied to enhance the image quality. Finally, the greyscale images were converted to binary images adjusting the threshold level (Figure 4d). At this stage, an *Otsu* threshold method was applied and when required, the level was manually refined. This segmentation process generates objects of interest (RBCs) as black ellipsoidal objects against a white background. At the end, the flowing RBCs in the binary images were measured frame by frame manually, by using *Wand tool* function in ImageJ. The

main output results of these measurements were the major and minor axis lengths of the RBCs and the x - y coordinates of their centroid.

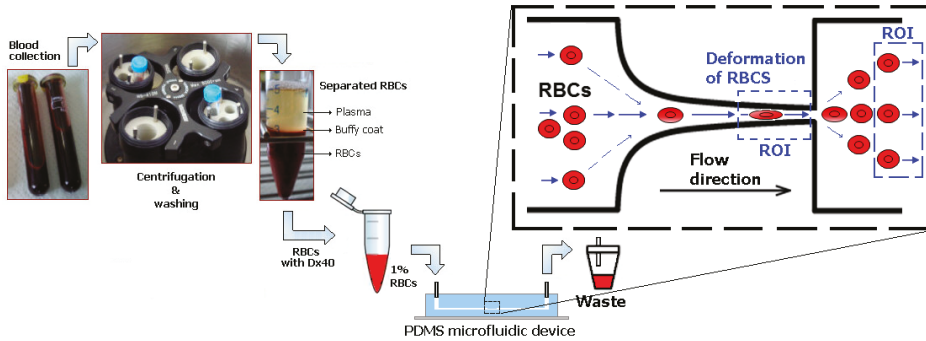


Figure 3. Schematic diagram from blood collection up to the flow microfluidic tests with RBCs. Samples with low hematocrit levels of ~1% were crucial in order to visualize individual RBC flowing through hyperbolic contraction. The ROI regions represent the regions of interest used to analyze the RBCs deformation index.

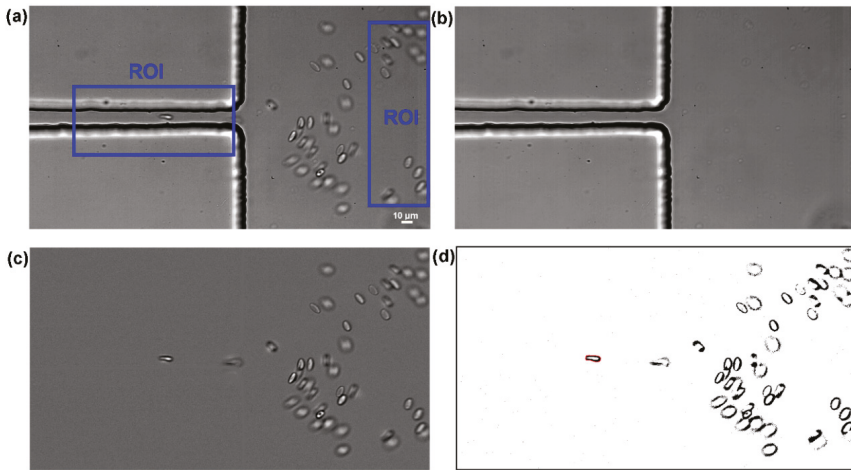


Figure 4. Images analysis sequence: (a) original image at the regions of interest (ROI) regions in which moving RBCs as well as microchannel boundaries are visible, (b) background image containing only static objects, (c) original image after background subtraction showing only moving RBCs, and (d) final binary image to perform measurements of the RBCs major and minor axis lengths.

The deformation ratio (DR) of all the measured RBCs was calculated and saved with the cell's positions, given by their x - y coordinates, using the set of data obtained for the cells at the regions of interest (ROI) at both constriction and expansion locations of the microchannel. In this study, DR was defined by the equation that is shown in Figure 5, where L_{major} and L_{minor} refer to the major and minor axis lengths of the RBC, respectively.

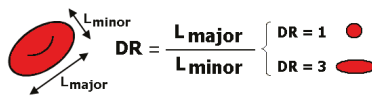


Figure 5. Definition of the deformation ratio, $DR = L_{\text{major}}/L_{\text{minor}}$, where L_{major} and L_{minor} are the major and minor axis lengths of the ellipse best fitted to the cell.

Although different automatic methods to track RBCs in microfluidic devices have been reported in the literature [45–49], further improvements still need to be achieved to perform reliable deformability measurements. Hence, in the present study, hundreds of RBCs were manually tracked by using the ImageJ plug-in, MTrackJ. By selecting this method, it is possible to easily track the cells by a centroid based strategy and obtain their centroid position (x - y coordinates), by carefully tracking individual RBCs and consequently determine their orientations and velocities within the hyperbolic contraction and downstream of the contraction region. In this study, measurements were only performed for the in focus cells flowing from the side, as it is possible to observe in the examples at the supplementary video. In this video, it is also possible to observe a RBC that flows from the top (the biconcave disc shape cell). However, the cells flowing with this orientation were not considered in our deformability measurements.

2.4. Statistical Analysis

The statistical analysis was performed by using one-way ANOVA (Microsoft Office Excel, version Office 365 ProPlus). Before performing the ANOVA analysis, the requirements regarding normal distribution were tested by means of the Shapiro–Wilk’s test. In this test, the null hypothesis that the population is normally distributed was accepted since $p > 0.05$. Overall, for the constriction region, we have measured the deformability of 1769 RBCs corresponding to 12 ESKD patients and a total of 736 measured RBCs, eight ESKDD patients and a total of 444 measured RBCs, and seven healthy controls and a total of 589 measured RBCs. All of the statistical tests were performed at a 95% confidence level; differences with $p < 0.05$ were considered to be statistically significant, and were represented as asterisks (*).

3. Results and Discussion

The determination of the RBC velocities plays an essential role in confirming whether the cells are deformed under similar flow conditions. Hence, before the deformability assessment of each sample, velocity measurements were performed and compared. After analyzing the average velocities of each sample at the contraction region, it was decided to compare the RBC deformability for all of the samples having similar flow conditions, i.e., both shear and extensional flows. Figure 6 shows representative RBC trajectories that were manually tracked within the hyperbolic contraction and downstream of the contraction region.

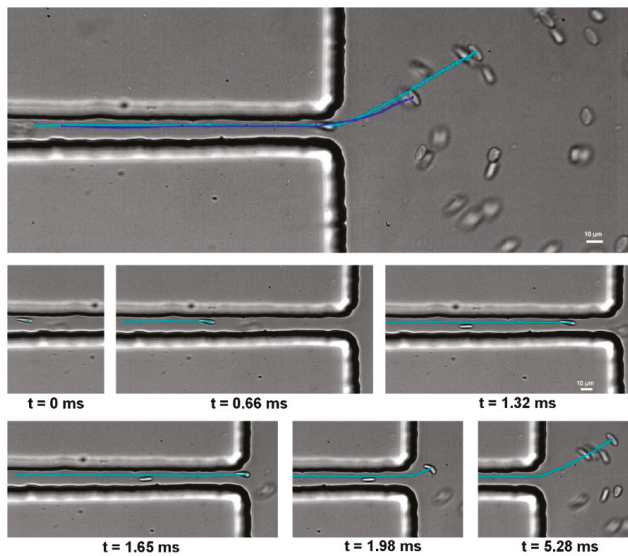


Figure 6. Trajectories of two RBCs flowing within the hyperbolic contraction and downstream of the contraction region (Upper part); detail of a representative trajectory of a RBC flowing near the microchannel wall at different times intervals (Bottom part).

Figure 7 shows the measurements of the velocity and DR of representative RBCs flowing through the hyperbolic-shaped contraction (ROI region) for both healthy donors and ESKD patients (see also supplementary video). The majority of the RBC velocities tend to slightly increase as they move through the exit of the contraction, and then they suffer a dramatic reduction of their velocities when flowing from the narrow to the wide region of the microchannel (cf. Figure 7a). Overall, the velocities of the RBCs of both control and ESKD patients present a similar qualitative flow behavior at the tested region of the device, which results in a good agreement in the deformability results obtained in all the samples (cf. Figure 7b). However, it should be noted that, quantitatively, the DR results indicate that the deformability of the ESKD RBCs under extensional flow tend to be smaller when compared to the control RBCs (cf. Figure 7b). These latter results are further confirmed with the measurements that were performed with several ESKD patients and healthy individual, as shown in Figure 8. Additionally, during all the flow visualization measurements at constriction region, the RBCs did not show any tumbling and rolling motion, which was mainly due to the uniform and strong extensional flow generated along the hyperbolic-shaped contraction. Note that, under shear flow, it is extremely common to observe RBCs flowing with complex dynamics, such as tumbling and rolling [26,46]. In the present study, the RBCs only exhibited such kind of complex flow motions at the expansion region, due to the dominant shear flow with respect to the extensional flow (cf. supplementary video). Hence, by using the proposed method, when the RBCs enter into the contraction region, they change from a circular to an elliptical shape, with a tendency to become increasingly elongated as they moved through the hyperbolic contraction. This latter flow behavior is possible to observe in Figure 7b. Additionally, in this figure, it can be observed that, at the downstream of the contraction region, the cells start to recover their nearly circular shape, exhibiting a DR that is close to one.

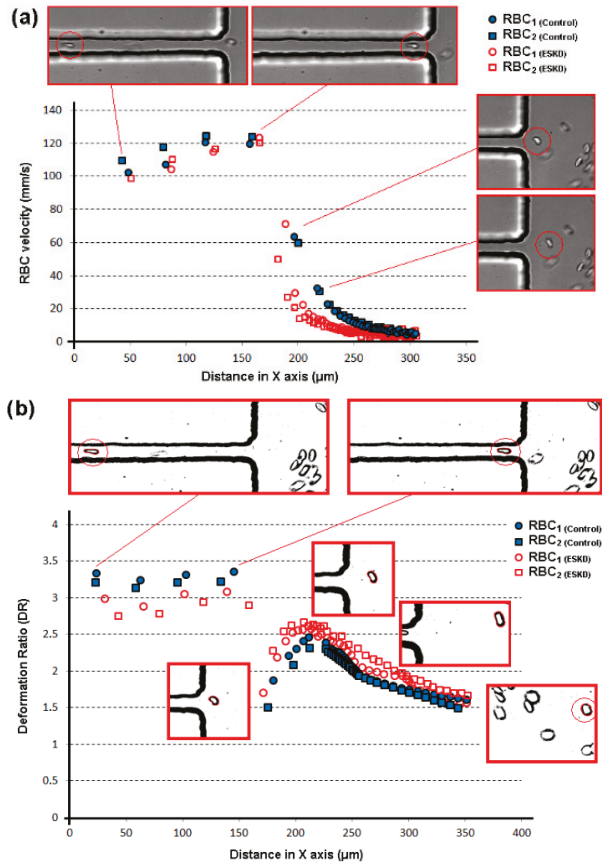


Figure 7. Measurements of RBCs from healthy donors and end-stage kidney disease (ESKD) patients, flowing within the hyperbolic contraction and downstream of the contraction region: (a) velocity measurements; (b) deformability measurements. The X axis represents the position of the cells centroid flowing through the microchannel.

Figure 8 shows the box plot of the deformation ratio (DR) for three different groups, i.e., samples of ESKD patients without diabetes type II ($n = 12$), samples of ESKD patients with diabetes ($n = 8$) type II, and samples from healthy donors ($n = 7$). For each patient sample, more than 60 RBCs with similar flow behavior were individually measured and analyzed at the hyperbolic constriction and recovering channel of the proposed microfluidic device (Figure 8). Additionally, Table 2 shows the data of the average DR and standard deviation (SD) of the RBCs deformation at both the contraction and expansion region for all of the tested samples. Overall, the deformability of ESKD patients (with and without diabetes) measured at the hyperbolic constriction is lower in comparison with the RBCs from the normal healthy controls ($p < 0.05$), as shown in Figure 8b. This difference is more evident when only the group of ESKD patients with diabetes is taken into consideration. For instance, RBCs from ESKD patients without diabetes elongates, on average, 8% less within the hyperbolic contraction when compared to healthy controls, whereas RBCs from ESKD patients with diabetes elongates on average 14% less than the healthy controls (cf. Figure 8b). On the other hand, all of the cells analyzed, both healthy and diseased, have been shown to have a similar DR (nearly to 1, i.e., close to a spherical-shape) at the expansion region of the microchannel (Figure 8c,d), where cells tend to recover to their normal

circular shape due to the low shear rate and a negligible strain rate. Therefore, the results from the present study demonstrate that the RBCs DR measured by using the proposed microfluidic device can be considered as a sensitive mechanical biomarker, as it was able to detect changes in DR of the RBCs from patients with different diseases in comparison with healthy ones. Moreover, this study also corroborates other previous research works [13,14], where, by using different deformability measurement techniques, it was shown that elongation of RBCs from patients with diabetes is lower in comparison with the non-diabetic healthy controls.

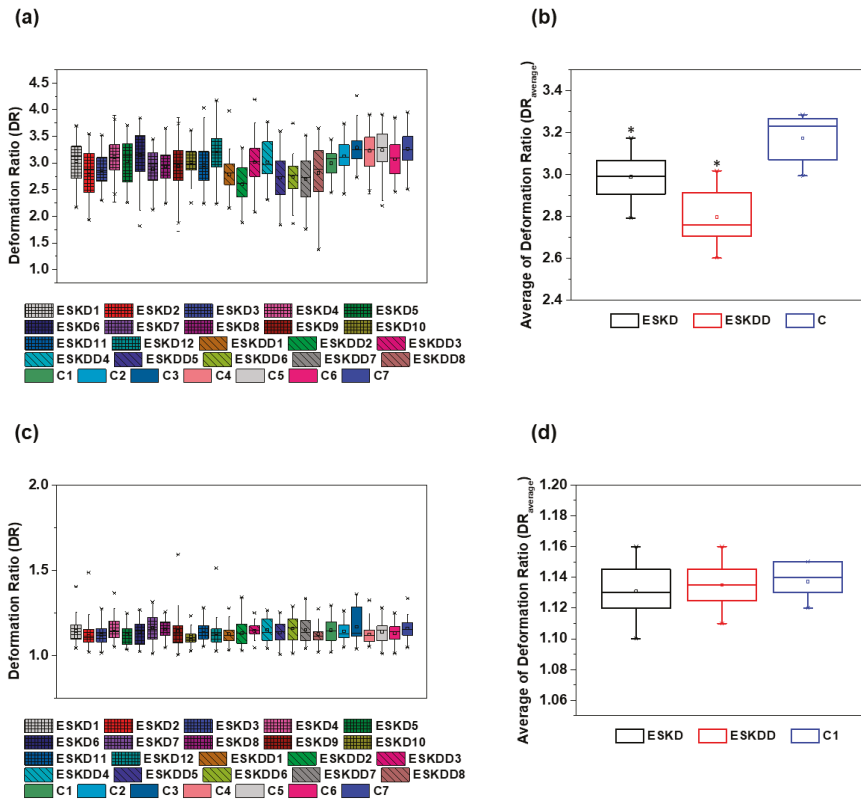


Figure 8. Box plot representation of RBC’s deformation ratio (DR) measured by the proposed microfluidic device: (a) DR of individual donors, including ESKD patients, ESKD patients with diabetes and healthy donors (control) in the hyperbolic constriction, (b) Average DR of the groups of donors, including ESKD patients, ESKD patients with diabetes and healthy donors (control) in the hyperbolic constriction, (c) DR of individual donors, including ESKD patients, ESKD patients with diabetes and healthy donors (control) at the expansion region, (d) Average DR of the groups of donors, including ESKD patients, ESKD patients with diabetes and healthy donors (control) at the expansion region. The asterisks (*) indicates statistically significant differences ($p < 0.05$) determined by Student’s *t* test.

Table 2. Average DR and standard deviation (SD) of the flowing RBCs at both contraction and expansion region for each sample.

Blood Samples	Contraction Region DR		Expansion Region DR	
	Average	SD	Average	SD
ESKD1	3.03	0.34	1.12	0.08
ESKD2	2.79	0.36	1.10	0.09
ESKD3	2.86	0.26	1.13	0.06
ESKD4	3.11	0.25	1.14	0.08
ESKD5	3.03	0.39	1.12	0.06
ESKD6	3.15	0.37	1.15	0.07
ESKD7	2.89	0.31	1.15	0.08
ESKD8	2.93	0.26	1.16	0.05
ESKD9	2.94	0.35	1.13	0.10
ESKD10	3.02	0.24	1.10	0.05
ESKD11	2.96	0.32	1.14	0.06
ESKD12	3.17	0.35	1.13	0.08
ESKDD1	2.78	0.25	1.12	0.05
ESKDD2	2.60	0.27	1.13	0.07
ESKDD3	3.01	0.32	1.15	0.05
ESKDD4	3.02	0.32	1.13	0.08
ESKDD5	2.72	0.37	1.14	0.07
ESKDD6	2.74	0.28	1.16	0.08
ESKDD7	2.69	0.34	1.14	0.08
ESKDD8	2.81	0.43	1.11	0.06
C1	2.99	0.21	1.14	0.07
C2	3.12	0.23	1.13	0.06
C3	3.28	0.22	1.13	0.10
C4	3.23	0.27	1.12	0.06
C5	3.24	0.31	1.15	0.07
C6	3.07	0.30	1.14	0.07
C7	3.27	0.27	1.15	0.06

As previously mentioned, RBCs occupy almost half of the total blood volume and, under healthy conditions, they are highly deformable in order to pass through capillaries with dimensions several times lower than the RBCs size [16]. Hence, it is well known that the RBC deformability plays a crucial role in the rheological properties of blood in microvessels, i.e., the decrease of the RBC deformability might result in an increase of the blood viscosity and, consequently, in an increased tendency for microvascular complications and associated diseases. The results that are presented in this study indicate that the ESKD patients with and without diabetes have a tendency to decrease the RBCs deformability and, as a result, might have a substantial impact in the whole blood viscosity of these patient's health. This can result in an elicit hemolysis in the capillaries and premature sequestration of RBCs by the reticulo-endothelial system, and altering tissue oxygenation. However, a larger scale study is required to confirm whether the decrease of the RBC deformability contributes to the increase of the blood viscosity, or not.

4. Limitations and Future Directions

The primary goal of the present work was to investigate the ability of hyperbolic converging microchannels to be used as an alternative clinical tool that is suitable to detect and diagnose RBC related diseases. To accomplish it, high speed microfluidic studies were performed in a hyperbolic contraction microchannel with a uniform depth of about 50 μm . The selection of this depth was a compromise solution mainly due to the limitation of our high-speed video camera: although, by decreasing the microchannel depth, the orientation of the cells tend to be more stable, the difficulty to measure the RBCs deformability increases due to the extremely high velocities that were generated at this region. The major advantage of this geometrical modification is the ability to use simple automatic

methods, which results in a significant increase of the number of cell measurements performed under similar flow conditions. Nevertheless, in this study, we opted for manual measurements to guarantee that only adequate cells were included.

Additionally, we would like to refer that recently, Schonbrun et al. [50] have shown that by using blue light the hemoglobin absorption makes cells extremely visible and easier to track in microchannels for low shear rates. Although this optical option looks promising, further research needs to be performed regarding the ability to measure blood cells at high shear rates. We consider that a combination of both strategies could result in a promising methodology to perform DR measurement of RBCs with high accuracy. The high-speed camera used due to its cost can be a limitation to consider the technique as a common tool; however, during the last two decades, the cost of this technology has been decreasing in an exponential way, thus we believe that it will be possible to have in a more affordable way a high-speed system in the future. Another way can be the use of compact CCD cameras due its capacity to achieve similar sensitivity and exposure, but in an affordable way.

5. Conclusions

RBCs deformability plays a crucial role in microcirculation and the loss of their deformability can be related to many pathologies. The present study investigated the ability of hyperbolic microfluidic channels to measure the deformation and RBC motion from the blood samples of patients with ESKD (with and without diabetes type II) compared to healthy individuals (used as control) and exploit the relevance of this method to be used as viable clinical tool suitable to detect and diagnose RBC related disease. This study has shown the potential of the proposed device to detect changes in DR of the RBCs from patients with different complications. Overall, the elongation of RBCs from the ESKD patients, with and without diabetes, was lower in comparison with the RBCs from the healthy controls, being the difference more evident for the group of ESKD patients with diabetes. Another important finding was related to the comparison of the cells at the expansion region, where the RBCs have recovered their normal circular shape. At this region, the cells were deformed under low shear rate and negligible strain rate. Under those conditions, we have not found any difference between the ESKD patients and the healthy controls. This latter result indicates that the RBCs need to be submitted to high mechanical stresses to deform the cells and, consequently, to detect different state of blood diseases.

Additionally, the results that are presented in this study indicate that the ESKD patients with and without diabetes have a tendency to decrease the RBCs deformability, which might have a substantial impact in the whole blood viscosity of these patients. However, a larger scale study would be necessary to confirm whether the decrease of the RBC deformability contributes to the increase of the blood viscosity, or not. Although the proposed microfluidic tool requires further improvements, the results that were obtained from the present study suggest that this technique is able to assure a simple and efficient cell deformability assessment at both physiological and pathological situations.

Supplementary Materials: The following are available online at <http://www.mdpi.com/2072-666X/10/10/645/s1>, Figure S1: Images from a video where it is possible to observe that the RBCs rotation only happens at the expansion region of the microchannel, and Video S1: Visualization of RBCs flowing within the hyperbolic contraction and downstream of the contraction region.

Author Contributions: Conceptualization, R.L., J.S.A. and E.C. Methodology, R.L., J.S.A. and E.C.; Software, V.F. and R.L. Formal Analysis, R.L., V.F., D.P., R.O.R.; Investigation, R.L., J.S.A., V.F., D.P., R.O.R., E.C. and A.S.-S.; Resources, R.L., J.S.A., E.C., A.S.-S., and V.M.; Data Curation, R.L., V.F., D.P., R.O.R., J.S.A.; Writing—Original Draft Preparation, R.L., J.S.A., E.C., and R.O.R.; Writing—Review & Editing, R.L., D.P., R.O.R., J.S.A. Supervision, R.L., J.S.A., E.C. and A.S.-S.; Project Administration, R.L. and J.S.A.; Funding Acquisition, R.L. and J.S.

Funding: Research supported by FCT with the reference projects POCI-01-0145-FEDER-016861 (PTDC/QEQ-FTT/4287/2014), NORTE-01-0145-FEDER-029394 (PTDC/EMD-EMD/29394/2017), NORTE-01-0145-FEDER-030171 (PTDC/EME-SIS/30171/2017), UID/EMS/04077/2019, UID/EEA/04436/2019, UID/EMS/00532/2019, PTDC/SAU-ENB/116929/2010, by FEDER funds through the COMPETE 2020, NORTE2020, PORTUGAL2020—Programa Operacional Competitividade e Internacionalização (POCI) with the reference project POCI-01-0145-FEDER-006941 and by the NORTE-01-0145-FEDER-028178 (PTDC/EEI-EEE/28178/2017) project, funded 85% from Programa Operacional Regional do Norte and 15% from FCT. This study was also supported by FCT/MEC through national funds and cofinanced by FEDER, under the Partnership Agreement PT2020 from

UCIBIO (UID/MULTI/04378/2013-POCI/01/0145/FEDER/007728), and North Portugal Regional Coordination and Development Commission (CCDR-N)/NORTE2020/Portugal 2020 (Norte-01-0145-FEDER-000024).

Acknowledgments: V.F. acknowledges the PhD scholarship SFRH/BD/99696/2014 attributed by FCT.

Conflicts of Interest: The authors declare no conflict of interest.

References

1. Lee, G.Y.; Lim, C.T. Biomechanics approaches to studying human diseases. *Trends Biotechnol.* **2007**, *25*, 111–118. [PubMed]
2. Tomaiuolo, G. Biomechanical properties of red blood cells in health and disease towards microfluidics. *Biomicrofluidics* **2014**, *8*, 051501. [PubMed]
3. Siddhartha, T.; Kumar, Y.V.B.V.; Amit, P.; Suhas, S.J.; Amit, A. Passive blood plasma separation at the microscale: A review of design principles and microdevices. *J. Micromech. Microeng.* **2015**, *25*, 083001.
4. Lima, R.; Ishikawa, T.; Imai, Y.; Yamaguchi, T. Blood Flow Behavior in Microchannels: Past, Current and Future Trends. In *Single and Two-Phase Flows on Chemical and Biomedical Engineering*; Dias, R., Martins, A.A., Lima, R., Mata, T.M., Eds.; Bentham Science: Sharjah, UAE, 2012; pp. 513–547.
5. Abkarian, M.; Faivre, M.; Horton, R.; Smistrup, K.; Best-Popescu, C.A.; Stone, H.A. Cellular-scale hydrodynamics. *Biomed. Mater.* **2008**, *3*, 034011. [PubMed]
6. Pinho, D.; Yaginuma, T.; Lima, R. A microfluidic device for partial cell separation and deformability assessment. *BioChip J.* **2013**, *7*, 367–374.
7. Bento, D.; Fernandes, C.; Miranda, J.; Lima, R. In vitro blood flow visualizations and cell-free layer (CFL) measurements in a microchannel network. *Exp. Therm. Fluid Sci.* **2019**, *109*, 109847.
8. Shevkopylas, S.S.; Yoshida, T.; Gifford, S.C.; Bitensky, M.W. Direct measurement of the impact of impaired erythrocyte deformability on microvascular network perfusion in a microfluidic device. *Lab Chip* **2006**, *6*, 914.
9. Sosa, J.M.; Nielsen, N.D.; Vignes, S.M.; Chen, T.G.; Shevkopylas, S.S. The relationship between red blood cell deformability metrics and perfusion of an artificial microvascular network. *Clin. Hemorheol. Microcirc.* **2014**, *57*, 275–289.
10. Boas, L.V.; Faustino, V.; Lima, R.; Miranda, J.M.; Minas, G.; Fernandes, C.S.V.; Catarino, S.O. Assessment of the Deformability and Velocity of Healthy and Artificially Impaired Red Blood Cells in Narrow Polydimethylsiloxane (PDMS) Microchannels. *Micromachines* **2018**, *9*, 384.
11. Shelby, J.P.; White, J.; Ganesan, K.; Rathod, P.K.; Chiu, D.T. A microfluidic model for single-cell capillary obstruction by Plasmodium falciparum-infected erythrocytes. *Proc. Natl. Acad. Sci. USA* **2003**, *100*, 14618–14622.
12. Dao, M.; Lim, C.T.; Suresh, S. Mechanics of the human red blood cell deformed by optical tweezers. *J. Mech. Phys. Solids* **2003**, *51*, 2259–2280.
13. Agrawal, R.; Smart, T.; Nobre-Cardoso, J.; Richards, C.; Bhatnagar, R.; Tufail, A.; Shima, D.; Jones, P.H.; Pavesio, C. Assessment of red blood cell deformability in type 2 diabetes mellitus and diabetic retinopathy by dual optical tweezers stretching technique. *Sci. Rep.* **2016**, *6*, 15873. [PubMed]
14. Shin, S.; Ku, Y.-H.; Ho, J.-X.; Kim, Y.-K.; Suh, J.-S.; Singh, M. Progressive impairment of erythrocyte deformability as indicator of microangiopathy in type 2 diabetes mellitus. *Clin. Hemorheol. Microcirc.* **2007**, *36*, 253–261. [PubMed]
15. Tsukada, K.; Sekizuka, E.; Oshio, C.; Minamitani, H. Direct Measurement of Erythrocyte Deformability in Diabetes Mellitus with a Transparent Microchannel Capillary Model and High-Speed Video Camera System. *Microvasc. Res.* **2001**, *61*, 231–239.
16. Bento, D.; Rodrigues, R.O.; Faustino, V.; Pinho, D.; Fernandes, C.S.; Pereira, A.I.; Garcia, V.; Miranda, J.M.; Lima, R. Deformation of Red Blood Cells, Air Bubbles, and Droplets in Microfluidic Devices: Flow Visualizations and Measurements. *Micromachines* **2018**, *9*, 151.
17. Musielak, M. Red blood cell-deformability measurement: Review of techniques. *Clin. Hemorheol. Microcirc.* **2009**, *42*, 47–64.
18. Xue, C.; Wang, J.; Zhao, Y.; Chen, D.; Yue, W.; Chen, J. Constriction Channel Based Single-Cell Mechanical Property Characterization. *Micromachines* **2015**, *6*, 1794–1804.

19. Pinho, D.; Campo-Deaño, L.; Lima, R.; Pinho, F.T. In vitro particulate analogue fluids for experimental studies of rheological and hemorheological behavior of glucose-rich RBC suspensions. *Biomicrofluidics* **2017**, *11*, 054105.
20. Pinho, D.; Rodrigues, R.O.; Faustino, V.; Yaginuma, T.; Exposto, J.; Lima, R. Red blood cells radial dispersion in blood flowing through microchannels: The role of temperature. *J. Biomech.* **2016**, *49*, 2293–2298.
21. Sousa, P.C.; Carneiro, J.; Vaz, R.; Cerejo, A.; Pinho, F.T.; Alves, M.A.; Oliveira, M.S. Shear viscosity and nonlinear behavior of whole blood under large amplitude oscillatory shear. *Biorheology* **2013**, *50*, 269–282.
22. Faustino, V.; Catarino, S.O.; Lima, R.; Minas, G. Biomedical microfluidic devices by using low-cost fabrication techniques: A review. *J. Biomech.* **2016**, *49*, 2280–2292. [[PubMed](#)]
23. Wei, Y.; Zheng, Y.; Nguyen, J.; Sun, Y. Recent advances in microfluidic techniques for single-cell biophysical characterization. *Lab Chip* **2013**, *13*, 2464.
24. Catarino, S.O.; Rodrigues, R.O.; Pinho, D.; Miranda, J.M.; Minas, G.; Lima, R. Blood Cells Separation and Sorting Techniques of Passive Microfluidic Devices: From Fabrication to Applications. *Micromachines* **2019**, *10*, 593.
25. Quinn, D.J.; Pivkin, I.; Wong, S.Y.; Chiam, K.H.; Dao, M.; Karniadakis, G.E.; Suresh, S. Combined simulation and experimental study of large deformation of red blood cells in microfluidic systems. *Ann. Biomed. Eng.* **2011**, *39*, 1041–1050. [[PubMed](#)]
26. Zeng, N.F.; Ristenpart, W.D. Mechanical response of red blood cells entering a constriction. *Biomicrofluidics* **2014**, *8*, 064123. [[PubMed](#)]
27. Zhao, R.; Marhefka, J.N.; Shu, F.; Hund, S.J.; Kameneva, M.V.; Antaki, J.F. Micro-Flow Visualization of Red Blood Cell-Enhanced Platelet Concentration at Sudden Expansion. *Ann. Biomed. Eng.* **2008**, *36*, 1130–1141. [[PubMed](#)]
28. Fujiwara, H.; Ishikawa, T.; Lima, R.; Matsuki, N.; Imai, Y.; Kaji, H.; Nishizawa, M.; Yamaguchi, T. Red blood cell motions in high-hematocrit blood flowing through a stenosed microchannel. *J. Biomech.* **2009**, *42*, 838–843.
29. Gossett, D.R.; Tse, H.T.K.; Lee, S.A.; Ying, Y.; Lindgren, A.G.; Yang, O.O.; Rao, J.; Clark, A.T.; Di Carlo, D. Hydrodynamic stretching of single cells for large population mechanical phenotyping. *Proc. Natl. Acad. Sci. USA* **2012**, *109*, 7630–7635.
30. Guillou, L.; Dahl, J.B.; Lin, J.-M.G.; Barakat, A.I.; Husson, J.; Muller, S.J.; Kumar, S. Measuring Cell Viscoelastic Properties Using a Microfluidic Extensional Flow Device. *Biophys. J.* **2016**, *111*, 2039–2050.
31. Lee, S.S.; Yim, Y.; Ahn, K.H.; Lee, S.J. Extensional flow-based assessment of red blood cell deformability using hyperbolic converging microchannel. *Biomed. Microdevices* **2009**, *11*, 1021–1027.
32. Rodrigues, R.O.; Bañobre-López, M.; Gallo, J.; Tavares, P.B.; Silva, A.M.T.; Lima, R.; Gomes, H.T. Haemocompatibility of iron oxide nanoparticles synthesized for theranostic applications: A high-sensitivity microfluidic tool. *J. Nanopart. Res.* **2016**, *18*, 1–17.
33. Rodrigues, R.O.; Lopes, R.; Pinho, D.; Pereira, A.I.; Garcia, V.; Gassmann, S.; Sousa, P.C.; Lima, R. In vitro blood flow and cell-free layer in hyperbolic microchannels: Visualizations and measurements. *BioChip J.* **2016**, *10*, 9–15.
34. Rodrigues, R.O.; Pinho, D.; Faustino, V.; Lima, R. A simple microfluidic device for the deformability assessment of blood cells in a continuous flow. *Biomed. Microdevices* **2015**, *17*, 108. [[PubMed](#)]
35. Yaginuma, T.; Oliveira, M.S.N.; Lima, R.; Ishikawa, T.; Yamaguchi, T. Human red blood cell behavior under homogeneous extensional flow in a hyperbolic-shaped microchannel. *Biomicrofluidics* **2013**, *7*, 54110. [[PubMed](#)]
36. Zografos, K.; Pimenta, F.; Alves, M.A.; Oliveira, M.S.N. Microfluidic converging/diverging channels optimised for homogeneous extensional deformation. *Biomicrofluidics* **2016**, *10*, 043508.
37. Henon, Y.; Sheard, G.J.; Fouras, A. Erythrocyte deformation in a microfluidic cross-slot channel. *RSC Adv.* **2014**, *4*, 36079.
38. Astor, B.C.; Muntner, P.; Levin, A.; Eustace, J.A.; Coresh, J. Association of kidney function with anemia: The Third National Health and Nutrition Examination Survey (1988–1994). *Arch. Intern. Med.* **2002**, *162*, 1401–1408.
39. Staples, A.O.; Wong, C.S.; Smith, J.M.; Gipson, D.S.; Filler, G.; Warady, B.A.; Martz, K.; Greenbaum, L.A. Anemia and risk of hospitalization in pediatric chronic kidney disease. *Clin. J. Am. Soc. Nephrol. CJASN* **2009**, *4*, 48–56.

40. Brines, M.; Grasso, G.; Fiordaliso, F.; Sfacteria, A.; Ghezzi, P.; Fratelli, M.; Latini, R.; Xie, Q.W.; Smart, J.; Su-Rick, C.J.; et al. Erythropoietin mediates tissue protection through an erythropoietin and common beta-subunit heteroreceptor. *Proc. Natl. Acad. Sci. USA* **2004**, *101*, 14907–14912.
41. Robinson, B.M.; Joffe, M.M.; Berns, J.S.; Pisoni, R.L.; Port, F.K.; Feldman, H.I. Anemia and mortality in hemodialysis patients: Accounting for morbidity and treatment variables updated over time. *Kidney Int.* **2005**, *68*, 2323–2330.
42. Yang, W.; Israni, R.K.; Brunelli, S.M.; Joffe, M.M.; Fishbane, S.; Feldman, H.I. Hemoglobin Variability and Mortality in ESRD. *J. Am. Soc. Nephrol. JASN* **2007**, *18*, 3164–3170. [[PubMed](#)]
43. Faustino, V.; Pinho, D.; Yaginuma, T.; Calhelha, R.C.; Ferreira, I.C.; Lima, R. Extensional flow-based microfluidic device: Deformability assessment of red blood cells in contact with tumor cells. *BioChip J.* **2014**, *8*, 42–47.
44. Faustino, V.; Pinho, D.; Yaginuma, T.; Calhelha, R.C.; Kim, G.M.; Arana, S.; Ferreira, I.C.F.R.; Oliveira, M.S.N.; Lima, R. Flow of Red Blood Cells Suspensions through Hyperbolic Microcontractions. In *Visualization and Simulation of Complex Flows in Biomedical Engineering*; Lima, R., Imai, Y., Ishikawa, T., Oliveira, M.S., Eds.; Springer: Dordrecht, The Netherlands, 2014; pp. 151–163.
45. Lima, R.A.; Saadatmand, M.; Ishikawa, T. Microfluidic Devices Based on Biomechanics. In *Integrated Nano-Biomechanics*; Yamaguchi, T., Ishikawa, T., Imai, Y., Eds.; Elsevier: Boston, MA, USA, 2018; pp. 217–263. [[CrossRef](#)]
46. Forsyth, A.M.; Wan, J.; Ristenpart, W.D.; Stone, H.A. The dynamic behavior of chemically “stiffened” red blood cells in microchannel flows. *Microvasc. Res.* **2010**, *80*, 37–43. [[PubMed](#)]
47. Pinho, D.; Lima, R.; Pereira, A.I.; Gayubo, F. Automatic tracking of labeled red blood cells in microchannels. *Int. J. Numer. Method Biomed. Eng.* **2013**, *29*, 977–987. [[CrossRef](#)] [[PubMed](#)]
48. Rodrigues, V.; Rodrigues, P.J.; Pereira, A.I.; Lima, R. Automatic tracking of red blood cells in micro channels using OpenCV. In *AIP Conference Proceedings*; AIP Publishing: Melville, NY, USA, 2013; Volume 1558, p. 594. [[CrossRef](#)]
49. Taboada, B.; Monteiro, F.; Lima, R. Automatic tracking and deformation measurements of red blood cells flowing through a microchannel with a microstenosis: The keyhole model. *Comput. Methods Biomech. Biomed. Eng. Imaging Vis.* **2016**, *4*, 229–237. [[CrossRef](#)]
50. Schonbrun, E.; Malka, R.; Di Caprio, G.; Schaak, D.; Higgins, J.M. Quantitative Absorption Cytometry for Measuring Red Blood Cell Hemoglobin Mass and Volume. *Cytometry A* **2014**, *85*, 332–338. [[CrossRef](#)] [[PubMed](#)]



© 2019 by the authors. Licensee MDPI, Basel, Switzerland. This article is an open access article distributed under the terms and conditions of the Creative Commons Attribution (CC BY) license (<http://creativecommons.org/licenses/by/4.0/>).



Article

Assessment of the Deformability and Velocity of Healthy and Artificially Impaired Red Blood Cells in Narrow Polydimethylsiloxane (PDMS) Microchannels

Liliana Vilas Boas ^{1,2}, Vera Faustino ^{1,3}, Rui Lima ^{3,4}, João Mário Miranda ⁴, Graça Minas ¹, Carla Sofia Veiga Fernandes ² and Susana Oliveira Catarino ^{1,*}

¹ Microelectromechanical Systems Research Unit (CMEMS-UMinho), University of Minho, 4800-058 Guimarães, Portugal; liliana.sv.boas@gmail.com (L.V.B.); id5778@alunos.uminho.pt (V.F.); gminas@dei.uminho.pt (G.M.)

² Instituto Politécnico de Bragança, ESTiG, C. Sta. Apolónia, 5300-253 Bragança, Portugal; cveiga@ipb.pt

³ METRICs, DEM, University of Minho, 4800-058 Guimarães, Portugal; rl@dem.uminho.pt

⁴ CEFT, University of Porto, 4000-008 Porto, Portugal; jmiranda@fe.up.pt

* Correspondence: scatarino@dei.uminho.pt; Tel.: +351-253-510-190

Received: 19 June 2018; Accepted: 30 July 2018; Published: 2 August 2018

Abstract: Malaria is one of the leading causes of death in underdeveloped regions. Thus, the development of rapid, efficient, and competitive diagnostic techniques is essential. This work reports a study of the deformability and velocity assessment of healthy and artificially impaired red blood cells (RBCs), with the purpose of potentially mimicking malaria effects, in narrow polydimethylsiloxane microchannels. To obtain impaired RBCs, their properties were modified by adding, to the RBCs, different concentrations of glucose, glutaraldehyde, or diamide, in order to increase the cells' rigidity. The effects of the RBCs' artificial stiffening were evaluated by combining image analysis techniques with microchannels with a contraction width of 8 μm , making it possible to measure the cells' deformability and velocity of both healthy and modified RBCs. The results showed that healthy RBCs naturally deform when they cross the contractions and rapidly recover their original shape. In contrast, for the modified samples with high concentration of chemicals, the same did not occur. Additionally, for all the tested modification methods, the results have shown a decrease in the RBCs' deformability and velocity as the cells' rigidity increases, when compared to the behavior of healthy RBCs samples. These results show the ability of the image analysis tools combined with microchannel contractions to obtain crucial information on the pathological blood phenomena in microcirculation. Particularly, it was possible to measure the deformability of the RBCs and their velocity, resulting in a velocity/deformability relation in the microchannel. This correlation shows great potential to relate the RBCs' behavior with the various stages of malaria, helping to establish the development of new diagnostic systems towards point-of-care devices.

Keywords: biomicrofluidics; red blood cells; deformability; velocity

1. Introduction

Malaria is a parasitic disease with more than half the world population at risk and around 500 thousand deaths per year, with 80% of infections occurring in children under 5 years old [1]. This disease is mainly widespread in underdeveloped regions, with lack of proper infrastructure and living conditions, worsening the chances of infection for the population. The control, effective treatment, and elimination of malaria require an early and accurate diagnosis. Currently, the malaria diagnosis is based on blood smear microscopy or rapid diagnostic tests (RDTs) [2,3], which have

limitations in the detection limit (only detect above 50 parasites/ μL of blood). Additionally, microscopy has limitations in the required time to perform the assays and in the need for specialized technicians and/or laboratories, compromising the reduction of global incidence. To fulfill these needs, innovative diagnosis based on molecular assays have been developed, with detection limits below 2 parasites/ μL , particularly using loop-mediated isothermal amplification [4] or more advanced portable devices such as QuantuMDx/Q-POC [5]. However, these techniques require disposable reagents, technicians, more than 30 min to get the test results, and imply aseptic conditions (hard to maintain in endemic regions). Therefore, there is a huge need for fast, reagent-free, and low-cost malaria diagnostic systems, without requiring special training and independent of the genetic variability of the parasite, and overall the final ideal device should comprise all these concerns.

The malaria parasite lifecycle passes from the mosquito vector to the human host by entering the liver cells where it matures, to further being released into the blood stream, invading the red blood cells (RBCs). At this stage, the infected RBCs (iRBCs) suffer biochemical, optical, and morphological changes [6,7], making these cells more rigid and thicker, resulting in a decrease of the cells velocity (when the cells are infected with *Plasmodium falciparum* parasite) [8]. Hemodynamic studies help to obtain information regarding the evolution of the disease. Particularly, the RBCs' deformability and the RBCs' velocity when crossing a geometric constriction can work as relevant markers for malaria diagnostics applications, since they are directly related to the changes that the parasite causes throughout the evolution of the disease [9]. The literature reports different methods for assessment of the RBCs' deformability, including filtration [10], ektacytometry [11,12], optical tweezers [13,14], micropipette aspiration [15], and microfluidic geometrical constrictions [16–22]. Some numerical and experimental studies in the literature already report the relation between RBCs' deformability and hemodynamics [23,24], or between deformability and the individual RBCs' velocities in specific geometrical conditions [9,25–28]. This work will be focused on a microfluidic system to measure the RBCs' deformability and velocity, as well as to establish a relation between these properties when the cells cross geometric microconstrictions, with the expectation to, in the future, compare this correlation with the real malaria effects in RBCs. The microfluidic systems are a potential alternative to the current diagnostic methods, since they are able to mimic the hemodynamic phenomena that happens in blood vessels and have advantages in terms of sample preparation and analysis (low volume of samples, easy handling, low-cost, and fast processing), eliminating the need for specialized personnel [22]. Additionally, microfluidic devices enhance the possibility of creating a fully automated and portable diagnostic device for malaria, when assembled in a microfluidic platform that includes microfluidic handling, control and readout electronics, and data acquisition.

In order to develop and evaluate those microfluidic methods for the deformability and velocity assessment, it is essential to synthetically impair the RBCs for mimicking malaria behavior, for testing the method's efficiency and reproducibility, without the constant need for parasites or infected samples, improving laboratorial safety, when testing, and decreasing the costs. For that purpose, glutaraldehyde, diamide, and glucose will be used for increasing the rigidity of the RBCs and, their effect in narrow constrictions will be compared [29–32]. When exposed to these chemicals, the RBCs will be rigidified and their dynamic behavior in narrow constrictions, relative to deformability and velocity, will be compared to healthy RBCs. The evaluation of the RBCs' velocity and deformability will be performed in a set of microchannels with abrupt constrictions, followed by abrupt expansions [25]. This approach takes advantage of the potential of these sudden geometrical contractions to deform the cells due to shear and extensional flows. The cells' behavior will be captured by a setup comprising a high-speed camera and a microscope, and the obtained images will be processed in two software tools (ImageJ and PIVLab) for determining both the RBCs' deformability and the RBCs' velocities, as well as determining the relationship between those properties.

2. Materials and Methods

This section presents the materials and samples used to perform the experimental assays, as well as the description of the microchannel fabrication method, experimental setup, and image processing techniques. In brief, RBC samples with low concentration (low hematocrit) will be exposed to glutaraldehyde, diamide, or glucose and will be tested in polydimethylsiloxane (PDMS) microchannels that comprise 8 μm widths abrupt contractions. The ability of the RBCs to flow through the microchannels contractions will be assessed.

2.1. Microchannels Fabrication

A polydimethylsiloxane (PDMS) microfluidic device was microfabricated by soft lithography techniques, using SU-8 molds (SU-8 purchased from Microchem Corporation, Westborough, MA, USA) [33,34]. PDMS (Sylgard 184 Silicone Elastomer kit obtained from Dow Corning, Midland, MI, USA) was chosen due to its transparency that is required for microscope visualization, easy fabrication, and low-cost for prototypes. The PDMS microchannels have a 25 μm height in order to reduce the flow volume and the number of RBCs within the microchannels, also making it easier to observe the RBCs. Each microchannel is composed by a linear transition zone followed by an abrupt contraction (at a 90° angle) with 8 μm width and 780 μm length (seen in Figure 1), designed to force the RBCs to deform and gain velocity when crossing it. The width of the contractions mimics capillary vessels with the same average dimensions of the RBCs (around 8 μm).

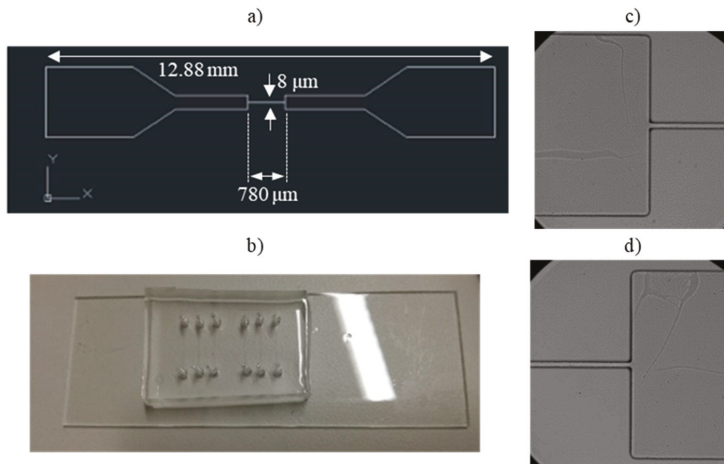


Figure 1. (a) 2D masks for microchannel fabrication. The narrow contractions in the central region of the microchannels have 8 μm width; (b) polydimethylsiloxane (PDMS) microchannels with a 12.88 mm total length; (c) Detail of the entrance of the 8 μm width contraction of the PDMS microchannel; (d) Detail of the outlet of the 8 μm width contraction of the PDMS microchannel. Magnification: 40 \times .

2.2. Samples

For the *in vitro* assays, samples containing human RBCs (hematocrit = 0.5%) in Dextran40 (D \times 40) were used. Human RBCs have a biconcave shape and typical diameters in the 6–8 μm range, being highly deformable.

The healthy human whole blood samples were taken from a female volunteer and provided by Instituto Politécnico de Bragança (Bragança, Portugal). All procedures for the blood collection, transport, and *in vitro* experiments were carried out in compliance with the EU directives 2004/23/CE, 2006/17/CE, and 2006/86/CE and approved by the Unidade Local de Saúde do Nordeste (Bragança,

Portugal). In order to evaluate the RBCs' deformability and velocity in the microchannels, the RBCs were separated from the other blood constituents through centrifugation (15 min, 2000 rpm, at room temperature). After that, RBCs were re-suspended and washed twice in a physiological solution (PSS) (from B. Braun Medical, Melsungen, Germany) with a NaCl concentration of 0.9%. The Dx40 solution, where the RBCs were suspended, was used as a plasma-volume expander to prevent RBC sedimentation and maintain the ideal osmotic physiological conditions for the RBCs. This solution was synthetically produced by mixing 68 μL of CaCl_2 with 201 μL of KC, 7.35 mL of NaCl, and 5 g of Dx40 (for 1 M solution) (all reagents purchased from Sigma-Aldrich, St. Louis, MO, USA). The 0.5% hematocrit, representing a 0.5% volume of RBCs in 5 mL of Dx40, was considered in order to assure that the RBCs are isolated when crossing the microchannel contraction. Although the 0.5% hematocrit is significantly lower than the physiological one, it was decided to study diluted samples, to improve the visualizations and measurements of each individual RBC and, as a result, to avoid effects such as interactions and aggregation of RBCs. Preliminary tests performed with hematocrit values ranging from 0.5% up to 2% have shown that as the concentration of RBCs was increased, it was difficult to individually follow the RBCs and, consequently, to measure the RBCs' velocity and deformation index. Hence, the current study was performed with a hematocrit of 0.5%.

The RBC samples were then modified with glucose (COPAN Diagnostics Inc., Murrieta, CA, USA), glutaraldehyde (Sigma-Aldrich Corporation, St. Louis, MO, USA), and diamide (Sigma-Aldrich Corporation, St. Louis, MO, USA) solutions, in order to rigidify the cells at different levels. These chemicals were selected since they are commonly used to perform deformability studies, are accessible, and have simple preparation protocols, as well as they allow one to rigidify the cells at different levels, according to the added concentration. To modify the RBCs with glucose, four different concentrations of glucose were considered: 2%, 5%, 10%, and 20% (*v/v*). First, glucose (powder) was diluted in a phosphate buffered saline solution (PBS: pH 7.4). Then, the RBCs (already separated from the other blood constituents and suspended in Dx40) were incubated for 20 min, at room temperature, at each of the referred glucose concentrations. The cells were then washed in PSS to remove the excess of glucose from the samples and re-suspended in Dx40. To modify the cells with glutaraldehyde, at 0.00625%, 0.0125%, 0.025%, and 0.08% glutaraldehyde concentrations (*v/v*), the RBCs (already separated from the other blood constituents and suspended in Dx40) were incubated for 10 min at each of the referred concentrations, washed in PSS, re-suspended in Dx40, and used right away. The RBCs were also modified with diamide, at 0.00625%, 0.0125%, 0.025%, 0.08%, 0.32%, and 1% diamide concentrations (*v/v*), using the same protocol: Incubation for 10 min at each of the referred concentrations, washing in PSS, and re-suspension in Dx40.

2.3. Experimental Setup

The cells' deformability and velocity assays were performed with an experimental setup comprising the microfluidic device placed on the stage of an inverted microscope (IX71; Olympus Corporation, Tokyo, Japan). A flow rate of 5 $\mu\text{L}/\text{min}$ was controlled using a syringe pump system (KD Scientific Inc., Holliston, MA, USA). For selecting the ideal flow rate, preliminarily studies were performed for four different flow rates (0.1, 1, 3, and 5 $\mu\text{L}/\text{min}$) and no significant differences were observed in the cells' deformability. Additionally, it was observed that the syringe pump system presented more stability for the highest tested flow rate, i.e., the 5 $\mu\text{L}/\text{min}$. The images of the RBCs were captured using a high-speed camera (Fastcam SA3, Photron, Motion Engineering Company, Westfield, IN, USA) at a 2000 frames/s rate and exported to a computer to be analyzed. Each assay was repeated 3 times.

2.4. Image Processing and Analysis Techniques

The images exported from the high-speed camera to the computer were analyzed using two software tools: ImageJ [35] and PIVLab [36,37]. For each assay, a sequence of 10,000 frames was considered. ImageJ was used to perform the pre-treatment of the acquired frames, in order to remove

the noise and image artifacts, as well as convert them into binary images. Initially, the image sequence was imported and the crop function was executed to define the region of interest (ROI) as a rectangle with $308 \mu\text{m} \times 332 \mu\text{m}$ dimension (Figure 2a). Then, by using the Z-Project function, the selected frames were stacked to determine an average of the frames. This averaged frame was subtracted from all the frames under analysis, eliminating all static objects, which resulted in frames comprising only the visible RBCs, without any additional information. Finally, by using a threshold function, the images were converted into binary images. The ImageJ software was also used to measure the cells size in order to calculate the RBCs' deformation index (DI). Using the ROI Manager and the Measure functions, it was possible to follow both the healthy and the impaired RBCs (example in Figure 2b) and calculate their DI along the microchannel, using the expression: $DI = (X - Y)/(X + Y)$, where X and Y represent the largest (X) and the smallest (Y) axis of the ellipse correspondent to the RBC under analysis. Typically, the RBCs' DI varies between 0 and 0.8, where 0 represents non-deformed cells and 0.8 represents cells at maximum elongation. For each assay, a group of RBCs was followed at the entrance and at the outlet of the contraction to measure their DI and determine an averaged value. Figure 2c presents the area at the entrance and at the outlet of the microchannel contraction (the areas inside the dashed lines in Figure 2c), where the deformability of the RBCs is measured. These areas were chosen after performing preliminary observations of the RBC flows. For the entrance of the contraction, a $121 \mu\text{m} \times 237 \mu\text{m}$ region of interest was selected, since it is in this area that the RBCs experience the highest extensional flow and consequently start to deform to enter the narrowing. For the outlet, in the region immediately after exiting the contraction, the RBCs are at maximum deformation, and outside that region, the cells start to recover their original shape. Then, for assuring a standard area at the outlet for all assays, an $86 \mu\text{m} \times 142 \mu\text{m}$ region of interest was selected. It should be noted that the evaluation area at the outlet of the contraction is significantly smaller than at the entrance. This difference is explained by the authors' intention, in future devices and prototypes, of integrating micro-sensors in the outlet of the contraction (occupying the smallest area possible) and, therefore, in this work it was expected to obtain relevant data from a small area of evaluation in the outlet.

In order to determine the average of the velocity values of the RBCs at the entrance and at the outlet of each contraction, the sequence of frames was analyzed using the PIVLab image analysis toolbox, integrated in MATLAB. First, the pre-treated images were imported into the software and calibrated (relatively to their dimensions and time between frames), and a ROI mask was applied to remove the areas where there are no RBCs. Following, the motion of the particles between the frames was analyzed and the instantaneous velocities were calculated by the variation of the distance traveled by the RBCs between each time step. Then, the average velocity vectors (U_x and U_y) were calculated in the x and y directions and the velocity field of each sample (U_{xy}) was determined based on the equation: $|U_{xy}| = \text{sqrt}(U_x^2 + U_y^2)$. Finally, a filter was applied to smooth the images and remove the high frequencies, which could indicate spikes of velocity without physical significance. Figure 2d presents an example of the velocity field distribution at the entrance of the contraction. It is possible to observe that the velocity of the RBCs is significantly higher in the zone of the narrowing entrance, reasoning that the abrupt transition causes an increase of the velocity of the RBCs. Note that, due to limitations of the available equipment, it was not possible to acquire frames with RBCs moving at high velocity in the interior of the microchannel contraction. As a result, almost no cells were registered in that region, explaining the 0 velocity in the interior of the contraction in the PIVLab image (Figure 2d), this way the results section will approach and compare the DI and velocity of the RBCs at the entrance and outlet of the contractions, neglecting the study of cells inside the contraction regions. Note that both RBC deformability and velocity are measured in the same area (as defined in Figure 2c, left and right) in order to establish a relation between the RBCs' deformability and their velocity. After obtaining the velocity distribution immediately before the entrance and after the outlet of the contraction, a criterion for determining the RBCs' velocity was defined (as presented in the Results Section 3): From the region of interest (Figure 2c, left and right), where the velocities are higher,

the 100 pixels with highest velocity (obtained in PIVLab) were selected and those velocities were averaged, neglecting the surrounding areas with lowest velocities.

Additional details on the ImageJ and PIVLab procedures for the determination of RBC deformability and velocity can be found in [25].

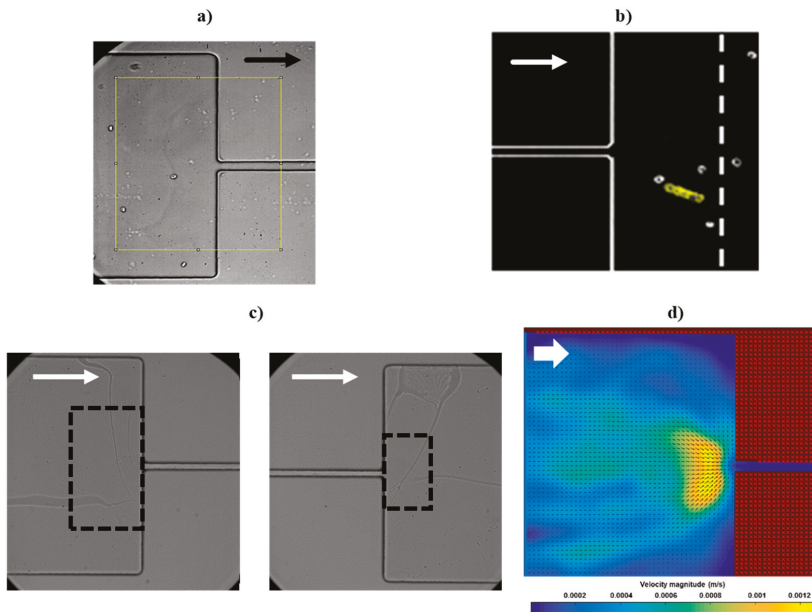


Figure 2. (a) Example of a cut-off of a transfer zone ($308 \mu\text{m} \times 332 \mu\text{m}$) in the entrance of the microchannel contraction, using the crop function of ImageJ; (b) Example of a tracked red blood cell (RBC) at the outlet of the microchannel contraction, using ImageJ, where the dashed line represents a region where the RBCs expand after the outlet (relaxation area); (c) Definition of the areas (inside the dashed lines) for measuring the RBCs' deformability and velocity at the entrance (left— $121 \mu\text{m} \times 237 \mu\text{m}$ region) and at the outlet (right— $86 \mu\text{m} \times 142 \mu\text{m}$ region) of the microchannel contraction (Magnification: $40\times$); (d) Example of the velocity distribution, obtained with PIVLab, of healthy RBCs (non-modified) at the entrance of the microchannel contraction (the arrows indicate the flow direction in each frame). Note that, due to limitations of the available equipment (frame rate acquisition), it was not possible to acquire frames with RBCs moving at high velocity in the interior of the microchannel contraction and, as a result, no cells were registered in that region, explaining the 0 velocity in the image.

3. Results and Discussion

This section presents the deformability and velocity results (obtained as in Section 2.4) of the comparison between healthy and chemically modified RBCs with glucose, glutaraldehyde, and diamide. All the presented results are an average of three assays. For each assay, a sequence of 10,000 frames was considered and around 10 RBCs were followed to measure their DI. Figure 3 shows examples of RBCs from different assays at the entrance and at the outlet of the contraction in the PDMS microchannel, for different percentages of glucose, considering a $5 \mu\text{L}/\text{min}$ flow rate, and for a healthy RBC sample (for control—0% glucose). From Figure 3a, it is possible to detect a difference between RBC deformability as the glucose percentage increases, i.e., the RBCs change from a deformed/stretched shape to a non-deformed shape, as the cells have more difficulties to deform and tend to keep their original shape.

Glucose %	Entrance of the contraction			Outlet of the contraction		
0 (Healthy)						
2						
5						
10						
20						

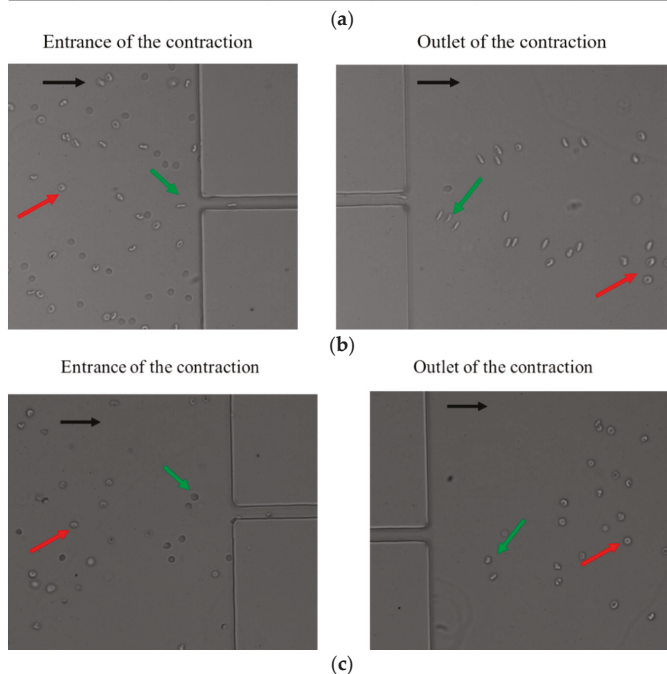


Figure 3. (a) Examples of healthy RBCs and RBCs modified with different glucose percentages at the entrance and at the outlet of the microchannel contraction, extracted from three assays; (b) Healthy RBCs (red arrow, left) deforming at the entrance of the contraction (green arrow, left), leaving the contraction still deformed (green arrow, right), and recovering their original shape following the outlet on an expansion area (red arrow, right); (c) 10% glucose-modified RBCs (red arrow, left) with almost no deformation at the entrance of the contraction (green arrow, left) and leaving the contraction (green arrow, right), recovering their original shape on an expansion area (red arrow, right). The black arrows indicate the flow direction.

These results suggest that the glucose concentration affects the RBCs’ deformability, in agreement with several past studies regarding the influence of glucose over RBC deformability [31,32]. The increase of glucose (hyperglycemia) in RBCs causes damage in the RBCs’ membranes and increases the blood viscosity, also increasing the cells’ aggregation, which leads to a significant decrease on the RBCs’ DI. When the RBCs were modified with glutaraldehyde or diamide, the results were similar to the ones observed for glucose (shown in Figure 3), and, therefore, only the glucose images are presented. Following the outlet of the microchannel contraction, the RBCs start to recover their shape, again decreasing their deformation index, as shown in Figure 3b,c, for an assay with healthy RBCs and one assay with 10% glucose-modified RBCs.

Figure 4 presents the DI for healthy and modified RBCs (with glucose, glutaraldehyde, and diamide), at the entrance and at the outlet of the microchannel 8 μm contraction, as well as at the relaxation area (see Figure 2b), for the 5 μL/min flow rate.

The results show that, as the percentage of glucose, glutaraldehyde, or diamide increases, the cells tend to become more rigid, decreasing their DI [29]. While the healthy cells deformed at the entrance of the contraction to pass throughout the contraction and then recovered their initial shape after reaching the microchannel expansion area, the modified RBCs did not deform and some aggregation of the cells was observed, increasing the difficulty to cross the contraction. At the outlet of the contraction, where the deformability was measured, the RBCs tend to start to recover their original shape, which is verified in Figure 4: The RBCs at the outlet have lower DI than at the entrance of the contraction. As the rigidity of the cells increases, the difference between the DI at entrance and at the outlet of the contraction decreases. Since the evaluation regions at entrance and at the outlet have a different total area (as defined in Figure 2c), it may also help to explain the hysteresis in the results between entrance and outlet (the entrance evaluation area is larger than the outlet evaluation area).

Table 1 presents the differences between the averaged RBC deformability at the entrance of the contraction and at the relaxation area, for all the tested conditions. This allows us to observe the cells’ maximum deformability, passing from their deformed shape entering the contraction, until their recovered shape after relaxation. The results show that, as the rigidity of the cells increases, the difference in the deformability between the entrance and the relaxation area (ΔDI) decreases, and this behavior is similar for the three chemicals tested: Glucose, glutaraldehyde, and diamide.

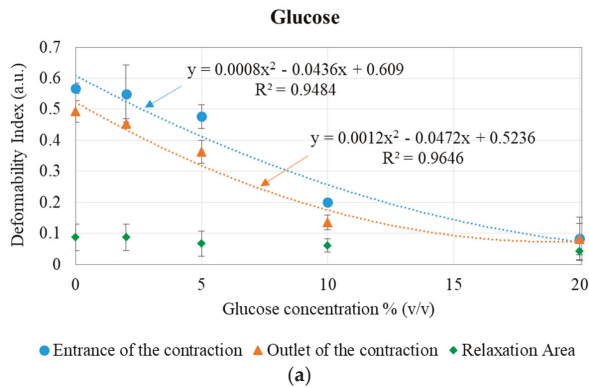


Figure 4. Cont.

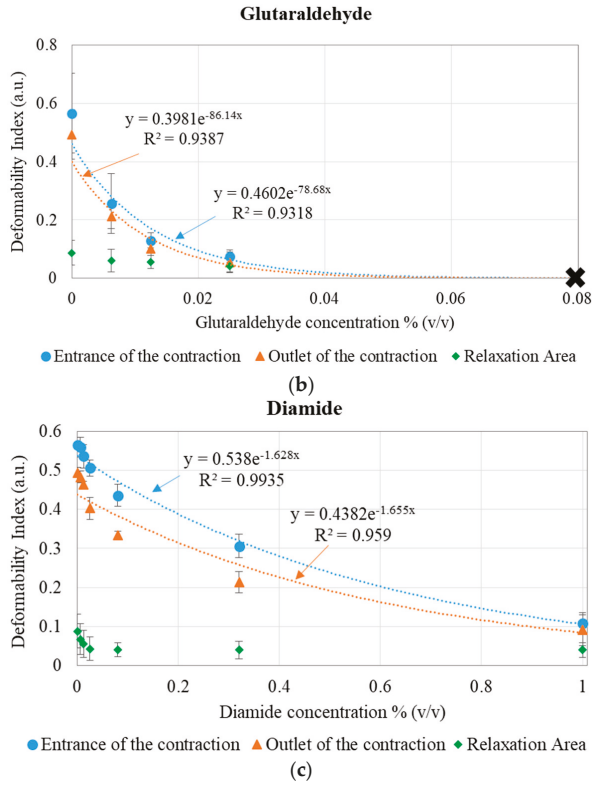


Figure 4. Deformation index (DI) and error bars for healthy and (a) glucose-, (b) glutaraldehyde-, and (c) diamide-modified RBCs, at the entrance (blue series), at the outlet (orange series) and at the relaxation area (green series) of the microchannel contraction and trend lines. In (b), the X represents the clogging of the microchannel, with no deformability or velocity data. Each point of the plots is the average of 30 RBCs (three assays for each condition and 10 RBCs followed in each assay).

Table 1. Difference of the deformation index (Δ DI) between red blood cell (RBC) deformability at the entrance of the contraction (Figure 2c, left) and at the relaxation area (Figure 2b) for all the tested conditions, obtained from the data presented in Figure 4.

Sample	Concentration (%)	Δ DI
Healthy RBCs	0	0.479
	2	0.463
	5	0.410
	10	0.139
	20	0.041
RBCs + Glutaraldehyde	0.00625	0.196
	0.0125	0.074
	0.025	0.034
	0.08	X
RBCs + Diamide	0.00625	0.493
	0.0125	0.482
	0.025	0.464
	0.08	0.396
	0.32	0.267
	1	0.068

It was also observed that, for 0.08% (*v/v*) glutaraldehyde-modified RBCs, the rigidified cells clogged the entrance of the contraction and no deformability or velocity data could be extracted (this is represented by X in Figure 4b). Therefore, for a high concentration of glutaraldehyde, it was unable to measure the transiting velocity of the cells. Figure 5 presents an example of clogging at the entrance of the contraction, when the RBCs were modified with a 0.08% (*v/v*) concentration of glutaraldehyde.

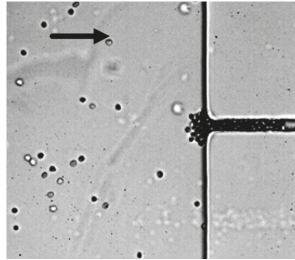


Figure 5. Detail of clogging at the entrance of the 8 μm contraction when the RBCs were modified with a 0.08% (*v/v*) concentration of glutaraldehyde.

Elevated blood glucose in the RBCs alters RBC membrane proteins through glycosylation and oxidation. Glutaraldehyde penetrates into cell membranes and non-specifically cross-links the cytosol, the cytoskeletal, and the transmembrane proteins, acting on all components of the cell and increasing the effective viscosity of the cytoplasm and lipid membrane. Diamide is a spectrin-specific cross-linker, oxidizing thiol groups while forming disulfide bonds within the structural region [30]. The obtained results indicate that viscous effects in the cytoplasm and/or lipid membrane are a dominant factor when dictating dynamic responses of RBCs in pressure-driven flows, explaining the higher effect of the glutaraldehyde in damaging the RBCs and the microchannel clogging, when compared to diamide and glucose [30].

Figure 6 presents the average cell velocity for healthy and modified RBCs (with glucose, glutaraldehyde, and diamide), at the entrance and at the outlet of the microchannel 8 μm contraction, for the 5 $\mu\text{L}/\text{min}$ flow rate.

Overall, the results agree with those of deformability. When the average velocity at the high velocity regions was evaluated, it was found that the impaired RBCs (by adding glucose, glutaraldehyde, or diamide) presented lower velocities than healthy RBCs, indicating that the increase of the RBCs' rigidity causes the non-deformed cells to follow streamlines that on average have lower velocity, while the stretched and healthy RBCs follow streamlines that on average have higher velocity. Supplementary material videos show how the cells gain velocity when entering the contraction, explaining the higher velocity immediately at the outlet of the contraction (when compared to the velocity at the entrance), before starting to relax and recover their original shape. Similarly to the deformability results, for 0.08% (*v/v*) glutaraldehyde-modified RBCs, the rigidified cells clogged at the entrance of the contraction and, as a result, no velocity data could be extracted (this is represented by X in Figure 6b).

Additionally, it would be interesting to quantitatively study the relation between deformation index and velocity inside the microchannel contraction, besides the data presented at entrance and outlet (Figures 4 and 6). However, due to technical limitations of the high speed acquisition system, it was not possible to acquire an enough number of RBCs with high quality contrast to perform the measurements of RBC deformability and velocity with the software tools referred in Section 2. Despite that limitation, some RBCs could still be observed within the contraction. Examples of RBCs (healthy, with 0.025% diamide, and with 10% glucose) flowing within the contraction are shown in Figure 7.

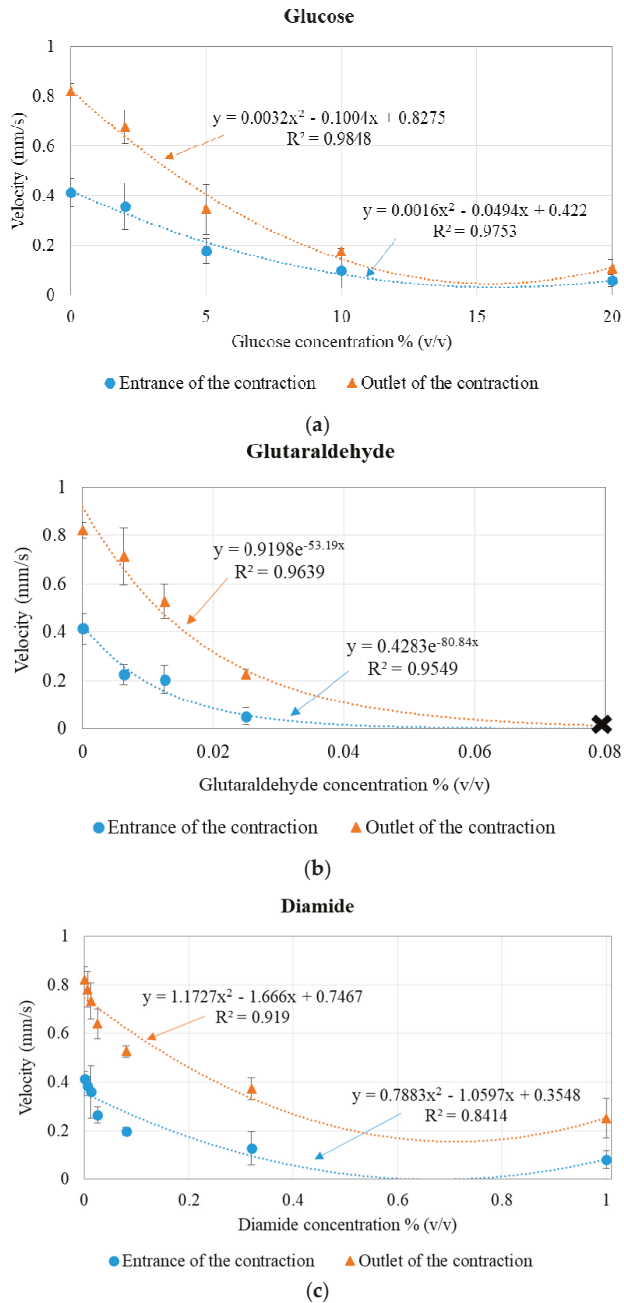


Figure 6. Velocity (mm/s) and error bars for healthy and (a) glucose-, (b) glutaraldehyde-, and (c) diamide-modified RBCs, at the entrance (blue series) and at the outlet (orange series) of the microchannel contraction and trend lines. In (b), the X represents the clogging of the microchannel, with no deformability or velocity data.

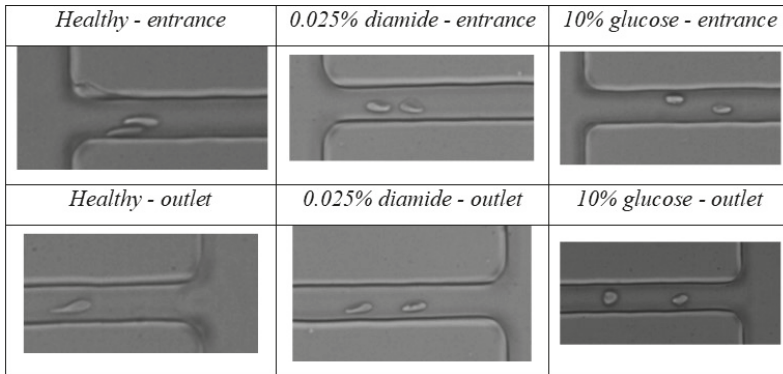


Figure 7. Examples of healthy RBCs, RBCs modified with 0.025% diamide, and RBCs modified with 10% glucose inside the 8 μm width microchannel contraction, at different areas (entrance and outlet of the contraction).

A qualitative analysis of the presented results shows that healthy RBCs cross the microchannel contraction in a more deformed shape than the 0.025% diamide and 10% glucose samples, and the 10% glucose samples are less deformable than the 0.025% diamide ones, which corroborates the quantitative results (before the entrance and after the outlet) presented in Figure 6. Supplementary material presents videos of healthy and modified RBCs flowing at the entrance and at the outlet of the contraction, allowing a better observation of the RBCs' behavior at the different regions of the microchannel contraction.

Since one of the main objectives of this work was to establish a relation between the RBCs' deformability and their velocity, Figure 8 presents the velocity vs DI calibration curves for glucose-, glutaraldehyde-, and diamide-modified RBCs at the entrance and at the outlet of the microchannel contraction. This figure purpose is to show the dispersion that occurs between the cells. Therefore, instead of presenting all RBCs averaged together (as in Figures 4 and 6), it is intended to evaluate how each small group of cells fits the deformability vs velocity curve, in order to understand their individualized behavior. Therefore, from the performed assays, the RBCs were gathered in groups of three cells measured under the same conditions and their average was calculated (each blue dot of the plots). Consequently, each plot of Figure 8 gathers data from a high number of RBCs (three RBCs \times number of dots in each plot, leading to a range of RBCs between $3 \times 16 = 48$ in Figure 8d and $3 \times 28 = 84$ in Figure 8e), measured in the areas defined in Figure 2.

Based on the results, it is observed that, overall and as expected, for all synthetically modified RBCs, an increase of cell deformation index leads to an increase of the cells' velocity, both at the entrance and at the outlet of a microchannel contraction. When comparing the velocity with the deformability correlation at entrance and at outlet, it is clear, for all the tested methods, that the results at the outlet present a better fitting to the linear tendency curve than at the entrance (based on the R^2 values). Therefore, in the future, when advancing for a diagnostic tool, the analysis must be performed at the outlet of the contraction (the place to integrate a sensor), where the RBCs' behavior is more reliable. Additionally, our results indicate that diamide is the most interesting approach for mimicking the malaria effects on RBCs with the intention of exploring sensor applications, as the velocity vs DI results show a better fitting to the linear tendency curve ($R^2 = 0.89$) and, consequently, it is easier to control the velocity vs deformability curve. These results are a promising step to help the development of integrated sensors in microfluidic devices that allow the design of an autonomous malaria detection system of high sensitivity, precise, low-cost, portable, and with low energy consumption.

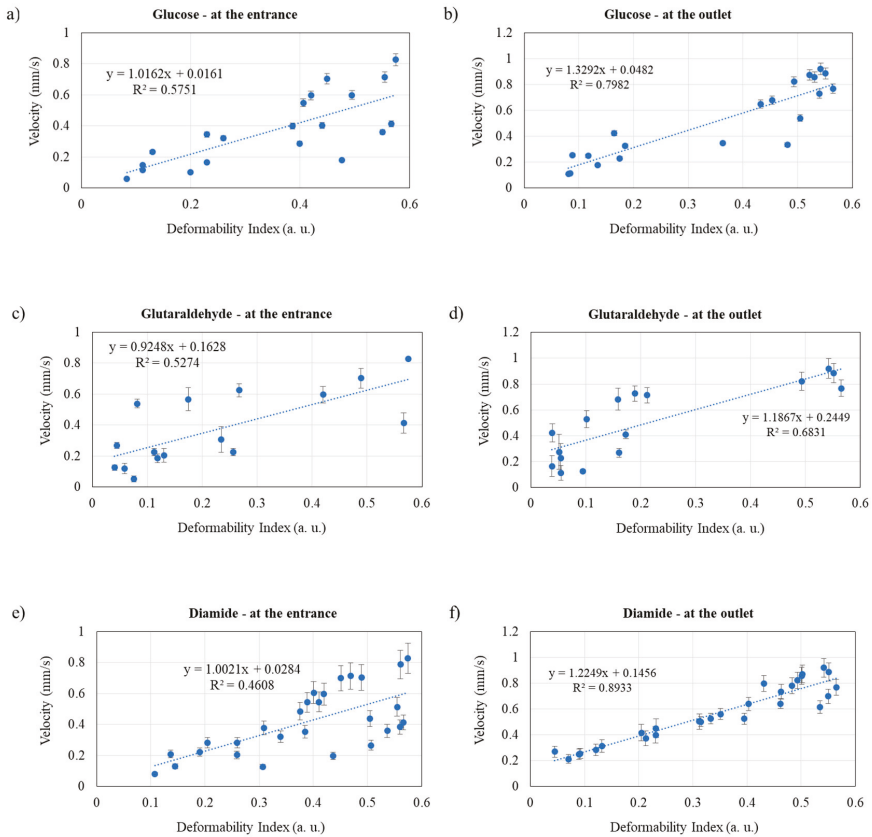


Figure 8. Velocity (mm/s) vs. deformability (a.u.) curve, measured at the entrance and at the outlet of the 8 μ m contraction, for the RBC samples modified with (a) at entrance; glucose, (b) at outlet; glucose (c) at entrance; glutaraldehyde; (d) at outlet; glutaraldehyde, (e) at entrance; diamide, and (f) at outlet; diamide.

4. Future Perspectives

Future works will include an increase in cell quantity in order to define the average property of the entire cell population with higher accuracy, since the physical properties of individual RBCs within the same RBC population can vary significantly [38]. Additionally, since the ultimate goal is to develop a clinical tool, more blood samples from different donors will be assessed to increase the RBCs' variability and to include more independent data. It is also planned to improve our high speed video microsystem, allowing the capture of good enough quality images to quantitatively measure both velocity and deformability of the RBCs flowing across the microchannel contraction. This improvement will allow to develop an improved association between RBC deformability and transiting velocity through the narrow constrictions. Finally, after obtaining an improved correlation with synthetically modified samples, it is intended to test real parasite-affected RBC samples [39] to measure their deformability and velocity, compare disease and artificially impaired RBCs, establish target values, and fully validate the proposed approach. This improved correlation will be used to relate the RBCs' behavior according to the various stages of malaria and to develop integrated sensors in microfluidic devices for RBC velocity measurements.

5. Conclusions

This work has investigated the deformability and the velocity of healthy and chemically modified RBCs, attempting to mimic the effect of malaria in RBCs and to establish a relation between RBCs' velocity and deformability. The glucose, glutaraldehyde, and diamide effect in the RBCs was compared using PDMS microchannels with 8 μm narrow contractions that forced the RBCs to undergo deformation when they passed through them. It was concluded that, by adding glucose, glutaraldehyde, or diamide, the RBC membrane tends to become stiffer, decreasing the cell's deformability and, consequently, decreasing the cell shape recovery capacity. Additionally, when the RBCs' rigidity increased, the RBCs' velocity decreased.

When the relation between deformability and velocity was evaluated, it was concluded that, for all synthetically modified RBCs, an increase of the cells' deformation index led to an increase of the cells' velocity. It was also verified that diamide was the most interesting approach to impair the cells and mimic the malaria effects on RBCs, as the velocity vs deformation index results have showed the best fitting to the linear tendency curve and, consequently, it would be easier to control the deformability and velocity of the cells based on this method.

Despite still being a challenge, this work will be a valuable contribution to help establishing the development of simple, reagent-free, inexpensive, and accurate new malaria diagnostic systems towards point-of-care devices.

Supplementary Materials: The following are available online at <http://www.mdpi.com/2072-666X/9/8/384/s1>, Video S1: 10% glucose RBCs at the entrance of the contraction, Video S2: 10% glucose RBCs at the outlet of the contraction, Video S3: Healthy RBCs at the entrance of the contraction, Video S4: Healthy RBCs at the outlet of the contraction.

Author Contributions: Conceptualization, R.L. and S.O.C.; Methodology, R.L. and S.O.C.; Validation, R.L., J.M.M., C.S.V.F. and G.M.; Investigation, L.V.B. and V.F.; Data Analysis, L.V.B. and V.F.; Writing-Original Draft Preparation, S.O.C.; Writing-Review & Editing, S.O.C., R.L., J.M.M., C.S.V.F. and G.M.; Supervision, C.S.V.F. and S.O.C.

Funding: This work results of the project NORTE-01-0145-FEDER-028178, MalariaChip, supported by Programa Operacional Regional do Norte—Norte Portugal Regional Operational Programme (NORTE 2020), under the PORTUGAL 2020 Partnership Agreement, through the European Regional Development Fund (ERDF) and by Fundação para a Ciência e Tecnologia (FCT), IP. Work also supported by Fundação para a Ciência e Tecnologia (FCT) with the reference project UID/EEA/04436/2013, by FEDER funds through the COMPETE 2020—Programa Operacional Competitividade e Internacionalização (POCI) with the reference project POCI-01-0145-FEDER-006941; and by project POCI-01-0145-FEDER-016861 (with associated reference PTDC/QEQ-FTT/4287/2014). S.O. Catarino thanks the FCT for the SFRH/BPD/108889/2015 grant, supported by national funds from Ministérios da Ciência, Tecnologia e Ensino Superior and by FSE through the POCH—Programa Operacional Capital Humano.

Acknowledgments: The authors would like to thank Diana Pinho from the IP Bragança for providing the blood samples and for the support in the experimental tests.

Conflicts of Interest: The authors declare no conflict of interest.

References

1. WHO. *Malaria World Report*; World Health Organization: Geneva, Switzerland, 2016.
2. WHO. *Malaria Rapid Diagnostic Test Performance: Results of WHO Product Testing of Malaria RDTs*; World Health Organization: Geneva, Switzerland, 2017.
3. Wongsrichanalai, C.; Barcus, M.J.; Muth, S.; Sutamihardja, A.; Wernsdorfer, W.H. A review of malaria diagnostic tools: Microscopy and rapid diagnostic test (RDT). *Am. J. Trop. Med. Hyg.* **2007**, *77*, 119–127. [PubMed]
4. Lucchi, N.; Ljolje, D.; Silva-Flannery, L.; Udhayakumar, V. Use of malachite green-loop mediated isothermal amplification for detection of *Plasmodium* spp. parasites. *PLoS ONE* **2016**, *11*, e0151437. [CrossRef] [PubMed]
5. QuantuMDx. Available online: <http://quantumdx.com/applications/malaria> (accessed on 1 March 2018).
6. Saha, R.; Karmakar, S.; Roy, M. Computational investigation on the photoacoustics of malaria infected red blood cells. *PLoS ONE* **2012**, *7*, e51774. [CrossRef] [PubMed]

7. Diez-Silva, M.; Dao, M.; Han, J.; Lim, C.T.; Suresh, S. Shape and biomechanical characteristics of human red blood cells in health and disease. *MRS Bull.* **2010**, *35*, 382–388. [[CrossRef](#)] [[PubMed](#)]
8. Handayani, S.; Chiu, D.T.; Tjitra, E.; Kuo, J.S.; Lampah, D.; Kenangalem, E.; Russell, B. High deformability of *Plasmodium vivax*-infected red blood cells under microfluidic conditions. *J. Infectious Dis.* **2009**, *199*, 445–450. [[CrossRef](#)] [[PubMed](#)]
9. Shelby, J.P.; White, J.; Ganesan, K.; Rathod, P.K.; Chiu, D.T. A microfluidic model for single-cell capillary obstruction by *Plasmodium falciparum*-infected erythrocytes. *Proc. Natl. Acad. Sci. USA* **2003**, *100*, 14618–14622. [[CrossRef](#)] [[PubMed](#)]
10. How, T.V.; Black, R.; Hughes, P. Hemodynamics of vascular prostheses. In *Advances in Hemodynamics and Hemorheology*; How, T.V., Ed.; Elsevier: Amsterdam, The Netherlands, 1996; Volume 1, pp. 373–423.
11. Tomaiuolo, G. Biomechanical properties of red blood cells in health and disease towards microfluidics. *Biomicrofluidics* **2014**, *8*, 051501. [[CrossRef](#)] [[PubMed](#)]
12. Johnson, R.M. Ektacytometry of red blood cells. *Methods Enzymol.* **1989**, *173*, 35–54. [[PubMed](#)]
13. Lim, C.; Dao, M.; Suresh, S.; Sow, C.; Chew, K. Large deformation of living cells using laser traps. *Acta Mater.* **2004**, *52*, 1837–1845. [[CrossRef](#)]
14. Grier, D.G. A revolution in optical manipulation. *Nature* **2003**, *424*, 810–816. [[CrossRef](#)] [[PubMed](#)]
15. Hochmuth, R. Micropipette aspiration of living cells. *J. Biomech.* **2000**, *33*, 15–22. [[CrossRef](#)]
16. Rodrigues, R.O.; Pinho, D.; Faustino, V.; Lima, R. A simple microfluidic device for the deformability assessment of blood cells in a continuous flow. *Biomed. Microdevices* **2015**, *17*, 108. [[CrossRef](#)] [[PubMed](#)]
17. Zhao, R.; Antaki, J.F.; Naik, T.; Bachman, T.N.; Kameneva, M.V.; Wu, Z.J. Microscopic investigation of erythrocyte deformation dynamics. *Biorheology* **2006**, *43*, 747–765. [[PubMed](#)]
18. Yaginuma, T.; Oliveira, M.S.N.; Lima, R.; Ishikawa, T.; Yamaguchi, T. Human red blood cell behavior under homogeneous extensional flow in a hyperbolic shaped microchannel. *Biomicrofluidics* **2013**, *7*, 054110. [[CrossRef](#)] [[PubMed](#)]
19. Faustino, V.; Pinho, D.; Yaginuma, T.; Calhelha, R.C.; Ferreira, I.C.; Lima, R. Extensional flow-based microfluidic device: Deformability assessment of red blood cells in contact with tumor cells. *BioChip J.* **2014**, *8*, 42–47. [[CrossRef](#)]
20. Lee, S.S.; Yim, Y.; Ahn, K.H.; Lee, S.J. Extensional flow-based assessment of red blood cell deformability using hyperbolic converging microchannel. *Biomed. Microdevices* **2009**, *11*, 1021–1027. [[CrossRef](#)] [[PubMed](#)]
21. Bento, D.; Rodrigues, R.O.; Faustino, V.; Pinho, D.; Fernandes, C.S.; Pereira, A.I.; Garcia, V.; Miranda, J.M.; Lima, R. Deformation of red blood cells, air bubbles, and droplets in microfluidic devices: Flow visualizations and measurements. *Micromachines* **2018**, *9*, 151. [[CrossRef](#)]
22. Hou, H.; Hou, H.W.; Bhagat, A.A.S.; Chong, A.G.L.; Mao, P.; Tan, K.S.W.; Han, J.; Lim, C.T. Deformability based cell margination—A simple microfluidic design for malaria-infected erythrocyte separation. *Lab Chip* **2010**, *10*, 2605–2613. [[CrossRef](#)] [[PubMed](#)]
23. Passos, A.; Sherwood, J.; Agrawal, R.; Pavesio, C.; Balabani, S. The effect of RBC stiffness on microhaemodynamics. In Proceedings of the 5th Micro and Nano Flows Conference, Milan, Italy, 11–14 September 2016.
24. Chien, S. Red blood cell deformability and its relevance to blood flow. *Ann. Rev. Physiol.* **1987**, *49*, 177–192. [[CrossRef](#)] [[PubMed](#)]
25. Vilas Boas, L.; Lima, R.; Minas, G.; Fernandes, C.S.; Catarino, S.O. Imaging of healthy and malaria-mimicked red blood cells in polydimethylsiloxane microchannels for determination of cells deformability and flow velocity. In *VipIMAGE—ECCOMAS 2017. Lecture Notes in Comp. Vision and Biomechanics*; Tavares, J., Natal Jorge, R., Eds.; Springer: New York, NY, USA, 2018; pp. 915–922.
26. Kaneko, M.; Ishida, T.; Tsai, C.D.; Ito, H.; Chimura, M.; Taniguchi, T.; Ohtani, T.; Sakata, Y. On-Chip RBC Deformability Checker Embedded with Vision Analyzer. In Proceedings of the 2015 IEEE International Conference on Mechatronics and Automation, Takamatsu, Japan, 6–9 August 2017; pp. 2005–2010.
27. Tsai, C.D.; Tanaka, J.; Kaneko, M.; Horade, M.; Ito, H.; Taniguchi, T.; Ohtani, T.; Sakata, Y. An On-Chip RBC Deformability Checker Significantly Improves Velocity-Deformation Correlation. *Micromachines* **2016**, *7*, 176. [[CrossRef](#)]
28. Jeong, J.H.; Sugii, Y.; Minamiyama, M.; Okamoto, K. Measurement of RBC deformation and velocity in capillaries in vivo. *Microvasc. Res.* **2006**, *71*, 212–217. [[CrossRef](#)] [[PubMed](#)]

29. Rodrigues, R.O.; Faustino, V.; Pinto, E.; Pinho, D.; Lima, R. Red Blood Cells deformability index assessment in a hyperbolic microchannel: The diamide and glutaraldehyde effect. *Webmed Cent. Biomed. Eng.* **2013**, *4*, WMC004375.
30. Forsyth, A.M.; Wan, J.; Ristenpart, W.D.; Stone, H.A. The dynamic behavior of chemically “stiffened” red blood cells in microchannel flows. *Microvasc. Res.* **2010**, *80*, 37–43. [[CrossRef](#)] [[PubMed](#)]
31. Babu, N.; Singh, M. Influence of hyperglycemia on aggregation, deformability and shape parameters of erythrocytes. *Clin. Hemorheol. Microcirc.* **2004**, *31*, 273–280. [[PubMed](#)]
32. Shin, S.; Ku, Y.H.; Suh, J.S.; Singh, M. Rheological characteristics of erythrocytes incubated in glucose media. *Clin. Hemorheol. Microcirc.* **2008**, *38*, 153–161. [[PubMed](#)]
33. Pinto, V.C.; Sousa, P.J.; Cardoso, V.F.; Minas, G. Optimized SU-8 Processing for Low-Cost Microstructures Fabrication without Cleanroom Facilities. *Micromachines* **2014**, *5*, 738–755. [[CrossRef](#)]
34. Faustino, V.; Catarino, S.O.; Lima, R.; Minas, G. Biomedical microfluidic devices by using low-cost fabrication techniques: A review. *J. Biomech.* **2016**, *49*, 2280–2292. [[CrossRef](#)] [[PubMed](#)]
35. Abramoff, M.; Magalhães, P.; Ram, S. Image processing with ImageJ. *Biophotonics Int.* **2004**, *11*, 36–42.
36. Thielicke, W.; Stamhuis, E.J. PIVlab—Towards User-friendly, Affordable and Accurate Digital Particle Image Velocimetry in MATLAB. *J. Open Res. Softw.* **2014**, *2*, e30. [[CrossRef](#)]
37. Thielicke, W.; Stamhuis, E.J. PIVlab—Time-Resolved Digital Particle Image Velocimetry Tool for MATLAB. Available online: https://figshare.com/articles/PIVlab_version_1_35/1092508 (accessed on July 2017).
38. Picot, J.; Ndour, P.A.; Lefevre, S.D.; El Nemer, W.; Tawfik, H.; Galimand, J.; Costa, L.D.; Ribeil, J.-A.; Montalembert, M.d.; Brousse, V.; et al. A biomimetic microfluidic chip to study the circulation and mechanical retention of red blood cells in the spleen. *Am. J. Hematol.* **2015**, *90*, 339–345. [[CrossRef](#)] [[PubMed](#)]
39. Barber, B.E.; Russell, B.; Grigg, M.J.; Zhang, R.; William, T.; Amir, A.; Lau, Y.L.; Chatfield, M.D.; Dondorp, A.M.; Anstey, N.M.; et al. Reduced red blood cell deformability in *Plasmodium knowlesi* malaria. *Blood Adv.* **2018**, *2*, 433–443. [[CrossRef](#)] [[PubMed](#)]



© 2018 by the authors. Licensee MDPI, Basel, Switzerland. This article is an open access article distributed under the terms and conditions of the Creative Commons Attribution (CC BY) license (<http://creativecommons.org/licenses/by/4.0/>).



Article

Multiple and Periodic Measurement of RBC Aggregation and ESR in Parallel Microfluidic Channels under On-Off Blood Flow Control

Yang Jun Kang ^{1,*} and Byung Jun Kim ²

¹ Department of Mechanical Engineering, Chosun University, 309 Pilmun-daero, Dong-gu, Gwangju 61452, Korea

² Department of Biomedical Science and Engineering, Gwangju Institute of Science and Technology (GIST), Gwangju 61005, Korea; gene392@gist.ac.kr

* Correspondence: yjkang2011@chosun.ac.kr; Fax: +82-62-234-7055

Received: 16 May 2018; Accepted: 21 June 2018; Published: 24 June 2018

Abstract: Red blood cell (RBC) aggregation causes to alter hemodynamic behaviors at low flow-rate regions of post-capillary venules. Additionally, it is significantly elevated in inflammatory or pathophysiological conditions. In this study, multiple and periodic measurements of RBC aggregation and erythrocyte sedimentation rate (ESR) are suggested by sucking blood from a pipette tip into parallel microfluidic channels, and quantifying image intensity, especially through single experiment. Here, a microfluidic device was prepared from a master mold using the xurography technique rather than micro-electro-mechanical-system fabrication techniques. In order to consider variations of RBC aggregation in microfluidic channels due to continuous ESR in the conical pipette tip, two indices (aggregation index (AI) and erythrocyte-sedimentation-rate aggregation index (EAI)) are evaluated by using temporal variations of microscopic, image-based intensity. The proposed method is employed to evaluate the effect of hematocrit and dextran solution on RBC aggregation under continuous ESR in the conical pipette tip. As a result, EAI displays a significantly linear relationship with modified conventional ESR measurement obtained by quantifying time constants. In addition, EAI varies linearly within a specific concentration of dextran solution. In conclusion, the proposed method is able to measure RBC aggregation under continuous ESR in the conical pipette tip. Furthermore, the method provides multiple data of RBC aggregation and ESR through a single experiment. A future study will involve employing the proposed method to evaluate biophysical properties of blood samples collected from cardiovascular diseases.

Keywords: red blood cell (RBC) aggregation; multiple microfluidic channels; master molder using xurography technique; RBC aggregation index; modified conventional erythrocyte sedimentation rate (ESR) method; regression analysis

1. Introduction

Normal red blood cell (RBC) in autologous plasma suspension tends to aggregate and form rouleaux (i.e., stacks-of-coins) under extremely low shear-rate conditions [1,2]. This reversible process is strongly dependent on several factors such as surface properties (membrane deformability and negative surface charge), plasma proteins (fibrinogen and globulins), shear stress, and hematocrit [3]. Additionally, RBC aggregation is considered a key determinant of blood viscosity, because it contributes to increasing blood viscosity at low shear rates. Thus, it causes to alter hemodynamic behaviors at low flow-rate regions of post-capillary venules [4,5]. Furthermore, RBC aggregation is significantly elevated in inflammatory or pathophysiological conditions [6,7]. As an indicator of RBC aggregation, erythrocyte sedimentation rate (ESR) is quantified by measuring setting distance of RBCs in a vertical

tube (inner diameter = 2.55 mm, length = 300 mm, and blood volume = 5 mL) for 1 h. In other words, ESR is measured as the height of an RBC-depleted region (or plasma region) of a blood sample in a vertical tube with a specific elapse of time (t) ($t = 1$ h). The ESR is widely used in clinical medicine, because it is a simple and inexpensive method [6–12]. However, the method involves several disadvantages such as large volume consumption (~2 mL) and long measurement time (~1 h). Conversely, after blood flow in a microfluidic channel is agitated with external sources such as pressure source [13], syringe pump [2,14], and pinch valve [3], RBC aggregation is immediately quantified by constructing variations of image intensity [3,13–15], laser back-scattering [16], ultrasound signal [17], or electrical impedance [18] with an elapse of time (i.e., sylvectogram). Previously, our group suggests the simple measurement method of ESR in the microfluidic device [15]. In other words, after setting a disposable syringe into a syringe pump, the syringe pump is reversely aligned with respect to gravitational direction. Then, blood is supplied from the top position of the syringe into a microfluidic device. Hematocrit of blood supplied into a microfluidic channel decreases over time due to continuous ESR in the disposable syringe. This variation in hematocrit is used to measure ESR by quantifying image intensity of blood within a region-of-interest (ROI) of a microfluidic channel [15]. The method is devised to monitor RBC-depleted region in a disposable syringe. However, it does not provide sufficient information on RBC aggregation of blood in a microfluidic channel. According to a previous study [17], RBC aggregation with microscopic, image-based intensity gave comparable value to RBC aggregation, compared with the ultrasonic method and conventional ESR methods. Recently, a simple method is devised to measure RBC aggregation under continuous ESR in a conical pipette tip [19]. According to the previous study [20], blood storage time at 25 °C should be limited to four hours for RBCs aggregation. Above four hours, RBC aggregation was varied with an elapse of time. In other words, when RBCs aggregation was varied over time, the repetitive test increased the scattering of the aggregation index significantly. Thus, multiple measurements of RBC aggregation were required to avoid large scattering due to repetitive tests being conducted for a long period of time. Thus, it is effective to obtain several data points without repetitive tests. Specifically, RBC aggregation should be quantified as mean \pm standard deviation in single experiment with respect to an elapse of time. Thus, it does not require repetitive tests, which cause rheological properties to vary continuously.

In this study, multiple measurements of RBC aggregation under continuous ESR are proposed by sucking blood from a pipette tip into parallel microfluidic channels and quantifying image intensity, especially throughout a single experiment. Furthermore, two indices (aggregation index (AI), and erythrocyte-sedimentation-rate aggregation index (EAI) [19]) are evaluated to consider variations in RBC aggregation due to continuous ESR in a conical pipette tip. The proposed method is demonstrated by using a microfluidic device that is composed of an inlet port, an outlet port, and identical-parallel-microfluidic channels. The microfluidic device is prepared from master mold using xurography technique rather than MEMS (micro-electro-mechanical-system) fabrication techniques. A pipette tip is fitted into the inlet port, and the outlet port is then connected to a disposable syringe with a polyethylene tube. A disposable syringe is installed into a syringe pump. The syringe pump is set to a constant flow rate and operates in the withdrawal mode. A pinch valve is installed between the outlet port and a disposable syringe to control blood delivery from the pipette tip to a microfluidic device. The blood flow stops or runs in parallel microfluidic channels when the pinch valve is periodically clamped or released. The image intensity of blood in each microfluidic channel is quantified to obtain several data points of RBC aggregation over an interval of time. Thus, the proposed method measures several data points of RBC aggregation under continuous ESR in a single experiment without requiring additional repetitive tests.

The feasibility of the proposed method is evaluated by conducting experimental tests with two RBC aggregation indices such as EAI and AI. The EAI is applied to quantify RBC aggregation under continuous ESR in conical pipette tip. Furthermore, AI as a conventional aggregation index is used to compare EAI. In order to evaluate the performance of the proposed method, AI and EAI are quantified for several blood samples (hematocrit = 20%, 30%, 40%, and 50%) that are prepared by adding normal

RBCs into autologous plasma. In order to elevate RBC aggregation, blood samples are prepared using normal RBCs with three different concentrations of dextran solution ($C_{\text{dextran}} = 5 \text{ mg/mL}$, 15 mg/mL , and 20 mg/mL). Subsequently, the proposed method is employed to quantify the effect of dextran solution on the RBC aggregation under continuous ESR in the pipette tip.

2. Materials and Methods

2.1. Blood Sample Preparation

Blood samples were prepared by adding human RBCs to autologous plasma to evaluate RBC aggregation and ESR. Concentrated RBCs and plasma were provided by the Gwangju-Chonnam Blood Bank (Gwangju, Korea). In blood bank, RBCs were collected by removing plasma from whole blood. Then, the RBCs were stored in anticoagulant citrate phosphate dextrose adenine solution (CPDA-1). After concentrated RBCs packed within blood bag (~320 mL) were provided by blood bank, they were immediately stored at $4 \text{ }^\circ\text{C}$. To collect pure RBCs from the concentrated RBCs, blood sample was prepared by adding concentrated RBCs (~8 mL) into $1 \times$ phosphate-buffered saline (PBS) solution (~8 mL). By operating centrifugal separator, pure RBCs were collected by removing buffy layer and PBS from the blood sample. This washing procedure was repeated three times. When blood storage time at $25 \text{ }^\circ\text{C}$ was over four hours, RBC aggregation was varied with an elapse of time [20]. Thus, after blood samples were prepared, they were stored at $4 \text{ }^\circ\text{C}$ before blood test. All experiments were finished within four hours. According to the previous studies [21,22], blood biophysical properties including blood viscosity, and RBC aggregation remained constant for up to 7 days of storage time. In other words, when storage time of RBCs was over 7 days, the RBCs were removed. Hematocrits of normal blood ($H_{\text{ct}} = 20\%$, 30% , 40% , and 50%) were adjusted by adding normal RBCs to autologous plasma. In order to elevate RBC aggregation in blood samples, three different concentrations of dextran solution (C_{dextran}) ($C_{\text{dextran}} = 5 \text{ mg/mL}$, 15 mg/mL , and 20 mg/mL) were prepared by adding dextran (*Leuconostoc* spp., MW = 450–650 kDa, Sigma-Aldrich, St. Louis, MO, USA) to a $1 \times$ PBS solution. Hematocrit of blood samples was adjusted to 30% by adding normal RBCs into a specific dextran solution. A control blood sample ($C_{\text{dextran}} = 0$) was prepared by adding normal RBCs into a $1 \times$ PBS solution.

2.2. Fabrication of a Microfluidic Device and Experimental Procedure

As shown in Figure 1A, a master mold was fabricated using a cutting plotter (i.e., xurography technique) [23–26]. Here, an adhesive sheet with a thickness of $100 \text{ }\mu\text{m}$ was employed for $100 \text{ }\mu\text{m}$ depth. A master mold was designed by using a commercial software program (AutoCAD 2014, Autodesk, San Rafael, CA, USA) [Figure 1A-a]. A cutter blade (CE6000-40, Graphtec, Irvine, CA, USA) was used to cut a cover of the adhesive sheet [Figure 1A-b]. The cover was peeled off from a liner [Figure 1A-c]. The master mold was finally prepared by attaching the liner on a glass slide [Figure 1A-d]. PDMS (polydimethylsiloxane) was mixed at a ratio of 10:1 with a curing agent, and the mixture was poured on the master mold positioned in a Petri dish. The air bubbles dissolved in the PDMS were completely removed by operating a vacuum pump for 1 h. The PDMS was cured in a convection oven at temperature of $75 \text{ }^\circ\text{C}$ for 1.5 h, and the PDMS block was peeled off from the master mold. Two biopsy punches were used, and the inlet port and outlet port was displayed through holes with diameters of 1.5 mm and 0.75 mm , respectively. Following the simultaneous treatment of oxygen plasma (CUTE-MPR, Femto Science Co., Gyeonggi, Korea) on the PDMS block and on a glass substrate, the microfluidic device was prepared by bonding the PDMS block to the glass substrate.

A microfluidic device was mounted on an optical microscope (IX53, Olympus, Tokyo, Japan) equipped with a $4 \times$ objective lens (numerical aperture (NA) = 0.1). As shown in Figure 1B, a pipette tip that was tightly fitted into inlet port after a pipette tip ($50\text{--}1000 \text{ }\mu\text{L}$, Eppendorf, Germany) was cut approximately 34 mm from the top surface. The outlet port was connected to a disposable syringe with a polyethylene tube. The flow rate was set to 2 mL/h (i.e., $Q = 2 \text{ mL/h}$) at the withdrawal mode. Blood (0.2 mL) was dropped into the pipette tip with a pipette. In order to avoid non-specific

binding of plasma protein, microfluidic channels and the pipette tip were filled with 1% bovine serum albumin (BSA) diluted with $1 \times$ PBS solution (pH 7.4, GIBCO, Life Technologies, Gangnam-gu, Korea) for 20 min. The BSA solution was removed from the microfluidic device by releasing the pinch valve. Subsequently, 0.2 mL of blood was dropped into the pipette tip, and it was ready to measure RBC aggregation under continuous hematocrit variations. As shown in Figure 1C-d, a high-speed camera (FASTCAM MINI, Photron, San Jose, CA, USA) was employed to capture blood flows in the microfluidic channels. The spatial resolution of the camera corresponded to 1280×1000 pixels. Each pixel corresponds to $10 \mu\text{m}$. A function generator (WF1944B, NF Corporation, Tokyo, Japan) triggered the high-speed camera at an interval of 1 s to sequentially capture two microscopic images at a frame rate of 1 kHz. All experiments were conducted at a room temperature of $25 \text{ }^\circ\text{C}$.

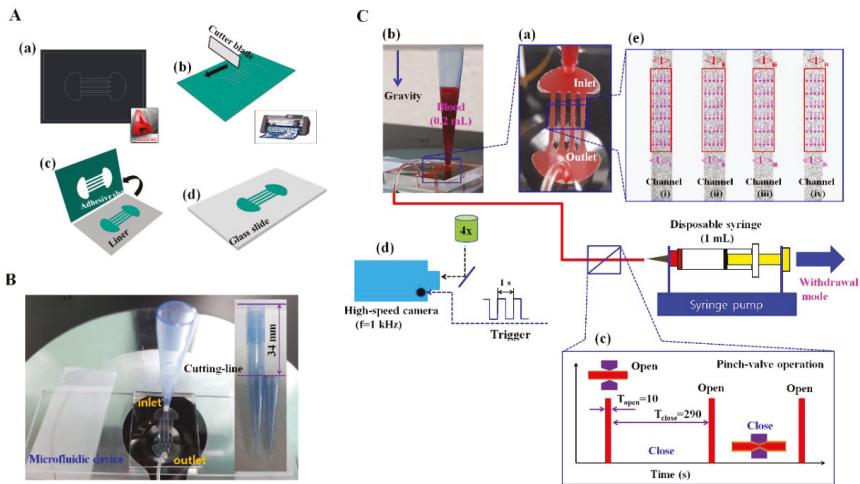


Figure 1. Details of a master mold using an adhesive sheet and a conical pipette tip, and schematic diagram of a proposed method for quantifying red blood cells (RBCs) aggregation and erythrocyte sedimentation rate (ESR) in a pipette tip. (A) Fabrication procedure for preparing an adhesive sheet for a master mold. (A-a) A pattern of master mold designed with commercial software. (A-b) A cutter blade to cut a cover of the adhesive sheet. (A-c) The cover was peeled off from a liner. (A-d) The master mold was finally prepared by attaching the liner on a glass slide. (B) A pipette tip tightly fitted into a microfluidic device. The pipette tip was prepared by cutting 34 mm from the top surface. (C) A schematic diagram of the proposed method including a pipette tip, a disposable microfluidic device, a pinch valve, and a syringe pump. (C-a) A microfluidic device is composed of an inlet port, an outlet port, and parallel microfluidic channels ($N = 4$, width = $600 \mu\text{m}$, depth = $100 \mu\text{m}$, and length = 8 mm). (C-b) A pipette tip fitted into inlet port is filled with 0.2 mL blood. The outlet port is connected to a disposable syringe (1 mL) with a polyethylene tube (inner diameter = $250 \mu\text{m}$, length = 600 mm). A disposable syringe is installed into the syringe pump. Flow rate is set to 2 mL/h (i.e., $Q = 2 \text{ mL/h}$) at the withdrawal mode. (C-c) A pinch valve was installed in front of the disposable syringe to control blood flow in parallel microfluidic channels. A pinch valve was manually opened for 10 s ($T_{\text{open}} = 10 \text{ s}$) and closed for 290 s ($T_{\text{close}} = 290 \text{ s}$) during a single period ($T = 300 \text{ s}$). (C-d) Image acquisition system including microscope, high-speed camera, and external trigger. (C-e) A specific region-of-interest (ROI) ($80 \text{ pixel} \times 400 \text{ pixel}$) for each microfluidic channel was selected to determine average velocity ($\langle U \rangle_i$, $\langle U \rangle_{ii}$, $\langle U \rangle_{iii}$ and $\langle U \rangle_{iv}$) and average image intensity ($\langle I \rangle_i$, $\langle I \rangle_{ii}$, $\langle I \rangle_{iii}$ and $\langle I \rangle_{iv}$), which were calculated by conducting time-resolved micro-particle image velocimetry (PIV) technique and digital image processing, respectively.

2.3. The Proposed Method for Quantifying RBCs Aggregation and ESR over Time

A simple measurement technique of RBC aggregation under continuous ESR is proposed by sucking blood from a pipette tip into parallel microfluidic channels, and quantifying image intensity of blood over an interval of time. Several data of RBC aggregation are obtained throughout a single experiment at an interval of specific time duration.

Figure 1C shows a schematic diagram of the proposed method including a disposable microfluidic device, a pipette tip, a pinch valve, and a syringe pump. A microfluidic device is designed with an inlet port, an outlet port, and parallel microfluidic channels ($N = 4$, width = 600 μm , depth = 100 μm , and length = 8 mm) [Figure 1C-a]. A pipette tip (50–1000 μL , Eppendorf, Hamburg, Germany) is cut approximately 34 mm from the top surface [Figure 1B], and the pipette tip is tightly fitted into an inlet port (inner diameter = 1.5 mm). The outlet port is connected to a disposable syringe (1 mL) with a polyethylene tube (inner diameter = 250 μm and length = 600 mm). After the disposable syringe is installed into a syringe pump, the flow rate was set to 2 mL/h ($Q = 2 \text{ mL/h}$) at the withdrawal mode. Subsequently, 0.2 mL blood is dropped into the pipette tip with a pipette [Figure 1C-b]. The RBC migrates towards the button position due to continuous ESR in the pipette tip, and thus the previous method quantifies ESR by measuring the height of the RBC-depleted region [15,17]. In contrast to previous ESR measurement, the proposed method is suggested to measure variations of RBC aggregation under continuous ESR by evaluating the microscopic image-based intensity of blood flow in microfluidic channels. Therefore, to evaluate variations in hematocrit due to continuous ESR in the pipette tip, blood is supplied from the conical pipette tip to the microfluidic channels over an interval of time. A pinch valve (Supa clip, Pankyo, Gyeonggi-do, Korea) was installed between the outlet port and the disposable syringe to periodically ensure blood delivery into the microfluidic device. A pinch valve is manually opened for 10 s ($T_{\text{open}} = 10 \text{ s}$) and closed for 290 s ($T_{\text{close}} = 290 \text{ s}$) during a single period ($T = 300 \text{ s}$) [Figure 1C-c]. As shown in Figure 1C-e, a specific ROI (80 \times 400 pixels) is selected for each microfluidic channel to determine an average value of blood velocity for each microfluidic channel ($\langle U \rangle_i$, $\langle U \rangle_{ii}$, $\langle U \rangle_{iii}$ and $\langle U \rangle_{iv}$) and an average value of image intensity for each microfluidic channel ($\langle I \rangle_i$, $\langle I \rangle_{ii}$, $\langle I \rangle_{iii}$ and $\langle I \rangle_{iv}$) that are calculated by conducting time-resolved micro-PIV technique and digital image processing, respectively.

As a preliminary study, blood with 30% hematocrit was prepared by adding normal RBCs into a specific dextran solution (i.e., $C_{\text{dextran}} = 15 \text{ mg/mL}$). Figure 2A shows temporal variations of averaged image intensity ($\langle I \rangle$) for individual microfluidic channel and averages blood velocity ($\langle U \rangle$) through four microfluidic channels. Here, to monitor temporal variations of blood flow depending on the operation of the pinch valve (i.e., open or close), velocity fields were obtained by conducting time-resolved micro-PIV technique. After guaranteeing the operation of the pinch valve sufficiently, we did not try to get velocity information. Sequential images for representing RBC-depleted regions in a pipette tip were captured with elapses of time (t) ([a] $t = 300 \text{ s}$, [b] $t = 600 \text{ s}$, [c] $t = 900 \text{ s}$, and [d] $t = 1200 \text{ s}$). With respect to an elapse of time, the RBC-depleted region tended to increase due to continuous ESR in conical tip. Additionally, image intensity ($\langle I \rangle$) tended to decrease due to an increase in the hematocrit. As shown in Figure 2B, temporal variations of $\langle I \rangle$ for each microfluidic channel are obtained for a single period ($T = 300 \text{ s}$). Temporal variations of image intensity ($\langle I \rangle$), which are called a syllectogram, are used to calculate three representative factors (S_A , S_B , and S_C) [19] as follows:

$$S_A = \int_{t=0}^{t=t_s} (\langle I \rangle - \langle I \rangle_{\min}) dt \quad (1)$$

$$S_B = \int_{t=0}^{t=t_s} (\langle I \rangle_{\max} - \langle I \rangle) dt \quad (2)$$

$$S_C = \int_{t=0}^{t=t_s} \langle I \rangle_{\min} dt \quad (3)$$

In Equations (1)–(3), $\langle I \rangle_{\min}$ and $\langle I \rangle_{\max}$ are denoted as $\langle I \rangle_{\min} = \langle I(t=0) \rangle$ and $\langle I \rangle_{\max} = \langle I(t=t_s) \rangle$, respectively. Furthermore, $\langle I \rangle_{\min}$ tended to decrease due to ESR in the pipette tip, and thus S_C was used to represent the dynamic behavior of ESR. According to most previous methods, a blood sample was directly dropped into an inlet port of the microfluidic device. Since hematocrit of the blood sample remained constant in a microfluidic channel, the previous methods did not require to consider the effect of continuous ESR in the reservoir on the RBCs aggregation. In other words, the previous method did not consider the effect of hematocrit variations on the syllectogram (i.e., $S_C = 0$). In other words, as shown in right panel of Figure 2B, RBC aggregation was quantified by calculating AI as $AI = S_A / (S_A + S_B)$. However, in this study, the proposed method involved simultaneously measuring RBC aggregation and ESR in conical pipette tip. The continuous ESR caused to increase hematocrit of blood supplied into a microfluidic channel. According to temporal variations of $\langle I \rangle$, $\langle I \rangle_{\min}$ decreased due to increases in hematocrit. In order to quantify RBC aggregation due to ESR in the conical pipette tip, it was necessary to simultaneously consider variations in $\langle I \rangle$ due to RBC aggregation (i.e., S_A) and $\langle I \rangle_{\min}$ due to ESR (i.e., S_C). Thus, EAI is evaluated as $EAI = S_A / S_C$. For convenience, t_s was fixed as $t_s = 250$ s. Sequential microscopic images for four microfluidic channels indicated that RBC tended to gradually aggregate with respect to an elapse of time (t) ([A-a] $t = 0$, [B-b] $t = 100$ s, [C-c] $t = 200$ s, and [D-d] $t = 300$ s). This preliminary result indicated that the proposed method measured variations of RBC aggregation under continuous ESR by quantifying image intensity of blood in each microfluidic channel.

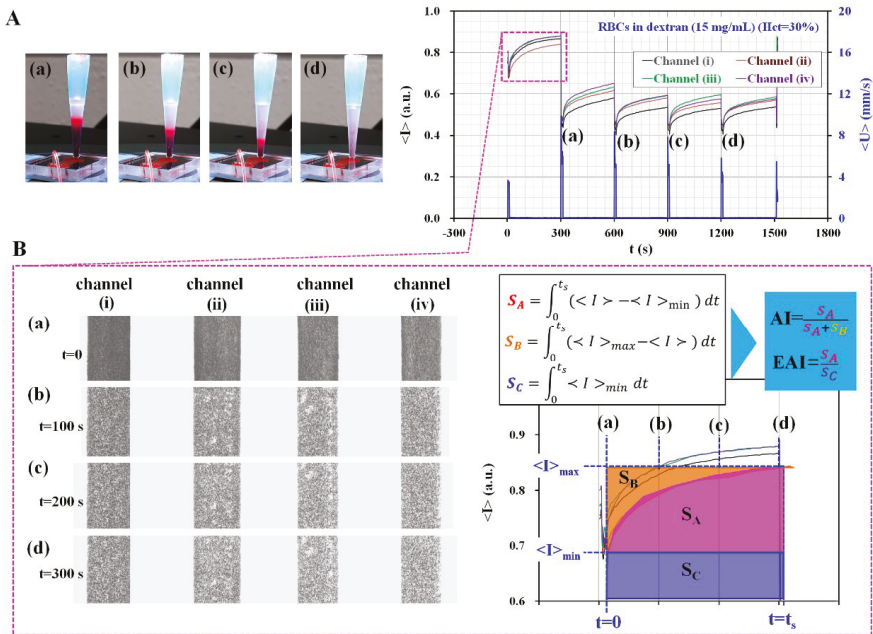


Figure 2. Quantification of two indices (AI and EAI) for quantifying RBCs aggregation and ESR in a conical pipette tip. (A) Temporal variations in $\langle I \rangle$ for each microfluidic channel and average velocity ($\langle U \rangle$) through four microfluidic channels. Sequential images for representing RBC-depleted regions in a pipette tip with an elapse of time (t) ([A-a] $t = 300$ s, [A-b] $t = 600$ s, [A-c] $t = 900$ s, and [A-d] $t = 1200$ s). (B) Temporal variations of $\langle I \rangle$ for each microfluidic channel over a single period. Sequential microscopic images represent RBC aggregation for each microfluidic channel with an elapse of time (t) ([B-a] $t = 0$, [B-b] $t = 100$ s, [B-c] $t = 200$ s, and [B-d] $t = 300$ s). Two indices (AI and EAI) were defined as $AI = S_A / (S_A + S_B)$ and $EAI = S_A / S_C$ from a syllectogram obtained for 300 s.

2.4. Quantifications of Image Intensity ($\langle I \rangle$) and Blood Velocity ($\langle U \rangle$)

In order to evaluate variations in image intensity of blood with an elapse of time, a specific ROI (80 pixel \times 400 pixel) was selected within each microfluidic channel as shown in Figure 1C-e. Average pixel values over the ROI ($\langle I \rangle_i$, $\langle I \rangle_{ii}$, $\langle I \rangle_{iii}$, and $\langle I \rangle_{iv}$) were estimated by performing digital image processing with a commercial software program (Matlab, Mathworks, Natick, MA, USA). To evaluate temporal variations of blood flow, velocity fields were obtained by conducting a time-resolved micro-PIV technique to evaluate temporal variations in blood flow. Specific ROIs (80 pixel \times 400 pixel) were selected for each microfluidic channel to obtain velocity fields of blood flow. The size of the interrogation window corresponded to 16 \times 16 pixels. The window overlap corresponded to 50%. The obtained velocity fields were validated with a median filter. The average velocities of blood flow for each microfluidic channel ($\langle U \rangle_i$, $\langle U \rangle_{ii}$, $\langle U \rangle_{iii}$, and $\langle U \rangle_{iv}$) were calculated as an arithmetic average over the ROI. Finally, average blood velocity in the parallel microfluidic channel ($\langle U \rangle$) was calculated as $\langle U \rangle = (\langle U \rangle_i + \langle U \rangle_{ii} + \langle U \rangle_{iii} + \langle U \rangle_{iv})/4$.

3. Results and Discussion

3.1. Variation of Width in Microfluidic Channel Fabricated by Using an Adhesive Sheet for Master Mold

In this study, the use of a liner cut from an adhesive sheet to form the master mold was employed to simplify the fabrication process, compared to MEMS fabrication. Variations of channel width were measured by analyzing microscopic images obtained from high-speed camera. After then, digital image processing was conducted to measure channel width of individual channel. Measurement for each channel was repeated ten times ($n = 10$). As shown in Figure 3A, the corresponding channel width (W) for each channel was measured as (a) $W = 615 \pm 12 \mu\text{m}$ for (i) channel, (b) $W = 615 \pm 23 \mu\text{m}$ for (ii) channel, (c) $W = 575 \pm 18 \mu\text{m}$ for (iii) channel, and (d) $W = 571 \pm 33 \mu\text{m}$ for (iv) channel. In other words, this simple technique could be employed to prepare microfluidic channel within 4% normal deviation in channel width of individual channel. Compared with MEMS fabrication, this simple technique was not feasible to fabricate a microfluidic channel with highly consistent dimensions. According to the previous studies, this xurography technique had poor resolution for dimensions smaller than 500 μm . However, it provides several advantages including inexpensive cost (material and equipment) and rapid fabrication without cleanroom [24,26]. Due to high advantages, it had been employed to fabricate biomedical device for blood flow analysis [25,27]. However, in this study, dynamic blood flow was required to disaggregate aggregated RBCs sufficiently. Since RBCs aggregation was quantified at stationary blood flows by clamping polyethylene tube with a pinch valve, blood flow in each channel does not have an influence on measurement of RBCs aggregation. Even though this technique has a little deviations in channel width, an adhesive sheet could be simply used as a master mold to prepare microfluidic device. On the other hand, to verify variations of each microfluidic device, channel width was measured with five microfluidic devices. Averaged channel width for each device was used to quantify device-to-device variation. Four channel widths of each device were arithmetically averaged as $W_{\text{ave}} = [W_{(i)} + W_{(ii)} + W_{(iii)} + W_{(iv)}]/4$. As shown in Figure 3B, averaged channel width (W_{ave}) remained consistent for five different devices. From these measurement results, the use of a liner cut from an adhesive sheet contributes to simplifying the fabrication process, and to preparing PDMS microfluidic channel reliably.

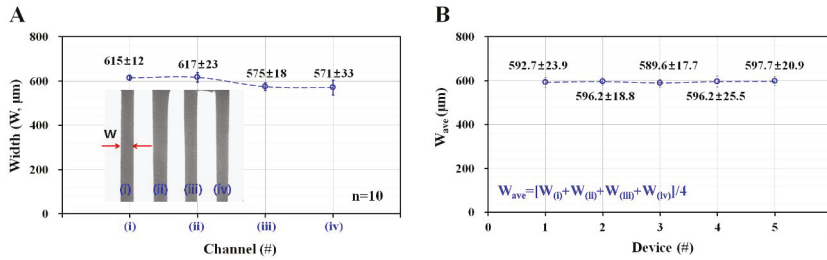


Figure 3. Quantitative measurement of width variations of four microfluidic channels fabricated by using an adhesive sheet for master mold. (A) Variations of channel width for four individual channels. (B) Variations of averaged channel width for five different devices.

3.2. Quantitative Evaluation of the Effects of Pinch-Valve Operation and Syringe Pump Flow-Rate

In order to analyze the dynamic effect of a microfluidic system (polyethylene tube and a microfluidic device) on the performance of the proposed method, image intensity ($\langle I \rangle$) and blood velocity ($\langle U \rangle$) of blood flow in parallel microfluidic channels were quantified with high resolution. Two sequential microscopic images were captured and recorded at an interval of 0.1 s. Hematocrit of blood was adjusted to 30% by adding normal RBCs into autologous plasma. A flow rate was set to 2 mL/h with a syringe pump. Figure 4A-a,A-b show temporal variations of image intensity ($\langle I \rangle$) and average of blood velocity ($\langle U \rangle$) obtained for specific durations of 120 s and 25 s. When a pinch valve clamps or releases the polyethylene tube, $\langle I \rangle$ and $\langle U \rangle$ showed transient behaviors with respect to time. The experimental results indicated that blood flow stopped shortly within 0.2 s. After clamping the tube, image intensity ($\langle I \rangle$) tended to increase immediately. According to previous studies [17,28], blood flow decreased gradually based on the compliance effect of the microfluidic system when a syringe pump was used to control blood flow in a microfluidic channel in the delivery mode. In other words, when the syringe pump was set to zero value of the flow rate (i.e., $Q = 0$), RBC aggregation did not occur due to transient blood flow in the microfluidic channel. Thus, RBC aggregation was quantified by using temporal variations in image intensity after an elapse of 20 s [28] or 60 s [17]. For this reason, a glass capillary tube [2] or detour channel [14] was applied to minimize time delay due to the compliance effect of the microfluidic system. However, in the proposed method, a syringe pump sets to constant flow rate as withdrawal mode. The pinch valve clamped or released the polyethylene tube, and thus the blood flow stopped or ran within a very short time. The experimental results indicated that RBC aggregation was measured immediately after clamping the tube with a pinch valve (i.e., close mode). Additionally, the compliance effect of fluidic system on RBC aggregation and ESR was negligible.

To verify the effect of syringe pump flow-rate on RBC aggregation (i.e., AI) and ESR (i.e., EAI), temporal variations of image intensity ($\langle I \rangle$) and velocity ($\langle U \rangle$) were obtained by varying flow rate of the syringe pump (Q) ($Q = 0.5$ mL/h, 1 mL/h, and 2 mL/h). Figure 4B-a shows temporal variations of $\langle I \rangle$ with respect to flow rate of syringe pump (Q). Here, $\langle I \rangle$ denotes average values of image intensity in four microfluidic channels. With increasing syringe pump flow-rate, $\langle I \rangle$ tends to decrease. For up to 600 s, minimum value of $\langle I \rangle$ (i.e., $\langle I \rangle_{min}$) tends to decrease gradually because of continuous ESR in the conical pipette tip. After 600 s, $\langle I \rangle$ remained constant without respect to syringe pump flow-rate. In addition, amplitude of $\langle I \rangle$ (i.e., ΔI) was decreased over time. Figure 4B-b shows temporal variations of $\langle U \rangle$ with respect to syringe pump flow-rate (Q). Here, $\langle U \rangle$ denotes averaged blood velocity through four microfluidic channels, especially for 10 s per each period. By increasing flow rate, blood velocity ($\langle U \rangle$) tends to increase distinctively. In addition, at the higher syringe pump flow-rate of $Q = 1\text{--}2$ mL/h, blood velocity was decreased gradually from $t = 300$ s to $t = 900$ s. Then ($t > 900$ s), blood velocity remained constant over time. However, at the lower syringe pump flow-rate of $Q = 0.5$ mL/h, blood velocity remained constant over time. Using temporal variations of $\langle U \rangle$ during a specific time duration of 1500 s, temporal variations of two indices (AI and EAI) were obtained by varying flow rates. As shown in

Figure 4B-c,B-d, AI as conventional RBC aggregation index remained constant without respect to flow rate but not with respect to the initial condition ($t = 0$). However, due to continuous ESR in the conical pipette tip, hematocrit of blood supplied from the conical tip into microfluidic channels was increased. Thus, EAI was decreased gradually over time. In addition, syringe pump flow-rate does not contribute to varying EAI. From these experimental demonstrations, it is found that syringe pump blood-flow rate does not have a significant influence on measurement of AI and EAI. In other words, the syringe pump flow-rate of $Q = 0.5$ mL/h is considered sufficient for removing and filling blood samples in each microfluidic channel for each period. In this study, for convenience, the higher syringe pump flow-rate of $Q = 2$ mL/h was selected to easily suck and remove blood samples from the bottom area of the pipette tip and change blood samples in each microfluidic channel.

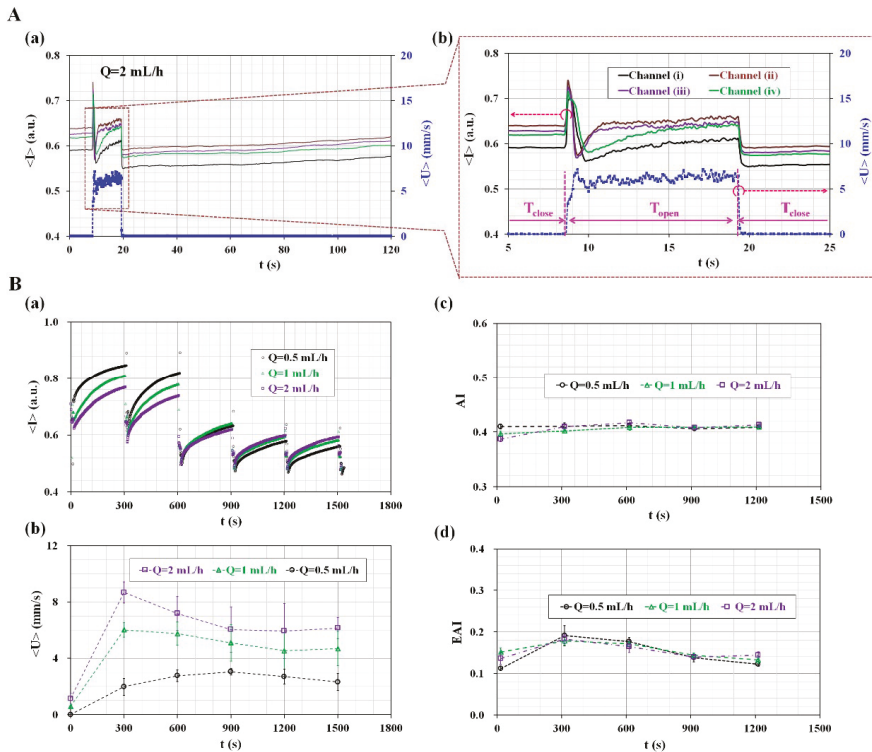


Figure 4. The quantitative evaluation of the effects of vital two factors including pinch-valve operation and syringe pump flow-rate on the measurement of RBC aggregation and ESR. (A) Dynamic characterization of image intensity ($\langle I \rangle$) and blood velocity ($\langle U \rangle$) based on operation of the pinch valve (open, close). To evaluate transient response with a high resolution, $\langle I \rangle$ and $\langle U \rangle$ were obtained at intervals of 0.1 s. Hematocrit of blood was adjusted to 30% by adding normal RBCs into the plasma solution. At the constant flow rate of 2 mL/h with syringe pump, temporal variations of $\langle I \rangle$ and $\langle U \rangle$ were obtained for specific duration of (A-a) 120 s and (A-b) 25 s. As a result, blood flow was stopped immediately within 0.2 s after clamping a tube with a pinch (i.e., close). (B) The effect of syringe pump flow-rate (Q) on the measurement of RBC aggregation (i.e., AI) and ESR (i.e., EAI). Temporal variations of $\langle I \rangle$ and $\langle U \rangle$ were obtained by varying flow rate of syringe pump (Q) ($Q = 0.5, 1,$ and 2 mL/h). (B-a) Temporal variations of $\langle I \rangle$ with respect to blood flow rate. (B-b) Temporal variations of $\langle U \rangle$ with respect to syringe pump flow-rate. (B-c) Temporal variations of AI with respect to syringe pump flow-rate. (B-d) Temporal variations of EAI with respect to syringe pump flow-rate.

3.3. Quantitative Evaluation of the Channel Number for Evaluating Variations of AI and EAI

To find out the effect of the channel number on measurement of RBCs aggregation and ESR, the variations of RBC aggregation and ESR (i.e., AI and EAI) were evaluated with respect to number of channel (n) ($n = 1, 2, 3,$ and 4). Figure S1 (Supplementary Materials) showed microscopic images for microfluidic device with multiple numbers of channel (n) [(a) $n = 1$, (b) $n = 2$, (c) $n = 3$, and (d) $n = 4$]. Blood sample was prepared by adding normal RBCs into plasma. Hematocrit was fixed at 30%. As shown in Figure 5A, temporal variations of $\langle I \rangle$ and $\langle U \rangle$ were simultaneously measured with respect to channel number. As a result, $\langle I \rangle$ and $\langle U \rangle$ were decreased with increasing channel numbers. When removing pinch valve (i.e., open mode) for 10 s, blood velocity tended to decrease with increasing channel number. Furthermore, image intensity of stasis blood flow tended to decrease for rest time of each period (~290 s). In other words, blood velocity for short duration time (~10 s) contributed to changing image intensity of blood. Temporal variations of two indices (AI and EAI) were obtained by analyzing temporal variations of image intensity for each duration of period. As shown in Figure 5B-a, AI does not show significant difference with respect to channel number. To compare with scattering of AI, coefficient of variation (COV) (~standard deviation/mean) was estimated as less than 0.05 from two channels to four channels. However, since minimum value of image intensity ($\langle I \rangle_{\min}$) for each period was inserted to calculate EAI, higher number of channels contributed to decreasing EAI. As shown in Figure 5B-b, four channels showed lower values of EAI compared with the rest of channel numbers. In addition, COV of EAI remained within 0.1 from two channels to four channels.

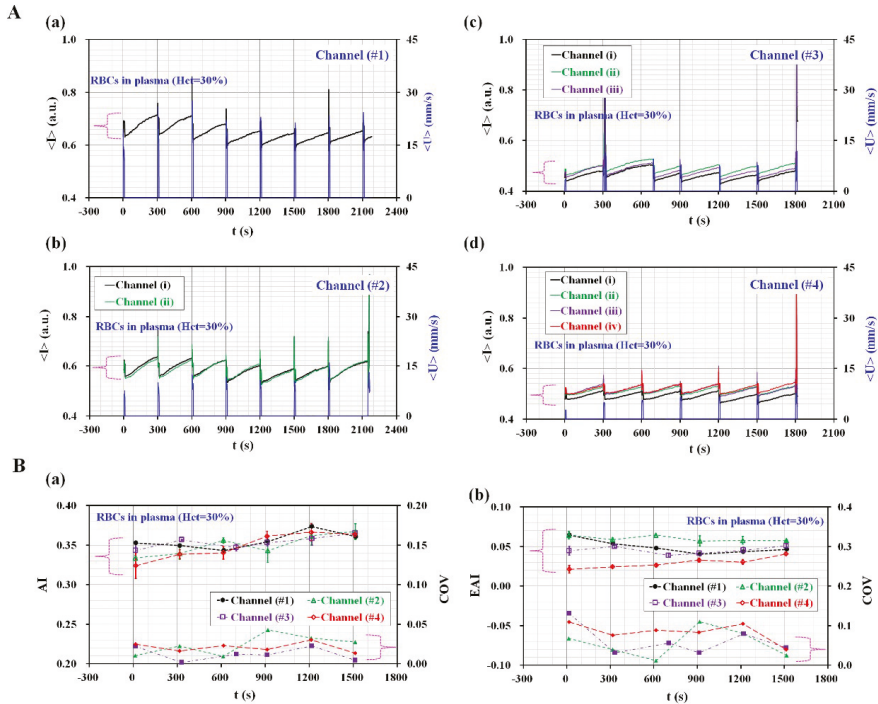


Figure 5. Quantitative evaluation of channel numbers for measuring scattering of two indices (AI and EAI). (A) Temporal variations of $\langle U \rangle$ and $\langle I \rangle$ with respect to channel number (n) ((A-a) $n = 1$, (A-b) $n = 2$, (A-c) $n = 3$, and (A-d) $n = 4$). (B) Temporal variations of AI and EAI with respect to channel number. (B-a) Temporal variation of AI and, coefficient of variation (COV) with respect to channel number. (B-b) Temporal variations of EAI and COV with respect to channel number.

3.4. Quantitative Evaluation of the Effect of Hematocrit Variations

In order to evaluate the effect of hematocrit on the RBC aggregation under continuous ESR, the four different hematocrits (H_{ct}) ($H_{ct} = 20\%$, 30% , 40% , and 50%) were prepared by adding normal RBCs into autologous plasma. RBC aggregation and ESR were quantified using AI and EAI, respectively. Figure 6A shows temporal variations of $\langle I \rangle$ with respect to each microfluidic channel and hematocrit level (H_{ct}) ([a] $H_{ct} = 20\%$, [b] $H_{ct} = 30\%$, [c] $H_{ct} = 40\%$, and [d] $H_{ct} = 50\%$). Image intensity ($\langle I \rangle$) varied over time with respect to each microfluidic channel and hematocrit. With respect to blood with 20% hematocrit, all RBCs were passed from a pipette tip to outlet port after 1200 s, and thus, variations in image intensity for four microfluidic channels were obtained up to 1200 s. With respect to blood with 30% hematocrit, variations of image intensity were obtained up to 1500 s. However, the other two blood types ($H_{ct} = 40\%$ and 50%) exhibited a lower value of ESR in a pipette tip, and thus, RBCs continued to exist in the microfluidic channels. Variations in image intensity were obtained up to 1800 s. Blood with lower hematocrit exhibited a higher value of S_A and S_C when compared with blood with higher hematocrit. This result indicated that blood sample with lower hematocrit exhibited higher values of ESR and RBC aggregation. Temporal variations of $\langle I \rangle$ were used for four microfluidic channels to obtain temporal variations of AI and EAI with respect to hematocrit. RBCs aggregation was quantified using temporal variations of image intensity from stasis blood flow ($t = 0$). The effect of shear rate on RBCs aggregation measurement was negligible (i.e., $\dot{\gamma} = 0$). As shown in Figure 6A, since temporal variations of image intensity were obtained by analyzing microscopic images captured at stasis blood flows, RBCs aggregation only contributed to varying image intensity of blood sample in each microfluidic channel. As shown in Figure 6B-a, AI did not display significant differences with respect to hematocrit (H_{ct}) and measurement time (t). Additionally, blood with lower hematocrit exhibited a higher value of AI when compared with blood with higher hematocrit. Furthermore, AI remained constant over time. Conversely, temporal variations of EAI were obtained with respect to hematocrit to include the effect of ESR. As shown in Figure 6B-b, EAI shows a significant difference with respect to hematocrit when compared with AI. Therefore, blood with 20% hematocrit exhibited a higher value of EAI when compared with other blood. Moreover, blood with 40–50% hematocrit exhibited a similar value to EAI after 900 s. The result indicated that EAI was more effective at evaluating the effect of hematocrit on the RBC aggregation when compared with that of AI, because EAI included the effect of ESR in the pipette tip.

As quantitative comparison, the effect of hematocrit on ESR measurement was quantified by using a modified conventional method [15,17]. Here, hematocrit of blood (H_{ct}) were adjusted to $H_{ct} = 20\%$, 30% , 40% , and 50% by adding normal RBCs into autologous plasma. After installing four disposable syringes vertically in base plate, blood with different hematocrit (~1 mL) was dropped into each syringe with a pipette as shown in Figure 6C-a. At intervals of 30 s, consecutive images were captured with a digital camera (D700, Nikon, Tokyo, Japan). The ESR was then quantified by measuring the height of RBCs-depleted layer (i.e., H) over time. As shown in Figure 6C-b, temporal variations of H were obtained by varying hematocrit. After then, to quantify relationship between proposed method (i.e., EAI) and conventional method (i.e., H), simple regression formula for each method was used as $EAI = a_1 + a_2 \exp(-t/\lambda_{EAI})$ and $H(t) = b_1 + b_2 \exp(-t/\lambda_H)$, respectively. Here, λ_{EAI} and λ_H denote corresponding time constants for proposed method and conventional method. By conducting nonlinear regression analysis with a commercial software (Matlab, Mathworks, Natick, MA, USA), variations of λ_{EAI} and λ_H were obtained with increasing hematocrit. As shown in Figure 6D-a, both time constants tend to increase gradually with respect to hematocrit. In other words, ESR is saturated within a short time for lower hematocrit, compared with higher hematocrit. In addition, EAI shows very similar trend with respect to hematocrit. To find out relationship between two time constants (λ_{EAI} and λ_H), linear regression analysis was conducted using EXCEL program (Microsoft™, Natick, MA, USA). As shown in Figure 6D-b, coefficient of R^2 shows sufficient high value of $R^2 = 0.9521$. From this result, both methods have significantly linear relation. Furthermore, it leads to conclusion that EAI

as newly suggested index can be effectively employed to monitor variation of ESR through quantifying image intensity of blood flowing in microfluidic channels.

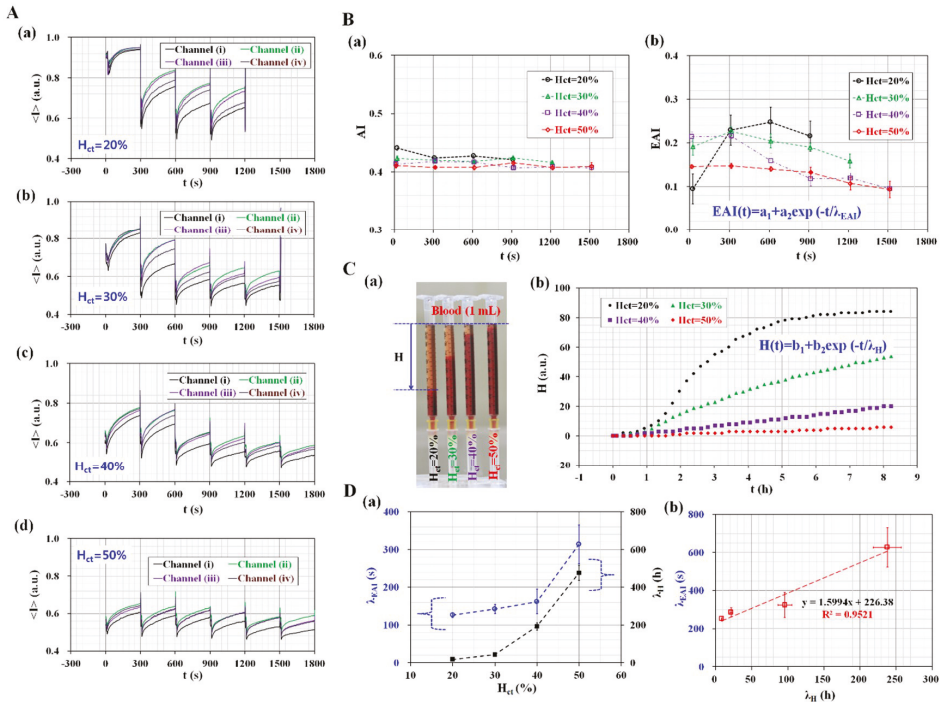


Figure 6. Quantitative evaluation of the effect of hematocrit on the performance of the proposed method. Specifically, RBC aggregation and ESR are quantified using two indices (AI and EAI). Hematocrit (H_{ct}) ($H_{ct} = 20\%$, 30% , 40% , and 50%) was adjusted by adding normal RBCs into autologous plasma. (A) Temporal variations of $\langle I \rangle$ with respect to each microfluidic channel and hematocrit (H_{ct}) [(A-a) $H_{ct} = 20\%$, (A-b) $H_{ct} = 30\%$, (A-c) $H_{ct} = 40\%$, and (A-d) $H_{ct} = 50\%$]. (B) Temporal variations of AI and EAI with respect to hematocrit. (B-a) Temporal variations of AI with respect to hematocrit. (B-b) Temporal variations of EAI with respect to hematocrit. (C) ESR measurement using a disposable syringe (~1 mL) as a conventional method. (C-a) Snapshot images for quantifying ESR method with respect to hematocrit. Here, H represents height in RBCs-depleted layer. (C-b) Temporal variations of H with respect to hematocrit. (D) Quantitative comparison between conventional method and proposed method. (D-a) Variations of λ_{EAI} and λ_H with respect to hematocrit (H_{ct}). (D-b) Linear relationship between λ_{EAI} and λ_H .

3.5. Quantitative Evaluation of RBC Aggregation under Continuous for Homogeneous Aggregated RBCs

A performance demonstration involved applying the proposed method to measure RBC aggregation under continuous for homogeneous aggregated RBCs. In order to elevate RBC aggregation for normal RBCs, three different concentrations of dextran solution ($C_{dextran}$) ($C_{dextran} = 5 \text{ mg/mL}$, 15 mg/mL , and 20 mg/mL) were prepared by adding dextran into $1 \times \text{PBS}$ solution. Subsequently, hematocrit of the blood sample was adjusted to 30% by adding normal RBCs into three different concentrations of the dextran solution. Additionally, a control blood sample was prepared by adding normal RBCs into $1 \times \text{PBS}$ solution ($C_{dextran} = 0$) to exclude the effect of RBC aggregation.

Figure 7A shows temporal variations of $\langle I \rangle$ and $\langle U \rangle$ for two different bloods prepared by adding normal RBCs into 20 mg/mL dextran solution and PBS solution, respectively. The tube opened shortly at an interval of 300 s, and thus, an average of blood velocity ($\langle U \rangle$) was measured as a periodic pulse-like shape. Image intensity ($\langle I \rangle$) tended to immediately increase over time when the pinch valve clamps the tube (i.e., in the close mode). A blood sample with a higher concentration of the dextran solution ($C_{\text{dextran}} = 20 \text{ mg/mL}$) exhibited larger variations in image intensity (i.e., S_A), when compared with that of the control blood sample ($C_{\text{dextran}} = 0$). For two blood samples, a minimum value of $\langle I \rangle$ ($\langle I \rangle_{\text{min}}$) exhibited a significant decrease at $t = 300 \text{ s}$. Following this, $\langle I \rangle_{\text{min}}$ remained constant with an elapse of time. This result indicated that ESR occurs dominantly within 300 s. After 300 s, ESR remained constant with time elapses.

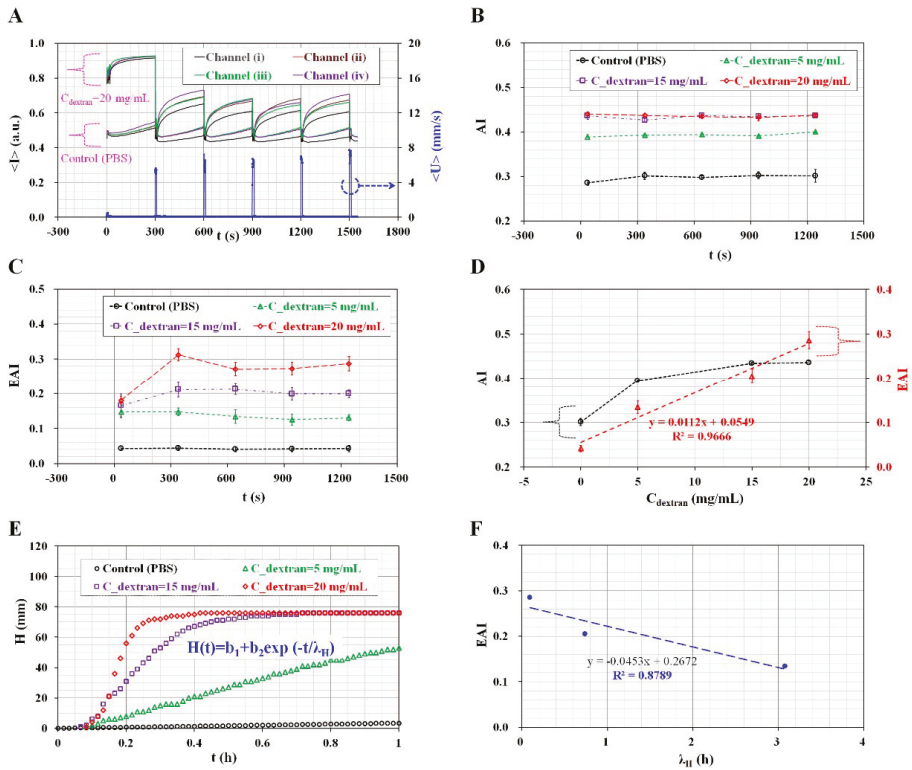


Figure 7. Quantitative evaluations of RBC aggregation (i.e., AI) and ESR (i.e., EAI) with the proposed method and the modified conventional ESR method. To elevate RBC aggregation and ESR, three concentrations of dextran solution (C_{dextran}) ($C_{\text{dextran}} = 5 \text{ mg/mL}$, 15 mg/mL , and 20 mg/mL) were prepared by adding dextran into a PBS solution. Hematocrit is adjusted to 30% by adding normal RBCs into three different concentrations of the dextran solution. (A) Temporal variations of $\langle I \rangle$ and $\langle U \rangle$ for two different blood samples ($C_{\text{dextran}} = 0, 20 \text{ mg/mL}$). (B) Temporal variations of AI with increasing concentrations of the dextran solution. (C) Temporal variations of EAI with increasing concentrations of the dextran solution. (D) Variations of AI and EAI with respect to the concentration of the dextran solution. (E) Temporal variations of H with respect to specific concentrations of dextran solution. Here, H denotes height of RBCs-depleted layer in a disposable syringe. (F) Linear relationship between proposed method (i.e., EAI) and the modified conventional ESR method (i.e., λ_{H1}).

In order to quantify RBC aggregation under continuous ESR, two indices (AI and EAI) were calculated using temporal variations of $\langle I \rangle$ for each microfluidic channel. As shown in Figure 7B, the temporal variations of AI were obtained with respect to concentrations of the dextran solution. The control blood sample (i.e., normal RBC in PBS suspension) showed a lower value of $AI = 0.30 \pm 0.01$ when compared with aggregated blood sample (i.e., normal RBCs in plasma), as shown in Figure 6B-a. Hence, the AI gives higher value of reference, since control blood sample was prepared to exclude RBC aggregation. Thus, it was estimated that lower hematocrit ($H_{ct} = 30\%$) contributed to a higher value of AI as a reference value. Additionally, the blood sample exhibited a higher value of AI with increases in the concentration of the dextran solution. However, AI did not indicate significant differences for blood samples, with concentrations of the dextran solution ranging from $C_{\text{dextran}} = 15 \text{ mg/mL}$ to $C_{\text{dextran}} = 20 \text{ mg/mL}$.

As shown in Figure 7C, temporal variation of EAI was calculated using temporal variations of image intensity ($\langle I \rangle$) with respect to concentrations of the dextran solution. As a result, EAI remained constant after 2 cycles. Since each cycle is continued for five min., the proposed method requires at least 10 min. The proposed method does remove necessity of repetitive test as significant advantage. The control blood sample exhibited a significantly lower value of EAI (i.e., $EAI = 0.04 \pm 0.01$) as a reference value when compared with that of the AI. Overall variations in EAI are significantly higher than those of AI within a specific dextran solution. Furthermore, EAI exhibited a significant difference at specific dextran concentrations ranging from $C_{\text{dextran}} = 15 \text{ mg/mL}$ to $C_{\text{dextran}} = 20 \text{ mg/mL}$.

Finally, as shown in Figure 7D, variations of AI and EAI were displayed with respect to a specific dextran solution. The linear regression analysis indicated a high value of R^2 (i.e., $R^2 = 0.9666$), and thus, EAI linearly varied within a specific concentration of dextran solution. However, AI varied gradually below 15 mg/mL dextran solution. Furthermore, AI approached saturation above 15 mg/mL dextran solution. According to most previous methods, a blood sample was directly dropped into an inlet port of the microfluidic device. Since hematocrit of the blood sample remained constant in a microfluidic channel, the previous methods did not require to consider the effect of continuous ESR in the reservoir on the RBCs aggregation. In other words, the previous method did not consider the effect of hematocrit variations on the sylectogram (i.e., $S_C = 0$). Based on previous methods [2,3], the RBC aggregation was quantified by calculating AI as $AI = S_A / (S_A + S_B)$. However, in this study, the proposed method involved simultaneously measuring RBC aggregation and ESR in conical pipette tip. The continuous ESR caused to increase hematocrit of blood supplied into a microfluidic channel. According to temporal variations of $\langle I \rangle$, minimum value of $\langle I \rangle$ (i.e., $\langle I \rangle_{\text{min}}$) decreased due to increases in hematocrit. In order to quantify RBC aggregation due to ESR in the conical pipette tip, it was necessary to simultaneously consider variations in $\langle I \rangle$ due to RBC aggregation (i.e., S_A) and $\langle I \rangle_{\text{min}}$ due to ESR (i.e., S_C). Thus, EAI is evaluated as $EAI = S_A / S_C$.

3.6. Quantitative Comparison between the Proposed Method and the Modified Conventional ESR Method

To compare with the experimental results obtained by the proposed method, blood was prepared by adding normal RBCs into a specific concentration of dextran solution (C_{dextran}) ($C_{\text{dextran}} = 0, 5 \text{ mg/mL}, 15 \text{ mg/mL}, \text{ and } 20 \text{ mg/mL}$). Here, $C_{\text{dextran}} = 0$ denotes $1 \times$ PBS solution. Thereafter, 1 mL blood was dropped into a disposable syringe (1 mL , BD Science, Singapore) as a modified conventional method [15,17]. Figure 7E shows temporal variations of H by varying various concentrations of dextran solution. As a result, dextran solution contributes to increasing H significantly, compared with control blood. To quantify variations of ESR, simple regression expression was suggested as $H(t) = b_1 + b_2 \exp(-t/\lambda_H)$. Then, time constant (i.e., λ_H) was obtained by conducting nonlinear regression analysis with commercial software. Figure 7F represents the quantitative comparison between proposed method (i.e., EAI) and the conventional method (i.e., λ_H). To verify the relationship between the proposed method and conventional method, a linear regression analysis was conducted with EXCEL program (Microsoft™, Natick, MA, USA). Since the coefficient of R^2 has higher value of $R^2 = 0.8789$, the EAI obtained by the proposed method can give comparable value of ESR, compared with the conventional

method. As shown in Figure 6B-b, EAI of normal blood ($H_{ct} = 30\%$) was varied from 0.16 to 0.22. According to Figure 7D, EAI was increased linearly with increasing concentration of dextran solution. Blood with lower concentration of dextran solution ($C_{\text{dextran}} = 5 \text{ mg/mL}$) had $EAI = 0.134 \pm 0.014$. In other words, 5 mg/mL dextran solution played a similar ESR behavior, compared with plasma solution. Blood prepared with higher concentration of dextran solution ($C_{\text{dextran}} = 20 \text{ mg/mL}$) had $EAI = 0.286 \pm 0.019$. From this result, maximum concentration of dextran solution (20 mg/mL) contributed to increasing EAI twice, compared with normal blood. According to previous study [22], using streptozotocin-induced rats, variations of ESR were measured by varying duration of diabetes (D_{Diabetes}). Compared with control, ESR was increased over twice. From this results, EAI obtained by the proposed method can be effectively used to detect variations of ESR or RBCs aggregation.

From this experimental demonstration, it is found that the suggested method is able to quantify variations of RBC aggregation under continuous ESR. In other words, EAI is more effective when compared with AI. Furthermore, the method provides multiple data of RBC aggregation and ESR through a single experiment. The rheological property varied continuously, and thus it is very effective at obtaining several data points without repetitive tests. Compared with the previous methods, this proposed method had some merits including fabrication, multiple channels, and quantitative comparison of ESR value. First, the use of a liner cut from an adhesive sheet to form the master mold was newly suggested to simplify the fabrication process, compared to MEMS fabrication. Since RBC aggregation is quantified under stasis blood flows or lower shear rates, it is not imperative that each microfluidic channel should have uniform sizes for consistent blood flows. Thus, this method can remove MEMS fabrications, which require high cost and technical expertise. Second, when RBC aggregation varied over time, the repetitive test caused to increase scattering of aggregation index largely. Thus, multiple measurement of RBC aggregation was required to avoid large scattering due to repetitive test conducted for long time. At last, ESR relationship between modified conventional method and proposed method was obtained by conducting regression analysis technique. As a result, the EAI obtained by the proposed method gave comparable value of ESR, compared with the modified conventional ESR method.

4. Conclusions

In this study, a simple measurement technique of RBC aggregation under continuous ESR was demonstrated by sucking blood from a conical pipette tip into parallel microfluidic channels and quantifying image intensity, especially throughout single experiment. Two indices (AI and EAI) were suggested to quantify variations of RBC aggregation due to ESR in the conical pipette tip. First, when clamping the fluidic tube with the pinch valve, blood flow in each microfluidic channel was stopped shortly within 0.2 s. RBCs aggregation was measured immediately after clamping the tube with a pinch valve (i.e., close mode). Additionally, the compliance effect of the fluidic system had a negligible effect on transient blood flows. In addition, AI and EAI remained constant without respect to flow rate (Q) ($Q = 0.5 \text{ mL/h}$, 1 mL/h , and 2 mL/h). From this result, RBC aggregation and ESR were measured immediately by clamping the tube with a pinch valve, at the constant flow rate of 2 mL/h . Second, the proposed method was applied to measure the effect of hematocrit on the RBC aggregation under continuous ESR. AI remained over time with respect to hematocrit. However, EAI showed a significant difference with respect to hematocrit and measurement time. Compared with AI, EAI was more effective for evaluating continuous ESR in the conical pipette. After that, to quantify the relationship between the proposed method (i.e., EAI) and the modified conventional ESR method (i.e., H) with respect to hematocrit level, time constants (λ_{EAI} , λ_{H}) were obtained by conducting regression analysis with simple regression formula [i.e., $EAI = a_1 + a_2 \exp(-t/\lambda_{\text{EAI}})$, $H = b_1 + b_2 \exp(-t/\lambda_{\text{H}})$]. For two time constants (λ_{EAI} , λ_{H}) with respect to hematocrit, linear regression analysis indicated that the coefficient of R^2 showed a sufficient high value of $R^2 = 0.9521$. Thus, EAI can be effectively employed to measure ESR in the reservoir, compared with a modified conventional ESR method. The proposed method was finally applied to evaluate RBC aggregation (AI) and ESR (EAI)

for homogeneous aggregated RBCs. As a result, EAI and AI were gradually increased by varying concentration of dextran solution ranging from $C_{\text{dextran}} = 5 \text{ mg/mL}$ to $C_{\text{dextran}} = 20 \text{ mg/mL}$. To evaluate the relationship between the proposed method and a modified conventional ESR method, EAI and λ_H were obtained at specific concentrations of dextran solution. Since regression analysis showed higher value of $R^2 = 0.8789$, the EAI obtained by the proposed method gave comparable value of ESR, compared with the modified conventional ESR method. These experimental demonstrations indicated that the proposed method simultaneously measures RBC aggregation and ESR by using two indices (AI and EAI). Moreover, the method provides multiple data of RBC aggregation and ESR through a single experiment. Future tests will involve employing the proposed method to evaluate biophysical properties of bloods collected from cardiovascular diseases.

Supplementary Materials: The following are available online at <http://www.mdpi.com/2072-666X/9/7/318/s1>: Figure S1: Microscopic images for showing a microfluidic device with parallel microfluidic channel (n) [(a) $n = 1$, (b) $n = 2$, (c) $n = 3$, and (d) $n = 4$].

Author Contributions: Y.J.K. proposed this proposed method. Y.J.K. and B.J.K. prepared the master mold with adhesive sheet. Y.J.K. devised all the experimental procedures including the microfluidic device and carried out experiments. Y.J.K. wrote the manuscript.

Funding: This work was supported by Basic Science Research Program through NRF funded by the Ministry of Science and ICT (MSIT) (NRF-2018R1A1A1A05020389).

Conflicts of Interest: The author declares no conflict of interest.

References

1. Lanotte, L.; Mauer, J.; Mendez, S.; Fedosov, D.A.; Fromental, J.-M.; Claveria, V.; Nicoud, F.; Gompper, G.; Abkarian, M. Red cells' dynamic morphologies govern blood shear thinning under microcirculatory flow conditions. *Proc. Natl. Acad. Sci. USA* **2016**, *113*, 13289–13294. [[CrossRef](#)] [[PubMed](#)]
2. Baskurt, O.K.; Meiselman, H.J. Time course of electrical impedance during red blood cell aggregation in a glass tube: Comparison with light transmittance. *IEEE Trans. Biomed. Eng.* **2010**, *57*, 969–978. [[CrossRef](#)] [[PubMed](#)]
3. Isiksacan, Z.; Erel, O.; Elbuken, C. A portable microfluidic system for rapid measurement of the erythrocyte sedimentation rate. *Lab Chip* **2016**, *16*, 4682–4690. [[CrossRef](#)] [[PubMed](#)]
4. Popel, A.S.; Johnson, P.C. Microcirculation and hemorrheology. *Annu. Rev. Fluid Mech.* **2005**, *37*, 43–69. [[CrossRef](#)] [[PubMed](#)]
5. Bishop, J.J.; Popel, A.S.; Intaglietta, M.; Johnson, P.C. Rheological effects of red blood cell aggregation in the venous network: A review of recent studies. *Biorheology* **2001**, *38*, 263–274. [[PubMed](#)]
6. Yayan, J. Erythrocyte sedimentation rate as a marker for coronary heart disease. *Vasc. Health Risk Manag.* **2012**, *8*, 219–223. [[CrossRef](#)] [[PubMed](#)]
7. Bochen, K.; Krasowska, A.; Milaniuk, S.; Kulczyńska, M.; Prystupa, A.; Dzida, G. Erythrocyte sedimentation rate—an old marker with new applications. *JPCCR* **2011**, *5*, 50–55.
8. Piva, E.; Pajola, R.; Temporin, V.; Plebani, M. A new turbidimetric standard to improve the quality assurance of the erythrocyte sedimentation rate measurement. *Clin. Biochem.* **2007**, *40*, 491–495. [[CrossRef](#)] [[PubMed](#)]
9. Larsson, A.; Hansson, L.-O. Inflammatory activity: Capillary electrophoresis provides more information than erythrocyte sedimentation rate. *Uppsala J. Med. Sci.* **2005**, *110*, 151–158. [[CrossRef](#)] [[PubMed](#)]
10. Fabry, T.L. Mechanism of erythrocyte aggregation and sedimentation. *Blood* **1987**, *70*, 1572–1576. [[PubMed](#)]
11. Cha, C.-H.; Park, C.-J.; Cha, Y.J.; Kim, H.K.; Kim, D.H.; Bae, J.H.; Jung, J.-S.; Jang, S.; Chi, H.-S.; Lee, D.S.; et al. Erythrocyte sedimentation rate measurements by test 1 better reflect inflammation than do those by the Westergren method in patients with malignancy, autoimmune disease, or infection. *Am. J. Clin. Pathol.* **2009**, *131*, 189–194. [[CrossRef](#)] [[PubMed](#)]
12. Plebani, M.; Toni, S.D.; Sanzari, M.C.; Bernardi, D.; Stockreiter, E. A New method for measuring the erythrocyte sedimentation rate. *Am. J. Clin. Pathol.* **1998**, *110*, 334–340. [[CrossRef](#)] [[PubMed](#)]
13. Kaliviotis, E.; Sherwood, M.; Balabani, S. Partitioning of red blood cell aggregates in bifurcating microscale flows. *Sci. Rep.* **2017**, *7*, 44563. [[CrossRef](#)] [[PubMed](#)]

14. Kang, Y.J. Continuous and simultaneous measurement of the biophysical properties of blood in a microfluidic environment. *Analyst* **2016**, *141*, 6583–6597. [[CrossRef](#)] [[PubMed](#)]
15. Kang, Y.J.; Ha, Y.-R.; Lee, S.-J. Microfluidic-based measurement of erythrocyte sedimentation rate for biophysical assessment of blood in an in vivo malaria-infected mouse. *Biomicrofluidics* **2014**, *8*, 044114. [[CrossRef](#)] [[PubMed](#)]
16. Shin, S.; Hou, J.X.; Suh, J.-S. Measurement of cell aggregation characteristics by analysis of laser-backscattering in a microfluidic rheometry. *Korea-Aust. Rheol. J.* **2007**, *19*, 61–66.
17. Yeom, E.; Lee, S.J. Microfluidic-based speckle analysis for sensitive measurement of erythrocyte aggregation: A comparison of four methods for detection of elevated erythrocyte aggregation in diabetic rat blood. *Biomicrofluidics* **2015**, *9*, 024110. [[CrossRef](#)] [[PubMed](#)]
18. Zhanov, A.; Yang, S. Effects of aggregation on blood sedimentation and conductivity. *PLoS ONE* **2015**, *10*, e0129337. [[CrossRef](#)] [[PubMed](#)]
19. Kang, Y.J. Microfluidic-based measurement method of red blood cell aggregation under hematocrit variations. *Sensors* **2017**, *17*, 2037. [[CrossRef](#)] [[PubMed](#)]
20. Uyklu, M.; Cengiz, M.; Ulker, P.; Hever, T.; Tripette, J.; Connes, P.; Nemeth, N.; Meiselman, H.J.; Baskurt, O.K. Effects of storage duration and temperature of human blood on red cell deformability and aggregation. *Clin. Hemorheol. Microcirc.* **2009**, *41*, 269–278. [[PubMed](#)]
21. Lim, H.-J.; Nam, J.-H.; Lee, B.-K.; Suh, J.-S.; Shin, S. Alteration of red blood cell aggregation during blood storage. *Korea-Aust. Rheol. J.* **2011**, *23*, 67–70. [[CrossRef](#)]
22. Berezina, T.L.; Zaets, S.B.; Morgan, C.; Spillert, C.R.; Kamiyama, M.; Spolarics, Z.; Deitch, E.A.; Machiedo, G.W. Influence of storage on red blood cell rheological properties. *J. Surg. Res.* **2002**, *102*, 6–12. [[CrossRef](#)] [[PubMed](#)]
23. Bartholomeusz, D.A.; Boutté, R.; Andrade, J.D. Xurography: Rapid prototyping of microstructures using a cutting plotter. *J. Microelectromech. Syst.* **2005**, *14*, 1364–1374. [[CrossRef](#)]
24. Faustino, V.; Catarino, S.O.; Lima, R.; Minas, G. Biomedical microfluidic devices by using low-cost fabrication techniques: A review. *J. Biomech.* **2016**, *49*, 2280–2292. [[CrossRef](#)] [[PubMed](#)]
25. Pinto, E.; Faustino, V.; Rodrigues, R.O.; Pinho, D.; Garcia, V.; Miranda, J.M.; Lima, R. A rapid and low-cost nonlithographic method to fabricate biomedical microdevices for blood flow analysis. *Micromachines* **2015**, *6*, 121–135. [[CrossRef](#)]
26. Islam, M.; Natu, R.; Martinez-Duarte, R. A study on the limits and advantages of using a desktop cutter plotter to fabricate microfluidic networks. *Microfluid. Nanofluid.* **2015**, *19*, 973–985. [[CrossRef](#)]
27. Bento, D.; Sousa, L.; Yaginuma, T.; Garcia, V.; Lima, R.; Miranda, J.M. Microbubble moving in blood flow in microchannels: Effect on the cell-free layer and cell local concentration. *Biomed. Microdevices* **2017**, *19*, 6. [[CrossRef](#)] [[PubMed](#)]
28. Yeom, E.; Kim, H.M.; Park, J.H.; Choi, W.; Doh, J.; Lee, S.J. Microfluidic system for monitoring temporal variations of hemorheological properties and platelet adhesion in LPS-injected rats. *Sci. Rep.* **2017**, *7*, 1801. [[CrossRef](#)] [[PubMed](#)]



© 2018 by the authors. Licensee MDPI, Basel, Switzerland. This article is an open access article distributed under the terms and conditions of the Creative Commons Attribution (CC BY) license (<http://creativecommons.org/licenses/by/4.0/>).



Article

Fabrication and Hydrodynamic Characterization of a Microfluidic Device for Cell Adhesion Tests in Polymeric Surfaces

J. Ponmozhi ¹, J. M. R. Moreira ², E. J. Mergulhão ², J. B. L. M. Campos ¹ and J. M. Miranda ^{1,*}

¹ Transport Phenomena Research Center (CEFT), Department of Chemical Engineering, Faculty of Engineering, University of Porto, Rua Dr. Roberto Frias s/n, 4200-465 Porto, Portugal; jponmozhi@gmail.com (J.P.); jmc@fe.up.pt (J.B.L.M.C.)

² Laboratory for Process Engineering, Environment (LEPABE), Biotechnology and Energy, Department of Chemical Engineering, Faculty of Engineering, University of Porto, Rua Dr. Roberto Frias s/n, 4200-465 Porto, Portugal; joanarm@fe.up.pt (J.M.R.M.); filipem@fe.up.pt (F.J.M.)

* Correspondence: jmiranda@fe.up.pt

Received: 15 February 2019; Accepted: 29 April 2019; Published: 5 May 2019

Abstract: A fabrication method is developed to produce a microfluidic device to test cell adhesion to polymeric materials. The process is able to produce channels with walls of any spin coatable polymer. The method is a modification of the existing poly-dimethylsiloxane soft lithography method and, therefore, it is compatible with sealing methods and equipment of most microfluidic laboratories. The molds are produced by xurography, simplifying the fabrication in laboratories without sophisticated equipment for photolithography. The fabrication method is tested by determining the effective differences in bacterial adhesion in five different materials. These materials have different surface hydrophobicities and charges. The major drawback of the method is the location of the region of interest in a lowered surface. It is demonstrated by bacterial adhesion experiments that this drawback has a negligible effect on adhesion. The flow in the device was characterized by computational fluid dynamics and it was shown that shear stress in the region of interest can be calculated by numerical methods and by an analytical equation for rectangular channels. The device is therefore validated for adhesion tests.

Keywords: cell adhesion; biomedical coatings; microfabrication; computational fluid dynamics; microfluidics

1. Introduction

The term ‘biofilm’ was coined in 1981 [1] and refers to a community of microbial cells that is attached to a surface and enclosed in a self-produced exopolymeric matrix mainly composed by polysaccharide material [2]. Biofilm formation is due to the onset of adhesion of cells to a surface. The development of biofilms in medical devices is a common problem, which can lead to hospitalization, revision surgery due to microbiological implant colonization or mortality.

Recent reviews provide a source of evidence to the undesirable biofilm formation in medical devices [3–9]. These biofilms pose a challenge to the health care community. Currently, to reduce biofouling, there is a spurring development of smart polymers that are used for coating biomedical implants, artificial organs, lab on chip surfaces, implantable drug delivery systems [10], giving way to the development of next generation biomedical devices with reduced fouling.

Many types of measures were proposed to combat biofilms, like conventional usage of antibiotics or surfaces designed to inhibit initial adhesion of cells, for the first stage of biofilm formation [11]. A clear understanding of the initial adhesion mechanisms can lead to the development of ideal

biomaterials in which cells are unable to attach and growth of biofilms would be hindered [12]. Consequently, there arises a need to quantify and understand the initial adhesion phenomenon over diverse materials.

Different types of biomaterials were used throughout the past 30 years, for different types of biomedical applications. Ramakrishna, et al. [13] have given a brief introduction of different biocompatible polymers used for different types of implants. For example, poly-L-lactide acid (PLLA) is a biodegradable polymer, which degrades over time without harmful consequences to the body [14,15]. Different types of pins and screws, coated with PLLA, are used to fix the implants. Autografts, namely suspensory fixation, hamstring fixation [16] are used as fixing agents for femoral implants to reduce operation failures.

Recently, researchers started taking advantage of microfluidic devices for biofilm research [17–19] due to several benefits:

- The different biological cells can be monitored in real time with microscopy visualization techniques;
- Low-cost assays and reagents can be used in the microliter range helping in cost cutting;
- Leak-proof inlet and outlet connections can be made easily as the poly-dimethylsiloxane (PDMS) microfluidic channels are deformable;
- The surface can be easily modified and the geometry can be designed according to the application;
- The flow is always laminar, even at a high shear stress range.

In the particular case of adhesion tests, tests can be conducted in a simpler and smaller setup. The pumps required have lower power, the amount of fluid is smaller, and the setup is more flexible. Multiple tests can be conducted in parallel in a single chip and new geometries are easy to produce. Additionally, by using microfluidic devices, researchers can easily mimic the dynamical conditions of biomedical settings. It has been shown that adhesion is influenced by the flow patterns near the wall, the wall shear stress being the most important parameter used to characterize the flow influence on adhesion. For this reason, microdevices to study the wall adhesion must have well characterized hydrodynamic conditions. It is crucial that the wall shear stress is predictable given the flow rate used in the experiments. Additionally, geometrical features of the device should not interfere with the flow or with adhesion in the regions of interest. For this reason, straight channels are the preferred configuration for dynamic adhesion tests. New cells need to be validated to assure they are adequate for routine adhesion tests. Computational fluid dynamics (CFD) is usually used to characterize the flow and calculate the wall shear stress.

To aid the vast developing applications based on microfluidics, there are many conventional rapid prototyping techniques developed for microchannels fabrication. Duffy, et al. [20] demonstrated a method to produce PDMS channels for microfluidic applications. First, the channel is designed in Computer-Aided Design (CAD) software. The design is printed in a transparency and used as a mask for making a positive relief master mold. The master mold is produced in SU-8 polymer epoxy photoresist, step described in detail by Blanco, et al. [21] and Che-Hsin, et al. [22]. The PDMS channels are then casted with this mold and baked to obtain irreversibly sealed channels. Other conventional methods are commercially used for micromolding such as: micromilling [23], micropowder blasting [24], hot embossing [25], laser ablation [26] and stereo lithography [27].

Xurography is a technique developed by Bartholomeusz, et al. [28] utilizing a simple cutter plotter. The microchannels can be cut, according to the application, on vinyl films or other types of films. Positive relief molds, of thicknesses ranging from 25 to 1000 μm , can be generated in the cutter plotter and made ready for casting microchannels in less than 30 min. These molds can also be used as normal molds to produce PDMS microchannels through soft lithographic technique [29].

The foremost advantages of xurography technique are the reduced capital cost and manufacture time. The alternative to xurography is photolithography, a technique that needs expensive machines and clean rooms. Design modifications using photolithography techniques require more than a day,

with procedures with long pre and post bake steps. The main disadvantage of xurography is the low resolution that precludes the production of microchannels with dimensions smaller than 200 μm .

Microfabrication techniques that increase the range of possible materials to be used in microfluidics adhesion tests would contribute significantly to the research progress. The objective of adhesion tests is to evaluate different materials in their original form, and therefore a fabrication procedure that changes the material must be avoided. The new techniques must be compatible with existing equipment and with microfabrication techniques, the PDMS soft lithography being the most used. In PDMS soft lithography, irreversible PDMS-PDMS sealing has some important advantages: the bond between the device and the cover is strong and there is no need to use plasma oxygen that would change the surface properties being tested. With existing techniques, PDMS does not bond easily with any polymer unless a surface treatment is applied that would change the surface properties of the polymer. The techniques must also be inexpensive and with short development cycles.

In this work we introduce a technique to incorporate a small wall patch into a PDMS microchannel produced from molds easily made in-house by xurography. The molds can be produced through any other technique, but xurography has low costs and large accessibility. The wall patch can be made of different polymers. The technique is useful to produce channels for adhesion tests, by adapting a standard PDMS soft-lithography. The procedure is compatible with irreversible PDMS-PDMS sealing and does not require plasma oxygen or any other surface treatment. Care was taken to validate the device for adhesion tests performing adhesion experiments and flow numerical simulations. Since one of the key factors influencing cell adhesion is the wall shear stress, the flow in the device was characterized by computational fluid dynamics and the wall shear stress was calculated for the conditions studied.

2. Materials and Methods

2.1. Mold Preparation

The molds of the microchannels were produced by xurography [28], a technique that uses a cutter-plotter to produce molds by removing excess material from adhesive films. The design of the models was made in CorelDRAW. Afterwards, the design was copied to GreatCut software, which instructed an Expert24 GCC plotter (GCC, New Taipei City, Taiwan) to cut the microchannels.

Four different polymer films were tested to check compatibility with PDMS soft lithography [29]. Adhesive film obtained from Sadipal (Girona, Spain) showed to be the most suitable and was selected for mold production. The thickness of the Sadipal adhesive films used was 100 μm and this was the height of the microchannel.

2.2. PDMS Soft Lithography

Microchannels were made from poly-dimethylsiloxane (PDMS) using soft lithography techniques [29]. The microchannels were prepared with a homogenous mixture of PDMS and curing agent (Sylgard 184, Dow Corning, Midland, MI, USA) at a ratio of 5:1. A desiccator connected to the vacuum pump was used to remove the air bubbles formed during the PDMS mixing process. The PDMS mixture was poured over a mold and kept in the oven for 20 min at 80 $^{\circ}\text{C}$. After curing, the PDMS microchannel was peeled off from the mold. Holes of 1 mm in diameter were punched through the PDMS replicas, at both ends of the channel, to provide inlet and outlet flow with the help of a syringe tip. The PDMS microchannels were sealed with a PDMS coated thin slab (usually a glass slide, see next section) and kept in the oven for approximately 12 h at 80 $^{\circ}\text{C}$. The sealing method is based on partial curing PDMS-PDMS bonding without plasma treatment described in the literature [30].

2.3. Insertion of Polymer Wall Patches in the Channels

To test the adhesion of cells in a given material, a patch of the material must be inserted in one of the walls of the channel (usually the bottom wall). With this in mind, channels comprising 5 different

wall materials were fabricated by modifying the sealing slides. In one case, polystyrene cover was used as substrate to fabricate microchannels with polystyrene wall surfaces, while in the other 4 cases different polymers were spincoated over the sealing glass slide to insert a patch of polymer in the wall of the channel.

The coated glass slides, used to seal the channels, were prepared by a two-layer spin coating technique (Figure 1) using a WS-650S-6NPP-Lite Laurell Technologies spin coater (North Wales, PA, USA). Different volatile polymers and solvents were mixed in appropriate volume percentages (Table 1). The polymer solution was spincoated over the substrate (Figure 1b). After the formation of a polymeric film, by evaporation of the solvent, a scotch tape was pasted over the polymer surface (Figure 1c) and the PDMS was spincoated for 50 s at 5000 rpm over both the polymer and the scotch tape (Figure 1d). The scotch tape was carefully peeled off (Figure 1e) and the slide was baked for 5 min in the oven at 80 °C. A lowered surface (3 × 3 mm²) was left on the slide. The level of the lowered surface was determined from the experimental relation between thickness, coating speed and time [31,32] and found to be approximately 10 µm. The PDMS slab with the channel imprinted on it was sealed over the slide. The PDMS slab and the slide were aligned to ensure that the microchannel crossed the lowered surface.

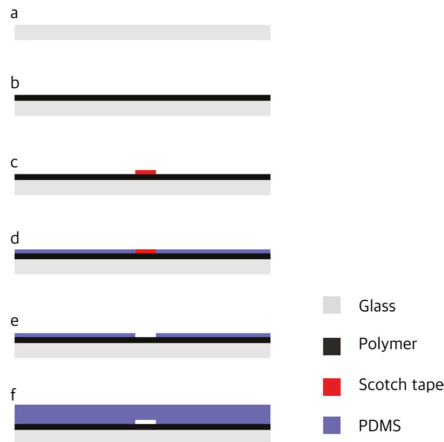


Figure 1. Fabrication procedure: (a) Substrate; (b) Polymer coating; (c) Scotch tape pasted over the polymer layer; (d) poly-dimethylsiloxane (PDMS) coating; (e) Removal of the Scotch tape; (f) Sealing with PDMS slab with the microchannel imprinted in it.

Table 1. Polymers and solvents used to prepare polymeric solutions.

Polymer	Solvent	Polymer Concentration (<i>w/w</i>)
Polyethylene oxide (PEO)	Dichloromethane (DCM)	1.14%
Poly-L-lactide acid (PLLA)	Dichloromethane (DCM)	5.00%
Polyamide (PA)	Trichloroethanol	0.49%
Polydimethylsiloxane (PDMS)	Curing agent (Sylgard 184)	10.0%

The procedure can also be used to test the adhesion to the substrate (e.g., polystyrene surfaces) and in this case the first layer spin coating step (Figure 1b) is skipped. This alternative procedure can be used to produce microchannels with other surfaces, such as glass, provided that a transparent thin slab is available.

The method described above produces microchannels with PDMS surface along most of its length and a small patch of a different material located in a lowered surface half-length from the inlet (see Figure 2). The lowered surface is an unavoidable side effect of the method. To allow for

PDMS-PDMS bonding, a layer of PDMS must be added above the polymer layer, with the exception of a small region that is not covered with PDMS and corresponds to the lowered surface of polymer. To test the effect of the lowered surface on bacterial cell adhesion, microchannels with PDMS walls along the full length of the microchannel were produced following the double layer technique, in which both layers are made of PDMS.

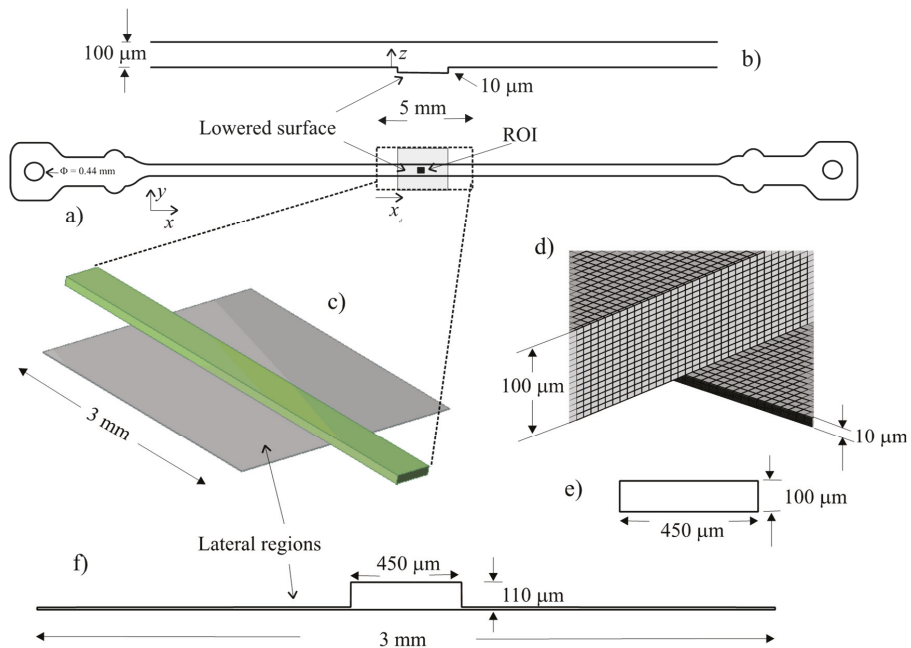


Figure 2. Microchannel representation and mesh details: (a) Microchannel, showing the lowered surface in grey, the region of interest in black and domain limits; (b) Profile representing the level of the upper and lower surfaces of the channel; (c) 3D representation of the numerical domain; (d) Lowered surface detail; (e) Microchannel cross-section outside the lowered region; (f) Cross-section available to the flow in the lowered surface region.

2.4. Bacteria and Culture Conditions

Escherichia coli JM109(DE3) was used, since this strain had already demonstrated a good adhesion capacity [33]. A starter culture was prepared as described by Teodosio, et al. [34] and incubated overnight. A volume of 60 mL from this culture was centrifuged (for 10 min at $3202\times g$) and the cells were washed twice with citrate buffer 0.05 M [35], pH 5.0. The pellet was then resuspended and diluted in the same buffer to obtain a cell concentration of 7.6×10^7 cell mL⁻¹.

2.5. Cell Adhesion Test

Cell adhesion tests with *E. coli* were performed with different polymer channels. Three trials were conducted for each material. The cell suspension was pumped using a syringe pump (Cetoni, neMESYS syringe pump, Korbussen, Germany) through a tygon® tube to the microfluidic channel. Adhesion was followed using a fluorescence inverted microscope (DMI 5000M, Leica Microsystems GmbH, Wetzlar, Germany) with a 40× objective. Microscopic images were captured with a CCD camera (Leica DFC350FX, Leica Microsystems GmbH, Wetzlar, Germany) with a time interval of 60 s. The image sequence obtained is in tiff format as recorded by Leica Application Suite software. The area of the region of interest was $312 \times 233 \mu\text{m}^2$. Initial adhesion experiments lasted for 1800 s.

2.6. Flow Conditions

The flow conditions studied are indicated in Table 2. With these conditions, the shear stress range is from 0.01 Pa to 1 Pa, covering the majority of shear stresses that can be found in the human body [36,37].

Table 2. Hydrodynamic conditions.

Flow Rate ($\mu\text{L}/\text{min}$)	Mean Velocity (m/s)	Reynolds Number	Nominal Wall Shear Stress (Equation (6)) (Pa)
0.667	2.50×10^{-4}	0.06	0.01
1.35	5.00×10^{-4}	0.12	0.02
15	5.56×10^{-3}	1.30	0.2
65.1	2.41×10^{-2}	5.65	1

2.7. Image Analysis

All the 30 images were imported to Image J software [38]. A low noise region was selected in the images using the crop tool. The images were converted from 8 bit to 32 bit to improve contrast. To set the scale for processing, the pixel aspect ratio was set to one. Depending on the images, they can be smoothed using the mean filter with 1 pixel as radius. Then, the background was subtracted with rolling ball radius ranging from 1 to 18 pixels. A light background was obtained with the *E. coli* cells bright and visible. The brightness and contrast were fine-tuned to get more accurate cell count. The threshold was adjusted, for the stack of images, to generate a black and white image containing black cells over a white background. Cells have a characteristic size range (from about $0.5 \mu\text{m}$ to $3 \mu\text{m}$) and particles and noise outside the size range were filtered out. Then the cells were automatically counted. The image for $t = 0$ already shows some cells, since the first image is taken some minutes after the flow starts. The number of cells for $t = 0$ was subtract from the total of cells counted.

By observation of the images obtained it was possible to distinguish cells from other particles due the characteristic shape of *E. coli* and the progressive increase of the number of cells throughout the experiments. The automatic counting method was compared with manual counting and this comparison showed that the automatic counting was accurate.

2.8. Hydrophobicity Test

The surface hydrophobicity can be determined by the contact angle formed between a surface and a polar and apolar liquid drop [39]. In this work, the contact angles were determined automatically by the sessile drop method in a contact angle meter (OCA 15 Plus; Dataphysics, Filderstadt, Germany) using water, formamide and α -bromonaphtalene (Sigma-Aldrich Corporation, St. Louis, MI, USA) as reference liquids [40]. For each surface, at least 10 measurements with each liquid were performed at $25 \pm 2 \text{ }^\circ\text{C}$.

According to van Oss [39], the total surface energy (γ^{TOT}) of a pure substance is the sum of the apolar Lifshitz-van der Waals components of the surface free energy (γ^{LW}) with the polar Lewis acid-base component (γ^{AB}):

$$\gamma^{\text{TOT}} = \gamma^{\text{LW}} + \gamma^{\text{AB}} \quad (1)$$

The polar AB component comprises the electron acceptor γ^+ and electron donor γ^- parameters, and is given by:

$$\gamma^{\text{AB}} = 2\sqrt{\gamma^+\gamma^-} \quad (2)$$

The surface energy components of a solid surface (s) are obtained by measuring the contact angles (θ) with the three different liquids (l), with known surface tension components, followed by the simultaneous resolution of three equations of the type:

$$(1 + \cos \theta)\gamma_l = 2\left(\sqrt{\gamma_s^{LW}\gamma_l^{LW}} + \sqrt{\gamma_s^+\gamma_l^-} + \sqrt{\gamma_s^-\gamma_l^+}\right) \quad (3)$$

The degree of surface hydrophobicity is expressed as the free energy of interaction ($\Delta G \text{ mJ}\cdot\text{m}^{-2}$) between two entities of that surface immersed in a polar liquid (such as water (w) as a reference solvent). ΔG was calculated from the surface tension components of the interacting entities, using the equation:

$$\Delta G = -2\left(\sqrt{\gamma_s^{LW}} - \sqrt{\gamma_w^{LW}}\right)^2 + 4\left(\sqrt{\gamma_s^+\gamma_w^-} + \sqrt{\gamma_s^-\gamma_w^+} - \sqrt{\gamma_s^+\gamma_s^-} - \sqrt{\gamma_w^+\gamma_w^-}\right) \quad (4)$$

If the interaction between the two entities is stronger than the interaction of each entity with water, $\Delta G < 0$, the material is hydrophobic and if $\Delta G > 0$, the material is hydrophilic.

Additionally, the surface charge of each polymer was characterized through the zeta potential. Particle suspensions of each material [41] were prepared in order to measure the electrophoretic mobility, using a Nano Zetasizer (Malvern Instruments, Malvern, Worcestershire, UK).

2.9. Numerical Simulations

The flow in the cell was simulated by numerical methods to clarify the stability and the predictability of the flow patterns near the observation region. The microchannel used has a rectangular cross section of $450 \times 100 \mu\text{m}$ and a length of 15 mm. The channel is represented in Figure 2a. In Figure 2a it is possible to observe the lowered surface represented in grey, the region of interest in black and the limits of the numerical domain. The inlet and outlet have a diameter (D_{in}) of 0.44 mm (represented in Figure 2a). A profile along the channel, showing the level of the lower and upper walls, is represented in Figure 2b.

A section of the microchannel, around the visualization region, was selected for simulation domain (Figure 2c). This region includes the lowered surface, which results from the fabrication method, where the region of interest is located. The length of the domain is 5 mm. The lowered surface has a length of 3 mm and a width of 3 mm. The lowered surface level is approximately $10 \mu\text{m}$. The cross section available for flow in the lowered surface region is shown in Figure 2f. Outside the lowered region the cross section available for the flow is rectangular (Figure 2e). A detail of the mesh used is shown in Figure 2d.

The flow regime was determined by the Reynolds number based on the equivalent diameter of the channel:

$$Re = \frac{2\rho Q}{(W + H)\mu} \quad (5)$$

where ρ and μ are the density and viscosity of the fluid, respectively, Q the flow rate, W the width of the channel and H the depth of the channel.

Numerical values of the wall shear stress (WSS) are compared with data from the analytical solution for the flow in a parallel plate channel [42]:

$$\tau = \mu \frac{3Q}{2\left(\frac{H}{2}\right)^2 W} \quad (6)$$

Nominal wall shear stress, used to distinguish the experiments, was calculated through the analytical Equation (6). The real wall shear stress, as given by the numerical simulation, is slightly different.

The equation for the lowered surface can be corrected by the following equation:

$$\tau_{ls} = \tau \left(\frac{H}{H_{ls}} \right)^2 \tag{7}$$

where τ is the wall shear stress in the straight channel (outside the lowered surface) and H_{ls} the depth of the channel in the lowered surface section.

Numerical simulations were made with the commercial code Ansys Fluent CFD package (version 14.5) by solving Navier–Stokes equations. A model of the microchannel was built in Design Modeler 14.5 and was discretized into a grid of 278,000 cells by Meshing 14.5. The QUICK scheme [43] was used for the discretization of the momentum equations and the PRESTO! scheme for the discretization of the pressure terms. The velocity–pressure coupled equations were solved by the PISO algorithm [44]. The no slip boundary condition was considered for all the walls. Simulations were made in steady state mode until convergence. The properties of water (density and viscosity) at 37 °C were used.

Corrected numerical results were calculated by applying Equation (7). The value of τ used was the wall shear stress of a straight channel (without a lowered surface) previously obtained numerically.

3. Results

3.1. Hydrophobicity

The surface properties of the different materials fabricated are presented in Table 3. Results showed that PLLA, PDMS, PA and PS are hydrophobic surfaces ($\Delta G < 0 \text{ mJ}\cdot\text{m}^{-2}$) whereas PEO is hydrophilic ($\Delta G > 0 \text{ mJ}\cdot\text{m}^{-2}$). For illustration, water droplets are shown in Figure 3 for different materials. Additionally, the zeta potential results showed that all the polymers’ surfaces have a negative charge. The range of surface characteristics assures that the procedure can be used to study a large range of surface parameters, a very important factor for bacterial adhesion studies, wherein it is desirable to cover the characteristics of all available materials used in medical or industrial applications.

Table 3. Surface properties of different materials.

Polymer Surface	Hydrophobicity $\Delta G \text{ (mJ}\cdot\text{m}^{-2})$	Zeta Potential (mV)
PLLA	−65.32	−27.9
PDMS	−61.82	−29.3
PA	−37.58	−28.0
PEO	0.350	−11.0
PS	−49.56	−29.8



Figure 3. Water droplet over the surfaces of PDMS, PA, PS, poly-L-lactide acid (PLLA) and Polyethylene oxide (PEO) illustrating the hydrophobicity of the materials.

3.2. Adhesion

Adhesion tests were performed for all 5 materials cited in Table 3. A subset of the results obtained (for PS, PLLA and PDMS) is represented in Figure 4. The images show the surface after 1800 s assays and the processed images. Cells are visible in all three surfaces studied and so the images can be processed to obtain a clean image for cell counting. Adhesion data for the 1800 s of test are shown in Figure 5. The data show that different materials have distinct adhesion behaviour. A higher bacterial adhesion was observed on the PDMS surface during the 1800 s assay while a lower bacterial adhesion was observed on the PS surface. Additionally, it was observed that bacterial adhesion increases linearly with time. Additional results are shown for PA and PEO in Figures 6 and 7.

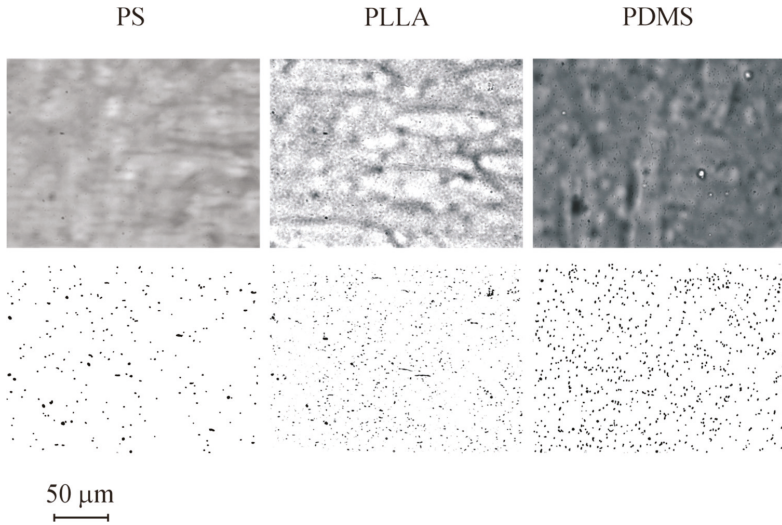


Figure 4. Images for adhesion in different materials for $t = 1800$ s: PS, PLLA and PDMS. Top row is before and bottom row after image processing. Results obtained for nominal wall shear stress of 0.02 Pa.

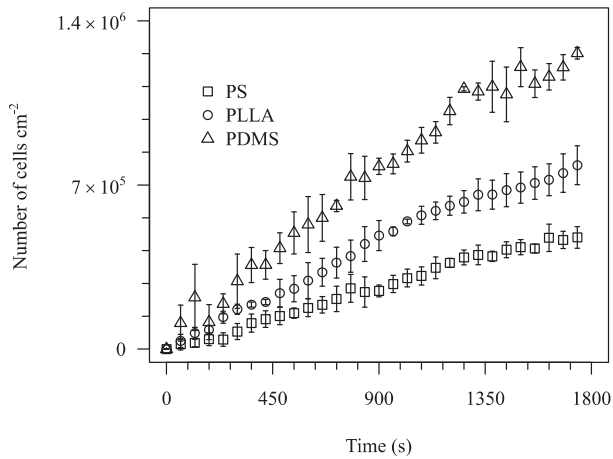


Figure 5. Number of adhered cells per cm² for PS, PLLA and PDMS for nominal wall shear stress of 0.02 Pa.

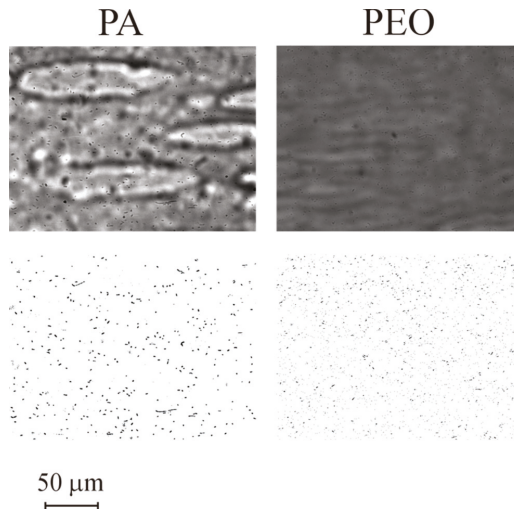


Figure 6. Images for adhesion in different materials for $t = 1800$ s: PA and PEO. Top row is before and bottom row after image processing. Results obtained for nominal wall shear stress of 0.01 Pa.

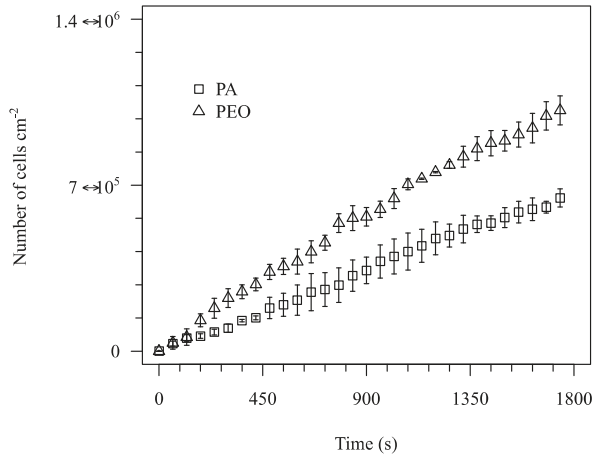


Figure 7. Number of adhered cells per cm² for PA and PEO for nominal wall shear stress of 0.01 Pa.

An experiment was performed to test if the unevenness of the channel can change significantly the adhesion rate. To achieve this goal, experiments were performed in a PDMS channel produced by the same fabrication method. First, a layer of PDMS was spincoated over a glass slide. Then, a scotch tape was used to protect a small region, as described in the methods section. Then, a second layer of PDMS was spincoated over the first one. The slide was then used to produce the channels. Figure 8 shows the bacterial cell density along the channel after 1800 s for three different shear stresses. As can be seen in the figure, the presence of a lowered surface in the scotch tape location is not perceptible. The variability of adhesion along the channel is much higher than any possible effect produced by the lowered surface.

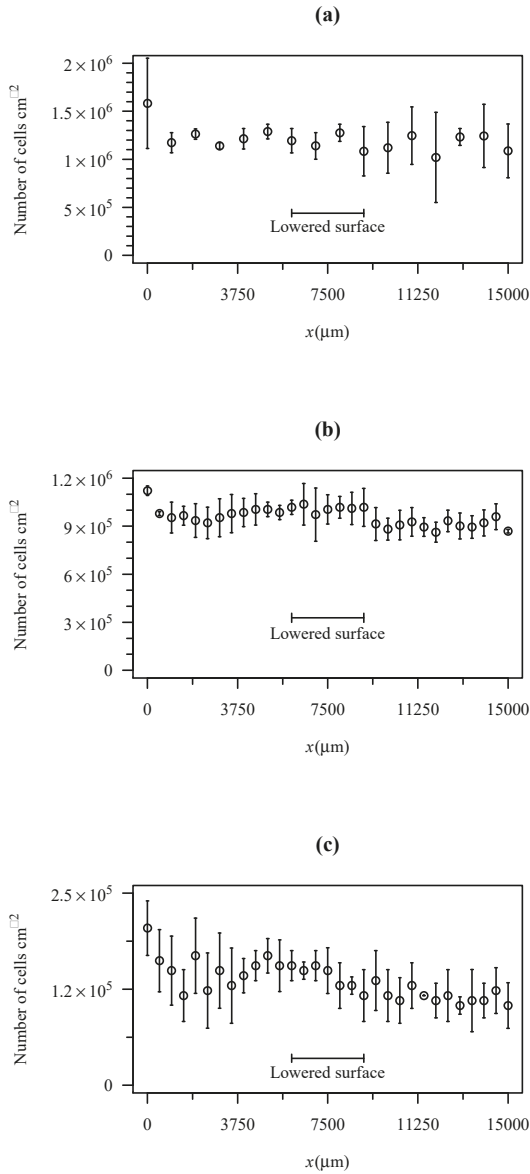


Figure 8. Cell density after 1800 s of adhesion on PDMS for three different nominal wall shear stresses. (a) WSS = 0.02 Pa; (b) WSS = 0.2 Pa; (c) WSS = 1 Pa.

3.3. Numerical Simulation

Wall shear stress (WSS) at the bottom wall and velocity fields at the midplan are represented in Figures 9 and 10, respectively. These figures show a small velocity decrease in the region of the channel crossing the lowered surface. Lateral regions (see Figure 2) of the lowered surface have an almost zero velocity. The wall shear stress is also smaller in the part of the channel that crosses the lowered surface region, where the region of interest is located.

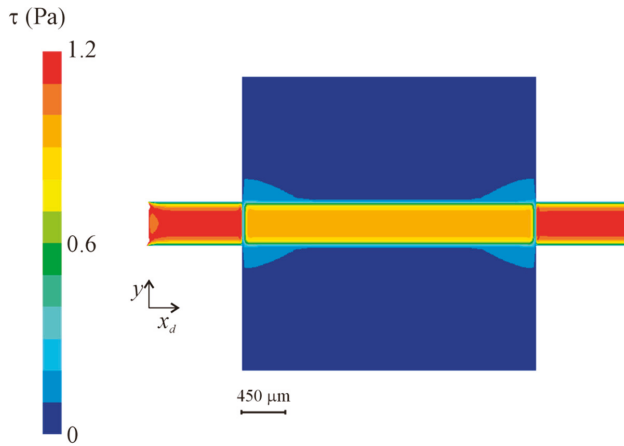


Figure 9. Wall shear stress (WSS) in the lowered surface region for a nominal wall shear stress of 1 Pa.

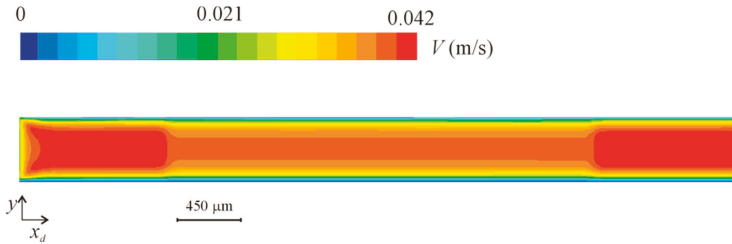


Figure 10. Velocity magnitude in the midplan in the lowered surface region for a nominal wall shear stress of 1 Pa.

Figure 11 shows the wall shear stress along the centreline of the bottom wall of the channel. The figure is for the higher nominal WSS studied (1 Pa), but results for the other wall shear stresses, not shown here, are similar. Some edge effects are observable, mainly due to the influence of the inlet and outlet boundary conditions. At the inlet, the edge effects are small, revealing that the flow develops in a short length, and enters fully developed in the lowered surface region. In this lowered region, the wall shear stress is smaller. A small transition region exists of about 300 μm .

The analytical Equation (6) underpredicts the numerical WSS data in the channel outside the lowered region. This result is expected since the analytical equation is exact only for channels with an infinite width. In the present case the ratio between the width and the height of the channel is 4.5, which implies that the velocity is higher than what would be in a channel with infinite width.

The correction—Equation (7)—made on the analytical equation underpredicts the WSS in the lowered surface, while the correction made to the numerical results predicts correctly the WSS in the lowered surface.

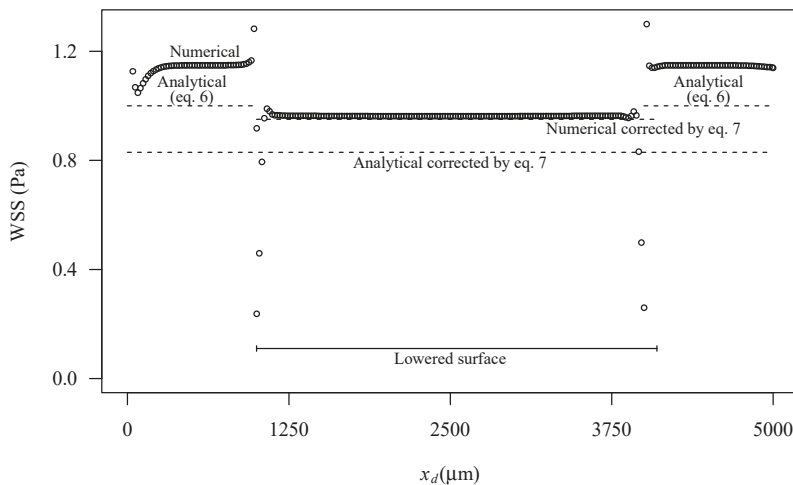


Figure 11. Wall shear stress along the centreline at the bottom surface in the lowered region for a nominal wall shear stress of 1 Pa. Figure shows numerical predictions (symbols), predictions based on analytical Equation (6) and predictions with corrections based on Equation (7). Local domain coordinates are used to represent the distance from the domain inlet.

4. Discussion

A technique developed to create microchannels with polymeric patches for adhesion tests allows the fabrication of patches with several different materials. Surface hydrophobicities of the materials used in this work, range from -65.32 to 0.350 mJ m^{-2} and zeta potential from -11.0 to -29.8 mV. From the bacterial adhesion results on five selected materials (PLLA, PDMS, PA, PEO and PS), it was verified that these different materials led to different adhesion behaviours. According to the thermodynamic theory, a higher bacterial adhesion would be expected on the most hydrophobic surface and a decrease would be expected with decreasing hydrophobicity [45]. A lower bacterial adhesion was in fact obtained in PS, the less hydrophobic surface. However, a higher number of adhered bacteria was observed in PDMS and not in the most hydrophobic surface, PLLA and PEO, which is hydrophilic, has a higher adhesion than PA, which is hydrophobic. Additionally, no correlation between bacterial adhesion and surface charge was found. Although it was verified that bacterial adhesion was not controlled by surface hydrophobicity or charge, other specific parameters of each surface, such as chemical composition, may have affected bacterial adhesion. The effect of surface properties may also be concealed by the flow conditions. The results presented in this paper are for WSS of 0.01 – 0.02 Pa and low Reynolds number, for which cell sedimentation has relevant contribution to cell adhesion. These results show that different materials, with different properties, were in fact placed in a specific position in the microchannel and induce different bacterial adhesion.

One of the inherent weaknesses of the method is the fact that a region of the microchannel is lowered, i.e., there is a small gap of about 10 μm in the edges of this region. The tests performed with PDMS surfaces (Figure 8) for wall shear stresses between 0.02 Pa and 1 Pa show that the lowered surface does not influence adhesion. Hydrodynamic consequences of this lowered surface were studied in detail by CFD. The CFD study shows that the region has a smaller WSS. Nevertheless, the WSS in this region is stable and calculable by Equation (7). Overall, the results obtained showed that the device performs predictably in adhesion tests and can be adopted for general use in routine tests.

The accuracy of the channels obtained by the current procedure is limited by the accuracy of the underlying microfabrication technique. In the current work the channels were fabricated by xurography, which has an error of approximately 5% to produce channels of 450 μm width [46].

5. Conclusions

A new low-cost device for adhesion tests in polymeric surfaces, which can be fabricated in a laboratory with low resources, was developed and characterized. The most expensive equipment used in the fabrication procedure is a spin coater. The fabrication method is suitable to produce microchannels to test bacterial adhesion in different materials, provided that the material is available as a transparent substrate or that the material is a spincoatable transparent polymer that can be casted by solvent evaporation.

The section of the channel containing the region of interest is lowered. However, this lowered surface has a predictable effect on wall shear stress and a negligible one on bacterial adhesion, as shown by adhesion tests and CFD.

The device was validated to be used to perform bacterial adhesion tests under relevant shear stresses. This work contributes to increase the options for experimenters to perform adhesion tests in microfluidic devices, with advantages related to reactant consumption and parallelization.

Author Contributions: J.P. conducted the experimental work and data processing and wrote the first draft of the paper. J.M.R.M. prepared the cell suspensions and contributed to the hydrophobicity tests. F.J.M. supervised the biological component of the work. J.B.L.M.C. contributed to computational fluid dynamics component of the work. J.M.M. conducted the numerical simulations and supervised the microfluidics component of the work. All authors read the paper and added contributions for improvements.

Funding: This work was funded by FEDER funds through the Operational Programme for Competitiveness Factors—COMPETE, ON.2—O Novo Norte—North Portugal Regional Operational Programme and National Funds through FCT- Foundation for Science and Technology under the projects: PEst-OE/EME/UI0532, PEst-C/EQB/UI0511, NORTE-07-0124-FEDER-000025—RL2_Environment&Health and PTDC/EQU-FTT/105535/2008.

Conflicts of Interest: The authors have no conflict of interests.

References

1. McCoy, W.F.; Bryers, J.D.; Robbins, J.; Costerton, J.W. Observations of Fouling Biofilm Formation. *Can. J. Microbiol.* **1981**, *27*, 910–917. [[CrossRef](#)]
2. Donlan, R.M. Biofilms: Microbial Life on Surfaces. *Emerg. Infect. Dis.* **2002**, *8*, 881–890. [[CrossRef](#)] [[PubMed](#)]
3. Costerton, J.W.; Stewart, P.S.; Greenberg, E.P. Bacterial Biofilms: A Common Cause of Persistent Infections. *Science* **1999**, *284*, 1318–1322. [[CrossRef](#)]
4. Harris, L.G.; Richards, R.G. Staphylococci and Implant Surfaces: A Review. *Injury* **2006**, *37* (Suppl. 2), S3–S14. [[CrossRef](#)] [[PubMed](#)]
5. Kong, K.F.; Vuong, C.; Otto, M. Staphylococcus Quorum Sensing in Biofilm Formation and Infection. *Int. J. Med. Microbiol. IJMM* **2006**, *296*, 133–139. [[CrossRef](#)] [[PubMed](#)]
6. Arciola, C.R.; Campoccia, D.; Speziale, P.; Montanaro, L.; Costerton, J.W. Biofilm Formation in Staphylococcus Implant Infections. A Review of Molecular Mechanisms and Implications for Biofilm-Resistant Materials. *Biomaterials* **2012**, *33*, 5967–5982. [[CrossRef](#)]
7. Bjarnsholt, T.; Alhede, M.; Alhede, M.; Eickhardt-Sorensen, S.R.; Moser, C.; Kuhl, M.; Jensen, P.O.; Hoiby, N. The in Vivo Biofilm. *Trends Microbiol.* **2013**, *21*, 466–474. [[CrossRef](#)] [[PubMed](#)]
8. Seth, A.K.; Geringer, M.R.; Hong, S.J.; Leung, K.P.; Mustoe, T.A.; Galiano, R.D. In Vivo Modeling of Biofilm-Infected Wounds: A Review. *J. Surg. Res.* **2012**, *178*, 330–338. [[CrossRef](#)] [[PubMed](#)]
9. Esposito, S.; Purrello, S.M.; Bonnet, E.; Novelli, A.; Tripodi, F.; Pascale, R.; Unal, S.; Milkovich, G. Central Venous Catheter-Related Biofilm Infections: An Up-To-Date Focus on Meticillin-Resistant Staphylococcus Aureus. *J. Glob. Antimicrob. Resist.* **2013**, *1*, 71–78. [[CrossRef](#)] [[PubMed](#)]
10. Middleton, J.C.; Tipton, A.J. Synthetic Biodegradable Polymers as Orthopedic Devices. *Biomaterials* **2000**, *21*, 2335–2346. [[CrossRef](#)]
11. Abu-Lail, N.I.; Beyenal, H. Chapter 5.2—Characterization of Bacteria–Biomaterial Interactions, from a Single Cell to Biofilms. In *Characterization of Biomaterials*; Bandyopadhyay, A., Bose, S., Eds.; Academic Press: Oxford, OH, USA, 2013; pp. 207–253.
12. Dillow, A.K.; Tirrell, M. Targeted Cellular Adhesion at Biomaterial Interfaces. *Curr. Opin. Solid State Mater. Sci.* **1998**, *3*, 252–259. [[CrossRef](#)]

13. Ramakrishna, S.; Mayer, J.; Wintermantel, E.; Leong, K.W. Biomedical Applications of Polymer-Composite Materials: A Review. *Compos. Sci. Technol.* **2001**, *61*, 1189–1224. [[CrossRef](#)]
14. Meng, B.; Wang, J.; Zhu, N.; Meng, Q.Y.; Cui, F.Z.; Xu, Y.X. Study of Biodegradable and Self-Expandable Plla Helical Biliary Stent in Vivo and in Vitro. *J. Mater. Sci. Mater. Med.* **2006**, *17*, 611–617. [[CrossRef](#)] [[PubMed](#)]
15. Tamai, H.; Igaki, K.; Kyo, E.; Kosuga, K.; Kawashima, A.; Matsui, S.; Komori, H.; Tsuji, T.; Motohara, S.; Uehata, H. Initial and 6-Month Results of Biodegradable Poly-L-Lactic Acid Coronary Stents in Humans. *Circulation* **2000**, *102*, 399–404. [[CrossRef](#)]
16. Colvin, A.; Sharma, C.; Parides, M.; Glasgow, J. What is the Best Femoral Fixation of Hamstring Autografts in Anterior Cruciate Ligament Reconstruction?: A Meta-Analysis. *Clin. Orthop. Relat. Res.* **2011**, *469*, 1075–1081. [[CrossRef](#)] [[PubMed](#)]
17. Beebe, D.J.; Mensing, G.A.; Walker, G.M. Physics and Applications of Microfluidics in Biology. *Annu. Rev. Biomed. Eng.* **2002**, *4*, 261–286. [[CrossRef](#)]
18. Jain, K.K. *Biochips and Microarrays: Technology and Commercial Potential*; Urch Publishing: London, UK, 2000.
19. Stone, H.A.; Stroock, A.D.; Ajdari, A. Engineering Flows in Small Devices Microfluidics Towards Lab-On-A-Chip. *Annu. Rev. Fluid Mech.* **2004**, *36*, 381–411. [[CrossRef](#)]
20. Duffy, D.C.; McDonald, J.C.; Schueller, O.J.; Whitesides, G.M. Rapid Prototyping of Microfluidic Systems in Poly (Dimethylsiloxane). *Anal. Chem.* **1998**, *70*, 4974–4984. [[CrossRef](#)] [[PubMed](#)]
21. Blanco, F.J.; Agirregabiria, M.; Garcia, J.; Berganzo, J.; Tijero, M.; Arroyo, M.T.; Ruano, J.M.; Aramburu, I.; Mayora, K. Novel Three-Dimensional Embedded Su-8 Microchannels Fabricated Using a Low Temperature Full Wafer Adhesive Bonding. *J. Micromech. Microeng.* **2004**, *14*, 1047–1056. [[CrossRef](#)]
22. Che-Hsin, L.; Gwo-Bin, L.; Bao-Wen, C.; Guan-Liang, C. A New Fabrication Process for Ultra-Thick Microfluidic Microstructures Utilizing Su-8 Photoresist. *J. Micromech. Microeng.* **2002**, *12*, 590.
23. Tseng, A.A. Recent Developments in Micromilling Using Focused Ion Beam Technology. *J. Micromech. Microeng.* **2004**, *14*, R15–R34. [[CrossRef](#)]
24. Schlautmann, S.; Wensink, H.; Schasfoort, R.; Elwenspoek, M.; Van Den Berg, A. Powder-Blasting Technology as an Alternative Tool for Microfabrication of Capillary Electrophoresis Chips with Integrated Conductivity Sensors. *J. Micromech. Microeng.* **2001**, *11*, 386–389. [[CrossRef](#)]
25. Becker, H.; Heim, U. Hot Embossing as a Method for the Fabrication of Polymer High Aspect Ratio Structures. *Sens. Actuators A Phys.* **2000**, *83*, 130–135. [[CrossRef](#)]
26. Morales, A.M.; Lieber, C.M. A Laser Ablation Method for the Synthesis of Crystalline Semiconductor Nanowires. *Science* **1998**, *279*, 208–211. [[CrossRef](#)]
27. Ikuta, K.; Hirowatari, K. In Real Three Dimensional Micro Fabrication Using Stereo Lithography and Metal Molding. In Proceedings of the IEEE Micro Electro Mechanical Systems, Fort Lauderdale, FL, USA, 7–10 February 1993; pp. 42–47.
28. Bartholomeusz, D.A.; Boutte, R.W.; Andrade, J.D. Xurography: Rapid Prototyping of Microstructures Using a Cutting Plotter. *J. Microelectromech. Syst.* **2005**, *14*, 1364–1374. [[CrossRef](#)]
29. Xia, Y.; Whitesides, G.M. Soft Lithography. *Annu. Rev. Mater. Sci.* **1998**, *28*, 153–184. [[CrossRef](#)]
30. Eddings, M.A.; Johnson, M.A.; Gale, B.K. Determining the Optimal Pdms–Pdms Bonding Technique for Microfluidic Devices. *J. Micromech. Microeng.* **2008**, *18*, 067001. [[CrossRef](#)]
31. Zhang, W.; Ferguson, G.; Tatic-Lucic, S. Elastomer-Supported Cold Welding for Room Temperature Wafer-Level Bonding. In Proceedings of the 17th IEEE International Conference on MEMS, Maastricht, The Netherlands, 25–29 January 2004; pp. 741–744.
32. Koschwanetz, J.H.; Carlson, R.H.; Meldrum, D.R. Thin Pdms Films Using Long Spin Times or Tert-Butyl Alcohol as a Solvent. *PLoS ONE* **2009**, *4*, e4572. [[CrossRef](#)] [[PubMed](#)]
33. Moreira, J.M.; Araujo, J.D.; Miranda, J.M.; Simoes, M.; Melo, L.F.; Mergulhao, F.J. The Effects of Surface Properties on Escherichia Coli Adhesion are Modulated by Shear Stress. *Coll. Surf. B Biointerfaces* **2014**, *123*, 1–7. [[CrossRef](#)] [[PubMed](#)]
34. Teodosio, J.S.; Simoes, M.; Melo, L.F.; Mergulhao, F.J. Flow Cell Hydrodynamics and Their Effects on E. Coli Biofilm Formation under Different Nutrient Conditions and Turbulent Flow. *Biofouling* **2011**, *27*, 1–11. [[CrossRef](#)] [[PubMed](#)]
35. Simoes, M.; Simoes, L.C.; Cleto, S.; Pereira, M.O.; Vieira, M.J. The Effects of a Biocide and a Surfactant on the Detachment of Pseudomonas Fluorescens from Glass Surfaces. *Int. J. Food Microbiol.* **2008**, *121*, 335–341. [[CrossRef](#)] [[PubMed](#)]

36. Ronald, L.S. *Analysis of Pathoadaptive Mutations in Escherichia Coli*; ProQuest: Michigan, MI, USA, 2008.
37. Michelson, A. *Platelets*, 2nd ed.; Academic Press: Cambridge, MA, USA, 2002.
38. Schneider, C.A.; Rasband, W.S.; Eliceiri, K.W. Nih Image to Imagej: 25 Years of Image Analysis. *Nat. Methods* **2012**, *9*, 671–675. [[CrossRef](#)]
39. Van Oss, C. *Interfacial Forces in Aqueous Media*; Marcel Dekker Inc.: New York, NY, USA, 1994.
40. Janczuk, B.; Chibowski, E.; Bruque, J.M.; Kerkeb, M.L.; Caballero, F.G. On the Consistency of Surface Free-Energy Components as Calculated from Contact Angles of Different Liquids—An Application to the Cholesterol Surface. *J. Colloid Interface Sci.* **1993**, *159*, 421–428. [[CrossRef](#)]
41. Simoes, L.C.; Simoes, M.; Vieira, M.J. Adhesion and Biofilm Formation on Polystyrene by Drinking Water-Isolated Bacteria. *Antonie Van Leeuwenhoek* **2010**, *98*, 317–329. [[CrossRef](#)]
42. Busscher, H.J.; Van Der Mei, H.C. Microbial Adhesion in Flow Displacement Systems. *Clin. Microbiol. Rev.* **2006**, *19*, 127–141. [[CrossRef](#)]
43. Leonard, B.P. A Stable and Accurate Convective Modelling Procedure Based on Quadratic Upstream Interpolation. *Comput. Methods Appl. Mech. Eng.* **1979**, *19*, 59–98. [[CrossRef](#)]
44. Issa, R.I. Solution of the Implicitly Discutised Fluid Flow Equations by Operating-Splitting. *J. Comput. Phys.* **1986**, *62*, 40–65. [[CrossRef](#)]
45. Absolom, D.R.; Lamberti, F.V.; Policova, Z.; Zingg, W.; Van Oss, C.J.; Neumann, A.W. Surface Thermodynamics of Bacterial Adhesion. *Appl. Environ. Microbiol.* **1983**, *46*, 90–97.
46. Pinto, E.; Faustino, V.; Rodrigues, R.; Pinho, D.; Garcia, V.; Miranda, J.; Lima, R. A Rapid and Low-Cost Nonlithographic Method to Fabricate Biomedical Microdevices for Blood Flow Analysis. *Micromachines* **2015**, *6*, 121–135. [[CrossRef](#)]



© 2019 by the authors. Licensee MDPI, Basel, Switzerland. This article is an open access article distributed under the terms and conditions of the Creative Commons Attribution (CC BY) license (<http://creativecommons.org/licenses/by/4.0/>).



Article

Multinucleation of Incubated Cells and Their Morphological Differences Compared to Mononuclear Cells

Shukei Sugita *, Risa Munechika and Masanori Nakamura

Department of Engineering, Nagoya Institute of Technology, Nagoya 466-8555, Japan; mmm5ar07dd@gmail.com (R.M.); nakamura.masanori@nitech.ac.jp (M.N.)

* Correspondence: sugita.shukei@nitech.ac.jp; Tel.: +81-52-735-7125

Received: 29 January 2019; Accepted: 22 February 2019; Published: 25 February 2019

Abstract: Some cells cultured in vitro have multiple nuclei. Since cultured cells are used in various fields of science, including tissue engineering, the nature of the multinucleated cells must be determined. However, multinucleated cells are not frequently observed. In this study, a method to efficiently obtain multinucleated cells was established and their morphological properties were investigated. Initially, we established conditions to quickly and easily generate multinucleated cells by seeding a *Xenopus* tadpole epithelium tissue-derived cell line (XTC-YF) on less and more hydrophilic dishes, and incubating the cultures with medium supplemented with or without Y-27632—a ROCK inhibitor—to reduce cell contractility. Notably, 88% of the cells cultured on a less hydrophilic dish in medium supplemented with Y-27632 became multinucleate 48 h after seeding, whereas less than 5% of cells cultured under other conditions exhibited this morphology. Some cells showed an odd number (three and five) of cell nuclei 72 h after seeding. Multinucleated cells displayed a significantly smaller nuclear area, larger cell area, and smaller nuclear circularity. As changes in the morphology of the cells correlated with their functions, the proposed method would help researchers understand the functions of multinucleated cells.

Keywords: multinucleated cells; XTC-YF cells; morphological analysis; Y-27632; hydrophobic dish

1. Introduction

Most cell types normally have a single nucleus, whereas some types of cells contain multiple nuclei. Nuclear division without cytokinesis occurs in some types of mammalian cells, including megakaryocytes, which produce blood platelets, and some hepatocytes and heart muscle cells [1]. Cells of the monocyte/macrophage lineage can fuse and form large multinucleated giant cells that have long been recognized as a histopathological hallmark of tuberculosis, schistosomiasis and other granulomatous diseases [2]. Even mononuclear cells sometimes become multinucleated cells in culture [3].

Some studies indicate concerns of multinucleated cells to pathophysiological events. When endothelial cells obtained from sites of arteriosclerosis are cultured, they exhibit a multinucleated morphology [4]. Multinucleated cells are frequently seen in malignant neoplasms [5]. Multinucleated giant cells are found in epulis, during unusual patterns of chronic inflammation, and are responsible for eliminating foreign bodies and cell debris by phagocytosis [6].

The mechanism by which the properties of mononuclear cells are altered to a multinucleated morphology is not completely understood. Since researchers have attempted to use cells cultured in vitro for tissue engineering [7], understanding of the properties of multinucleated cells is important to produce risk-free tissues.

The ultimate goal of the present study is to investigate the properties of multinucleated cells. For the purpose, we initially established a method to efficiently obtain multinucleated cells because people still struggle with harvesting multinucleated cells. The existence of multinucleated cells of NMFH-2 and NMFH-1 cells were 10.2% and 5.00%, respectively [5]. If experimental systems to collect many multinucleated cells are established, various biochemical, molecular and immunological assays can be made. Although a method designed to incubate multinucleated cells by exclusively selecting and sub-culturing these cells has been reported, the procedure took 10 months [3]. Zang et al. observed multinucleated cells after culture on a hydrophobic substrate in the absence of myosin [8]. In this study, we tested the administration of Y-27632, a ROCK inhibitor that decreases myosin activity and cell contractility, to efficiently obtain any type of cell without gene transfer. The cells were incubated on a less hydrophilic dish and cultured with Y-27632. After establishing the method for generating multinucleated cells, the nature of the multinucleated cells was evaluated based on the morphology of the cells and cell nuclei. This experiment is based on reports that alterations in the nuclear size and shape are associated with and diagnostic markers of human diseases, including cancer and other pathologies [9,10].

2. Materials and Methods

2.1. Contact Angle of Dishes

Reportedly, multinuclear cells are more frequently observed after culture on a hydrophobic surface [8]. Thus, we initially assessed the hydrophobicity of a dish. The contact angle θ of the dish surface was measured to evaluate its hydrophobicity. A 5 μ L water drop was placed on ϕ 35 mm plastic dish (430165, CORNING, Corning, NY, USA) and ϕ 35 mm glass bottom dish from Fine Plus International (FC27-10N, FPI, Kyoto, Japan) and Matsunami Glass Industry (D11140H, Matsunami, Kishiwada, Japan). After imaging the droplet from the lateral side of the dish with a digital camera (CX3, Ricoh Imaging, Tokyo, Japan), the radius r of the contact area and height h of the droplet was measured using image analysis software (ImageJ 1.48v, National Institutes of Health, Bethesda, MD, USA) as follows. First, ten points on the edge of the droplet were spotted manually and their coordinates (x_i, y_i) ($i = 1, 2, 3, \dots, 10$) were measured. Then, a circle that fits the measured points was calculated using the least squared method:

$$\begin{pmatrix} A \\ B \\ C \end{pmatrix} = \begin{pmatrix} \sum x_i^2 & \sum x_i y_i & \sum x_i \\ \sum x_i y_i & \sum x_i^2 & \sum y_i \\ \sum x_i & \sum y_i & \sum 1 \end{pmatrix}^{-1} \begin{pmatrix} -\sum (x_i^3 + x_i y_i^2) \\ -\sum (x_i^2 y_i + y_i^3) \\ -\sum (x_i^2 + y_i^2) \end{pmatrix} \tag{1}$$

where A , B , and C are parameters of the circle. The equation of the circle is given by:

$$x^2 + y^2 + Ax + By + C = 0. \tag{2}$$

Finally, the radius r of the circle was determined as:

$$r = \sqrt{\frac{A^2}{4} + \frac{B^2}{4} - C}. \tag{3}$$

The height of the droplet h was directly measured from lateral images of the droplet. The contact angle was calculated with the equation:

$$\theta = 2\arctan \frac{h}{r} \tag{4}$$

using the half angle method [11].

2.2. Cells

Xenopus laevis cells derived from tadpoles (XTC-YF, RCB0771, RIKEN BioResource Center, Tsukuba, Japan) were used for ease of handling. The cells were cultured at 25 °C in culture medium (Leibovitz's L-15 Medium, Wako Pure Chemical Industries, Osaka, Japan) that had been diluted two-fold with sterilized distilled water. The medium included 10% fetal bovine serum (S1820, Biowest, Nuaille, France) and a 1% antibiotic solution (P4333, Sigma-Aldrich, St. Louis, MO, USA).

2.3. Conditions Used to Prepare Multinucleated Cells

XTC-YF cells were seeded on the FPI and Matsunami glass bottom dishes to investigate the conditions required to generate multinucleated cells. Y-27632 (257-00511, Wako Pure Chemical Industries) was added to the culture medium at a concentration of 100 µM to suppress myosin-induced contraction.

The cultured cells were fixed with 10% neutral buffered formalin for 10 min followed by washes with phosphate-buffered saline (PBS(-)) to confirm the multinucleated phenotype. The cells were immersed in 32 µM Hoechst 33342 (Molecular Probes, Thermo Fisher Scientific, Tokyo, Japan) for 20 min to fluorescently stain the cell nuclei and washed with PBS(-). Phase contrast images of the cells and fluorescently stained cell nuclei were captured using an inverted fluorescence microscope (IX-71, Olympus, Tokyo, Japan) equipped with an EM-CCD camera (iXon Ultra 888, Andor Technology, Belfast, UK) through a 20× (UPLFLN20X, Olympus) or 40× (LUCPLFLN40X, Olympus) objective lens.

For image analysis, 680 µm × 680 µm images at 20× magnification and 340 µm × 340 µm images at 40× magnification were captured. The image analysis software (ImageJ 1.48v) was used to create a superimposition of the phase contrast and fluorescence images. The total numbers of cells, N_{all} , and multinucleated cells, N_{multi} , in the images were counted. The percentage of multinucleated cells R_{multi} was defined as follows:

$$R_{multi} = \frac{N_{multi}}{N_{all}} \times 100 [\%]. \quad (5)$$

2.4. Time-Lapse Imaging

Time-lapse images were captured to directly observe cell division. The XTC-YF cells were seeded on the FPI glass bottom dish, as described in Section 2.3, and observed under an inverted microscope (IX-73, Olympus) equipped with a CCD camera (DP73, Olympus). The phase contrast images of the cells were captured through the 20× objective lens at 5 min intervals from 3 to 72 h after seeding.

2.5. Morphometry of the Cells and Cell Nuclei

The XTC-YF cells were seeded on FPI glass bottom dishes, and half of the cultures were treated with 100 µM Y-27632. After a 48 h incubation, cells were fixed and stained as described in Section 2.3. The phase contrast images and images of the fluorescently labeled nuclei were captured using the setup described in Section 2.3. The images of the fluorescently labeled cell nuclei were binarized to obtain nuclear outlines. The cell shapes were manually outlined in the phase contrast image. From the outlines of the cells and nuclei, the cellular area S_{cell} and nuclear area $S_{nucleus}$ were measured. In the case of multinucleated cells, the areas of individual nuclei were measured. The cellular (α_{cell}) and nuclear ($\alpha_{nucleus}$) circularity values were measured using the following equations:

$$\alpha_{cell} = \frac{S_{cell}}{M_{cell}^2} \times \frac{4}{\pi} \quad (6)$$

$$\alpha_{nucleus} = \frac{S_{nucleus}}{M_{nucleus}^2} \times \frac{4}{\pi} \quad (7)$$

where M_{cell} and $M_{nucleus}$ represent the major axis of the best fit ellipse of the cellular and nuclear areas, respectively. A circularity value of 1 represents a perfect circle and a value of 0 indicates a (segmented) line.

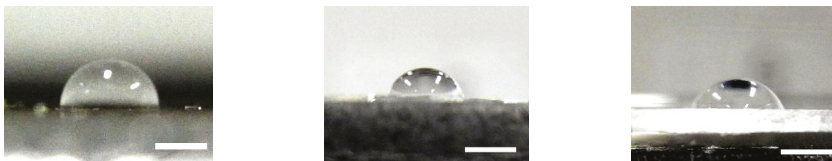
2.6. Statistical Analysis

The difference in contact angle between the dishes was determined using the Tukey method. The differences in morphological data between mononuclear and multinucleated cells were determined using unpaired *t*-tests. The data are presented as the means \pm standard deviations (SD), and the significance level was set to $p = 0.05$.

3. Results and Discussion

3.1. Contact Angle of Glass Bottom Dishes

Images of droplets on dishes are shown in Figure 1. The glass bottom dish manufactured by FPI had a significantly larger contact angle ($93 \pm 2^\circ$, $n = 10$; Figure 1a) than the glass bottom dish from Matsunami Glass Industry ($71 \pm 4^\circ$, $n = 10$; Figure 1b) and plastic dishes ($66 \pm 3^\circ$, $n = 10$; Figure 1c). All groups had a significant difference in the contact angle. Based on these results, the dish manufactured by FPI is less hydrophilic than the dish manufactured by Matsunami Glass Industry and plastic dishes. Thus, in the following experiments, we used the glass bottom dish manufactured by FPI as a less hydrophilic dish and the dish from Matsunami Glass Industry as a more hydrophilic dish.



(a) Glass bottom dish (FPI) (b) Glass bottom dish (Matsunami) (c) Plastic dish (Corning)

Figure 1. Typical images of droplets plated on (a) glass bottom dishes manufactured by Fine Plus International (FPI) and (b) Matsunami and (c) a plastic dish. Image contrast was enhanced for visibility. Bars correspond to 2 mm calibrated at the surface of the dish.

3.2. Comparison of Multinucleated Cells Plated on Different Dishes

Figure 2 shows typical images of XTC-YF cells after the administration 100 μ M Y-27632 at 48 h after seeding. Many multinucleated cells were observed after seeding on a less hydrophilic glass bottom dish (manufactured by FPI) and an incubation in medium containing Y-27632 (Figure 2a). On the other hand, when cells were seeded on a more hydrophilic dish (manufactured by Matsunami) or seeded on a less hydrophilic dish but incubated in normal medium, few multinucleated cells were observed (Figure 2b–d). Figure 3 plots the percentage of multinucleated XTC-YF cells (R_{multi}) as a function of time after seeding. On the less hydrophilic glass bottom dishes, the R_{multi} gradually increased, reaching 88% after 48 h. When the cells were seeded on the less hydrophilic dish without Y-27632 or on a more hydrophilic dish, the R_{multi} was $\leq 5\%$, even after 48 h. Therefore, the condition required to produce multinucleated XTC-YF cells was incubation on a less hydrophilic dish in media containing 100 μ M Y-27632. These results were in good agreement with a previous report showing that cells exhibited a multinucleated morphology after culture on a hydrophobic surface under conditions that inhibited myosin shrinkage [8]. Since Y-27632 is a Rho-kinase inhibitor that suppresses cellular contraction, the reagent is considered to inhibit cytokinesis.

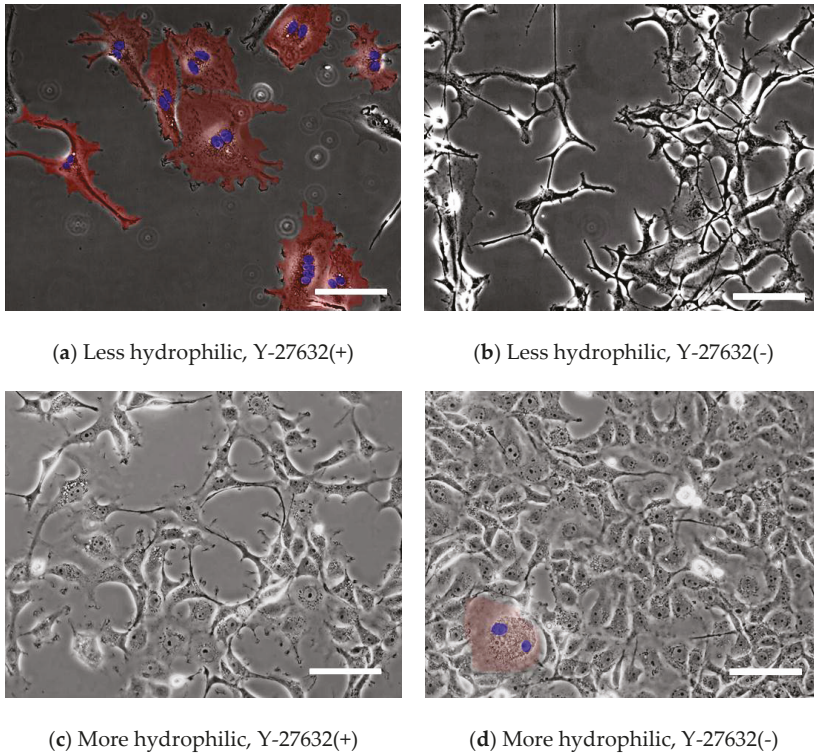


Figure 2. Typical images of XTC-YF cells seeded on (a,b) less hydrophilic (FPI) and (c,d) more hydrophilic (Matsunami) glass bottom dishes. Cells were incubated with (a,c) normal medium containing 100 μ M Y-27632 and (b,d) normal medium alone. Multinucleate cells are shown in red and their nuclei are shown in blue. Scale bars represent 100 μ m.

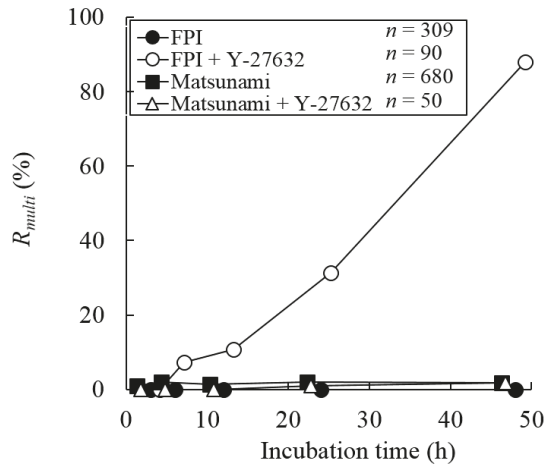


Figure 3. The percentage of multinucleated cells (R_{multi} , as defined in Equation (5)) of XTC-YF cells after seeding on less (FPI) and more hydrophilic (Matsunami) dishes and culture in the presence or absence of Y-27632. n , Number of cells.

Multinucleated cells are produced at a high rate when the contractile force of myosin is inhibited and after culture on a relatively less hydrophilic dish. Unlike the long-term culture method [3], the present method yields multinucleated cells in the usual culture period. Additionally, unlike the gene transfer method [8], the present method is designed to study multinucleated cells *in situ* since the modification of gene expression is not required. The present method is thus beneficial for studying effects of multinucleation on cellular functions.

The surface hydrophobicity can be controlled by coating octadecyltriethoxysilane or fluorine resin-coating. The tuning of hydrophobicity for efficient production of multinuclear cells remain as future tasks.

3.3. Changes in the Number of Nuclei during the Incubation

Time-lapse images were captured to confirm that the multinucleated cells were not generated by fusion but instead through inefficient division. The time-lapse images of XTC-YF cells seeded on the less hydrophilic dish and cultured with medium containing 100 μM Y-27632 are shown in Figure 4 and Video S1. Over time, the projected area of the cells gradually increased (Figure 4b), and cells exhibiting a mononuclear morphology at the time of adhesion developed multiple nuclei following a subsequent cell division without cytokinesis (Figure 4c–e). Thus, the XTC-YF cells became multinucleated through inefficient division. The time of the first cell division after seeding was 21.5 ± 11.5 h. Some multinuclear cells divided again and the number of nuclei increased over time (Figure 4e–h). When multinucleated cells divided, all nuclei divided at the same time (Figure 4f). However, multinucleate cells with two nuclei sometimes divided into odd numbers of nuclei, such as three or five cell nuclei (Figure 4h). As shown in Figure 4 and Video 1, cells underwent multipolar mitosis and two clusters of chromosomes segregated into a single nucleus. This chromosomal mis-segregation is likely to produce aneuploid progeny [12], which is a condition associated with cancer [13,14].

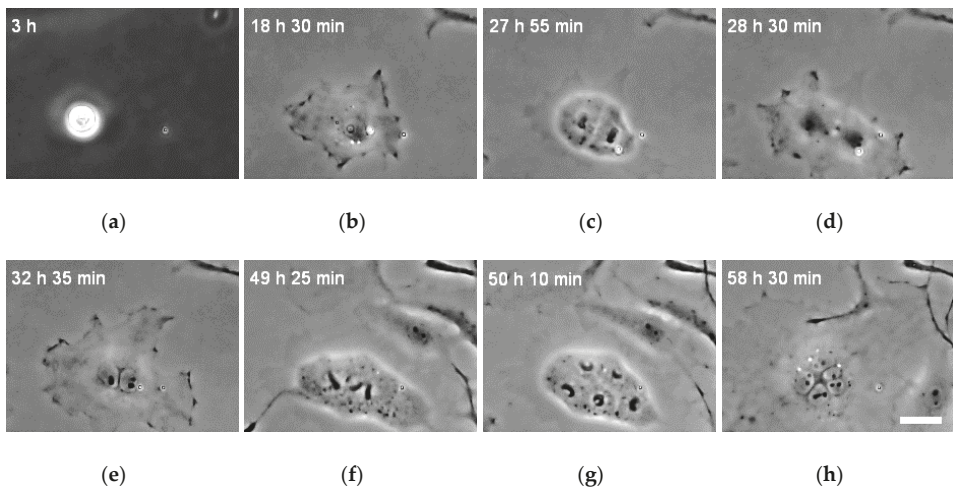


Figure 4. Typical time-lapse images of the XTC-YF cells incubated in medium containing 100 μM Y-27632 and seeded on a less hydrophilic glass bottom dish. Bars in (h) = 30 μm and are applicable to all images. The numbers in the upper left of the panels indicate the time after seeding.

Figure 5 shows the relationship between the elapsed time and the number of nuclei per cell. Forty-eight hours after seeding, many cells contained two nuclei. As shown in Figure 4 and Video 1, multinucleated cells further divided at later time points. This division increased the number of cells with more than two nuclei and decreased the number of cells with two nuclei at 72 h after seeding.

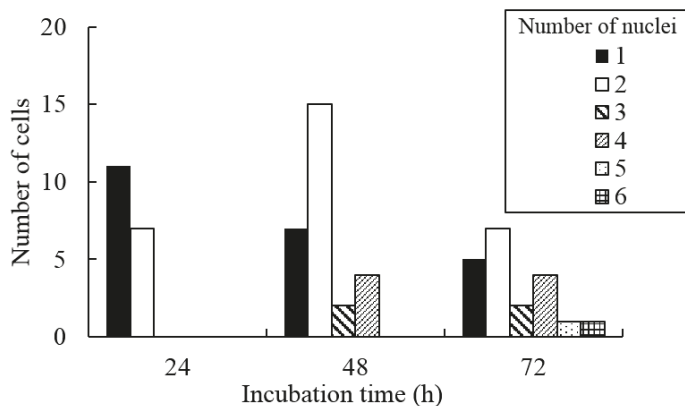


Figure 5. The number of nuclei in XTC-YF cells incubated with medium containing 100 μ M Y-27632 and seeded on less hydrophilic glass bottom dishes.

3.4. Morphology of the Cells and Cell Nuclei of Multinucleated and Mononuclear Cells

Figure 6a shows the nuclear area ($S_{nucleus}$) of multinucleated and mononuclear cells. The $S_{nucleus}$ of the multinucleated cells was significantly smaller than mononuclear cells. As confirmed in Video 1, chromosome division definitely occurred, and thus the smaller nuclei observed in multinuclear cells indicated chromosomal condensation. Since the nuclear size positively correlates with nuclear import rates and the concentrations of two transport factors, importin α and Ntf2 [15], the concentrations of these factors might be reduced in multicellular cells compared with mononuclear cells. Importin α and Ntf2 modulate the import of lamin B3 [15], a major component of the nuclear lamina that supports the nuclear envelope and is involved in DNA replication [16], suggesting a possible difference in DNA replication between multinucleated and mononuclear cells.

A cell nucleus divided, as confirmed in the time-lapse movie (Video S1). Thus, normal numbers of chromosomes would be present in a single nucleus, even in the multinucleated cells. As shown in the results presented in Figure 6a, the $S_{nucleus}$ of the multinucleated cells was much smaller than mononuclear cells. Since the nuclear volume in cancer cells influences the proliferative activity [17], multinucleated cells might display differences in cell proliferation.

Figure 6b shows the cellular area (S_{cell}) of multinucleated and mononuclear cells. The S_{cell} of the multinucleated cells was significantly larger than mononuclear cells. In this study, Y-27632 was administered to obtain multinucleated cells. Since Y-27632 interferes with myosin II activity and reduces the tension of stress fibers, a cell treated with Y-27632 spreads and exhibits an increased cellular area [18]. Thus, the significant increase in the cell area of multinucleated cells might be due to the effect of Y-27632. Further experiments will be needed to determine whether Y-27632 or multinucleation increased the cell area.

According to Wilson, the ratio of the area of the cell nucleus to the area of the cell is a constant value [19]. If the ratio in multinucleated cells is defined for each nucleus within a cell, the ratio observed for multinucleated cells at 48 h after seeding ($2.4 \pm 0.6\%$) was smaller than mononuclear cells ($5.9 \pm 2.1\%$). However, multinuclear cells contain at least two nuclei. Thus, if the sum of the nuclear area in a single multinucleated cell is considered, the ratio is comparable to the nuclear area of mononuclear cells ($5.0 \pm 1.3\%$). In this sense, the ratio proposed by Wilson [19] is applicable to multinuclear cells.

Figure 6c shows the nuclear circularity ($\alpha_{nucleus}$) of multinucleated and mononuclear cells. The nuclear circularity of the multinucleated cells was significantly smaller than mononuclear cells. The circularity of the nucleus tends to decrease in the presence of an abnormal number of chromosomes

in cancer cells [20]. Thus, we speculated that the nuclei of multinucleated cells contain an abnormal number of chromosomes.

Figure 6d shows the cellular circularity (α_{cell}) of the multinucleated and mononuclear cells. There were no significant differences in the cellular circularity between the multinucleated and mononuclear cells, and the cellular circularity appeared to be lower in the multinuclear cells. The cells treated with Y-27632 exhibited an increased degree of polarization and decreased circularity [21–24], or no change in cellular circularity [25]. Since Y-27632 was administered to obtain multinucleated cells in this study, the multinucleation of cells appears to decrease their circularity.

As shown in Figure 6, the morphology of the cell and cell nucleus of the multinucleated cells was completely different from the mononuclear cells. Since defects in nuclear size and shape are associated with and diagnostic markers of human disease, including cancer and other pathologies [9,10], further investigations focusing on cellular functions and their mechanisms will be required.

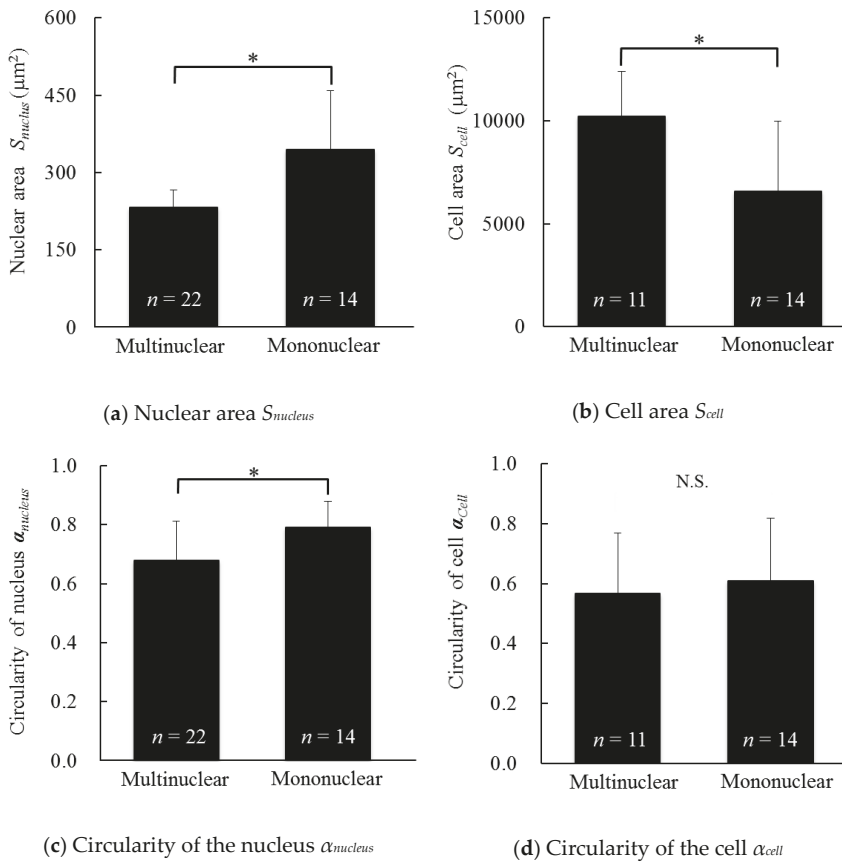


Figure 6. Morphology of multinucleated and mononuclear XTC-YF cells 48 h after seeding on the less hydrophilic glass bottom dish. Morphological data, such as (a) the nuclear area, (b) cell area, (c) circularity of the nucleus, and (d) circularity of the cell, are shown. *n*, Number of nuclei; *, $p < 0.05$.

4. Conclusions

In summary, the present study established conditions to generate multinucleated XTC-YF cells, by seeding the cells on a less hydrophilic dish in a medium containing Y-27632. The present method quickly and easily produced multinucleated cells compared to pioneering methods [3,8]. Some cells

divided to produce cells with an odd number of nuclei. The multinucleated cells had a significantly smaller nuclear area, larger cell area, and smaller nuclear circularity. The present method could contribute to improving our understanding of the nature of multinuclear cells.

Supplementary Materials: The following materials are available online at <http://www.mdpi.com/2072-666X/10/2/156/s1>, Video S1: Time-lapse images of cell division.

Author Contributions: Conceptualization, S.S.; methodology, R.M.; formal analysis, R.M.; resources, S.S.; writing—original draft preparation, R.M.; writing—review and editing, S.S. and M.N.; supervision, S.S.; project administration, S.S.; funding acquisition, S.S.

Funding: This research received no external funding.

Conflicts of Interest: The authors declare no conflicts of interest.

References

1. Alberts, B.; Wilson, J.H.; Johnson, A.; Hunt, T.; Lewis, J.; Raff, M.; Roberts, K.; Walter, P. *Molecular Biology of the Cell: Reference edition*, 5th ed.; John, H., Wilson, T.H., Eds.; Garland Science: New York, NY, USA, 2008; p. 1099.
2. Helming, L.; Gordon, S. Macrophage fusion induced by IL-4 alternative activation is a multistage process involving multiple target molecules. *Eur. J. Immunol.* **2007**, *37*, 33–42. [[CrossRef](#)] [[PubMed](#)]
3. Sedlak, B.J.; Booyse, F.M.; Bell, S.; Rafelson Jr., M.E. Comparison of two types of endothelial cells in long term culture. *Thromb. Haemost.* **1976**, *35*, 167–177. [[CrossRef](#)] [[PubMed](#)]
4. Tokunaga, O.; Fan, J.L.; Watanabe, T. Atherosclerosis- and age-related multinucleated variant endothelial cells in primary culture from human aorta. *Am. J. Pathol.* **1989**, *135*, 967–976. [[PubMed](#)]
5. Ariizumi, T.; Ogose, A.; Kawashima, H.; Hotta, T.; Umezumi, H.; Endo, N. Multinucleation followed by an acytokinetic cell division in myxofibrosarcoma with giant cell proliferation. *J. Exp. Clin. Cancer Res.* **2009**, *28*, 44. [[CrossRef](#)] [[PubMed](#)]
6. Boşca, A.B.; İlea, A.; Eovrea, A.S.; Constantin, A.M.; Ruxanda, F.; Rus, V.; Rațiu, C.; Miclăuș, V. Multinucleated Giant Cells Polymorphism in Epulis. *Bull. Univ. Agric. Sci. Vet. Med. Cluj-Napoca. Agric.* **2015**, *72*, 47–52. [[CrossRef](#)]
7. Herring, M.; Gardner, A.; Glover, J. A single-staged technique for seeding vascular grafts with autogenous endothelium. *Surgery* **1978**, *84*, 498–504. [[PubMed](#)]
8. Zang, J.H.; Cavet, G.; Sabry, J.H.; Wagner, P.; Moores, S.L.; Spudich, J.A. On the role of myosin-II in cytokinesis: division of Dictyostelium cells under adhesive and nonadhesive conditions. *Mol. Biol. Cell* **1997**, *8*, 2617–2629. [[CrossRef](#)] [[PubMed](#)]
9. Webster, M.; Witkin, K.L.; Cohen-Fix, O. Sizing up the nucleus: nuclear shape, size and nuclear-envelope assembly. *J. Cell Sci.* **2009**, *122*, 1477–1486. [[CrossRef](#)] [[PubMed](#)]
10. Zink, D.; Fischer, A.H.; Nickerson, J.A. Nuclear structure in cancer cells. *Nat. Rev. Cancer* **2004**, *4*, 677. [[CrossRef](#)] [[PubMed](#)]
11. Kohli, R.; Mittal, K.L. *Developments in Surface Contamination and Cleaning—Vol 6: Methods of Cleaning and Cleanliness Verification*, 1st ed.; Elsevier Science: Waltham, MA, USA, 2013; p. 169.
12. Shi, Q.; King, R.W. Chromosome nondisjunction yields tetraploid rather than aneuploid cells in human cell lines. *Nature* **2005**, *437*, 1038. [[CrossRef](#)] [[PubMed](#)]
13. Draviam, V.M.; Xie, S.; Sorger, P.K. Chromosome segregation and genomic stability. *Curr. Opin. Genet. Dev.* **2004**, *14*, 120–125. [[CrossRef](#)] [[PubMed](#)]
14. Santaguida, S.; Amon, A. Short- and long-term effects of chromosome mis-segregation and aneuploidy. *Nat. Rev. Mol. Cell Biol.* **2015**, *16*, 473. [[CrossRef](#)] [[PubMed](#)]
15. Levy, D.L.; Heald, R. Nuclear Size Is Regulated by Importin α and Ntf2 in Xenopus. *Cell* **2010**, *143*, 288–298. [[CrossRef](#)] [[PubMed](#)]
16. Camps, J.; Erdos, M.R.; Ried, T. The role of lamin B1 for the maintenance of nuclear structure and function. *Nucleus* **2015**, *6*, 8–14. [[CrossRef](#)] [[PubMed](#)]
17. Martin, R.; Nieto, S.; Santamaria, L. Stereologic estimates of volume-weighted mean nuclear volume in colorectal adenocarcinoma: correlation with histologic grading, Dukes' staging, cell proliferation activity and p53 protein expression. *Gen. Diagn. Pathol.* **1997**, *143*, 29–38. [[PubMed](#)]

18. Jackson, B.; Peyrollier, K.; Pedersen, E.; Basse, A.; Karlsson, R.; Wang, Z.; Lefever, T.; Ochsenbein, A.M.; Schmidt, G.; Aktories, K.; et al. RhoA is dispensable for skin development, but crucial for contraction and directed migration of keratinocytes. *Mol. Biol. Cell* **2011**, *22*, 593–605. [[CrossRef](#)] [[PubMed](#)]
19. Wilson, E.B. *The Cell in Development and Inheritance*, 3rd ed.; Macmillan Company: New York, NY, USA, 1925; pp. 727–739.
20. Yamamoto, T.; Horiguchi, H.; Kamma, H.; Ogata, T.; Fukasawa, M.; Ikezawa, T.; Inage, Y.; Akaogi, E.; Mitsui, K.; Hori, M. The effect of nuclear DNA content on nuclear atypia and clinicopathological factors in non-small cell lung carcinoma. *J. Jpn. Soc. Clin. Cytol.* **1993**, *32*, 846–852. [[CrossRef](#)]
21. Omelchenko, T.; Vasiliev, J.M.; Gelfand, I.M.; Feder, H.H.; Bonder, E.M. Mechanisms of polarization of the shape of fibroblasts and epitheliocytes: Separation of the roles of microtubules and Rho-dependent actin-myosin contractility. *Proc. Natl. Acad. Sci. USA* **2002**, *99*, 10452–10457. [[CrossRef](#)] [[PubMed](#)]
22. Babich, A.; Li, S.; O'Connor, R.S.; Milone, M.C.; Freedman, B.D.; Burkhardt, J.K. F-actin polymerization and retrograde flow drive sustained PLC γ 1 signaling during T cell activation. *J. Cell Biol.* **2012**, *197*, 775–787. [[CrossRef](#)] [[PubMed](#)]
23. Kharitonova, M.A.; Vasiliev, J.M. Length control is determined by the pattern of cytoskeleton. *J. Cell Sci.* **2004**, *117*, 1955–1960. [[CrossRef](#)] [[PubMed](#)]
24. Jones, B.C.; Kelley, L.C.; Loskutov, Y.V.; Marinak, K.M.; Kozyreva, V.K.; Smolkin, M.B.; Pugacheva, E.N. Dual Targeting of Mesenchymal and Amoeboid Motility Hinders Metastatic Behavior. *Mol. Cancer Res.* **2017**, *15*, 670–682. [[CrossRef](#)] [[PubMed](#)]
25. Kazmers, N.H.; Ma, S.A.; Yoshida, T.; Stern, P.H. Rho GTPase signaling and PTH 3–34, but not PTH 1–34, maintain the actin cytoskeleton and antagonize bisphosphonate effects in mouse osteoblastic MC3T3-E1 cells. *Bone* **2009**, *45*, 52–60. [[CrossRef](#)] [[PubMed](#)]



© 2019 by the authors. Licensee MDPI, Basel, Switzerland. This article is an open access article distributed under the terms and conditions of the Creative Commons Attribution (CC BY) license (<http://creativecommons.org/licenses/by/4.0/>).



Article

Mechanophenotyping of B16 Melanoma Cell Variants for the Assessment of the Efficacy of (-)-Epigallocatechin Gallate Treatment Using a Tapered Microfluidic Device

Masanori Nakamura *, Daichi Ono and Shukei Sugita

Department of Electrical and Mechanical Engineering, Nagoya Institute of Technology, Nagoya 466-8555, Japan; 30413043@stn.nitech.ac.jp (D.O.); sugita.shukei@nitech.ac.jp (S.S.)

* Correspondence: masanorin@nitech.ac.jp; Tel.: +81-52-735-5569

Received: 31 January 2019; Accepted: 17 March 2019; Published: 25 March 2019

Abstract: Metastatic cancer cells are known to have a smaller cell stiffness than healthy cells because the small stiffness is beneficial for passing through the extracellular matrix when the cancer cells instigate a metastatic process. Here we developed a simple and handy microfluidic system to assess metastatic capacity of the cancer cells from a mechanical point of view. A tapered microchannel was devised through which a cell was compressed while passing. Two metastasis B16 melanoma variants (B16-F1 and B16-F10) were examined. The shape recovery process of the cell from a compressed state was evaluated with the Kelvin–Voigt model. The results demonstrated that the B16-F10 cells showed a larger time constant of shape recovery than B16-F1 cells, although no significant difference in the initial strain was observed between B16-F1 cells and B16-F10 cells. We further investigated effects of catechin on the cell deformability and found that the deformability of B16-F10 cells was significantly decreased and became equivalent to that of untreated B16-F1 cells. These results addressed the utility of the present system to handily but roughly assess the metastatic capacity of cancer cells and to investigate drug efficacy on the metastatic capacity.

Keywords: microfluidics; mechanophenotyping; cancer; metastatic potential

1. Introduction

Metastasis is the spread of cancer cells from the primary site of origin to other sites of the body. When cancer cells metastasize, some cells known as circulating tumor cells (CTC), penetrate the endothelium and the basement membrane and pass through a tiny gap in the extracellular matrix [1–3]. It is therefore thought that having smaller stiffness is beneficial for cancer cells to instigate the metastatic process [4]. In support of this, only few studies show that cancer cells are stiffer, and a large majority of experiments indicate that cancerous cells are softer than their benign counterparts and that cellular rigidity decreases with the progression of the disease—as summarized in Aliber et al. [4]—although it remains unclear whether such cell softening is a universal feature [5].

Various tests were conducted to mechanically characterize living cells including cancer cells [6–15]. Mechanical studies on cancer cells and related cancer biology are thoroughly reviewed in Darling et al. [16], Aliber et al. [4], and Chaudhuri et al. [17]. Using atomic force microscopy, Cross et al. [8] demonstrated that metastatic cancer cells taken from the pleural fluids of patients with suspected lung, breast, and pancreas cancer have stiffness as much as 70% smaller than the benign cells. Remmerbach et al. [11] measured the compliance of cells from cell lines and primary samples of healthy donors and cancer patients using a microfluidic optical stretcher. They found that cancer cells were on average 3.5 times more compliant than those of healthy donors. Swaminathan et al. [12] showed

that cancer cells with the highest migratory and invasive potential are five times less stiff than cells with the lowest potential. Furthermore, they reported that invasiveness decreased when cell stiffness, by restoring expression of the metastasis suppressor $T\beta RIII$ /betaglycan, increased. It was also reported that the more motile and metastatic cancer cells were, the softer they were, indicating that nanomechanical stiffness was inversely correlated with the migration potential of the cancer cell [13,14]. These results suggest that the cell stiffness is a reliable quantitative indicator or a good biomarker of migration and the invasive potential of cancer cells. However, the conventional methods of mechanical tests such as atomic force microscopy, optical tweezers, and micropipette aspiration are time-consuming, labor-intensive, and often require difficult manipulation and mastery skills although they give relatively accurate data [18]. Additionally, each method has its own drawback. For instance, atomic force microscopy requires a cell adhering to a basement. Micropipette aspiration involves difficult manipulation and fine adjustment of pressure. In order to use the cell stiffness as a biomarker of the metastatic potential of cancer cells in clinical practice, more viable methods are demanded.

Microfluidic devices have high throughputs in selecting cancer cells and assessing their metastatic functions [19–24]. For example, Hou et al. [22] and Khoo et al. [23] established a spiral microfluidic channel to separate CTCs from blood cells. Tse et al. [24] evaluated the mechanical properties of cells sampled from malignant pleural effusions using a crossed microfluidic channel, proposed by Gossett et al. [25]. These studies addressed a great potential of microfluidic techniques to handily characterize the mechanical properties of cancer cells in clinical practice.

Epigallocatechin gallate (EGCG) is a major component of green tea. Taniguchi et al. [26] reported that EGCG inhibited the spontaneous metastasis of B16-F10 cells and B16-BL6 cells to the lungs of mice. EGCG binds to various proteins and both DNA and RNA molecules [27], it also inhibits binding of ligands and tumor promoters to their receptors in the cell membrane, and the receptor signaling pathway of epidermal growth factor (EGF) [28]. EGCG also works as an immune check point inhibitor [29]. EGCG acts on the cell membrane of cancer cells, hardens the cell membrane [30], and suppresses cancer cell migration and invasion [31]. EGCG blocks induction of carcinogenic factors by hardening the cell membrane and inhibits metastasis of cancer cells [32]. Taking these facts together, it is considered that hardening of cancer cells with EGCG could be another way of inhibiting metastasis of cancer cells.

Better and more appropriate cancer therapies, including a choice of drugs (weak or strong) with minimal side effects, could be applied if the metastatic potentials of the circulating tumor cells were easier to evaluate in clinical practice. The aim of the present study is therefore to investigate the mechanical properties of cancer cells, in particular highlighting internal cytoskeletal structures and changes brought by EGCG treatment. A microflow channel of a simple design was used to evaluate cell stiffness. Here we used two cell types that are known to have different metastatic potential and investigated whether these cells can be differentiated from their viscoelastic properties. The same assessment process was also applied to untreated and EGCG-treated cells to see whether effectiveness of EGCG treatment can be detected using the same procedure as used in differentiating the metastatic potential.

2. Materials and Methods

2.1. Cell Sample

Mouse melanoma cell lines B16-F1 and B16-F10 were used. B16-F1 was obtained by a one-time selective procedure and B16-F10 by a ten-time selective procedure using Fidler's method [33], meaning that B16-F10 was a select group of cancer cells having greater invasive and metastatic capacity than B16-F1. The characteristics of the cells were reported in Fidler [33], Poste et al. [34], and Nakamura et al. [35]. The cells were cultured in DMEM (05919, Nissui, Tokyo, Japan) containing 10% fetal bovine serum (172012, Sigma-Aldrich, St. Louis, MO, USA) in a humidified atmosphere of 5% of CO_2 at 37 °C.

Trypsin (25200-056, Gibco, Gaithersburg, MD, USA) was added to the cells that were semi-confluent to detach them from dishes. After the cells were washed with phosphate buffered saline (PBS(-)), cell samples with a concentration of $3\text{--}4 \times 10^5$ cells/ml were prepared.

2.2. Microflow Channel

Lee et al. [36] and Lima's group [37,38] used hyperbolic-shaped contraction for the ability to impose a constant strain rate along the centerline of the contraction, as well as to achieve high extensional and shear flows. Although the hyperbolic-shaped contraction was efficient for causing cell deformation, here we used a linearly tapered microflow channel, as shown in Figure 1a. The geometry of the channel is similar to that in TruongVo et al. [39], who also used it to characterize breast cancer cells. The channel has four ports: (a) Inlet for cell flow, (b) and (c) inlets for sheath flow, and (d) outlet. In design, the main flow channel has a taper with an inlet width of $40 \mu\text{m}$, an outlet width of $15 \mu\text{m}$, and a length of $200 \mu\text{m}$. The height of the main channel is $20 \mu\text{m}$, providing a rectangular cross-section.

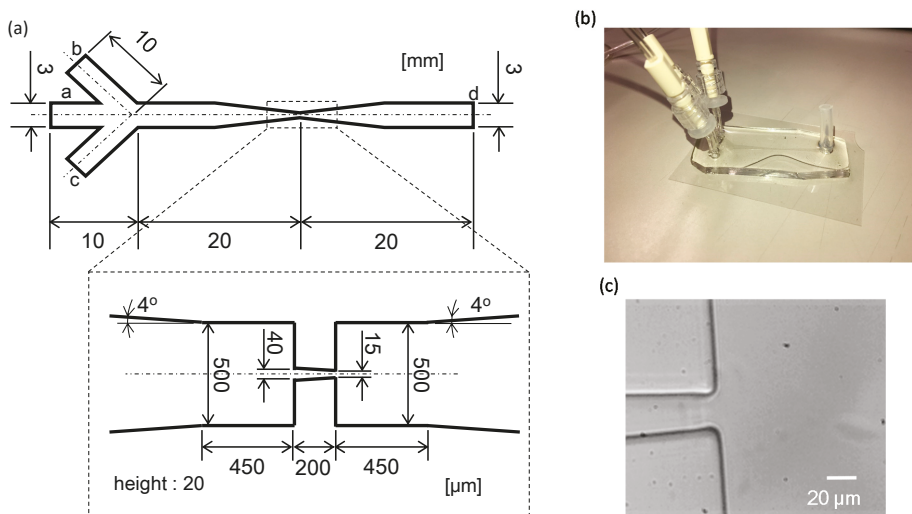


Figure 1. (a) Schematic drawing of the microflow channel—a, inlet port for cell flow; b and c, inlet ports for sheath flow; and d, outlet. (b) A fabricated microfluidic device and (c) a magnified view of the tip of the microflow channel.

The flow channel was fabricated according to standard photolithography and soft lithography techniques. The negative photoresist pattern was fabricated on a silicon wafer (Matsuzaki, Tokyo, Japan) with SU8-3050 (Nippon Kayaku, Tokyo, Japan). PDMS prepolymer (Sylgard 184 silicone elastomer kit, Toray Dow Corning, Tokyo, Japan) was poured onto the silicon wafer and baked at 80°C for 1 h. Plasma treatment was used to chemically bond the PDMS mold to a glass slide with a thickness of 0.12–0.17 mm (C050701, Matsunami, Bellingham, WA, USA). The fabricated microfluidic device and the microscopic image of the tapered part are shown in Figure 1b,c, respectively. In the final product, the width of the tip was $20 \mu\text{m}$ and the channel height was $32 \mu\text{m}$.

2.3. Experimental Setup

Figure 2 provides a schematic illustration of the experimental setup. The experimental setup mainly consists of an inverted microscope (IX-71, Olympus, Tokyo, Japan), a high-speed camera (FASTCAM Mini AX200, Photron, Tokyo, Japan), syringe pumps (KDS-210, KD Scientific, Holliston, MA, USA), and a flow channel. Cells were introduced to the flow channel by one of the syringe

pumps. Along with cell flow, sheath flow was also introduced to direct cells to the center of the channel. The total flow rate of the cell flow and sheath flows was set to 66 $\mu\text{L}/\text{min}$ that gave approximately 1.5 m/s at the tip of the tapered channel. The ratio of the flowrate between cell flow and sheath flow was 1:6. A cell shape at the tip of the taper and its downstream was recorded with a high-speed camera at a frame rate of 100,000 fps via an objective lens of 60x (N.A. 0.7, LUCPlanFLN 60x, Olympus). The cell height $h(t)$ —defined as cell length in a direction perpendicular to the flow, exemplified in Figure 3—was measured using image analysis software (ImageJ 1.48v, National Institutes of Health, Bethesda, MD, USA).

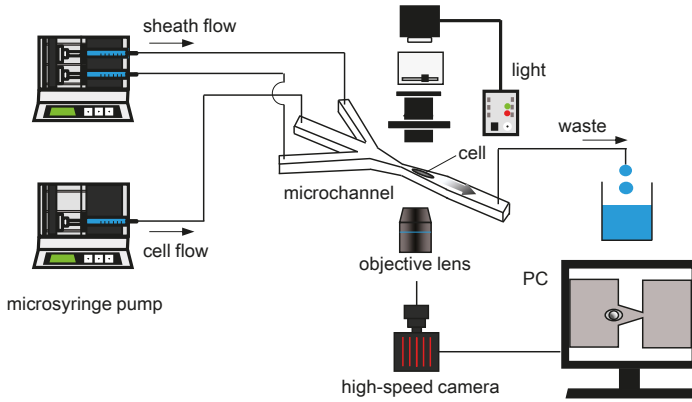


Figure 2. Schematic illustration of the experimental setup. The microflow channel was placed under the microscope and cell deformation was recorded with a high-speed camera.

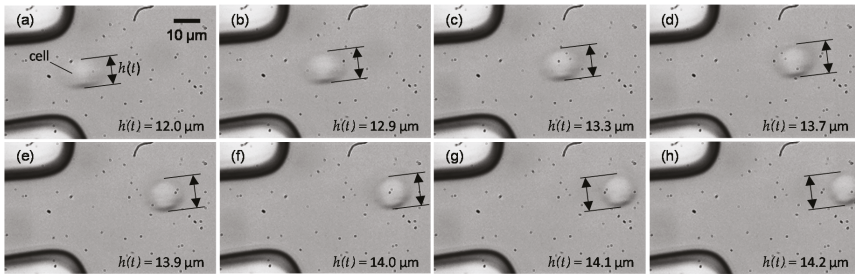


Figure 3. A time series of snapshots of a cell showing how the cell was recovering its shape after it had left the tip of the tapered channel (a). The time interval between consecutive snapshots (b–h) is 20 μs . The scale bar in Figure 3a applies to all images.

2.4. Mechanical Characterization of a Cell

Cells leaving the tapered channel are released from compressive forces and gradually recover to their original shape. Here, the compression strain $\varepsilon(t)$ of a cell at time t after leaving the tapered channel—was defined by the following formula:

$$\varepsilon(t) = \frac{h_{\infty} - h(t)}{h_{\infty}} \quad (1)$$

where $h(t)$ is the cell height at time t , and h_{∞} is the cell height in the last frame where the cell is sufficiently far from the tip of the tapered channel.

The recovery process of the cell diameter was expressed with a Kelvin–Voigt model that has a purely viscous damper with a viscosity of μ and a purely elastic spring with a spring constant k

connected in parallel. When a cell leaves the tapered channel, it is released from the compressive force. Under this condition, the compressive strain of the cell, $\epsilon(t)$, is expressed with the following formula:

$$\epsilon(t) = \epsilon_0 \exp\left(-\frac{t}{\tau}\right) \quad (2)$$

where τ is a time constant of shape recovery and equal to μ/k .

2.5. EGCG Treatment

EGCG is the main polyphenolic constituent of green tea [26]. Reportedly, EGCG inhibits tumor promotion induced by teleocidin in a two-stage carcinogenesis experiment on mouse skin [40] and duodenal carcinogenesis with N-ethyl-N'-nitro-IV-nitrosoguanidine [41]. It is also reported that EGCG inhibits lung colonization of B16-F10 cells and spontaneous metastasis of B16-BL6 cells from the foot to the lung [26]. Clinical trials have demonstrated that green tea catechins including EGCG are effective for cancer prevention [42–45]. Here, EGCG was used to stiffen cells by following a protocol described in Fujiki and Okuda [46]. An EGCG culture medium of 200 $\mu\text{M}/\text{L}$ was prepared by diluting an EGCG/PBS(-) solution of 25 mM/L in DMEM. Cells were cultured with the EGCG culture medium for 4 h. After the culture, the cells were removed from dishes by treatment with trypsin, which was followed by centrifuge and removal of the medium. Finally, EGCG-treated cells were suspended in PBS(-) such that the cell concentration became $3\text{--}4 \times 10^5$ cells/mL.

2.6. Staining

The cell nucleus and actin filaments of B16-F1 and B16-F10 cells were stained. Staining was conducted for both cells that were attached to dishes and cells that were floating. The latter group was prepared by detaching the cells from the dishes with trypsin and leaving them for 30 min at room temperature until the cells become stably spherical. In the following staining processes, the floating cells were always centrifuged at a relative centrifugal force of 17.9 g for 5 min at washing and liquid exchange. First, cells were fixed with 10% neutral buffered formalin for 10 min at room temperature then washed with PBS(-). The cells were then permeated with 0.2% Triton X-100 in PBS(-) for 10 min then washed. This was followed by blocking with 4% albumin from bovine serum (Wako)/PBS(-) solution for 15 min then washing. For staining actin filaments, cells were treated with Alexa Fluor 488 phalloidin, diluted to 1:200 times with PBS(-) in a dark room for 30 min at room temperature. For staining the cell nucleus, cells were treated with Hoechst 33342 diluted to 1:10,000 with 0.2% BSA/PBS(-) solution in a dark room for 30 min at room temperature. Images were obtained using a confocal laser scanning microscope (FV3000, Olympus) with a 60x oil immersion objective lens (N.A. 1.35, UPLSAPO60XO, Olympus). A laser (OBIS, Coherent, Santa Clara, CA, USA) with an excitation wavelength of 488 nm and 405 nm was used to observe actin filaments and cell nuclei, respectively.

2.7. Statistical Method

Student's unpaired *t*-test was used in all statistical analyses. A significance level of 0.05 was used.

3. Results

Figure 3 shows a series of snapshots of a B16-F10 cell flowing downstream from the tip of the tapered channel. Note that the snapshots in Figure 3 were the ones obtained every two snapshots that were recorded. The cell size at rest was $15.4 \pm 1.6 \mu\text{m}$ for B16-F1 cells and $15.4 \pm 1.4 \mu\text{m}$ for B16-F10 cells, and no statistical difference was found in cell size between them. As seen, the cell that was compressed at the tip gradually recovered its shape to being spherical as it flowed further downstream. A temporal variation of the compressive strain of the cell, $\epsilon(t)$, is shown in Figure 4 where Figure 4a–d is for untreated B16-F1 cells, untreated B16-F10 cells, EGCG-treated B16-F1 cells, and EGCG-treated B16-F10 cells, respectively. Note that the graphs in Figure 4 are a representative case of each cell and treatment condition. All the figures demonstrate an exponential decrease in $\epsilon(t)$ as a function of time.

Fitting Equation (2) to the data in Figure 4 clearly indicates that a change in the compressive strain could be represented by the Kelvin–Voigt model.

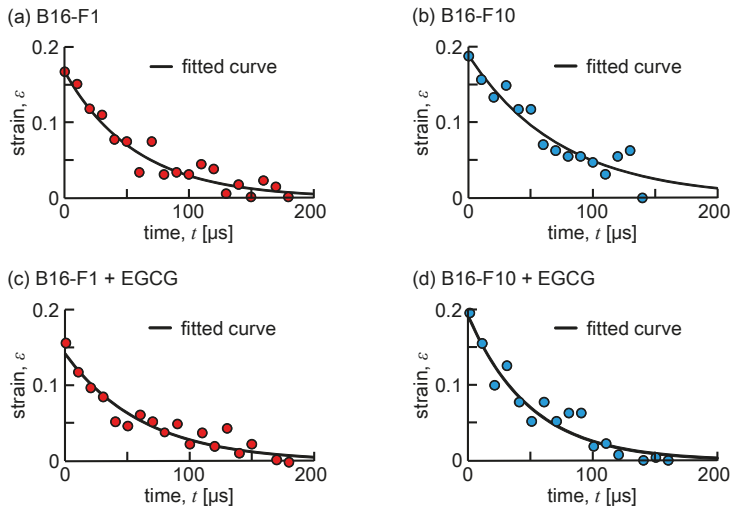


Figure 4. Time variations of the compressive strain of the cell. (a) Untreated B16-F1, (b) untreated B16-F10, (c) epigallocatechin gallate (EGCG)-treated B16-F1, and (d) EGCG-treated B16-F10.

Figure 5 compares the initial compression strain, ϵ_0 , when a cell was at the tip of the taper. The mean \pm SD of ϵ_0 was 0.15 ± 0.06 for untreated B16-F1 cells, 0.17 ± 0.09 for untreated B16-F10 cells, 0.15 ± 0.03 for EGCG-treated B16-F1 cells, and 0.18 ± 0.05 for EGCG-treated B16-F10 cells. No statistical difference was found in ϵ_0 between any combinations.

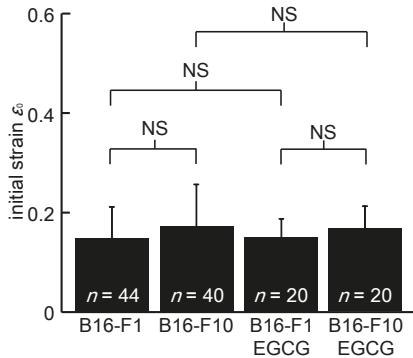


Figure 5. A comparison of the initial compressive strain, ϵ_0 . n : Number of cells.

A comparison of a time constant of the shape recovery τ is presented in Figure 6. The mean \pm SD of τ was $50 \pm 15 \mu\text{s}$ for untreated B16-F1 cells, 70 ± 23 for untreated B16-F10 cells, $59 \pm 22 \mu\text{s}$ for EGCG-treated B16-F1 cells, and $60 \pm 12 \mu\text{s}$ for EGCG-treated B16-F10 cells. A statistical difference in τ was found in a pair of untreated B16-F1 cells vs. untreated B16-F10 cells ($p < 0.05$) and untreated B16-F1 vs EGCG-treated B16-F1 cells ($p < 0.05$), while no statistical difference was noted in a pair of untreated B16-F10 cells vs. EGCG-treated B16-F10 cells and EGCG-treated B16-F1 cells vs EGCG-treated B16-F10 cells.

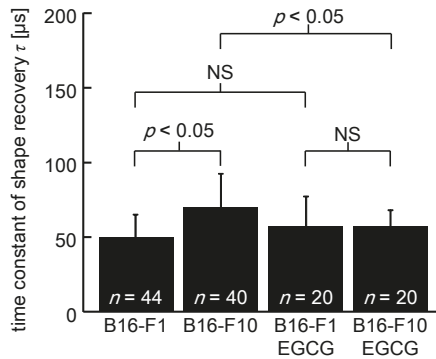


Figure 6. A comparison of the time constant of shape recovery τ . *n*: Number of cells.

Figure 7 provides fluorescent images of cellular nuclei and the actin filaments of cells. Figure 7a,b show the cells that remained adhered to dishes, and Figure 7c,d show the cells that were detached from the dishes. Cell lines were B16-F1 for a and c, and B16-F10 for b and d. The detached cells appeared to be spherical, while those adhering to dishes spread with extending processes. In looking at Figure 7a,b, we found that when the cells adhere to dishes, B16-F1 cells had thicker actin filaments than B16-F10 cells, although both cell lines showed fibrous structure of actin filaments. To confirm this perceptual finding, thickness of actin filaments was evaluated with the standard deviation of a Gaussian function fitted to the intensity profile across stress fibers. This is because the spatial resolution of 0.083 $\mu\text{m}/\text{pixel}$ in the present images is not fine enough to measure the thickness of actin filaments with a certain accuracy. The evaluation was conducted for three locations for each of the actin filaments arrowed in Figure 7. The results demonstrated 2.15 ± 0.71 pixels for B16-F1 cells and 0.99 ± 0.14 pixels for B16-F10 cells ($p < 0.05$), supporting the perceptual finding of a difference in the thickness. For the cells that were detached from the dishes, the fibrous structure disappeared and no remarkable difference in the structure and amount of actin filaments was noticed between B16-F1 cells and B16-F10 cells.

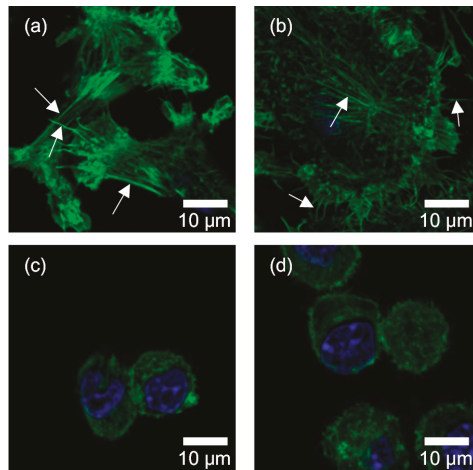


Figure 7. Fluorescent images of actin filaments (green) and nuclei (blue). (a) Adhered B16-F1 cells, (b) adhered B16-F10 cells, (c) floating B16-F1 cells, and (d) floating B16-F10 cells. Arrows in (a,b) indicate actin filaments whose thickness was evaluated.

4. Discussion

Microfluidic devices have been used in prior studies to find circulating tumor cells in blood. Recently, Tse et al. [24] invented a microfluidic device of a crossed flow channel at the junction where a cell was deformed by counter striking flows. They successfully classified cells based on cell deformability and took the initiative in diagnosing malignant pleural effusions by microfluidics. Raj et al. [47] fabricated a microfluidic device comprised of multiple parallel microconstrictions. They introduced a theoretical model of cell flow and deformation in the channels and succeeded in quantifying cell elasticity. The present study is situated in part as an extension of these studies. As demonstrated in Figure 6, we found that a time constant of shape recovery could be a useful index to rate the metastatic potentials of cancer cells. Moreover, the time constant could be useful to assess drug-screening applications where biophysical changes occur in cells. The present microfluidic system is totally label-free, which would relieve clinicians from the tangled procedure of labeling and reduce their workload. The microfluidic system proposed here is simple, but its use is not limited to screening of metastatic cells, it has the potential to be used in many areas of medicine other than cancer diagnostics. Although some improvements such as quantification of cell viscoelasticity is necessary, extensive applications of the present system will enable rapid mechanophenotyping of various cells.

Since a tapered portion of the channel was sufficiently long compared to cell size, viscous deformation was assumed to have completed before a cell left the taper. In other words, in the current system, it was considered that the effect of cell viscosity on cell deformation or shape at the tip of the taper was considered to be small and the initial strain ϵ_0 was determined mostly by cell elasticity. As shown in Figure 5, the initial strain ϵ_0 of B16-F1 cells was almost the same as that of B16-F10 cells, leading to an assumption that there was no difference in cell elasticity between B16-F1 cells and B16-F10 cells. Moreover, as shown in Figure 6, B16-F10 cells had a significantly larger time constant τ than B16-F1. As time constant τ is a ratio of the viscosity to the elasticity of a cell, μ/k , the assumption that there was no difference in cell elasticity between B16-F1 cells and B16-F10 cells indicated that B16-F10 cells had larger cell viscosity than B16-F1 cells. In light of a biological viewpoint that more metastatic and invasive cells should be softer to pass through a narrow gap in extracellular matrix, larger cell viscosity could be unbeneficial for metastatic cells. The biological relevance of larger viscosity for more metastatic cells remains inconclusive and should be clarified in future research.

The width of the flow channel at the exit of the tapered channel was 20 μm . This width might not be small enough to cause large deformation to cells if we consider that the cell size was 15.4 μm in diameter on average. In fact, as shown in Figure 5, we did not find a statistically significant difference in cell stiffness between B16-F1 and B16-F10 cells in the present experimental condition. Two possible reasons were considered. First, loaded cell deformation was not large enough to reflect a difference in cell stiffness. Second, B16-F1 and B16-F10 cells have a comparable level of stiffness in the floating state. Experiments with larger loading by using a device with smaller width will answer this question. At the same time however, narrowing the channel increases the risk of clogging with cells or other debris. Taking into account the practical applications of the proposed channel, clogging has to be avoided. As shown in the present study, a statistically significant difference in the time constant was noticed even with the current width. In this sense, though it was limited to the cell types examined here, the width of 20 μm was considered to be sufficient.

The sheath flow was established in the present flow channel. The sheath flow is necessary as the cell is much smaller than the taper tip and it is important to control cells at a particular position. In this sense, the sheath flow was redundant in the current experiment because the channel width of the taper tip was comparable with cell size.

Although cells flowed along the centerline of the flow channel at the tip, they may have had some rotational motions when they were released into a large pool beyond the taper tip. Due to deformation, cells would have not stayed in the centerline, although they moved downstream by inertia. As a consequence, fluid shear was exerted on cells such that they exhibited rotational motions. Once cells are out of the centerline, they experience a shear-induced lift force that drives them toward channel

walls [48]. As deformed cells recover their shape, a time period of the rotation decreases [49], meaning that cells rotate more quickly. However, we did not observe significant cell rotation when looking at cell behaviors in the present experiment. This could be because the experiment's duration was not long enough to observe cell rotation. As shown in Figures 3 and 4, cell deformations were tracked for only 200 μs in the present experiment. During that period of time, the cell traveled approximately 30 μm , which is 1.5 times as large as a cell size. The cell rotation would have introduced fluctuating errors in cell height, thereby giving errors in the measurement of the time constant of shape recovery. In fact, the time variation of cell height shown in Figure 4a showed fluctuating behaviors. Further experiments are needed to assess the effect of cell rotations on the time constant of shape recovery.

Actin filaments are concerned with the structural strength, shape stability, and deformation behaviors of cells [50–53]. As seen in Figure 7a,b, in adherent cells, B16-F1 cells appeared to have thicker actin fibers than B16-F10 cells. This observation was consistent with Sadano et al. [54], who found that actin fibers provide cells with mechanical integrity and structurally support the plasma membrane. In this sense, B16-F1 cells that were rich in actin fibers should be stiffer than B16-F10 cells. This speculation was congruent with Watanabe et al. [14], who demonstrated larger elasticity in B16-F1 than B16-F10 using atomic force microscopy. In contrast, the present results demonstrated no difference in cell elasticity between B16-F1 cells and B16-F10 cells. In fact, cell deformation might not be large enough to reflect a difference in elasticity in the present experimental condition. But, assuming that cells were sufficiently deformed, we attribute a discrepancy between Watanabe et al. [14] and the present result to a difference in cell state—cells analyzed in this study were detached from dishes and were suspended in PBS(-). In suspended cells, actins did not have firm fiber structures. The cell detachment from a dish caused depolymerization of filamentous actins (F-actin) into the monomeric globular form of actin (G-actin) as a part of cytoskeletal remodeling. In fact, filamentous structures were not found in floating B16-F1 cells (Figure 7c) anymore, and no remarkable difference was noticed in the structure and amount of actin filaments between B16-F1 cells and B16-F10 cells. These observations indicated that the leveling in cell elasticity of B16-F1 cells and B16-F10 cells was due to the loss of F-actin by cell detachment. Depolymerization of F-actin would have resulted in an increase in the amount of G-actin. Dispersion of G-actin, or a solid particulate phase in a liquid phase of cytoplasm might have resulted in changing the rheological properties of cytoplasm. As shown in Figure 6, the viscosity of B16-F10 cells was larger than that of B16-F1 cells. This would imply that an increase in G-actin provides cytoplasm with its pseudoplastic nature, by which apparent viscosity decreased with increased stress. Future studies should warrant these speculations.

As shown in Figures 5 and 6, for B16-F1 cells, no changes in ϵ_0 and shape recovery time constant τ were observed, regardless of the catechin treatment. In contrast, the shape recovery time constant τ of B16-F10 cells was significantly decreased by catechin treatment and was almost the same value as that of B16-F1 cells, indicating that the catechin treatment promoted fast shape recovery of the B16-F10 cells. On the other hand, Figure 5 showed no change in ϵ_0 of B16-F10 cells between catechin-treated and untreated groups. Since a fluid force is continuously applied to the cells while passing through the tapered part of the flow channel, ϵ_0 is hardly influenced by the cell viscosity and is thought to be solely determined by cell stiffness. If so, the decrease in the shape recovery time constant τ is thought to be due to the decrease in cell viscosity μ by catechin treatment. Although the mechanism of how catechin brings a change in the viscosity of cancer cells is unclear, these results suggest that it would be possible to evaluate drug efficacy, at least in highly metastatic cancer cells, using the shape recovery time constant τ .

Cells were potentially dead after they passed through microflow channels. A significant loss of cancer cell viability can occur at shear stress levels above 10 Pa [55]. In the present experimental condition, the maximum shear stress of a channel flow was roughly estimated to be 638 Pa under the assumption of the Poiseuille flow. In the study by Zhou et al. [55], cell viability was 83% for the maximum shear stress calculated to be 199 Pa. Their flow channels with smaller maximum shear stress levels reduced cell viability, although a direct application of their results to our study is difficult

as their channel is different from the present flow channel in design. However just for cancer cell screening, cells were not necessarily viable after they passed through the flow channel. Cell viability must be cared if filtration, concentration or sorting of cells are included in the scope of application.

Microfluidic techniques and devices offer rapid high throughput in cell mechanophenotyping compared to conventional analytical techniques such as atomic force microscopy (AFM), microaspiration, and optical tweezers [23,24,56–59]. In AFM, cell samples need to be indented one by one with care, although it allows researchers to map the mechanical properties of a single cell and provide information on cellular structures including cytoskeletal structure. One of the drawbacks of AFM is that it is applicable only to cells that adhere to the base or dish, and thus the use of AFM for floating cancer cells in circulation is not appropriate. Microaspiration and optical tweezers are more conventional approaches for the mechanical characterization of cells. These techniques provide both local and global mechanical properties of cells but are laborious and require partial technical skill. In our experience, it takes more than an hour to measure a few cells. Microfluidic techniques, including that used in the present study, reduce such laboratory workload. A comparison of microfluidic techniques with AFM, microaspiration, and optical tweezers for measuring red blood cell deformability is summarized in Bento et al. [18]. In microfluidic techniques, cells can be continuously scanned once cell flow is supplied. Combined with imaging analysis, cell mechanophenotyping can be automated. As the present system is not equipped with the automatic imaging analysis, cell deformability was assessed manually after the experiment. Yet, indices of the cell deformability such as the time constant were immediately obtained once a cell was identified in a series of recorded images—after some assessments of image quality. Future improvement of imaging analysis will achieve rapid mechanophenotyping of cancer cells.

Spring constant and viscosity coefficient cannot be determined independently with only the present experiment data. Tajikawa et al. [60] and Kohri et al. [61] studied red blood cells using a similar experimental setup, measured the Young's modulus of red blood cells by a uniaxial tensile test in a separate experiment and estimated the spring constant. This approach however, requires the cell type to be known in advance, and it cannot be applied to this study where it is desired to identify an unknown cell type and evaluate its metastatic potential. Recently, Raj et al. [62] developed a method to estimate the Young's modulus of the cell. A different approach to estimate the Young's modulus of floating cells is also given in TruongVo et al. [39], who used a flow channel similar to the present design. If the spring constant k can be determined from the Young's modulus of the cell using the method of Raj et al. [62] and TruongVo et al. [39], the viscosity coefficient μ can then be estimated from the shape recovery time constant τ and a more detailed analysis of the cell's mechanical properties can be made.

In the present experiment, the exposure time was 10 μ s and the spatial resolution was 0.083 μ m/pixel. Because of these conditions, some images were blurred and the boundary of cells was not clear. In the present analysis, cell shape was manually determined. This may have resulted in errors in measuring the cell height and in turn estimating the time constant of shape recovery. If a cell whose diameter at rest is 15.4 μ m is imaged and its diameter is measured as 14.8 μ m, the compressive strain for this case is approximately 0.039. If a cell diameter is measured two pixels larger, the diameter is quantified as 14.966 μ m and the compressive strain is calculated as 0.028. This yields approximately 10% error in the compressive strain. Careful tuning of the exposure time and the use of better spatial resolution will improve the accuracy of the measurement such that an even tiny difference in the mechanical properties between cells is appreciated.

5. Conclusions

The present study proposes a method to evaluate metastatic potential by evaluating the viscoelastic properties of cancer cells on a tapered microchannel. The shape recovery time constant τ became larger as cancer cells had higher metastatic potential. The results suggested that it would be possible to evaluate the metastatic potential of cancer cells using the shape recovery time constant τ .

The method is simple, but its use is not limited to screening of metastatic cells. It can be extensively applied to various medical and biological areas other than cancer diagnostics, such as the assessment of drug efficacy. Although further improvements are necessary, the present method will help with rapid mechanophenotyping and screening of metastatic cancer cells in clinical practice.

Author Contributions: Conceptualization, M.N.; methodology, M.N. and D.O.; formal analysis, D.O.; resources, M.N.; writing—original draft preparation, D.O. and M.N.; writing—review and editing, S.S. and M.N.; supervision, M.N.; project administration, M.N.; funding acquisition, M.N.

Funding: This research was supported by the Nitto Foundation and a Grand-in-Aid for Scientific Research 18K12055 from the Ministry of Education, Culture, Sports, Science and Technology (MEXT), Japan.

Conflicts of Interest: The authors declare no conflict of interest.

References

1. Orr, F.W.; Wang, H.H.; Lafrenie, R.M.; Scherbarth, S.; Nance, D.M. Interactions between cancer cells and the endothelium in metastasis. *J. Pathol.* **2000**, *190*, 310–329. [[CrossRef](#)]
2. Eger, A.; Mikulits, W. Models of epithelial–mesenchymal transition. *Drug Dis. Today Dis. Models* **2005**, *2*, 57–63. [[CrossRef](#)]
3. Chambers, A.F.; Groom, A.C.; MacDonald, I.C. Dissemination and growth of cancer cells in metastatic sites. *Nat. Rev. Cancer* **2002**, *2*, 563–572. [[CrossRef](#)]
4. Alibert, C.; Goud, B.; Manneville, J.B. Are cancer cells really softer than normal cells? *Biol. Cell* **2017**, *109*, 167–189. [[CrossRef](#)]
5. Jonietz, E. Mechanics: The forces of cancer. *Nature* **2012**, *491*, S56–S57. [[CrossRef](#)]
6. Binnig, G.; Quate, C.F.; Gerber, C. Atomic force microscope. *Phys. Rev. Lett.* **1986**, *56*, 930–933. [[CrossRef](#)]
7. Hochmuth, R.M. Micropipette aspiration of living cells. *J. Biomech.* **2000**, *33*, 15–22. [[CrossRef](#)]
8. Cross, S.E.; Jin, Y.S.; Rao, J.Y.; Gimzewski, J.K. Nanomechanical analysis of cells from cancer patients. *Nat. Nanotechnol.* **2007**, *2*, 780–783. [[CrossRef](#)] [[PubMed](#)]
9. Suresh, S. Nanomedicine: Elastic clues in cancer detection. *Nat. Nanotechnol.* **2007**, *2*, 748–749. [[CrossRef](#)]
10. Zhang, H.; Liu, K.; Soc, J.R. Optical tweezers for single cells. *J. R. Soc. Interface* **2008**, *5*, 671–690. [[CrossRef](#)] [[PubMed](#)]
11. Remmerbach, T.W.; Wottawah, F.; Dietrich, J.; Lincoln, B.; Wittekind, C.; Guck, J. Oral cancer diagnosis by mechanical phenotyping. *Cancer Res.* **2009**, *69*, 1728–1732. [[CrossRef](#)]
12. Swaminathan, V.; Mythereye, K.; O'Brien, E.T.; Berchuck, A.; Blobel, G.C.; Superfine, R. Mechanical stiffness grades metastatic potential in patient tumor cells and in cancer cell line. *Cancer Res.* **2011**, *71*, 5075–5080. [[CrossRef](#)] [[PubMed](#)]
13. Plodinec, M.; Loparic, M.; Monnier, C.A.; Obermann, E.C.; Zanetti-Dallenbach, R.; Oertle, P.; Hyotyla, J.T.; Aebi, U.; Bentires-Alj, M.; Lim, R.Y.H.; et al. The nanomechanical signature of breast cancer. *Nat. Nanotechnol.* **2012**, *7*, 757–765. [[CrossRef](#)]
14. Watanabe, T.; Kuramochi, H.; Takahashi, A.; Imai, K.; Katsuta, N.; Nakayama, T.; Fujiki, H.; Suganuma, M. Higher cell stiffness indicating lower metastatic potential in B16 melanoma cell variants and in (-)-epigallocatechin gallate-treated cells. *J. Cancer Res. Clin. Oncol.* **2012**, *138*, 859–866. [[CrossRef](#)]
15. Hayashi, K.; Iwata, M. Stiffness of cancer cells measured with an AFM indentation method. *J. Mech. Behav. Biomed. Mater.* **2015**, *49*, 105–111. [[CrossRef](#)]
16. Darling, E.M.; Di Carlo, D. High-throughput assessment of cellular mechanical properties. *Annu. Rev. Biomed. Eng.* **2015**, *17*, 35–62. [[CrossRef](#)]
17. Chaudhuri, P.K.; Low, B.C.; Lim, C.T. Mechanobiology of tumor growth. *Chem. Rev.* **2018**, *118*, 6499–6515. [[CrossRef](#)] [[PubMed](#)]
18. Bento, D.; Rodrigues, R.O.; Faustino, V.; Pinho, D.; Fernandes, C.S.; Pereira, A.I.; Garcia, V.; Miranda, J.M.; Lima, R. Deformation of red blood cells, air bubbles, and droplets in microfluidic devices: Flow visualizations and measurements. *Micromachines* **2018**, *9*, 151. [[CrossRef](#)] [[PubMed](#)]
19. Tan, S.J.; Yobas, L.; Lee, G.Y.H.; Ong, C.N.; Lim, C.T. Microdevice for the isolation and enumeration of cancer cells from blood. *Biomed. Microdevices* **2009**, *11*, 883–892. [[CrossRef](#)]

20. Chen, J.; Li, J.; Sun, Y. Microfluidic approaches for cancer cell detection, characterization, and separation. *Lab Chip* **2012**, *12*, 1753–1767. [[CrossRef](#)]
21. Ma, Y.H.V.; Middleton, K.; You, L.; Sun, Y. A review of microfluidic approaches for investigating cancer extravasation during metastasis. *Microsys. Nanoeng.* **2018**, *4*, 17104. [[CrossRef](#)]
22. Hou, H.W.; Warkiani, M.E.; Khoo, B.L.; Li, Z.R.; Soo, R.A.; Tan, D.S.W.; Lim, W.T.; Han, J.; Bhagat, A.A.S.; Lim, C.T. Isolation and retrieval of circulating tumor cells using centrifugal forces. *Sci. Rep.* **2013**, *3*, 1259. [[CrossRef](#)]
23. Khoo, B.L.; Warkiani, M.E.; Tan, D.S.W.; Bhagat, A.A.S.; Irwin, D.; Lau, D.P.; Lim, A.S.T.; Lim, K.H.; Krisna, S.S.; Lim, W.T.; et al. Clinical validation of an ultra high-throughput spiral microfluidics for the detection and enrichment of viable circulating tumor cells. *PLoS ONE* **2014**, *9*, e99409. [[CrossRef](#)]
24. Tse, H.T.; Gossett, D.R.; Moon, Y.S.; Masaeli, M.; Sohsman, M.; Ying, Y.; Misllick, K.; Adams, R.P.; Rao, J.; Di Carlo, D. Quantitative diagnosis of malignant pleural effusions by single-cell mechanophenotyping. *Sci. Transl. Med.* **2013**, *5*, 212ra163. [[CrossRef](#)]
25. Gossett, D.R.; Henry, T.K.; Lee, S.A.; Ying, Y.; Lindgren, A.G.; Yang, O.O.; Rao, J.; Clark, A.T.; Carlo, D.D. Hydrodynamic stretching of single cells for large population mechanical phenotyping. *Proc. Natl. Acad. Sci. USA* **2012**, *109*, 7630–7635. [[CrossRef](#)]
26. Taniguchi, S.; Fujiki, H.; Kobayashi, H.; Go, H.; Miyado, K.; Sadano, H.; Shimokawa, R. Effect of (-)-epigallocatechin gallate; the main constituent of green tea; on lung metastasis with mouse B16 melanoma cell lines. *Cancer Lett.* **1992**, *65*, 51–54. [[CrossRef](#)]
27. Kuzuhara, T.; Sei, Y.; Yamaguchi, K.; Suganuma, M.; Fujiki, H. DNA and RNA as new binding targets of green tea catechins. *J. Biol. Chem.* **2006**, *281*, 17446–17456. [[CrossRef](#)]
28. Sah, J.F.; Balasubramanian, S.; Eckert, R.L.; Rorke, E.A. Epigallocatechin-3-gallate inhibits epidermal growth factor receptor signaling pathway. Evidence for direct inhibition of ERK1/2 and AKT kinases. *J. Biol. Chem.* **2004**, *279*, 12755–12762. [[CrossRef](#)] [[PubMed](#)]
29. Rawangkan, A.; Wongsirisin, P.; Namiki, K.; Iida, K.; Kobayashi, Y.; Shimizu, Y.; Fujiki, H.; Suganuma, M. Green tea catechin is an alternative immune checkpoint inhibitor that inhibits PD-L1 expression and lung tumor growth. *Molecules* **2018**, *23*, 2071. [[CrossRef](#)] [[PubMed](#)]
30. Tsuchiya, H.; Nagayama, M.; Tanaka, T.; Furusawa, M.; Kashimata, M.; Takeuchi, H. Membrane-rigidifying effects of anti-cancer dietary factors. *Biofactors* **2002**, *16*, 45–56. [[CrossRef](#)] [[PubMed](#)]
31. Fang, C.Y.; Wu, C.C.; Hsu, H.Y.; Chuang, H.Y.; Huang, S.Y.; Tsai, C.H.; Chang, Y.; Tsao, G.S.W.; Chen, C.L.; Chen, J.Y. EGCG inhibits proliferation, invasiveness and tumor growth by up-regulation of adhesion molecules, suppression of gelatinases activity, and induction of apoptosis in nasopharyngeal carcinoma cells. *Int. J. Mol. Sci.* **2015**, *16*, 2530–2558. [[CrossRef](#)] [[PubMed](#)]
32. Takahashi, A.; Watanabe, T.; Mondal, A.; Suzuki, K.; Kururu-Kanno, M.; Li, Z.; Yamazaki, T.; Fujiki, H.; Suganuma, M. Mechanism-based inhibition of cancer metastasis with (-)-epigallocatechin gallate. *Biochem. Biophys. Res. Commun.* **2014**, *443*, 1–6. [[CrossRef](#)] [[PubMed](#)]
33. Fidler, I.J. Selection of successive tumour lines for metastasis. *Nat. New Biol.* **1973**, *242*, 148–149. [[CrossRef](#)] [[PubMed](#)]
34. Poste, G.; Doll, J.; Hart, I.R.; Fidler, I.J. In vitro selection of murine B16 melanoma variants with enhanced tissue-invasive properties. *Cancer Res.* **1980**, *40*, 1636–1644. [[PubMed](#)]
35. Nakamura, K.; Yoshikawa, N.; Yamaguchi, Y.; Kagota, S.; Shinozuka, K.; Kunitomo, M. Characterization of mouse melanoma cell lines by their mortal malignancy using an experimental metastatic model. *Life Sci.* **2002**, *70*, 791–798. [[CrossRef](#)]
36. Lee, S.S.; Yim, Y.; Ahn, K.H.; Lee, S.J. Extensional flow-based assessment of red blood cell deformability using hyperbolic converging microchannel. *Biomed. Microdevices* **2009**, *11*, 1021–1027. [[CrossRef](#)]
37. Yaginuma, T.; Oliveira, M.S.N.; Lima, R.; Ishikawa, T.; Yamaguchi, T. Human red blood cell behavior under homogeneous extensional flow in a hyperbolic-shaped microchannel. *Biomicrofluidics* **2013**, *7*, 054110. [[CrossRef](#)] [[PubMed](#)]
38. Rodrigues, R.O.; Lopes, R.; Pinho, D.; Pereira, A.I.; Garcia, V.; Gassmann, S.; Sousa, P.C.; Lima, R. In vitro blood flow and cell-free layer in hyperbolic microchannels: Visualizations and measurements. *BioChip J.* **2016**, *10*, 9–15. [[CrossRef](#)]

39. TruongVo, T.N.; Kennedy, R.M.; Chen, H.; Chen, A.; Berndt, A.; Agarwal, M.; Zhu, L.; Nakshatri, H.; Wallace, J.; Na, S. Microfluidic channel for characterizing normal and breast cancer cells. *J. Micromech. Microeng.* **2017**, *27*, 035017. [[CrossRef](#)]
40. Yoshizawa, S.; Horiuchi, T.; Fujiki, H.; Yoshida, T.; Okuda, T.; Sugimura, T. Antitumor promoter activity of (-)-epigallocatechin gallate, the main constituent of “tannin” in green tea. *Phytother. Res.* **1987**, *1*, 44–47. [[CrossRef](#)]
41. Fujita, Y.; Yamane, T.; Tanaka, M.; Kuwata, K.; Okuzumi, J.; Takahashi, T.; Fujiki, H.; Okuda, T. Inhibitory effect of (-)-epigallocatechin gallate on carcinogenesis with IV-ethyl-IV'-nitro-N-nitrosoguanidine in mouse duodenum. *Jpn. J. Cancer Res.* **1989**, *80*, 503–505. [[CrossRef](#)]
42. Bettuzzi, S.; Brausi, M.; Rizzi, F.; Castagnetti, G.; Peracchia, G.; Corti, A. Chemoprevention of human prostate cancer by oral administration of green tea catechins in volunteers with highgrade prostate intraepithelial neoplasia: A preliminary report from a one-year proof-of-principle study. *Cancer Res.* **2006**, *66*, 1234–1240. [[CrossRef](#)]
43. Tsao, A.S.; Liu, D.; Martin, J.; Tang, X.M.; Lee, J.J.; El-Naggar, A.K.; Wistuba, I.; Culotta, K.S.; Mao, L.; Gillenwater, A.; et al. Phase II randomized, placebocontrolled trial of green tea extract in patients with high-risk oral premalignant lesions. *Cancer Prev. Res.* **2009**, *2*, 931–941. [[CrossRef](#)] [[PubMed](#)]
44. Singh, B.N.; Shankar, S.; Srivastava, R.K. Green tea catechin, epigallocatechin-3-gallate (EGCG): Mechanisms, perspectives and clinical applications. *Biochem. Pharmacol.* **2011**, *82*, 1807–1821. [[CrossRef](#)] [[PubMed](#)]
45. Yang, C.S.; Wang, X. Green tea and cancer prevention. *Nutr. Cancer* **2010**, *62*, 931–937. [[CrossRef](#)]
46. Fujiki, H.; Okuda, T. (–)-Epigallocatechin gallate. *Drugs Future* **1992**, *17*, 462–464. [[CrossRef](#)]
47. Raj, A.; Dixit, M.; Doble, M.; Sen, A.K. A combined experimental and theoretical approach towards mechanophenotyping of biological cells using a constricted microchannel. *Lab Chip* **2017**, *17*, 3704–3716. [[CrossRef](#)]
48. Zhou, J.; Papautsky, I. Fundamentals of inertial focusing in microchannels. *Lab Chip* **2013**, *13*, 1121–1132. [[CrossRef](#)]
49. Masaeli, M.; Sollier, E.; Amini, H.; Mao, W.; Camacho, K.; Doshi, N.; Mitragotri, S.; Alexeev, A.; Di Carlo, D. Continuous inertial focusing and separation of particles by shape. *Phys. Rev. X* **2012**, *2*, 031017. [[CrossRef](#)]
50. Peeters, E.A.G.; Bouten, C.V.C.; Oomens, C.W.J.; Bader, D.L.; Snoeckx, L.H.E.H.; Baaijens, F.P.T. Anisotropic, three-dimensional deformation of single attached cells under compression. *Ann. Biomed. Eng.* **2004**, *32*, 1443–1452. [[CrossRef](#)]
51. Hu, S.; Eberhard, L.; Chen, J.; Love, J.L.; Butler, J.P.; Fredberg, J.J.; Whitesides, G.M.; Wang, N. Mechanical anisotropy of adherent cells probed by a three-dimensional magnetic twisting device. *Am. J. Physiol. Cell Physiol.* **2004**, *287*, C1184–C1191. [[CrossRef](#)]
52. Kumar, S.; Maxwell, I.Z.; Heisterkamp, A.; Polte, T.R.; Lele, T.P.; Salanga, M.; Mazur, E.; Ingber, D.E. Viscoelastic retraction of single living stress fibers and its impact on cell shape, cytoskeletal organization, and extracellular matrix mechanics. *Biophys. J.* **2006**, *90*, 3762–3773. [[CrossRef](#)] [[PubMed](#)]
53. Titushkin, I.; Cho, M. Modulation of cellular mechanics during osteogenic differentiation of human mesenchymal stem cells. *Biophys. J.* **2007**, *93*, 3693–3702. [[CrossRef](#)] [[PubMed](#)]
54. Sadano, H.; Shimokawa-Kuroki, R.; Taniguchi, S. Intracellular localization and biochemical function of variant β -Actin, which inhibits metastasis of B16 melanoma. *Cancer Res.* **1994**, *85*, 735–743. [[CrossRef](#)]
55. Zhou, J.; Giridhar, P.V.; Kasper, S.; Papautsky, I. Modulation of rotation-induced lift force for cell filtration in a low aspect ratio microchannel. *Biomicrofluidics* **2014**, *8*, 044112. [[CrossRef](#)]
56. Liu, Z.; Huang, F.; Du, J.; Shu, W.; Feng, H.; Xu, X.; Cheng, Y. Rapid isolation of cancer cells using microfluidic deterministic lateral displacement structure. *Biomicrofluidics* **2013**, *7*, 0011801. [[CrossRef](#)]
57. Du, G.; Fang, Q.; den Toonder, J.M.J. Microfluidics for cell-based high throughput screening platforms—A review. *Anal. Chim. Acta* **2016**, *903*, 36–50. [[CrossRef](#)]
58. Jiang, J.; Zhao, H.; Shu, W.; Tian, J.; Huang, Y.; Song, Y.; Wang, R.; Li, E.; Slamon, D.; Hou, D.; et al. An integrated microfluidic device for rapid and high-sensitivity analysis of circulating tumor cells. *Sci. Rep.* **2017**, *7*, 42612. [[CrossRef](#)] [[PubMed](#)]
59. Nivedita, N.; Garg, N.; Lee, A.P.; Papautsky, I. A high throughput microfluidic platform for size-selective enrichment of cell populations in tissue and blood samples. *Analyst* **2017**, *142*, 2558–2569. [[CrossRef](#)]

60. Tajikawa, T. Quantitative evaluation of erythrocyte deformability by using micro-visualization technique—Measurement of time constant of shape recovery process as a visco-elastic specification of each blood cells. *J. Vis. Soc. Jpn.* **2014**, *34*, 16–21. (In Japanese)
61. Kohri, S.; Kato, Y.; Tajikawa, T.; Yamamoto, Y.; Bando, K. Measurement of erythrocyte deformability by uniaxial stretching—Measurement of apparent Young's modulus and time constant of shape recovering. *Trans. Jpn. Soc. Med. Biol. Eng.* **2015**, *53*, 1–7. (In Japanese)
62. Raj, A.; Sen, A.K. Entry and passage behavior of biological cells in a constricted compliant microchannel. *R. Soc. Chem.* **2018**, *8*, 20884–20893. [[CrossRef](#)]



© 2019 by the authors. Licensee MDPI, Basel, Switzerland. This article is an open access article distributed under the terms and conditions of the Creative Commons Attribution (CC BY) license (<http://creativecommons.org/licenses/by/4.0/>).



Article

Measurement of Carcinoembryonic Antigen in Clinical Serum Samples Using a Centrifugal Microfluidic Device

Zhigang Gao ^{1,†}, Zongzheng Chen ^{2,†}, Jiu Deng ¹, Xiaorui Li ¹, Yueyang Qu ¹, Lingling Xu ¹, Yong Luo ^{1,*}, Yao Lu ³, Tingjiao Liu ⁴, Weijie Zhao ^{1,*} and Bingcheng Lin ^{1,3}

¹ School of Pharmaceutical Science and Technology, Dalian University of Technology, Dalian 116024, China; gzg1980@dlut.edu.cn (Z.G.); dengjiu@mail.dlut.edu.cn (J.D.); xrli@mail.dlut.edu.cn (X.L.); yyqu@mail.dlut.edu.cn (Y.Q.); nongxuexueshi@gmail.com (L.X.); bclin@dicp.ac.cn (B.L.)

² Integrated Chinese and Western Medicine Postdoctoral research station, Jinan University, Guangzhou 510632, China; chenmond@foxmail.com

³ Dalian Institute of Chemical Physics, Chinese Academy of Sciences, Dalian 116023, China; luyao@dicp.ac.cn

⁴ College of Stomatology, Dalian Medical University, Dalian 116024, China; tingjiao@dlmedu.edu.cn

* Correspondence: yluo@dlut.edu.cn (Y.L.); zyzhao@dlut.edu.cn (W.Z.);

Tel.: +86-0411-8498-6360 (Y.L.); +86-0411-8498-6195 (W.Z.)

† These authors have equally contributed to this work.

Received: 26 July 2018; Accepted: 10 September 2018; Published: 17 September 2018

Abstract: Carcinoembryonic antigen (CEA) is a broad-spectrum tumor marker used in clinical applications. The primarily clinical method for measuring CEA is based on chemiluminescence in serum during enzyme-linked immunosorbent assays (ELISA) in 96-well plates. However, this multi-step process requires large and expensive instruments, and takes a long time. In this study, a high-throughput centrifugal microfluidic device was developed for detecting CEA in serum without the need for cumbersome washing steps normally used in immunoreactions. This centrifugal microdevice contains 14 identical pencil-like units, and the CEA molecules are separated from the bulk serum for subsequent immunofluorescence detection using density gradient centrifugation in each unit simultaneously. To determine the optimal conditions for CEA detection in serum, the effects of the density of the medium, rotation speed, and spin duration were investigated. The measured values from 34 clinical serum samples using this high-throughput centrifugal microfluidic device showed good agreement with the known values (average relative error = 9.22%). These results indicate that the high-throughput centrifugal microfluidic device could provide an alternative approach for replacing the classical method for CEA detection in clinical serum samples.

Keywords: centrifugal microfluidic device; CEA detection; density medium; fluorescent chemiluminescence

1. Introduction

Carcinoembryonic antigen (CEA) is a polysaccharide-protein complex with a molecular weight that ranges from 180 to 220 kD, and has 28 potential N-linked glycosylation sites. CEA is primarily produced by the embryonic intestinal mucous membranes prior to birth. Thus, the concentration of CEA is usually very low in the serum of a healthy adult. However, the serum concentration of CEA can become elevated in the presence of several types of cancer, such as lung [1,2], breast [3,4], colorectal [5,6], or gastric [7] cancers, as well as colon adenocarcinoma [8]. This means that CEA can be considered a broad-spectrum biomarker for cancer diagnosis and prognosis.

A variety of immunoassay methods have been developed for detecting CEA in serum, such as enzyme-linked immunosorbent assays (ELISA) [9], radioimmunoassays [10], fluorescence

immunoassays [11], chemiluminescence immunoassays [12] and amperometric immunoassays [13]. However, a common drawback of these testing methods is that multiple washing steps are required. These repeated washing steps can give rise to increasing measuring errors, which decreases the efficiency while requiring complex instrumentation. Recently, a wash-free one-step immunoassay [14] was developed using a centrifugal microfluidic device, which has great potential for use in clinical applications. This immunoassay method is based on the principle of centrifugal density gradient equilibrium, which takes place inside a microfluidic device. Analytes with fluorescent labels were separated from the bulk serum in one step, using the centrifugal force, through the dense medium located in the microchannels. Afterwards, the fluorescence microbeads, which aggregated at the end of microchannel, could be collected for quantitative analysis.

Following this strategy, Interleukin 6 was rapidly measured (within 15 min) in whole blood by Ulrich et al. [14]. Chung-Yan Koh et al. accomplished the ultrasensitive detection of botulinum toxin in a 2 µL unprocessed sample in 30 min from sample to answer [15]. These studies showed that it is possible to develop a rapid, accurate, high-throughput centrifugal microfluidic chip for the detection of CEA in serum.

In this study, chitosan, which is safe and has good biocompatibility, was used as the dense medium in the centrifugal microfluidic. When combined with ELISA testing, the CEA could be separated by the action of the centrifugal force produced by the rotation, and the concentration of CEA could be detected using a semi-quantitative fluorescence method. This enables the rapid and convenient detection of CEA in serum with high throughput.

2. Materials and Methods

2.1. Design and Manufacture of the Centrifugal Microfluidic Device

A polydimethylsiloxane (PDMS, Sylgard 184, DowDuPont Inc., Midland, MI, USA) glass microfluidic device was designed, as shown in Figure 1A. The height, width, and length of the individual microchannels were 150 µm, 4.2 mm and 1.5 cm, respectively. The diameter of the inlet hole was 5 mm. The distance between the center of the chip and the inlet hole was 6.5 cm. With this geometry, the micro-channels were patterned in PDMS using replica molding. The mold was prepared by spin-coating a thin layer of negative photoresist (SU-8, MicroChem, Corp., Westborough, MA, USA) onto a single side of a polished silicon wafer, which was patterned using UV exposure. Next, the micro-channel layer was obtained by pouring PDMS with a 10:1 (*w/w*) base-to-crosslinker ratio onto the mold to a thickness of approximately 3 mm. After curing the elastomer for 2 h at 80 °C, the PDMS slab was peeled from the mold, and was then punched and hermetically bonded to a coverslip by plasma oxidation.

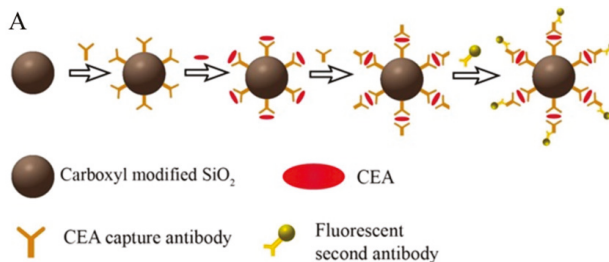


Figure 1. Cont.

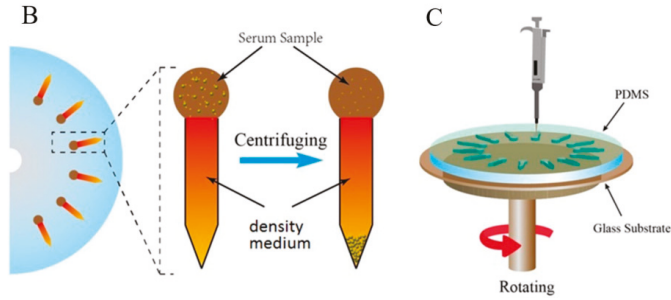


Figure 1. Design of the centrifugal microfluidic device. (A) schematic representation of the sandwiched immunocomplex formed by the binding of the target analyte; (B) schematic of the centrifugal microfluidic platform immunoassay, depicting the multiplexed analysis of the serum; (C) operating principle of the centrifugal microfluidic device.

2.2. Medium Density Screening

Based on the sedimentation process, a theoretical calculation pertaining to the relationship between the density of a material and the centrifugal sedimentation has been proposed [16]. In the case of particle transport in fluids, as in a sedimentation processes, the particles are subject to a viscous force, called drag (F_d). It is given by:

$$F_d = C_d \frac{\rho_{\text{fluid}}}{2} u^2 A_{\text{particle}}, \quad (1)$$

where ρ_{fluid} and u are the density and velocity of the fluid relative to a particle, respectively, A_{particle} is the particle cross-sectional area, and C_d is the drag coefficient. In the laminar flow regime (Stoke's drag), the drag coefficient is proportional to the fluid viscosity μ and inversely proportional to its velocity u relative to the particle, so that for a spherical particle with radius r , the drag force is

$$F_S = 6\pi\mu r u. \quad (2)$$

Based on this, materials with intermediate densities, but various viscosities were tested. The isolating effects of Percoll (Aladdin Inc., Los Angeles, CA, USA) at a concentration at 1.13 g/mL, 7% or 14% dextran (Aladdin Inc.), as well as 1% or 2% chitosan (Aladdin Inc.) were compared in this study. To start, 1.4 g of dextran and 0.01 g Poloxamer (127 F) were dissolved in 9.8 mL hot water, and then mixed with 0.2 mL 5% bovine serum albumin (BSA) solution and stored at 4 °C. Then, 2 g chitosan powder was dissolved in a 0.1 M hydrochloric acid solution for 24 h using a centrifugal mixer. Finally, the solution was used as the dense medium to be added to the centrifugal microfluidic channel.

2.3. Optimization of the Rotation Speed and Spin Time

After the channels of the microfluidic device were cleaned with Phosphate Buffered Saline (PBS), 10 μL of 1% BSA (Aladdin Inc.) were added, and the devices were stored in a refrigerator at 4 °C to block the protein binding sites on the PDMS. Prior to adding 5 μL of 2% chitosan into the microfluidic device, the channels were washed five times with PBS, and stored in a 4 °C refrigerator until just before use. Then, 30 μL carboxyl-modified silica microspheres (Mozhidong Ltd., Beijing, China) were added to a 500 μL centrifuge tube, diluted to 200 μL , and then packaged with 10 μL of the primary antibodies (18.1 g/mL, Abcam, London, UK). After incubation on a table concentrator at room temperature for 2 h, and being stored at 4 °C in a refrigerator overnight, the beads with antibodies became stabilized. Then, the bead–antibody complexes were washed three times with PBS (pH 7.4), and diluted to 200 μL . Then, 5 μL BSA at a concentration at 5% was added to the solution, which was incubated at room temperature on a table concentrator for 2 h to block the remaining protein binding sites. Then,

30 ng/mL CEA samples (Abcam), with labeled primary antibodies and fluorescence labeled secondary antibodies, were successively added into microchannels with syringes or pipettes. The microfluidic device was centrifuged at various angular velocities (1000, 1500, 2000, 2500, 3000, 3500 or 4000 rpm) or at 2500 rpm for various spin durations (60, 90, 120, 150, 180 or 240 s). Afterwards, fluorescence images were obtained using a fluorescence microscope (IX71, Olympus, Tokyo, Japan) that used a high-power mercury lamp as the fluorescence light source and an exposure time of 3.5 s. After the fluorescence images were obtained, the fluorescence intensity values, with the background subtracted, were read by ImageJ software (version 2.1, National Institutes of Health, Bethesda, MD, USA). Then, statistical analyses were performed based on the particular requirements.

2.4. Establishing a CEA Standard Curve

CEA antigen samples at various concentrations, with labeled primary antibodies and fluorescence-labeled secondary antibodies, were successively added and incubated. Finally, the microfluidic device was centrifuged for 150 s at 2500 rpm in a horizontal centrifuge. At the same time, fluorescence images were obtained using a fluorescence microscope with exposure time of 3.5 s. The fluorescence images were analyzed with ImageJ software to establish a standard curve between the concentration of CEA and the corresponding fluorescence intensity.

2.5. Detection of CEA in Human Serum

BSA blocked bead–antibody complexes, and labeled primary antibodies and fluorescence-labeled secondary antibodies were added to the centrifuge microfluidic device and incubated at room temperature for 2 h. Then, clinical serum samples, which were collected and provided by the Affiliated Hospital of Dalian Medical University from both healthy and cancer person, were added to the centrifuge chip, and spun at 2500 rpm for 2.5 min. After obtaining the fluorescence images using the fluorescence microscope and processing with the ImageJ software, the standard concentration curve were used to obtain the experimental CEA concentrations.

2.6. Statistical Analysis

The SPSS 18.0. (IBM, New York, NY, USA) was used for mean value and standard deviation calculation as well as significance testing.

3. Results

3.1. Design, Fabrication, and Verification of the Centrifugal Microfluidic Device

Figure 1 shows the centrifugal microfluidic platform for detecting CEA using a sedimentation-based immunoassay. The sample was mixed with a detection cocktail consisting of silica microbeads (1 μm diameter), which were coated with specific antibodies for the target of interest, in this case, CEA. The detection antibodies were labeled with a fluorescent tag, which binds to the capture beads in the presence of the corresponding antigen (Figure 1A). After the serum samples were mixed with the antibody-conjugated capture beads and fluorescent detection antibodies in solution, they were added to a preloaded dense medium. The beads were pushed to the bottom of the channel to form pellets by the centrifugal force. Eventually, the target analytes separated from the rest of the sample (Figure 1B). The entire process of CEA detection could be completed in one step, as shown in Figure 1C. The samples were added at the entrance of the centrifugal microfluidic platform, which was split into 14 radially arranged pencil-like microchannels. Then, the target analyte could be detected using a sedimentation-based immunoassay. This simple, one-step centrifugal microfluidic platform provides high analytical accuracy and repeatability, which cannot be achieved by processes that require multiple steps.

To validate the effectiveness of the chemiluminescence immunoassay used in this device, CEA standard samples were measured using a double-antibody sandwich ELISA with the conventional

method and the centrifugal microfluidic device. The proposed method was shown to be equivalent to the conventional method based on the linearity of the response (see supplementary material in the supporting information).

3.2. Medium Screening and Structure Optimization of the Microfluidic Device

Based on Equation (2), we screened various media to determine the optimal density and viscosity, as one of the critical aspects in this study. Percoll, dextran (7% or 14%), and chitosan (1% or 2%) were tested as dense media, as shown in Figure 2. It was suggested that the microbeads could not be separated in a Percoll solution at a concentration of 1.13 g/mL (Figure 2A). However, if the sample is whole blood with a density of 1.09 to 1.11 g/mL of red blood cells, Percoll can separate red blood cells from plasma. Although dextran can separate the microbeads from solution as a clinical plasma substitute, the separating effect is not as good as with the chitosan solution (Figure 2B,C). Because the concentration of the dense medium solution is 1%, the modified antigen antibody beads can become separated at the end of the microchannel. Furthermore, the rest of the solution will have been mixed with the medium because this is beyond the abilities of the separation process (Figure 2D,E). In addition, if the concentration of the dense medium is 2%, the modified antigen antibody beads can pass through the medium to reach the bottom of the channel. Therefore, a chitosan solution with a concentration of 2% was selected as the dense medium in the centrifugal microfluidic device to separate the microbeads modified by antigen antibodies in solution.

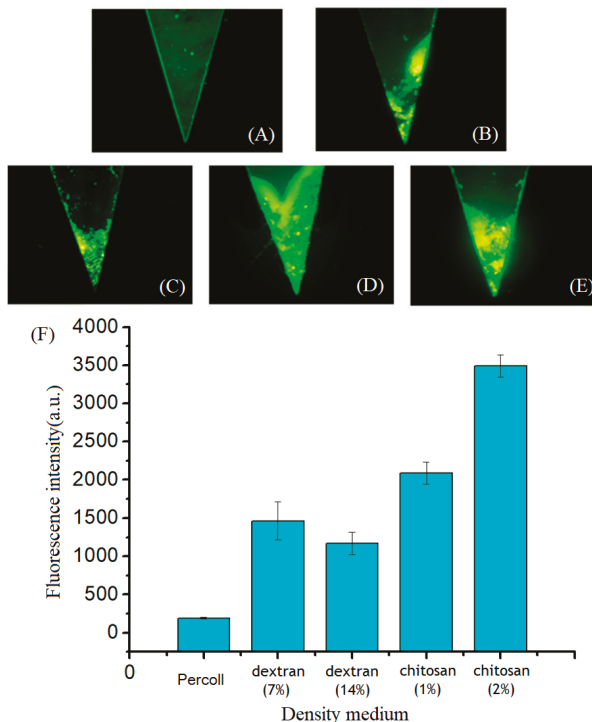


Figure 2. Effect of the dense medium on isolation efficiency in the centrifugal microfluidic platform. Separating effects of (A) Percoll, dextran ((B) 7% or (C) 14%), and chitosan ((D) 1% or (E) 2%) as dense media and (F) their histogram comparison.

3.3. Effects of Rotation Speed and Spin Duration on the Detection of CEA

The effects of rotation speed and spin duration were also considered in this study. In the centrifugal microfluidic device with chitosan as the dense medium, the effects of various angular velocities on the isolation power of CEA standard samples (25 ng/mL) were investigated.

In Figure 3A, the fluorescence intensity of aggregated microbeads increased as the rotation speed increased from 1000 to 2500 rpm. However, even if the rotation speed was set to greater than 2500 rpm, the fluorescence intensity of the aggregated microbeads did not increase, and instead plateaued at a constant value. This indicates that spinning at 2500 rpm caused all the microbeads in the bulk serum to migrate to the end of the microchannel. Thus, 2500 rpm was used as the rotation speed for CEA detection.

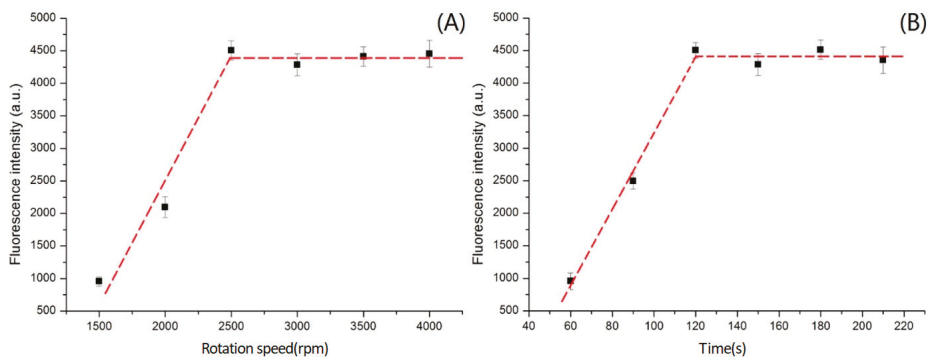


Figure 3. Effects of rotation speed and spin duration on carcinoembryonic antigen (CEA) isolation. (A) the effect of rotation speed on CEA isolation; (B) the effect of spin duration on CEA isolation.

Similarly, the effects of various spin durations of the centrifugal microfluidic device using chitosan as the dense medium on the isolation of CEA in a standard sample (25 ng/mL) were investigated at 2500 rpm. As shown in Figure 3B, in the first two minutes, the microbeads were gradually separated to the end of the microchannel, and the fluorescence intensity increased over time. After two minutes, the microbeads in the sample were almost completely in the detection area, and the fluorescence intensity was constant thereafter. To have a margin of safety, 2.5 min was selected as the centrifugal spin duration.

3.4. CEA Detection in Human Serum Samples

CEA standard samples with various concentrations were measured using this device, and the relationship between CEA concentration (x) and the fluorescence intensity (y) was established with a standard curve ($y = 1647.3x + 5432.9$). It is suggested that the analytical sensitivity of the standard curve is 1673.4. Based on Figure 4, the repeatability at each concentration was good ($n = 4$), and the curve was linear within the CEA concentration range of 0.7–22.5 ng/mL ($R^2 = 0.993$). Thus, these equations can be used as a standard curve for sample detection, including human serum samples.

CEA in clinical human serum samples with known concentrations were measured using the centrifugal microfluidic device, and comparisons between the known and measured concentrations are shown in Table 1 and Figure 4. It can be seen from the table that the sample testing errors from 90% of the samples are less than 20%, and the average relative error was only 9.22%. This indicates that the detection results obtained by this device were reliable. In addition, as shown in Figure 5A, in these tests, excluding the poor repeatability of certain outlier samples, the repeatability of the remaining samples was good for CEA concentrations in the range of 0.5 ng/mL to 27 ng/mL. In addition, it was determined from Figure 5B that, when the carcinoembryonic antigen concentration was less than

2.0 ng/mL, the detection concentration was consistent with the known concentration, and when the concentration of the serum sample was higher than 10 ng/mL, there were some slight differences between the actual and measured concentrations.

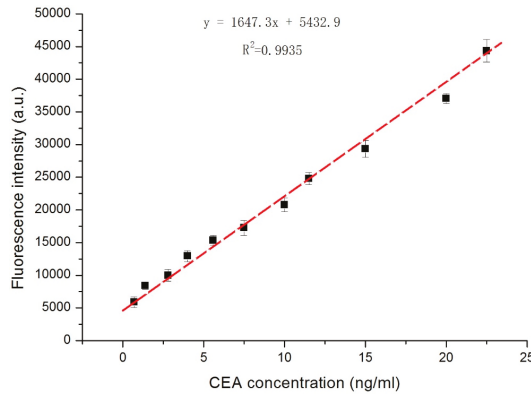


Figure 4. Relationship between fluorescence intensity of aggregated microbeads and CEA concentration in the serum.

Table 1. Results from 32 clinical serum samples.

No.	Known Value (ng/mL)	Measured Value (ng/mL), <i>n</i> = 3	Relative Error
1	12.94	12.82 ± 0.33	0.96%
2	3.69	3.82 ± 0.26	3.52%
3	0.71	0.58 ± 0.52	18.59%
4	2.4	2.43 ± 0.21	1.45%
5	5.76	6.10 ± 0.30	5.87%
6	2.75	2.94 ± 0.15	7%
7	0.91	1.03 ± 0.29	13.14%
8	2.55	3.31 ± 0.10	29.96%
9	2.01	2.04 ± 0.07	1.55%
10	2.02	2.23 ± 0.85	10.50%
11	2.52	2.47 ± 0.22	1.99%
12	8.01	7.46 ± 0.29	6.86%
13	14.07	13.59 ± 0.69	3.43%
14	24.16	24.54 ± 0.93	1.59%
15	9.12	9.48 ± 0.39	3.99%
16	26.54	25.69 ± 3.57	3.19%
17	3.35	3.29 ± 0.28	1.66%
18	2.98	3.27 ± 0.48	9.61%
19	1.34	1.57 ± 0.10	17.39%
20	9.63	9.48 ± 0.44	1.59%
21	2.04	2.08 ± 0.19	1.94%
22	4.58	4.60 ± 0.31	0.36%
23	0.91	0.93 ± 0.11	1.91%
24	0.53	0.55±0.15	4.67%
25	2.72	3.05 ± 0.37	12.31%
26	1.71	1.63 ± 0.46	4.48%
27	0.25	0.30 ± 0.08	21.68%
28	2.24	2.83 ± 0.57	26.23%
29	1.38	1.29 ± 0.18	6.55%
30	2.17	2.73 ± 0.51	25.8%
31	0.66	0.52 ± 0.36	21.22%
32	1.81	2.24 ± 0.97	24.02%

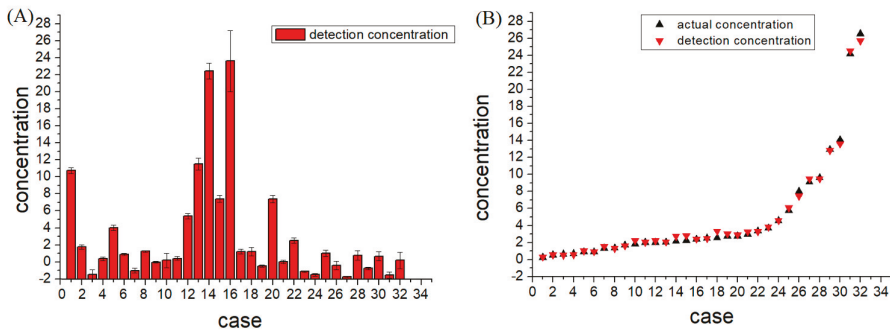


Figure 5. CEA detection in clinical human serum samples. (A) the repeatability of actual samples; (B) comparison of known and measured concentrations.

The CEA detection results using the centrifugal microfluidic device and the hospital instruments were compared. As shown in Table 2, when excluding samples 7, 18 and 26, the *p*-value of samples were above 0.05. This suggests that there were no significant differences between the detection method of the centrifugal microfluidic device and the hospital’s method.

Table 2. *p*-values between paired samples.

Samples	<i>p</i> -Value	Samples	<i>p</i> -Value	Samples	<i>p</i> -Value
1	0.299	12	0.655	23	0.514
2	0.752	13	0.728	24	0.953
3	0.497	14	0.114	25	0.112
4	0.655	15	0.13	26	0.032
5	0.474	16	0.761	27	0.162
6	0.748	17	0.662	28	0.545
7	0.016	18	0.001	29	0.394
8	0.389	19	0.164	30	0.255
9	0.762	20	0.084	31	0.471
10	0.437	21	0.32	32	0.668
11	0.453	22	0.71	–	–

4. Discussion

A centrifugal microfluidic chip was constructed for detecting CEA in clinical serum samples. The device is based on a sandwiched immunoassay with biocompatible chitosan as the dense medium. It is driven by centrifugal force to implement rapid, high-throughput detection of serum CEA and other biomarkers. This centrifugal microfluidic chip does not require any washing steps, and can simplify the experimental procedure with increased accuracy and efficiency, compared with traditional immunoassays. Thus, this centrifugal microfluidic device can be expected to be used for CEA determination in hospitals.

The dense medium used in this microfluidic device was 2% chitosan to eliminate the need for the complicated washing steps of the traditional detection method. This device was able to separate the analyte from the solution in a one-step centrifugal process. Therefore, the samples could be detected directly and easily. In addition, the 14 individual pencil channels acted as parallel systems on the centrifugal microfluidic chip, with a relative standard deviation (RSD) value of just 4.95%.

The rotation speed and spin duration were optimized for the microfluidic device. It was determined that 2500 rpm for 150 s was able to completely move the analytes of the samples to the detection area. Thus, this microfluidic device can improve upon the current clinical detection methods.

Finally, the CEA detection results obtained from this centrifugal microfluidic device were compared and verified with clinical values. Thirty clinical serum samples were measured based on the

standard curve established between the CEA concentration and fluorescence intensity. The detection error in 90% of the samples was less than 20% (Table 1), and the repeatability of the samples was good over the range of concentrations of 0.5 ng/mL to 27 ng/mL. Although a few samples showed low reproducibility, this might have been because the CEA was not uniformly distributed in the serum, and the volume of samples added to microfluidic device was microscale, thus making the contents to be measured in each sample unstable.

In conclusion, this study describes a centrifugal microfluidic device that was developed for detecting CEA. This method uses density gradient centrifugation and is free of washing steps, and is thus more accurate than traditional ELISA methods. It also can achieve high-throughput detection, with the potential to be used in central labs.

Supplementary Materials: The following are available online at <http://www.mdpi.com/2072-666X/9/9/470/s1>, Figure S1: Chip channel parallelism measurement, Figure S2: Standard curve for determination of protein content, Figure S3: The comparison of fluorescence concentration curve between conventional ELISA method and centrifugal microfluidic device. (A) conventional ELISA method; (B) centrifugal microfluidic device.

Author Contributions: Z.G., Y.L. (Yong Luo), W.Z., B.L., Y.L. (Yao Lu) and T.L. conceived and designed the experiments; Z.G., X.L., and L.X. performed the experiments; Z.G., J.D., Y.L. (Yong Luo) and L.X. analyzed the data; Z.C., Y.Q., W.Z., B.L., Y.L. (Yao Lu) and T.L. contributed reagents/materials/analysis tools; Z.G., Z.C. and Y.L. (Yong Luo) wrote the paper.

Funding: This work was supported by the National Natural Science Foundation of China (No. 21675017), and the National Key Research and Development Program of China (No. SQ2017YFC170204-01).

Acknowledgments: The authors would like to appreciate Affiliated Hospital of Dalian Medical University to provide CEA Clinical samples.

Conflicts of Interest: All authors declare no conflict of interest.

References

1. Braik, T.; Gupta, S.; Poola, H.; Jain, P.; Beiranvand, A.; Lad, T.E.; Hussein, L. Carcino embryonic antigen (CEA) elevation as a predictor of better response to first line pemetrexed in advanced lung adenocarcinoma. *J. Thorac. Oncol.* **2012**, *7*, S310.
2. Yu, D.H.; Li, J.H.; Wang, Y.C.; Xu, J.G.; Pan, P.T.; Wang, L. Serum anti-p53 antibody detection in carcinomas and the predictive values of serum p53 antibodies, carcino-embryonic antigen and carbohydrate antigen 12-5 in the neoadjuvant chemotherapy treatment for III stage non-small cell lung cancer patients. *Clin. Chim. Acta* **2011**, *412*, 930–935. [[CrossRef](#)] [[PubMed](#)]
3. Bao, H.; Yu, D.; Wang, J.; Qiu, T.; Yang, J.; Wang, L. Predictive value of serum anti-p53 antibodies, carcino-embryonic antigen, carbohydrate antigen 15-3, estrogen receptor, progesterone receptor and human epidermal growth factor receptor-2 in taxane-based and anthracycline-based neoadjuvant chemotherapy in locally advanced breast cancer patients. *Anti-Cancer Drug* **2008**, *19*, 317–323.
4. Thriveni, K.; Krishnamoorthy, L.; Ramaswamy, G. Correlation study of carcino embryonic antigen & cancer antigen 15.3 in pretreated female breast cancer patients. *India J. Clin. Biochem.* **2007**, *22*, 57–60.
5. Cierpinski, A.; Stein, A.; Ruessel, J.; Ettrich, T.; Schmoll, H.J.; Arnold, D. Prognostic impact of carcino embryonic antigen (CEA), carbohydrate antigen (CA 19-9), and lactate dehydrogenase (LDH) decrease in patients with metastatic colorectal cancer (mCRC) receiving a bevacizumab- or cetuximab-chemotherapy combination. *Onkologie* **2011**, *34*, 250.
6. Wang, Y.R.; Yan, J.X.; Wang, L.N. The diagnostic value of serum carcino-embryonic antigen, alpha fetoprotein and carbohydrate antigen 19-9 for colorectal cancer. *J. Cancer Res. Ther.* **2014**, *10*, 307–309. [[PubMed](#)]
7. Lai, H.; Jin, Q.; Lin, Y.; Mo, X.; Li, B.; He, K.; Chen, J. Combined use of lysyl oxidase, carcino-embryonic antigen, and carbohydrate antigens improves the sensitivity of biomarkers in predicting lymph node metastasis and peritoneal metastasis in gastric cancer. *Tumor Biol.* **2014**, *35*, 10547–10554. [[CrossRef](#)] [[PubMed](#)]
8. Szajda, S.D.; Snarska, J.; Jankowska, A.; Roszkowska-Jakimiec, W.; Puchalski, Z.; Zwierz, K. Cathepsin D and carcino-embryonic antigen in serum, urine and tissues of colon adenocarcinoma patients. *Hepatogastroenterology* **2008**, *55*, 388–393. [[PubMed](#)]

9. Zhao, L.; Xu, S.; Fjaertoft, G.; Pauksen, K.; Hakansson, L.; Venge, P. An enzyme-linked immunosorbent assay for human carcinoembryonic antigen-related cell adhesion molecule 8, a biological marker of granulocyte activities in vivo. *J. Immunol. Methods* **2004**, *293*, 207–214. [[CrossRef](#)] [[PubMed](#)]
10. Chester, S.J.; Maimonis, P.; Vanzuiden, P.; Finklestein, M.; Bookout, J.; Vezeridis, M.P. A new radioimmunoassay detecting early stages of colon cancer: a comparison with CEA, AFP, and Ca 19-9. *Dis. Markers* **1991**, *9*, 265–271. [[PubMed](#)]
11. Yan, F.; Zhou, J.; Lin, J.; Ju, H.; Hu, X. Flow injection immunoassay for carcinoembryonic antigen combined with time-resolved fluorometric detection. *J. Immunol. Methods* **2005**, *305*, 120–127. [[CrossRef](#)] [[PubMed](#)]
12. Lin, J.; Yan, F.; Hu, X.; Ju, H. Chemiluminescent immunosensor for CA19-9 based on antigen immobilization on a cross-linked chitosan membrane. *J. Immunol. Methods* **2004**, *291*, 165–174. [[CrossRef](#)] [[PubMed](#)]
13. Zhang, S.; Yang, J.; Lin, J. 3,3'-diaminobenzidine (DAB)-H₂O₂-HRP voltammetric enzyme-linked immunoassay for the detection of carcinoembryonic antigen. *Bioelectrochemistry* **2008**, *72*, 47–52. [[CrossRef](#)] [[PubMed](#)]
14. Schaff, U.Y.; Sommer, G.J. Whole blood immunoassay based on centrifugal bead sedimentation. *Clin. Chem.* **2011**, *57*, 753–761. [[CrossRef](#)] [[PubMed](#)]
15. Koh, C.-Y.; Schaff, U.Y.; Piccini, M.E.; Stanker, L.H.; Cheng, L.W.; Ravichandran, E.; Singh, B.-R.; Sommer, G.J.; Singh, A.K. Centrifugal microfluidic platform for ultrasensitive detection of botulinum toxin. *Anal. Chem.* **2015**, *87*, 922–928. [[CrossRef](#)] [[PubMed](#)]
16. Strohmeier, O.; Keller, M.; Schwemmer, F.; Zehnle, S.; Mark, D.; Von Stetten, F.; Zengerle, R.; Paust, N. Centrifugal microfluidic platforms: advanced unit operations and applications. *Chem. Soc. Rev.* **2015**, *44*, 6187–6229. [[CrossRef](#)] [[PubMed](#)]



© 2018 by the authors. Licensee MDPI, Basel, Switzerland. This article is an open access article distributed under the terms and conditions of the Creative Commons Attribution (CC BY) license (<http://creativecommons.org/licenses/by/4.0/>).



Article

High-Precision Lens-Less Flow Cytometer on a Chip

Yuan Fang ^{1,2}, Ningmei Yu ^{1,*}, Yuquan Jiang ¹ and Chaoliang Dang ¹

¹ School of Automation and Information Engineering, Xi'an University of Technology, Xi'an 710048, China; fangyuanmy@163.com (Y.F.); yqjiang@xaut.edu.cn (Y.J.); dangclkk@163.com (C.D.)

² School of Electrical and Electronic Engineering, Baoji University of Arts and Sciences, Baoji 721016, China

* Correspondence: yunm@xaut.edu.cn

Received: 17 April 2018; Accepted: 9 May 2018; Published: 10 May 2018

Abstract: We present a flow cytometer on a microfluidic chip that integrates an inline lens-free holographic microscope. High-speed cell analysis necessitates that cells flow through the microfluidic channel at a high velocity, but the image sensor of the in-line holographic microscope needs a long exposure time. Therefore, to solve this problem, this paper proposes an S-type micro-channel and a pulse injection method. To increase the speed and accuracy of the hologram reconstruction, we improve the iterative initial constraint method and propose a background removal method. The focus images and cell concentrations can be accurately calculated by the developed method. Using whole blood cells to test the cell counting precision, we find that the cell counting error of the proposed method is less than 2%. This result shows that the on-chip flow cytometer has high precision. Due to its low price and small size, this flow cytometer is suitable for environments far away from laboratories, such as underdeveloped areas and outdoors, and it is especially suitable for point-of-care testing (POCT).

Keywords: cell analysis; lens-less; microfluidic chip; twin-image removal; POCT

1. Introduction

Cell analysis using an optical microscope or a flow cytometer is an important technique in biology and medicine [1]. Optical microscopes can obtain focus images of cells for biomedical applications, and flow cytometers can collect the signature of a large number of cells in liquid specimens with high analysis speed. However, these instruments are unsuitable for outdoor and undeveloped areas because of their high price and large size. Currently, there is a need for a small and inexpensive cell analysis device that combines the properties of the above two devices.

Over the past decade, lens-less imaging has been considered a good way to reduce the volume and cost of cell analysis tools. Seung Ah Lee and Guoan Zheng designed opto-fluidic microscopes using a complementary metal oxide semiconductor (CMOS) image sensor (CIS) and a microfluidic channel [2–7]. To weaken the shadow-imaging diffraction, the distance between the cells and the surface of the image sensor must be shorter than 2 μm . These researchers mounted a micro-channel on a CIS by removing the protective glass and Bayer filter. To improve the spatial resolution of cell images obtained with a 4 \times object lens, they used a multi-frame, super-resolution algorithm based on the sub-pixel movement of cells flowing through the micro-channel. At the same time, Aydogan Ozcan and Serhan O. Isikman designed numerous lens-free on-chip microscopes based on incoherent digital holography [8–25]. The lens-free on-chip microscopes capture digital diffractive images of cells by using an in-line holographic structure. The diffractive images were used to reconstruct clear images of the cells using angular spectrum theory [26], and the resultant clear cell images are comparable to those obtained by a 10 \times object lens with a numerical aperture of ~ 0.1 – 0.2 . Later, Se-Hwan Paek and Sungkyu Seo proposed a new method to classify different types of cells using digital diffractive images [27–30]. Mei Yan and Hao Yu conducted a blood cell analysis with a single-frame super

resolution [31]. The concept of a lens-less microscopy technique is a novel idea for the miniaturization of flow cytometry, but the accuracy and speed of cell counting in such a method are challenges. At present, most devices based on a lens-less platform use only one frame to count cells, and this leads to inaccurate cell counting [27]. It is not easy to distinguish between cells and dust using a static image, which has a great influence on the ability to count with high precision.

In this manuscript, we propose an on-chip flow cytometer system based on lens-less imaging and a microfluidic control technique to improve the speed of cell analysis. The system causes cells to flow through a micro-channel in a polydimethylsiloxane (PDMS) microfluidic chip above a CIS. A near-coherent light source is mounted above the microfluidic chip (~5 cm), and diffraction shadow images of cells generated by the near-coherent light source are then captured by the CIS. To obtain clear images of cells, a phase iterative reconstruction algorithm is used for image diffraction [32]. In addition, the system can obtain a very accurate image without cells absented for background removal. After the background is removed, images of each segmented cell can be acquired from the whole image more precisely. Therefore, we can more accurately extract features from each cell image and quickly classify and count cells.

Because of the low intensity of near-coherent light caused by a pinhole, the exposure time of the image sensor in the system is longer than 400 ms. Therefore, there is stronger motion blur while the cells are quickly flowing in the micro-channel. To solve this problem, this manuscript proposes a method in which the cells in the micro-channel are imaged simultaneously in a large field of view (FOV) instead of with a flow cytometer method in which the cells pass through the testing area at high speed. In other words, the method takes advantage of the larger FOV of the CIS to reduce the cell flow velocity. To utilize the large FOV of the CIS, we design an “S” channel shape. As a result, we can ensure that the CIS captures the maximum possible number of cells in a frame. In addition, the cells in current frame flow out of the micro-channel completely before the next exposure of the CIS. Thus, all the cells in each frame are new cells, and the cells in each individual frame can be evaluated to increase the number of tested cells. Regarding cost, the CIS is commonly used in industrial cameras and mobile phones, so the price is very low (below \$10). The microfluidic chip comprises a PDMS channel and a piece of thin glass (0.18 mm), making it very cheap and easy to replace. Overall, this manuscript proposes an on-chip cytometer that can test blood cells, bacteria, and other micro-particles in liquids. Because of the low price and small volume, the system is especially suitable for places far away from the laboratory and undeveloped areas and for family health tests.

2. Materials and Methods

2.1. System Setup

The flow cytometer utilized a lens-less imaging technique based on an in-line holography structure, and the overall structure is shown in Figure 1.

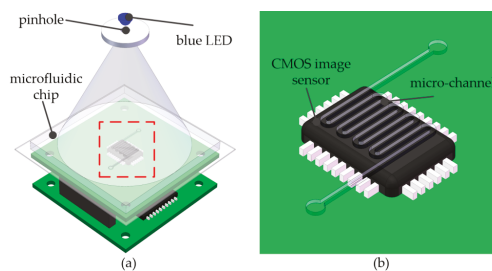


Figure 1. The structure of an on-chip flow cell counting system: (a) The general structure of the system; (b) the micro-channel on the image sensor (CIS) surface in the red box in (a).

As shown in Figure 1, the flow cytometer comprised a greyscale CIS (Aptina MT9P031, Micron Technology, Pennsylvania, ID, USA), a PDMS microfluidic chip and a blue light-emitting diode (LED) light source (central wavelength of ~ 465 nm). The pixel size of the CIS was $2.2 \mu\text{m}$, the effective pixel size was $2592 \text{ H} \times 1944 \text{ V}$ ($5.7 \text{ mm} \times 4.2 \text{ mm}$), and the imaging area reached $\sim 24.4 \text{ mm}^2$. To obtain holographic diffraction patterns on the surface of the CIS, the blue light LED was located 5 cm above the surface of the image sensor. In addition, there was a plate with a pinhole (diameter of 0.1 mm) at the front of the LED to obtain a coherent light source. To utilize the large FOV of the CIS, an S-type micro-channel was designed that could easily determine the volume of liquid samples and count the maximum possible number of cells in a frame. Moreover, the concentration of cells in a specimen could be calculated accurately, similar to a classic cell counting chamber. We used a PDMS channel and a piece of thin glass bonded together to obtain a microfluidic chip to capture the holograms of cells (the diffractive shadow images of cell) and fix the microfluidic chip on the surface of the CIS. We briefly introduce the fabricated process of the microfluidic below.

The photoresist (SU-8 2015, Microchem, Westborough, MA, USA) and a silicon wafer (4 inches in diameter) were used to fabricate positive model. The 3 mL of photoresist was dropped in the centrality of a wafer, and the photoresist film was $30 \mu\text{m}$ in thickness after using the spin coater at 1500 r/min for 15 s. Then, the silicon wafer was pre-baked for 15 min at $95 \text{ }^\circ\text{C}$. The pre-designed channel photolithography plate was used for exposure on the lithography machine for 125 s. Next, the exposed wafer was after-baked for 3 min at $95 \text{ }^\circ\text{C}$, and developed for 3 min. Then, we poured 30 g of liquid PDMS on the positive film, and put it in baking box for 40 min at $95 \text{ }^\circ\text{C}$ to solidify. The solidified PDMS layer and a piece of thin glass were bonded by vacuum plasma technique. Finally, the PDMS layer was drilled the holes of the inlet and outlet to finish the microfluidic chip.

However, since a microfluidic chip was used, a cell sample could be continuously detected, similar to a flow cytometer, as shown in Figure 2.

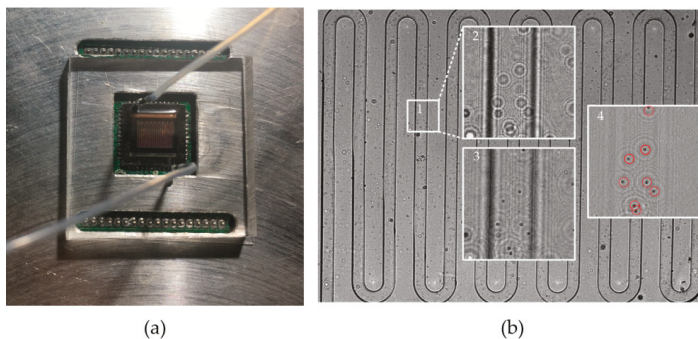


Figure 2. The proposed flow cytometer: (a) The flow cytometer system; (b) the holograms of the microfluidic chip captured by the system. Box 2 is an amplificatory image of box 1, and box 3 is a diffractive reconstruction image of box 2. Box 4 is the image of box 3 with the background removed, where the red circles mark the cells.

Next, we prepared an experimental platform to obtain the features and parameters of the proposed system. In addition, we found that the exposure time of the image sensor in this system was greater than 400 ms. Unfortunately, motion blur is caused by the movement of cells in the sample when the image sensor is operating during the exposure time. Therefore, we considered that instead of the cells flowing through the detection area at high speed, a large number of cells passed through the exposure region at one time. In other words, the system utilized the large FOV of the CIS to obtain a large number of images of cells from each frame. To avoid the motion blur caused by cell flowing, we used a method of periodically controlling the flow velocity of the specimen. There was only one inlet and

one outlet in the micro-channel, ensuring that the flow of all the tested cells out of the micro-channel and that of the new cells flow into the micro-channel took a short time. To obtain a sufficient processing time for the image processing algorithm, the new cells were injected into the micro-channel during the image processing period. Subsequently, all the tested cells flowed out the micro-channel, and then the flow of the cells stopped and the cell images were captured by the image sensor. With several repetitions, the device was able to collect the maximum possible number of cell signatures to improve the accuracy of the analysis.

2.2. Sample Preparation

The flow cytometer is suitable for samples with a large number of cells, such as blood. Therefore, we performed an experiment with whole blood. The concentration range of red blood cells (RBCs) in whole blood is from $\sim 4 \times 10^{12}/L$ to $5.5 \times 10^{12}/L$. To ensure the reconstruction of the wavefront in the in-line holography system, we had to reduce the concentration of cells in the whole blood. According to the experiments, we found that 1:400 was a suitable volume dilution to count blood cells. When RBCs were tested, the dilution ratio was 1:400, corresponding to 10 μL of whole blood diluted with 4 mL of phosphate buffer saline (PBS, 0.0067 M PO_4), and the resulting solution was pumped into the microfluidic chip for testing.

The concentration of white blood cells (WBCs) in whole blood is $4 \times 10^9/L$ – $10 \times 10^9/L$, and the ratio of WBCs to RBCs is close to 1:1000. When WBCs were tested, 200 μL of a whole blood sample was diluted with 400 μL of RBC lysis buffer and this was then injected into the micro-channel after one minute of delay. The study was approved by the School of Automation and Information Ethics Committee, Xi'an University of Technology.

2.3. Reconstruction of Lens-Less Holographic Images

The lens-less imaging technique utilizes an in-line holographic structure proposed by Gabor [33] to reconstruct the image of the cell plane. The lens-less holographic imaging system is mainly composed of a blue LED light source, a pinhole plate, a microfluidic chip and a CIS, as shown in Figure 3.

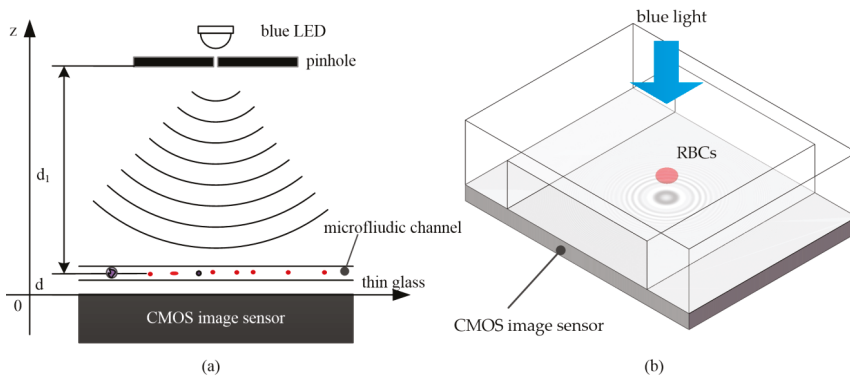


Figure 3. Graphic sketch of an in-line holographic microscope: (a) the structure of the lens-less holographic imaging system; (b) the procedure for capturing the lens-less hologram by the CIS.

Because of the infinitesimal size of blood cells (~ 2 – $15 \mu m$), the shadows of the blood cells on the surface of the CIS are diffraction images. Due to the influence of diffraction phenomenon, the shorter the wavelength of light source is, the higher the spatial resolution of the microscopic image becomes. In the most commonly used LED of single frequency light sources, a blue light source has the shortest wavelength. So we chose a blue LED as the light source. For convenience, we assumed that the cell plane was the object plane and that the surface of CIS was the image plane. The distance from the

pinhole to the object plane was d_1 , and the distance from the object plane to the image plane was d ($d_1 \gg d$). According to the angular spectrum theory of diffraction, we can reconstruct an image of the object plane by recording the image plane. We assumed that the transmittance of the sample was $O(x, y)$ and that the complex amplitude of the wavefront through the object plane was as below:

$$U_d(x, y) = 1 - O(x, y) \tag{1}$$

Here, the image plane is assumed as the plane of $z = 0$, and the object plane is assumed as the plane of $z = d$. According to the Rayleigh–Sommerfeld diffraction theory, the transfer function of light waves in two planes separated by a distance d is defined as:

$$H_d(\varepsilon, \eta) = \begin{cases} \exp\left[jd\frac{2\pi}{\lambda}\sqrt{1 - (\lambda\varepsilon)^2 - (\lambda\eta)^2}\right], & \varepsilon^2 + \eta^2 < \frac{1}{\lambda^2} \\ 0, & \text{otherwise} \end{cases} \tag{2}$$

Here, ε and η denote the coordinates of a frequency domain and have been transformed by x and y into a spatial domain. λ is the wavelength of the light source. According to the transfer function, we can obtain the complex amplitude of the image plane:

$$U_0(x, y) = H_d^+[1 - O(x, y)] \tag{3}$$

where H_d^+ and H_d^- represent the optical forward and backward propagation operators, which carry out a fast Fourier transform and an inverse fast Fourier transform, respectively, belonging to a convolution operator. d denotes the distance of the light propagation; in other words, it is the distance between the object plane and the image plane. + and – denote forward propagation and backward propagation along the z -axis, respectively. The light intensity in the holographic plane recorded by the image sensor is the square of the amplitude of the light wave, and the light intensity is as below:

$$I_0(x, y) = |U_0(x, y)|^2 \tag{4}$$

In Equation (4), $U_0(x, y)$ is the complex amplitude of the actual light wave in the image plane, but the image sensor can receive only the light intensity, I_0 , and the phase is discarded. Normally, image sensor acquisition of the holographic plane light intensity is a linear process, so the light intensity information collected by image sensor can be expressed as:

$$I_s(x, y) = \alpha + \beta I_0(x, y) \tag{5}$$

The amplitude of the light wave in the object plane can be obtained by the reconstruction of the distance image at the back of the image plane:

$$U_r(x, y) = H_d^+[I_s(x, y)] \tag{6}$$

With Equations (1)–(6), we obtain Equation (7):

$$U_r(x, y) = D - O^*(x, y) - H_{2d}^+[O(x, y)] + H_d^+\left\{|H_d^+[O(x, y)]|^2\right\} \tag{7}$$

In Equation (7), the first term is the direct current (DC) component; the second term is the focus image; the third term is the holographic image, which is the focus image backward propagated a distance of $2d$; and the fourth term is the intermodulation. The second and third terms constitute the twin image, which still appears after the forward transfer reconstruction of the diffraction plane and is difficult to separate. In fact, the twin-image phenomenon, which is caused by the absence of a light phase, is a major problem in the in-line holographic system. In addition, we used micro-bead images obtained with a $10\times$ objective lens to simulate the twin-image problem (Figure 4).

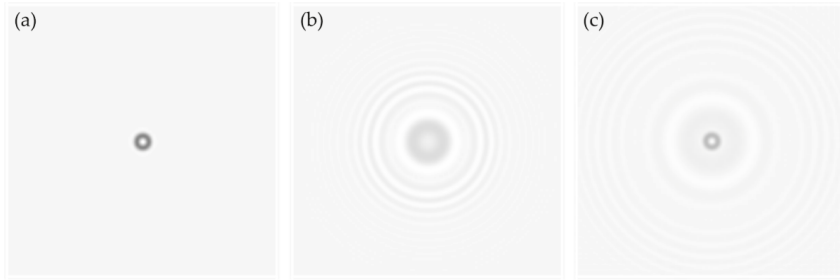


Figure 4. The twin-image problem: (a) a 7 μm micro-bead image was used to simulate the reconstruction of lens-less holographic images. (b) By simulating the holographic imaging with Equations (1)–(4), we retained the amplitude of the complex number and discarded the phase to simulate the recording procedure of a CIS. (c) We used Equation (6) to reconstruct the focus image of object plane, but it was polluted by the twin-image phenomenon.

According to Gabriel Koren’s research [32], we can use only one diffractive to reconstruct a focus image of the object plane and suppress the twin-image phenomenon. In our proposed algorithm, only a holographic diffraction image and a cell-absent background image were needed to reconstruct the phase and obtain a focus image of the object plane. The general steps were as follows:

Step 1: Using the square root of the light intensity and the initial value of the phase (generally 0), reversely transfer the diffractive pattern of the image plane back to the object plane by the transfer function to obtain the focus image. However, the initial estimation of the object plane seriously suffers from the twin-image phenomenon. Thus, it is necessary to use the following steps to suppress the twin images. The main operation of the reconstruction process is similar to the frequency domain filter in digital image processing. The transfer function of the filter is shown by Equation (2), and the reconstruction algorithm of the object plane is shown below:

$$U_r^1(x, y) = H_d^- \left[\sqrt{I_s(x, y)} \right] \tag{8}$$

Step 2: The region information of the object is extracted from the preliminary estimated object image, which is used for the object plane constraint. Classic image segmentation algorithms, such as the gradient boundary extraction algorithm and the threshold segmentation algorithm can be used to find the object plane constraint. Because of the low signal-to-noise ratio (SNR) of the image extracted by the CIS, the threshold segmentation algorithm is more reliable. The threshold is 0.34 in this manuscript; in other words, the grey value of cell regions on the object plane is usually less than 0.34.

Step 3: The cell region is the C region, and the background is the non-C region. Through an iterative algorithm, the cell regions are close to the real image, and the twin-image phenomenon will be weakened on the object plane. The algorithm is

$$U_r^{(i+1)}(x, y) = \begin{cases} m \times D(x, y), x, y \notin C \\ U_r^i(x, y), x, y \in C \end{cases} \tag{9}$$

where $D(x, y)$ is the background image, which is obtained by the image sensor without cells, and m is shown with

$$m = \text{mean}(U_r^i(x, y)) / \text{mean}(D(x, y)) \tag{10}$$

Step 4: The new complex amplitude of the image is obtained by the forward transfer operation. The phase of the newly calculated complex amplitude is retained, and the amplitude is replaced by the original known image plane amplitude. This process is called the image plane constraint:

$$U_0^i(x, y) = |U_0^1(x, y)| \times \exp(j \times \varphi_0^i(x, y)) \tag{11}$$

The iteration can be completed by repeating the third and fourth steps and can converge after 5–6 iterations. To obtain the missing phase, the algorithm iterates between two planes (object plane and image plane) through the amplitude and makes the iteration convergent using the object plane constraint (Equation (9)) and the image plane constraint (Equation (11)). However, the algorithm converges rapidly in the initial several iterations, and then the convergence is almost stagnant. Furthermore, there is a large error in the estimation of the initial phase when the distance between the object plane and the image plane has a deviation in an actual system. Therefore, the classic phase recovery algorithm is necessary to improve an actual system. The manuscript proposes an initial phase constraint algorithm based on the classic algorithm, in which Equation (8) is replaced by Equation (12):

$$U_r^1 = H_d^- \left[\sqrt{I_s(x, y)} \times \exp \left(j \times \left(1 - \sqrt{I_s(x, y)} \right) \right) \right]. \tag{12}$$

In general, there is no linear relationship between the amplitude and phase in a complex number. However, the phase changes of near-coherent light passing through a cell are related to the cell transmittance, and the cell transmittance is also expressed in amplitude. Therefore, there is a weak correlation between amplitude and phase. Using this property, we can estimate the initial phase of the iteration by transmittance. Through the initial phase constraint, the iterative convergent speed is faster, the reconstruction precision is higher, and the anti-jamming ability is stronger.

To test the performance of the algorithm, we used a dyed leucocyte captured by a 20× object lens microscope to perform a simulation. Using Equations (1)–(5) to establish a diffractive degradation model, we obtained the diffractive pattern of the leucocytes. To replicate our flow cytometer, we chose the same parameters as the actual system for simulation. The central wavelength of the light source was 465 nm, the distance between the object plane and the image plane was 0.875 mm, and the pixel size was 2.2 μm. The iterative algorithm without the initial phase constraint was compared to the iterative algorithm with the initial phase constraint, and the result is shown in Figure 5.

To test the performance of the two methods, we calculated the root-mean-square error (RMSE) for the reconstructed image of the object plane and original image. Finally, the proposed algorithm was used to reconstruct the cell image on the object plane and compared with the original image to calculate the RMSE:

$$RMSE = \sqrt{\frac{1}{MN} \sum_{m=1}^M \sum_{n=1}^N (|U_r^i(x, y)| - |U_d(x, y)|)^2} \tag{13}$$

According to the distance between the object plane and image plane, we conducted two groups of comparative experiments. The first was without deviation, and the second was with 20% deviation. The RMSEs of the two method were calculated by Matlab (Version: 2016b, MathWorks, Endogenous, MA, USA) and are shown in Figure 6.

In Figure 6, the ‘phase constraint’ is our proposed method, and the ‘non-phase constraint’ is the classic method. The proposed method has a faster convergence rate and a lower error rate, making it more conducive to counting and analyzing cells. As shown in Figures 5 and 6, by comparing the two groups with the two methods, we found that the iteration method with initial phase constraints had a faster iteration speed. In the case of a 20% distance deviation, the proposed method was able to restore the cell image, whereas the original method could not restore the image effectively, which has a great influence on the actual system. Moreover, when all the parameters were accurate, the proposed method converged faster, and the RMSE of image reconstruction was smaller. The results in Figure 6

show that our proposed method can greatly reduce the time consumption of the image processing algorithm and provide a guarantee for the real-time implementation of the system.

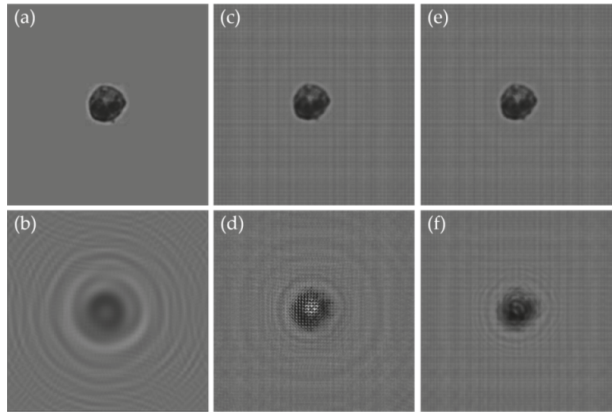


Figure 5. The result of our proposed method and classic method without a phase constraint. (a) The image captured by a 20× object lens microscope; (b) the diffractive image on the image plane; (c) the image reconstructed by Gabriel Koren’s method with 0% deviation in distance; (d) the image reconstructed by Gabriel Koren’s method with 20% deviation in distance; (e) the image reconstructed by our modified method with 0% deviation in distance; (f) the image reconstructed by our modified method with 20% deviation in distance.

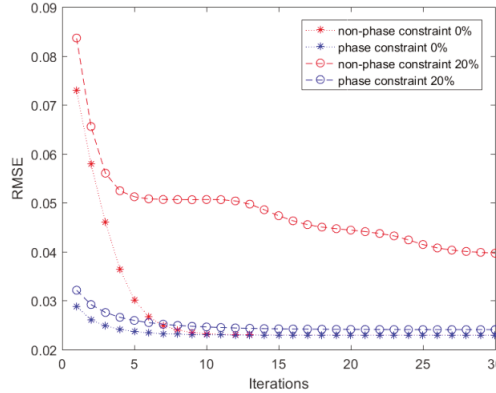


Figure 6. The root-mean-square error (RMSE) of our proposed method and the classic method without a phase constraint.

Finally, we used a frame image of whole blood cells captured by the lens-less flow cytometer to test the computation time. We used Matlab to reconstruct the holographic image, and the hardware was graphics workstation (Xeon E5-2600, 16 GB DIMM DDR4, Intel, Santa Clara, CA, USA). The time consumed for one iteration was about 2 s with the classic method of phase iterative reconstruction, and the proposed method took ~0.1 s longer than the classic method. However, the method we proposed only needed 5 iterations, and the classic method needed 10 times to achieve the same reconstruction effect. Therefore, the time consumed by the propose method was ~12.82 s, and that of the classic one was ~24.42 s. In other words, it means that the proposed method reduced the computational time by

~48%. In general, the two algorithms have almost the same computational complexity. Our algorithm only adds one phase constraint to the first image reconstruction, but its time computation is ~0.19 s.

2.4. Blood Cell Analysis Method

In the on-chip flow cytometer, the blood cells flow in the micro-channel above the image sensor, and their holographic diffraction image is transmitted onto the sensor surface by the near-coherent light source. To reduce the cost and volume of the device, an ordinary blue LED with a limited light intensity was used. The light on the plane of the cells is further weakened because the light is illuminated through a pinhole. Therefore, the exposure time of the image sensor needs to be longer than 400 ms to capture a bright enough hologram. If the blood cells move during the exposure time of the CIS, there is a motion blur, as shown in Figure 7a. To solve this problem, we used a pulse injection method, which is shown in Figure 7b.

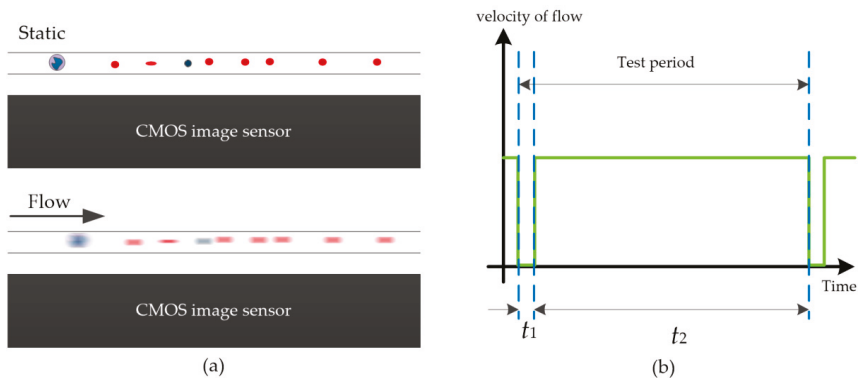


Figure 7. The pulse flow control mode: (a) The flow of cells stops in the micro-channel during the CIS exposure time to capture a holographic image of the cells. (b) When the system is processing images of cells captured in the last exposure, the tested cells flow out of the micro-channel, and the new cells flow into the micro-channel.

In Figure 7, t_1 is the exposure time, and t_2 is the injection time. This process can be controlled by a micro-pump. Due to the high precision of micro-pump control, the injection time and stationary time of the blood cells can be fixed. Therefore, the algorithm can be processed according to fixed parameters. After an experiment, accurate cell image collection and injection of new samples in micro-pump mode can be ensured.

In addition, instead of the micro-pump method, a hand-push model can be used to reduce the cost and volume of the device. In the hand-push model, the motion state of the cells in the microfluidic chip can be detected by the image processing algorithm. The system acquisition accuracy can generally be guaranteed with $t_1 > 5$ s and $t_2 > 20$ s. The state of cell motion in the microfluidic chip is detected by the RMSE between two frames.

In addition, there are two important problems, which relate to cell overlap. The first is the cell overlap in the holographic image. As mentioned earlier, the raw image captured by the lens-less platform is a holographic image, so the size of a diffractive image of the cell is ~4 times bigger than that of a focus image. The inevitable cell image overlap was solved by the phase iterative reconstruction algorithm. The other problem relates to the position of cell overlap and the 3D structure of the micro-channel leads to the shadow image overlap. The problem is difficult to solve by digital image processing algorithms. Therefore, we used a diluted cell sample to solve the problem. According to the experiment, the 1:400 dilution ratio is an acceptable ratio for the blood cells, and cell overlap is almost impossible at 1:1000 dilution. Considering the speed of counting, we chose a 1:400 dilution.

The microfluidic chip was mounted above the CIS so that we could easily obtain the background image without cells. In addition, we then injected a fluid sample of cells into the micro-channel to record the holograms and reconstruct the focus images of the cells. The location and size of the cells were determined by threshold segmentation with images with background interference removed. According to our experiment, the flow velocity was 100 $\mu\text{L}/\text{min}$. Because of the infinitesimal volume of the micro-channel (0.246 μL), the digital injection pump was able to replace all cells in the channel less than 1s. However, it took ~ 15 s to 20 s for the cells in the fluid to become static. Fortunately, were able to use this time to process the cell image. Since the pixel number of the CIS was about 5.04 million, the computer took ~ 16 s to process the full resolution image.

The on-chip flow cytometry capability of this method, together with its ease of use, may offer a highly precise and lower cost alternative to existing whole blood analysis tools, urine analysis tools and plankton analysis tools, especially for point-of-care biological and medical tests.

3. Results and Discussion

To test the performance of our proposed system, we performed an experiment with whole blood cells. In the results section, we show the results of focus image reconstruction for cell counting in our proposed system.

Figure 8 shows that the images of the cells were captured by removing the background in the reconstructed image and that the quantity and size of the sample were determined by the image threshold segmentation algorithm. The system obtained an accurate background image, effectively removed the background effect, accurately acquired the location of the sample, and greatly improved the counting accuracy. Finally, the cell concentration was calculated based on the number of cells and the volume of the micro-channel. The micro-channel was 30 μm in height, 150 μm in width, and ~ 54.6 mm in length; thus, it was easy to calculate its volume as ~ 0.246 μL and projective area as 8.19 mm^2 .

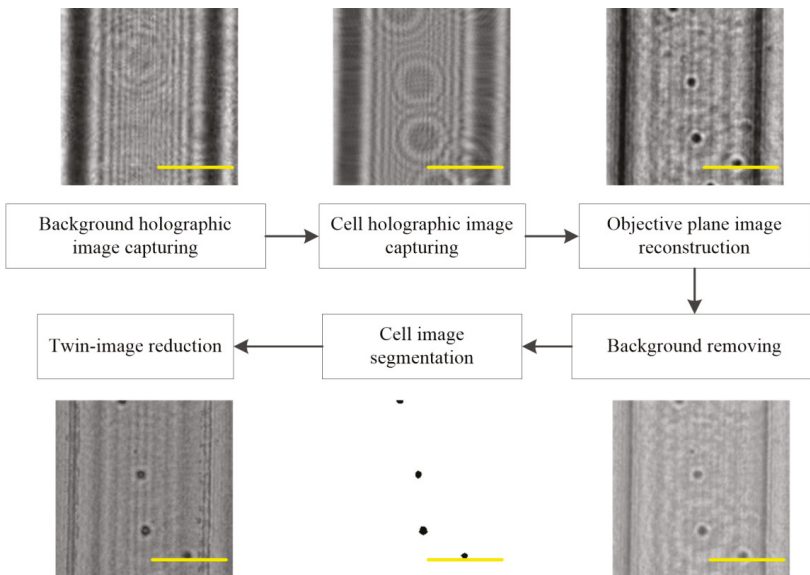


Figure 8. The reconstruction of the focus cell images flow path. To better observe the effect of holographic image reconstruction, which is a small segment of the whole image, all scale bars indicate 100 μm .

Then, we used different concentrations of the whole blood samples to test the linearity and the accuracy of the proposed method. We diluted seven groups of different concentrations of blood cells with a dilution ratio to perform an experiment. The results of this experiment are indicated in Figure 9.

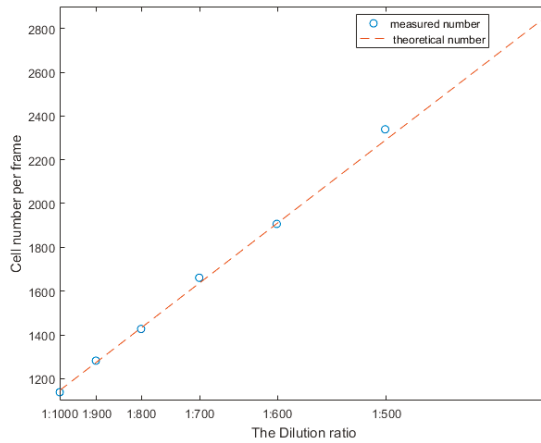


Figure 9. The result of linearity of different concentrations.

Ultimately, we used whole blood cells to count RBCs and WBCs in order to verify the effectiveness of the cell counting procedure. According to the above preparation method, diluted whole blood cells and lysed whole blood cells were divided twice. In addition, we needed to subtract the concentration of WBCs from the concentration of whole blood cells to get the concentration of RBCs. Then, the test results of the proposed system were compared with those of an automatic blood cell analyser (BC-5180, Mindray, Shenzhen, China), and the results are shown in Table 1.

Table 1. The result of different sample concentrations.

Sample No.	Tools	White Blood Cells (WBCs) Concentration	Error	Red Blood Cells (RBCs) Concentration	Error
1	Our system	$6.83 \times 10^9/L$	1.4%	$5.22 \times 10^{12}/L$	2.4%
		BC-5180		$6.93 \times 10^9/L$	
2	Our system	$4.80 \times 10^9/L$	1.2%	$5.28 \times 10^{12}/L$	1.5%
		BC-5180		$4.86 \times 10^9/L$	
3	Our system	$6.33 \times 10^9/L$	0.6%	$4.64 \times 10^{12}/L$	1.9%
		BC-5180		$6.29 \times 10^9/L$	
4	Our system	$5.10 \times 10^9/L$	2.3%	$4.61 \times 10^{12}/L$	1.5%
		BC-5180		$5.22 \times 10^9/L$	
5	Our system	$6.78 \times 10^9/L$	2.6%	$4.87 \times 10^{12}/L$	2.7%
		BC-5180		$6.96 \times 10^9/L$	

Table 1 shows that the average fractional errors of RBC and WBC counting were 2% and 1.6%, respectively. In other words, the relative error between the proposed system and the whole blood cell counter was less than 2%. This accuracy indicates the potential for applying the proposed system to the early detection of some liquid samples, such as blood tests, urine tests, semen tests, and microbiological tests. In areas where the use of large-scale, high-precision instruments is inconvenient, such as the outdoors, the battlefield, and underdeveloped areas, the tool proposed here can enable early and real-time detection.

4. Conclusions

The current paper improved the twin-image recovery algorithm in a coaxial holography system and increased the convergence speed of the iterative algorithm. In addition, this paper proposed a flow cytometer based on lens-less holographic microscopy that improved the counting accuracy to 2.3%. The on-chip flow cytometer based on a pulse injection method can continuously count cells and continuously collect a large number of cell images for subsequent cell analysis. Ultimately, this on-chip flow cytometer is very suitable for use in underdeveloped areas and areas far away from the laboratory because of its low price and tiny size and is in full compliance with the current development trend of point-of-care testing (POCT).

Author Contributions: Yuan Fang conceived and designed the experiments; Yuan Fang and Yuquan Jiang performed the experiments; Yuan Fang and Chaoliang Dang analysed the data; Ningmei Yu contributed reagents/materials/analysis tools; Yuan Fang wrote the paper.

Acknowledgments: This work was supported by the National Natural Science Foundation of China (No. 61471296), the National Natural Science Foundation of China (No. 61771388) and the key research project of Baoji University of Arts and Sciences (No. 209010439).

Conflicts of Interest: The authors declare no conflict of interest.

References

1. Tang, W.; Tang, D.; Ni, Z.; Xiang, N.; Yi, H. Microfluidic impedance cytometer with inertial focusing and liquid electrodes for high-throughput cell counting and discrimination. *Anal. Chem.* **2017**, *89*, 3154–3161. [[CrossRef](#)] [[PubMed](#)]
2. Zheng, G. Innovations in Imaging System Design: Gigapixel, Chip-Scale and Multi-Functional Microscopy. Ph.D. Thesis, California Institute of Technology, Pasadena, CA, USA, 2013.
3. Lee, A.S. Bright-Field and Fluorescence Chip-Scale Microscopy for Biological Imaging. Ph.D. Thesis, California Institute of Technology, Pasadena, CA, USA, 2014.
4. Lee, S.A.; Yang, C. A smartphone-based chip-scale microscope using ambient illumination. *Lab Chip* **2014**, *14*, 3056–3063. [[CrossRef](#)] [[PubMed](#)]
5. Lee, S.A.; Leitao, R.; Zheng, G.; Yang, S.; Rodriguez, A.; Yang, C. Color capable sub-pixel resolving optofluidic microscope and its application to blood cell imaging for malaria diagnosis. *PLoS ONE* **2011**, *6*, e26127. [[CrossRef](#)] [[PubMed](#)]
6. Zheng, G.; Lee, S.A.; Yang, S.; Yang, C. Sub-pixel resolving optofluidic microscope for on-chip cell imaging. *Lab Chip* **2010**, *10*, 3125–3129. [[CrossRef](#)] [[PubMed](#)]
7. Zheng, G.; Lee, S.A.; Antebi, Y.; Elowitz, M.B.; Yang, C. The ePetri dish, an on-chip cell imaging platform based on subpixel perspective sweeping microscopy (SPSM). *Proc. Natl. Acad. Sci. USA* **2011**, *108*, 16889–16894. [[CrossRef](#)] [[PubMed](#)]
8. Greenbaum, A.; Luo, W.; Khademhosseini, B.; Su, T.-W.; Coskun, A.F.; Ozcan, A. Increased space-bandwidth product in pixel super-resolved lensfree on-chip microscopy. *Sci. Rep.* **2013**, *3*, 1717. [[CrossRef](#)]
9. Isikman, S.O.; Bishara, W.; Mudanyali, O.; Sencan, I.; Su, T.-W.; Tseng, D.K.; Yaglidere, O.; Sikora, U.; Ozcan, A. Lensfree on-chip microscopy and tomography for bio-medical applications. *IEEE J. Sel. Top. Quantum Electron.* **2011**, *18*, 1059–1072. [[CrossRef](#)] [[PubMed](#)]
10. Weidling, J.; Isikman, S.O.; Greenbaum, A.; Ozcan, A.; Botvinick, E. Lens-free computational imaging of capillary morphogenesis within three-dimensional substrates. *J. Biomed. Opt.* **2012**, *17*, 126018. [[CrossRef](#)] [[PubMed](#)]
11. Oh, C.; Isikman, S.O.; Khademhosseini, B.; Ozcan, A. On-chip differential interference contrast microscopy using lensless digital holography. *Opt. Express* **2010**, *18*, 4717–4726. [[CrossRef](#)] [[PubMed](#)]
12. Mudanyali, O.; Tseng, D.; Oh, C.; Isikman, S.O.; Sencan, I.; Bishara, W.; Oztoprak, C.; Seo, S.; Khademhosseini, B.; Ozcan, A. Compact, light-weight and cost-effective microscope based on lensless incoherent holography for telemedicine applications. *Lab Chip* **2010**, *10*, 1417–1428. [[CrossRef](#)] [[PubMed](#)]
13. Tseng, D.; Mudanyali, O.; Oztoprak, C.; Isikman, S.O.; Sencan, I.; Yaglidere, O.; Ozcan, A. Lensfree microscopy on a cellphone. *Lab Chip* **2010**, *10*, 1787–1792. [[CrossRef](#)] [[PubMed](#)]

14. Seo, S.; Isikman, S.O.; Sencan, I.; Sencan, I.; Mudanyali, O.; Su, T.-W.; Bishara, W.; Erlinger, A.; Ozcan, A. High-throughput lens-free blood analysis on a chip. *Anal. Chem.* **2010**, *82*, 4621–4627. [[CrossRef](#)] [[PubMed](#)]
15. Bishara, W.; Su, T.W.; Coskun, A.F.; Ozcan, A. Lensfree on-chip microscopy over a wide field-of-view using pixel super-resolution. *Opt. Express* **2010**, *18*, 11181–11191. [[CrossRef](#)] [[PubMed](#)]
16. Mudanyali, O.; Oztoprak, C.; Tseng, D.; Erlinger, A.; Ozcan, A. Detection of waterborne parasites using field-portable and cost-effective lensfree microscopy. *Lab Chip* **2010**, *10*, 2419–2423. [[CrossRef](#)] [[PubMed](#)]
17. Su, T.W.; Erlinger, A.; Tseng, D.; Ozcan, A. Compact and light-weight automated semen analysis platform using lensfree on-chip microscopy. *Anal. Chem.* **2010**, *82*, 8307–8312. [[CrossRef](#)] [[PubMed](#)]
18. Khademhosseini, B.; Biener, G.; Sencan, I.; Ozcan, A. Lensless on-chip color imaging using nano-structured surfaces and compressive decoding. In Proceedings of the 2011 Conference on Lasers and Electro-Optics, Baltimore, MD, USA, 1–6 May 2011.
19. Zhu, H.; Yaglidere, O.; Su, T.; Tseng, D.; Ozcan, A. Cost-effective and compact wide-field fluorescent imaging on a cell-phone. *Lab Chip* **2011**, *11*, 315–322. [[CrossRef](#)] [[PubMed](#)]
20. Coskun, A.F.; Sencan, I.; Su, T.W.; Ozcan, A. Wide-field lensless fluorescent microscopy using a tapered fiber-optic faceplate on a chip. *Analyst* **2011**, *136*, 3512–3518. [[CrossRef](#)] [[PubMed](#)]
21. Coskun, A.F.; Sencan, I.; Su, T.W.; Ozcan, A. Lensfree fluorescent on-chip imaging of transgenic *Caenorhabditis elegans* over an ultra-wide field-of-view. *PLoS ONE* **2011**, *6*, e15955. [[CrossRef](#)] [[PubMed](#)]
22. Bishara, W. Holographic pixel super-resolution in portable lensless on-chip microscopy using a fiber-optic array. *Lab Chip* **2011**, *11*, 1276–1279. [[CrossRef](#)] [[PubMed](#)]
23. Isikman, S.O.; Bishara, W.; Sikora, U.; Yaglidere, O.; Yeah, J.; Ozcan, A. Field-portable lensfree tomographic microscope. *Lab Chip* **2011**, *11*, 2222–2230. [[CrossRef](#)] [[PubMed](#)]
24. Isikman, S.O.; Bishara, W.; Zhu, H.; Ozcan, A. Optofluidic tomography on a chip. *Appl. Phys. Lett.* **2011**, *98*, 161109. [[CrossRef](#)] [[PubMed](#)]
25. Isikman, S.O.; Bishara, W.; Mavandadi, S.; Yu, F.W.; Feng, S.; Lau, R.; Ozcan, A. Lens-free optical tomographic microscope with a large imaging volume on a chip. *Proc. Natl. Acad. Sci. USA* **2011**, *108*, 7296–7301. [[CrossRef](#)] [[PubMed](#)]
26. Nordin, G.P.; Mellin, S.D. Limits of scalar diffraction theory and an iterative angular spectrum algorithm for finite aperture diffractive optical element design. *Opt. Express* **2001**, *8*, 705–722.
27. Roy, M.; Jin, G.; Seo, D.; Nam, M.-H.; Seo, S. A simple and low-cost device performing blood cell counting based on lens-free shadow imaging technique. *Sens. Actuators B Chem.* **2014**, *201*, 321–328. [[CrossRef](#)]
28. Lee, J.; Kwak, Y.H.; Paek, S.-H.; Han, S.; Seo, S. CMOS image sensor-based ELISA detector using lens-free shadow imaging platform. *Sens. Actuators B Chem.* **2014**, *196*, 511–517. [[CrossRef](#)]
29. Jin, G.; Yoo, I.H.; Pack, S.P.; Yang, J.W.; Ha, U.H.; Paek, S.H.; Seo, S. Lens-free shadow image based high-throughput continuous cell monitoring technique. *Biosens. Bioelectron.* **2012**, *38*, 126–131. [[CrossRef](#)] [[PubMed](#)]
30. Seo, D.; Oh, S.; Lee, M.; Hwang, Y.; Seo, S. A field-portable cell analyzer without a microscope and reagents. *Sensors* **2017**, *18*, 85. [[CrossRef](#)] [[PubMed](#)]
31. Huang, X.; Jiang, Y.; Liu, X.; Xu, H.; Han, Z.; Rong, H.; Yang, H.; Yan, M.; Yu, H. Machine learning based single-frame super-resolution processing for lensless blood cell counting. *Sensors* **2016**, *16*, 1836. [[CrossRef](#)] [[PubMed](#)]
32. Koren, G.; Polack, F.; Joyeux, D. Iterative algorithms for twin-image elimination in in-line holography using finite-support constraints. *J. Opt. Soc. Am. A* **1993**, *10*, 423–433. [[CrossRef](#)]
33. Gabor, D. A new microscopic principle. *Nature* **1948**, *161*, 777–778. [[CrossRef](#)] [[PubMed](#)]



© 2018 by the authors. Licensee MDPI, Basel, Switzerland. This article is an open access article distributed under the terms and conditions of the Creative Commons Attribution (CC BY) license (<http://creativecommons.org/licenses/by/4.0/>).

MDPI
St. Alban-Anlage 66
4052 Basel
Switzerland
Tel. +41 61 683 77 34
Fax +41 61 302 89 18
www.mdpi.com

Micromachines Editorial Office
E-mail: micromachines@mdpi.com
www.mdpi.com/journal/micromachines



MDPI
St. Alban-Anlage 66
4052 Basel
Switzerland

Tel: +41 61 683 77 34
Fax: +41 61 302 89 18

www.mdpi.com



ISBN 978-3-03921-825-7